

Design and Evaluation of a Powered Four-Bar Prosthetic Hip Joint

Michael Botros

Thesis submitted to the Faculty of Engineering
in partial fulfillment of the requirements for the degree of

MASTER OF APPLIED SCIENCE

in Biomedical Engineering

Ottawa-Carleton Institute for Biomedical Engineering
University of Ottawa
Ottawa, Ontario, Canada

May 2024

© Michael Botros, Ottawa, Canada, 2024

Abstract

Hip-level amputees face challenges in ambulation due to the lack of residuum musculature and prosthetic hip actuator power. A powered four-bar hip, providing augmenting hip flexion-extension moments, was successfully designed, prototyped, and tested. The powered hip contains the Össur Power Knee 2 harmonic drive DC motor, providing up to 96 N·m of torque. Additionally, the powered hip contains a four-bar linkage to guide hip flexion-extension, and a torque transmission linkage to convert motor torque to a hip flexion-extension moment. Link lengths were optimized to balance size, weight, range of motion, mechanical advantage, and component forces. The powered hip prototype has mostly met the design criteria and has passed all ISO 15032:2000 A100 static compression tests. Furthermore, three able-bodied individuals, with an average weight of 96 kg, walked successfully with the powered hip by means of a hip-knee-ankle-foot prosthesis simulator. No prototype cracking or deformation were observed during testing. The powered hip would benefit from a supplementary bearing to reduce output bearing loading. Moreover, future design optimization could reduce device weight, improve cosmesis, and provide more mechanical advantage at larger hip flexion angles to improve device performance beyond level walking. Future powered hip evaluation with hip-level amputees will further inform device performance.

Table of Contents

Abstract	ii
Table of Contents	iii
List of Figures	vii
List of Tables	xvi
Definitions.....	xix
Abbreviations	xx
Acknowledgments.....	xxi
Chapter 1: Introduction	1
1.1 Rationale.....	2
1.2 Objectives.....	4
1.3 Project Scope.....	4
1.4 Thesis Contributions	5
1.5 Thesis Outline	5
Chapter 2: Literature Review	6
2.1 Hip-Level Amputations.....	6
2.2 Hip-Knee-Ankle-Foot Prostheses with Single-Axis Hip Joints	7
2.2.1 Early Hip Disarticulation Prostheses	7
2.2.2 Canadian-Type Hip Disarticulation Prostheses	8
2.2.3 Modern Single-Axis Hip Joints	10
2.3 Four-bar Linkages in Lower-Limb Prostheses	12
2.3.1 Four-Bar Linkages in Prosthetic Knee Joints	12
2.3.2 Prosthetic Four-Bar Knee Joints Mounted in Reverse at the Hip.....	17
2.3.3 Helix3D (7E10) Hip Joint.....	18
2.4 Overview of Prosthetic Hip Joint Specifications.....	25
2.5 Lower-Limb Amputee Gait	25

2.5.1 Gait Compensation Mechanisms and Gait Deviations	25
2.5.2 Hip and Knee Joint Kinematics and Kinetics	26
2.6 Powered Prostheses	30
2.6.1 Össur Power Knee 2	30
2.6.2 Powered Hip Prostheses	33
2.7 Summary	35
Chapter 3: Design Criteria	36
3.1 Range of Motion.....	36
3.2 Body Weight	36
3.3 Device Weight.....	36
3.4 Actuator Specifications	37
3.5 Mechanical Loading.....	37
3.6 Size and Cosmesis.....	38
3.7 Prosthetic Shortening	39
3.8 Lifespan.....	39
3.9 Summary	40
Chapter 4: Powered Hip Design.....	41
4.1 Design Overview.....	41
4.2 Range of Motion and Average Mechanical Advantage	42
4.3 Linkage Optimization.....	45
Chapter 5: Force Analysis	58
5.1 ISO 15032:2000	58
5.2 Powered Hip Instantaneous Center of Rotation	65
5.3 Link Forces Throughout the Gait Cycle.....	67
5.4 Motor-Only Analysis.....	73
5.5 Results	76
5.6 Chosen Load Case Scenarios for Further Analysis	80

Chapter 6: Stress Analysis	83
6.1 Failure Criteria	83
6.2 Powered Hip Materials.....	84
6.3 Link Thicknesses.....	86
6.4 Shaft Diameters	89
6.5 Finite Element Analysis	91
6.6 Deflection Analysis.....	112
Chapter 7: Bearing Analysis	113
7.1 Link Bearings	113
7.2 Output Bearing	114
Chapter 8: Prototype	117
Chapter 9: Evaluation.....	130
9.1 Static Compression Testing.....	130
9.2 Functional Testing.....	134
Chapter 10: Summary and Conclusions	141
10.1 Design Performance	142
10.2 Future Work	144
References	148
Appendix A: Candidate Designs	169
A.1 Single-Axis Powered Four-Bar Hip	169
A.2 Direct Drive Four-Bar Hip with Posterior Motor	169
A.3 Direct Drive Four-Bar Hip with Anterior Motor.....	172
A.4 Summary	174
Appendix B: MATLAB Code	175
Appendix C: Linkage Geometry	225
Appendix D: Link Length Optimization Iterations	235
Appendix E: Thread Engagement Lengths	242

Appendix F: Screw Preload Torques	245
Appendix G: 3D Printed Prototype	250
Appendix H: Screw Safety Factors	253
Appendix I: Engineering Drawings	254
Appendix J: Ethics Approval	265

List of Figures

Figure 2-1: Types of lower limb amputations. Adapted from [64], [65]. ..	6
Figure 2-2: Frontal view (left) and sagittal views (right) of the saucer-type prosthesis. Hip joint stability shown by the hip line being anterior to the center of mass (COM)-knee-ankle line. Adapted from [72]. ..	7
Figure 2-3: Frontal view (left) and sagittal views (right) of the tilting-table prosthesis. The center of mass (COM), and hip, knee, and ankle joints are aligned. Adapted from [72]. ..	8
Figure 2-4: Canadian hip disarticulation prosthesis a) without cosmetic cover, b) with cosmetic cover. Hip joint stability shown by the hip line being anterior to the center of mass (COM)-knee-ankle line. Adapted from [72]. ..	9
Figure 2-5: Otto Bock's single-axis hip joints from oldest to newest: a) 7E4 [78], b) 7E5 [79], c) 7E7 [44], d) 7E8 [81], e) 7E9 [82]. ..	11
Figure 2-6: Load line (black), joint loads (red), joint centers (red), and limb segments (red) at different parts of stance phase: a) foot strike, b) push-off, c) early and late stance phase superimposed with knee stability zone (black cross hatching). F is ground reaction force and M is the prosthetic side hip flexion-extension moment exerted by the transfemoral amputee. Adapted from [93]. ..	13
Figure 2-7: Alignment of hip, knee, and ankle joint centers to reduce required hip moment for knee stability. P is ground reaction force. M_h and M_k are hip and knee flexion-extension moments [90]..	14
Figure 2-8: Voluntary control four-bar knee prostheses: a) linkage configuration and resulting load lines, b) University of California Biomechanics Laboratory four-bar knee with centrode, c) Hosmer four-bar knee with centrode. Adapted from [91]. ..	15
Figure 2-9: a) Monocentric and polycentric prosthetic knee joints with instantaneous centers of rotation labelled with a grey dot, b) millimeter lengths of shank shortening (black) and toe clearance (grey) of prosthetic knee joints. 'FP 1', 'FP 2', 'Knee 0' and 'Knee+5' refer to knee alignment positions. Adapted from [99]. ..	16
Figure 2-10: a) Sagittal views of different hip flexion angles with a hip-knee-ankle-foot prosthesis containing the 3R21 knee joint at the hip (adopted from [19]), b) sagittal view (left) and frontal view (right) of the 3R21 knee joint (adapted from [130]). ..	17
Figure 2-11: a) EBS (3R60) knee joint for hip disarticulation or hemipelvectomy, b) EBS knee joint centrode when mounted at the hip from 0° to 140° flexion. Adapted from [132]. ..	18
Figure 2-12: a) Otto Bock Helix3D (7E10) hip joint for right leg prosthesis – anterior, medial, and posterior views from left to right, b) principle of the RSSR four-bar linkage with an axis tilted relative to the sagittal plane, medial view (left) and posterior view (right), adapted from [76]. ..	19

Figure 2-13: a) Hip-knee-ankle-foot prosthesis containing the Helix3D hip joint and the C-Leg knee [60]. b) Prosthetic leg alignment with the Helix 3D hip joint positioned anterior to the load line and the knee positioned 30 ± 10 mm posterior to the load line (adapted from [60])......	20
Figure 2-14: Frontal plane alignment adjustment for the Helix3D hip joint [60].....	20
Figure 2-15: Helix3D transverse hip motion to compensate for natural pelvic rotation - interior/exterior rotation versus time. Adapted from [17]......	21
Figure 2-16: Location of the Helix3D hip joint's instantaneous center of rotation (ICR) throughout the gait cycle based on hip flexion/extension. Adapted from [76].....	21
Figure 2-17: a) Helix3D anterior view showing hydraulic stride control parameters stance phase resistance (ST), free-swing range (FSW), swing phase resistance (SW), and two PU bands for swing initiation; b) medioanterior view showing the PU element location on the anterior link; c) medioposterior view showing the hydraulic cylinder connected to the anterior link.....	22
Figure 2-18: Effects of stance phase resistance (ST) on the time (expressed as percent gait cycle) to reach the hip extension stop [76].	23
Figure 2-19: Effects of swing phase resistance (SW) on step length [76].	23
Figure 2-20: Mean gait data with the Helix3D and 7E7 hip joints in comparison to able-bodied gait (± 1 standard deviation): a) flexion/extension moments, b) flexion/extension angles, c) pelvic tilt angle [13]......	24
Figure 2-21: Sagittal plane prosthetic hip joint kinematics and kinetics over one level-ground gait cycle for different levels of lower-limb amputation. HD/HP amputee data obtained from [13]. Mean curves shown starting from foot strike. Pelvic tilt data obtained from The Ottawa Hospital Rehabilitation Center. Other TF amputee data obtained from [149]. Able-bodied data obtained from [13], [154]..	27
Figure 2-22: Sagittal plane prosthetic knee joint kinematics and kinetics over one level-ground gait cycle for different levels of lower-limb amputation. Mean curves shown. HD/HP amputee data obtained from [13]. TF amputee data obtained from [149]. Able-bodied data obtained from [154]..	28
Figure 2-23: a) Össur Power Knee with a brushless DC motor at the proximal end [10], b) harmonic drive implemented in the Össur Power Knee brushless DC motor (adapted from [169]), c) harmonic drive operation (adapted from [170])......	31
Figure 2-24: Össur Power Hip – a) fully extended (23°), b) fully flexed (122°), c) user with Power Hip and Genium X2 setup. Adapted from [183].....	33
Figure 2-25: Powered hip joints not on the market: a) dual DC motor harmonic drive pulley system by Ueyama et al. (adapted from [14]), b) 2-UPR/URR joint by Song et al. (adapted from [15]), c) remote center mechanism by Fan et al. (adapted from [167]).....	34

Figure 3-1: Helix3D hip joint anteriorly mounted on the socket with an anterior protrusion of 2 cm. Adapted from [134].....	39
Figure 4-1: Powered four-bar hip joint (left) for use in a right-leg prosthesis (right).....	41
Figure 4-2: Powered four-bar hip joint operation, and motor components.....	42
Figure 4-3: Chosen design range of motion. Hip flexion-extension angle is in blue, motor angle is in red, and link dimensions are in green.....	43
Figure 4-4: Linkage optimization steps for each iteration.	45
Figure 4-5: Inputs (pink) and outputs (green) of powered hip geometry calculations at four-bar linkage singularity points and standing and sitting positions. Lateral view shown. Dimensions shown on an earlier powered hip model with the motor protruding medially. Origin at point A. Positive y is anterior and positive z is superior.....	46
Figure 4-6: Drive flange motor arm design region. The drive arm shaft should lie between the circle of diameter d_{cavity} and the circle of diameter d_{motor} . Original drive flange from the Össur Power Knee 2 motor shown.....	52
Figure 4-7: Powered hip extension singularity points and motor linkage configuration that produces hip flexion with clockwise motor rotation from hip extension singularity point. Medial view shown. Positive y is anterior and positive z is superior.....	52
Figure 4-8: Powered hip extension singularity points and motor linkage configuration that produces hip flexion with counterclockwise motor rotation from hip extension singularity point. Medial view shown. Positive y is anterior and positive z is superior.....	53
Figure 4-9: Powered hip flexion singularity points and motor linkage configuration that produces hip flexion with counterclockwise motor rotation from hip extension. ‘FBL’ designates ‘four-bar linkage’ and ‘MoL’ designates ‘motor linkage’	54
Figure 4-10: Powered hip sagittal plane motion from the four-bar linkage hip extension singularity position to the four-bar linkage hip flexion singularity position.....	55
Figure 4-11: Hip flexion angle θ_{flex} ($^{\circ}$) versus relative motor angle θ_m ($^{\circ}$).	55
Figure 4-12: Change in prosthetic thigh length from late stance phase to mid swing phase. Powered hip shortening of 23.8 mm at mid swing.....	56
Figure 5-1: ISO 15032:2000 compression: a) A-P extension, b) A-P flexion, c) M-L. The u' axis passes through the effective hip and knee joint centers (points 2 and 3). Equal and opposite forces F' and F act on the proximal and distal end attachments of the prosthetic thigh. Adapted from [186].....	59
Figure 5-2: ISO 15032 A-P extension end attachment free body diagrams. Adapted from [186].....	59
Figure 5-3: ISO 15032 A-P flexion end attachment free body diagrams. Adapted from [186].....	60
Figure 5-4: ISO 15032 M-L end attachment free body diagrams. Adapted from [186].	60

Figure 5-5: Powered hip free body diagrams for the ISO 15032:2000 A-P compression conditions. Motor turned off. Lateral view of older powered hip model shown at an arbitrary hip flexion angle.	62
Figure 5-6: Powered hip upper portion free-body diagram for the ISO 15032:2000 M-L compression condition. Older powered hip model shown. No forces are shown on the drive arm or the motor because the motor is turned off during ISO 15032:2000 compression tests.....	64
Figure 5-7: Location of the powered hip joint's instantaneous center of rotation throughout the TF amputee gait cycle. Plot created with TOHRC Computer-Assisted Rehabilitation Environment (CAREN) data.....	66
Figure 5-8: Mean plus-minus one standard deviation of unilateral transfemoral amputee level-ground gait kinematics and kinetics. Data collected at TOHRC CAREN.	68
Figure 5-9: Hip-knee-ankle-foot prosthesis free-body diagram. Older powered hip model shown....	69
Figure 5-10: Prosthetic leg COM position relative to the origin at point A.....	70
Figure 5-11: Powered hip free body diagrams at an instance of the gait cycle. Motor provides the required torque for stable gait at each gait cycle instance. Lateral view of older powered hip model shown at an arbitrary hip flexion angle.....	72
Figure 5-12: Powered hip free body diagrams when subjected to motor torque only. Motor assumed to provide its full 96 N-m torque at each instance of the powered hip range of motion. Lateral view of older powered hip model shown at an arbitrary hip flexion angle.....	74
Figure 5-13: Powered hip moment, stabilizing motor torque, and mechanical advantage throughout the gait cycle. Mean plus-minus one standard deviation curves are shown. Approximate local maxima and minima are in blue.....	77
Figure 5-14: Posterior link, anterior link, and drive arm forces throughout the gait cycle. Mean plus-mins one standard deviation curves are shown. Approximate local maxima and minima are in blue.	78
Figure 5-15: Powered hip mechanical advantage throughout its range of motion. Maximum mechanical advantage and its corresponding hip flexion angle are in blue.	79
Figure 5-16: Link force magnitudes throughout powered hip range of motion. Maximum link forces and the corresponding hip flexion angle are in blue.	80
Figure 6-1: Three-dimensional stress state [197].	83
Figure 6-2: Posterior link free-body diagram with a cross-section at extension stop force application point. Older model shown.....	87
Figure 6-3: Anterior link free-body diagram with a cross-section at middle of its length. Older model shown.....	88

Figure 6-4: Drive arm free-body diagram. Older model shown.....	89
Figure 6-5: Posterosuperior shaft free-body diagram with a cross-section at the posterior link superior force F_{5s} application point	90
Figure 6-6: Powered hip motor and upper FEA units. ISO 15032 M-L loading case shown. Drive arm force shown for example only.....	93
Figure 6-7: Screw connections for powered hip finite element analysis.....	93
Figure 6-8: Powered hip upper unit with a mock pelvic and a mock socket. Mock pelvis dimensions determined from [187], [190]. Hip joint distance from the midline determined from [210].	94
Figure 6-9: Non-simplified powered hip motor unit containing all motor internal components.	96
Figure 6-10: Fully simplified powered hip motor unit with all internal components removed.	96
Figure 6-11: Semi-simplified powered hip motor unit with most internal components removed. Ring insert and output bearing included.	97
Figure 6-12: Upper unit FEA mesh. Large elements assigned to pelvic components. Small elements assigned to powered hip components.....	97
Figure 6-13: Motor unit FEA mesh. Large elements assigned to thick, geometrically simple regions, and low stress magnitude regions. Small elements assigned to thin, geometrically more complex regions, and high stress magnitude regions.....	98
Figure 6-14: FEA meshes for drive arms 1 (left), 2 (middle), and 3 (right). Mostly uniform meshing.	98
Figure 6-15: Upper unit FEA with ISO 15032:2000 A-P extension loading: posterior link force $F_5 = 3895 N \angle 88.5^\circ$ (compression), anterior link force $F_6 = 268 N$ (tension), drive arm force $F_7 = 0 N$. Maximum von Mises stresses shown for various levels of posterior link weight reduction.....	101
Figure 6-16: Upper unit FEA with ISO 15032:2000 M-L extension loading: posterior link forces $F_5 = 717 N \angle 79.6^\circ$, $F_{5x} = 196 N$ (outward), anterior link forces $F_{6m1} = 4056 N$ (tension), $F_{6l1} = 6697 N$ (compression), $F_{6x} = 138 N$ (outward on lateral link), drive arm force $F_7 = 0 N$. Maximum von Mises stresses shown for each material.....	103
Figure 6-17: Motor unit FEA with ISO 15032:2000 M-L extension loading: posterior link forces $F_5 = 717 N \angle 79.6^\circ$, $F_{5x} = 196 N$ (outward), anterior link forces $F_{6m1} = 4056 N$ (tension), $F_{6l1} = 6697 N$ (compression), $F_{6x} = 138 N$ (outward on lateral link), drive arm force $F_7 = 0 N$. Maximum von Mises stresses shown for each material.....	104
Figure 6-18: Drive arm under the motor only loading case ($F_7 = 9599 N$ (tension)): a) anterior-posterior weight reduction, b) medial-lateral weight reduction, c) no weight reduction.	106

Figure 6-19: Upper unit FEA with motor-only loading: posterior link forces $F_5 = 5533\text{ N}$ (compression), anterior link force $F_6 = 2310\text{ N}$ (compression), drive arm force $F_7 = 9599\text{ N}$ (tension). Maximum von Mises stresses shown for each material.....	107
Figure 6-20: Motor unit FEA with motor-only loading: posterior link forces $F_5 = 5533\text{ N}$ (compression), anterior link force $F_6 = 2310\text{ N}$ (compression), drive arm force $F_7 = 9599\text{ N}$ (tension). External maximum von Mises stresses shown for each material.....	108
Figure 6-21: Medial-lateral cross-section of motor unit FEA with motor-only loading. Internal maximum von Mises stresses shown for each material.....	110
Figure 6-22: Upper unit and motor unit screw connectors: superior screws (S), lateral screws (L), lateral internal screws (LI), medial internal screws (MI), and medial screws (M).	111
Figure 6-23: Medial-lateral cross-section of motor unit FEA with motor-only loading. Internal upward displacements (UZ) and minimum gaps between rotating parts shown.....	112
Figure 7-1: Motor unit medial-lateral cross-section demonstrating the drive arm bending effect on the output bearing due to the drive arm force.	114
Figure 7-2: Maximum allowable motor torque for safe operation as a function of hip flexion angle.	116
Figure 8-1: Lateral isometric view of powered four-bar hip prototype. Parts are listed in Table 8-1.	118
Figure 8-2: Medial isometric view of powered four-bar hip prototype. Parts are listed in Table 8-1.	119
Figure 8-3: Powered four-bar hip prototype orthogonal views in third angle projection. Dimensions in mm.	121
Figure 8-4: Powered four-bar hip protrusions when integrated in a hip-knee-ankle-foot prosthesis. Sitting and standing positions shown. No sitting interference.	122
Figure 8-5: Powered hip CNC machined components. The superior link, drive arm, anterior links, posterior link, drive flange, and motor housing are made of Al 2024-T351. The drive arm screw-on pieces, and motor cover are made of 17-4 PH SS H900.	123
Figure 8-6: Powered hip motor assembly.	125
Figure 8-7: Powered four-bar hip.....	126
Figure 8-8: Powered four-bar hip with chassis containing the battery and electronics.....	129
Figure 9-1: Powered hip compression test force-time profile.	130
Figure 9-2: Powered hip A-P extension static compression test setup. Setup resulted in hip moment arm $L_H = 134.79\text{ mm}$ and knee moment arm $L_K = 23.93\text{ mm}$	131

Figure 9-3: Powered hip M-L static compression test setup. Setup resulted in hip moment arm $L_H = 99.96 \text{ mm}$ and knee moment arm $L_K = 57.41 \text{ mm}$	132
Figure 9-4: Powered hip A-P extension compression test force-displacement profile.....	133
Figure 9-5: Powered hip M-L compression test force-displacement profile.....	133
Figure 9-6: Hip disarticulation prosthesis simulator with full lower-limb prosthesis containing the powered four-bar hip.....	135
Figure 9-7: Ensemble average across all participants for pelvic tilt, prosthetic side hip and knee flexion-extension angles for level-walking. Mean plus-minus one standard deviation.....	137
Figure 9-8: Medial-laterally translated anterosuperior pins observed after the completion of level-walking trials with three able-bodied participants.....	140
Figure 10-1: Medial-lateral cross-section of powered four-bar hip design concept containing a supplementary bearing that will potentially reduce output bearing loading.....	145
Figure 10-2: Hypothetical mechanical advantage profile centering the peak at 60° hip flexion to optimize stair ascent and descent, ramp ascent and descent, sit-to-stand, and stand-to-sit.....	147
Figure A-1: Single-axis powered hip with the motor attached to the anterior face of the socket....	169
Figure A-2: Direct-drive posterior motor hip for a right-leg prosthesis: a) hip joint integrated within prosthetic thigh, b) motor torque transmission to the linkage, c) motor-linkage interfacing.....	170
Figure A-3: Direct-drive posterior motor hip range of motion. Hip flexion-extension angle is in blue, motor angle is in red, and link dimensions are in green.....	171
Figure A-4: Direct-drive anterior motor hip for a right-leg prosthesis.....	172
Figure A-5: Direct-drive anterior motor hip range of motion. Hip flexion-extension angle is in blue, motor angle is in red, and link dimensions are in green.....	173
Figure C-1: Engineering analysis coordinate system.....	225
Figure C-2: Powered hip sagittal plane dimensions at arbitrary and singularity hip flexion-extension positions. Lateral view shown. Dimensions shown on an earlier powered hip model with the motor protruding medially. Origin at point A. Positive y is anterior and positive z is superior.....	225
Figure C-3: Triangle BCF defining motor housing geometry.....	226
Figure C-4: Triangle BCD at hip extension (left) and hip flexion (right) singularity positions.....	226
Figure C-5: Triangle BDF (left) and triangle DEF (right) at the hip extension singularity position.....	227
Figure C-6: Triangle BDF (left) and triangle DEF (right) at the hip flexion singularity position ...	228
Figure C-7: Triangles DEF and DCF at an arbitrary hip flexion-extension position, and motor-related angular parameters near point F.....	228
Figure C-8: Linkage vector diagram from point A to point F.....	229

Figure C-9: Triangle ADE at an arbitrary hip flexion-extension position.	230
Figure C-10: Linkage ABCD loop closure and dot product diagrams at an arbitrary hip flexion-extension position.....	230
Figure C-11: Point C represented as the rightmost intersection point of two circles.....	232
Figure C-12: Powered hip sagittal plane dimensions at sitting and standing. Lateral view shown. Dimensions shown on an earlier powered hip model with the motor protruding medially. Origin at point A. Positive y is anterior and positive z is superior.....	233
Figure F-1: Superior link screw loads acting at the screw pair centroid. $F_{hx} = 334.3 \text{ N}$, $F_{hy} = 0 \text{ N}$, $F_{hz} = 3343 \text{ N}$, $M_{10x} = 33.43 \text{ Nm}$, and $M_{hy} = 287.5 \text{ Nm}$ are static compression loads in the ISO 15032:2000 ML condition. $\theta_{lp} = 117^\circ$ is the lamination plate obtuse angle. Older model shown.	245
Figure F-2: Drive arm screw-on free-body diagram and equivalent free-body diagram with loads distributed among the component's four screws. $F_7 = 9599 \text{ N}$ under maximum motor torque. Older model shown.	247
Figure F-3: Motor housing screw loads acting at the screw pattern centroid and equivalent screw loading distributed among the component's six screws. $F_7 = 9599 \text{ N}$ under maximum motor torque ($T_{mx} = 96 \text{ Nm}$). Older model shown.	248
Figure G-1: 3D printed powered hip joint. Design based on link length optimization iteration 29..	250
Figure G-2: 3D printed powered hip prototype behavior as it nears or crosses ROM singularity points. θ_D' is the angle used to determine the motor linkage singularity point near full hip flexion. $\Delta\theta_{m1}$ and $\Delta\theta_{m2}$ are angles measuring the range of servomotor rotation in which hip motion stalled.....	252
Figure I-1: Powered four-bar hip assembly. Lateral isometric view.....	254
Figure I-2: Powered four-bar hip assembly. Medial isometric view.....	255
Figure I-3: Powered four-bar hip assembly. Orthogonal views.	255
Figure I-4: Superior link.....	256
Figure I-5: Posterior link.....	256
Figure I-6: Lateral anterior link.....	257
Figure I-7: Medial anterior link.....	257
Figure I-8: Motor housing.....	258
Figure I-9: Motor cover.....	258
Figure I-10: Motor shell.....	259
Figure I-11: Drive flange.	259
Figure I-12: Drive arm screw-on inside half.....	260
Figure I-13: Drive arm screw-on outside half.....	260
Figure I-14: Drive arm.	261

Figure I-15: Posterosuperior shaft.....	261
Figure I-16: Posteroinferior shaft.....	262
Figure I-17: Anteroinferior shaft.....	262
Figure I-18: Lateral anterosuperior shaft.	263
Figure I-19: Medial anterosuperior shaft.	263
Figure I-20: Drive arm bushing.....	264

List of Tables

Table 2-1: Specifications for Otto Bock's 7E series hip joints and EBS knee joint mounted at the hip.	25
.....
Table 2-2: Össur's Power Knee 2 and chosen battery specifications.	32
Table 2-3: Comparison of the Össur Power Knee 2 brushless DC motor to three Hathaway Emoteq Inc. High Torque (HT) series brushless DC motors. Lengths and diameters include the motor housing. Hathaway Emoteq specifications obtained from [182]......	32
Table 3-1: Power hip design requirements and criteria.....	40
Table 4-1: Geometric inputs and outputs for an ideal linkage optimization iteration.....	46
Table 4-2: Performance specifications for ideal linkage optimization.....	47
Table 4-3: Target geometric inputs and outputs for a linkage optimization iteration.	47
Table 4-4: Target performance specifications for linkage optimization.	47
Table 4-5: Linkage optimization iteration 179 chosen for powered hip design.....	48
Table 4-6: Fixed inputs for linkage optimization iteration 179.....	48
Table 4-7: Changes in powered hip performance with changes to α and β relative to $\alpha = 35^\circ$ and $\beta = 65^\circ$, $\theta_4 \cong 207^\circ$, $r_c = 5.35\text{ cm}$, and $r_4 = 2.20\text{ cm}$. Approximate increases and decreases are provided.	50
Table 4-8: Changes in powered hip performance with changes in r_4 relative to $\alpha = 35^\circ$ and $\beta = 65^\circ$, $\theta_4 \cong 207^\circ$, $r_c = 5.35\text{ cm}$, and $r_4 = 2.20\text{ cm}$. Approximate increases and decreases are provided... ..	51
Table 4-9: Performance specifications for linkage optimization iteration 179.	57
Table 5-1: Parameters for ISO 15032:2000 A100 A-P and M-L loading conditions.	61
Table 5-2: Free-body diagram distances and angles used for ISO 15032:2000 static equilibrium analyses.	65
Table 5-3: ISO 15032:2000 A100 A-P extension and A-P flexion link forces.....	76
Table 5-4: ISO 15032:2000 A100 M-L link forces.....	76
Table 5-5: Governing load cases for powered hip design. Signs are with respect to assumed force directions in the free-body diagrams for each load case.	82
Table 6-1: Engineering materials considered for powered hip project. R is the ratio of the minimum load to the maximum load during fatigue loading.	84
Table 6-2: Maximum radial link loads and bearing thicknesses, and radial static load capacities.	86
Table 6-3: Governing von Mises link stresses with cross-sectional locations.	89
Table 6-4: Maximum radial loads on link bearings and bearing bore diameters.	90

Table 6-5: Thread engagement lengths and preload torques for powered hip FEA screw connections.....	94
Table 6-6: FEA meshing properties.....	98
Table 6-7: Structural component von Mises stress safety factors for A-P extension, M-L, and motor-only loading.....	110
Table 6-8: Screw von Mises stress yielding and 1 million load cycle fatigue safety factors for the governing motor-only load case.....	111
Table 7-1: Link bearing static safety factors.....	113
Table 7-2: Link bearing lives at 90% reliability for the motor-only load case.....	113
Table 8-1: List of mechanical components in powered four-bar hip prototype.....	120
Table 8-2: ISO 286-2 hole and shaft tolerances for 6 to 10 mm and 10 to 18 mm diameter ranges.	124
Table 8-3: Elastic moduli and Poisson ratios for interference fit materials.....	127
Table 8-4: Ranges of expected pressing forces for powered hip assembly at room temperature....	127
Table 9-1: Spatiotemporal results for powered four-bar hip level-walking tests. Mean plus-minus one standard deviation shown for each participant and for the ensemble.....	136
Table 10-1: Powered four-bar hip requirements, criteria, and performance.....	144
Table A-1: Design specifications for the posterior motor direct-drive four-bar hip and the anterior motor direct-drive four-bar hip.....	174
Table D-1: Fixed inputs for link length optimization iterations 1 to 4.....	235
Table D-2: Link length optimization iterations 1 to 4.....	235
Table D-3: Fixed inputs for link length optimization iterations 5 and 6.....	235
Table D-4: Link length optimization iterations 5 and 6.....	235
Table D-5: Fixed inputs for link length optimization iterations 7 to 54.....	235
Table D-6: Link length optimization iterations 7 to 54.....	236
Table D-7: Fixed inputs for link length optimization iterations 55 to 58.....	236
Table D-8: Link length optimization iterations 55 to 58.....	236
Table D-9: Fixed inputs for link length optimization iterations 59 to 62.....	236
Table D-10: Link length optimization iterations 59 to 62.....	237
Table D-11: Fixed inputs for link length optimization iterations 63 to 66.....	237
Table D-12: Link length optimization iterations 63 to 66.....	237
Table D-13: Fixed inputs for link length optimization iterations 67 to 70.....	237
Table D-14: Link length optimization iterations 67 to 70.....	237
Table D-15: Fixed inputs for link length optimization iterations 71 to 78.....	237
Table D-16: Link length optimization iterations 71 to 78.....	237

Table D-17: Fixed inputs for link length optimization iterations 79 and 80.....	237
Table D-18: Link length optimization iterations 79 and 80.....	237
Table D-19: Fixed inputs for link length optimization iterations 81 to 148.....	238
Table D-20: Link length optimization iterations 81 to 148.....	238
Table D-21: Fixed inputs for link length optimization iterations 149 and 150.....	239
Table D-22: Link length optimization iterations 149 and 150.....	239
Table D-23: Fixed inputs for link length optimization iterations 151 and 152.....	239
Table D-24: Link length optimization iterations 151 and 152.....	239
Table D-25: Fixed inputs for link length optimization iterations 153 and 154.....	239
Table D-26: Link length optimization iterations 153 and 154.....	239
Table D-27: Fixed inputs for link length optimization iterations 155 and 156.....	239
Table D-28: Link length optimization iterations 155 and 156.....	239
Table D-29: Fixed inputs for link length optimization iterations 157 and 158.....	239
Table D-30: Link length optimization iterations 157 and 158.....	239
Table D-31: Fixed inputs for link length optimization iterations 159 and 160.....	239
Table D-32: Link length optimization iterations 159 and 160.....	240
Table D-33: Fixed inputs for link length optimization iterations 161 to 164.....	240
Table D-34: Link length optimization iterations 161 to 164.....	240
Table D-35: Fixed inputs for link length optimization iterations 165 to 171.....	240
Table D-36: Link length optimization iterations 165 to 171.....	240
Table D-37: Fixed inputs for link length optimization iterations 172 to 179.....	240
Table D-38: Link length optimization iterations 172 to 179.....	240
Table D-39: Extra inputs for link length optimization iterations 180 to 184.....	240
Table D-40: Link length optimization iterations 180 to 184.....	241
Table E-1: FEA model specifications for powered hip screw sets including thread engagement lengths.....	243
Table F-1: Calculated and corrected screw preload torques used for powered hip FEA.....	249
Table G-1: Linkage optimization iteration 29. Variables defined in Figure 4-5.....	250
Table G-2: Fixed inputs for linkage optimization iteration 29. Variables defined in Figure 4-5.....	250
Table H-1: Yielding and one million load cycle fatigue safety factors for powered hip FEA model screws. Screw nomenclature defined by Figure 6-22.....	253

Definitions

Abduction	Movement of a limb away from the body midline
Adduction	Movement of a limb toward the body midline
Circumduction	Distal limb circular motion with the proximal end fixed
Double-support time	Duration during which both legs are contacting the ground
Gait compensation	Additional body movement to stabilize gait
Gait deviation	Change in gait kinematics and kinetics due to compensation
Harmonic drive	Torque augmenting device with a flexible elliptical gear
Hemipelvectomy	Amputation of the entire leg and a portion of the pelvis
Hip disarticulation	Amputation of the entire leg from below the hip joint
Hip extension	Backward sagittal plane thigh rotation toward the buttocks
Hip flexion	Forward sagittal plane thigh rotation toward the abdomen
Hip hiking	Prosthetic hip elevation to increase prosthetic toe clearance
Hip-knee-ankle-foot prosthesis	Prosthetic leg with a mechanical hip, knee, ankle, and foot
Hyperlordosis	Exaggerated concave curvature of the lumbar spine
Instantaneous center of rotation	Intersection point of anterior and posterior link lines
Mechanical advantage	Ratio of linkage output load to linkage input load
Passive hip joint	External prosthetic hip with no actuator
Pelvic obliquity	Frontal plane pelvic motion
Pelvic rotation	Transverse plane pelvic motion
Pelvic tilt	Sagittal plane pelvic motion
Powered hip joint	External prosthetic hip containing one or more actuators
Prosthesis simulator	Wearable device for emulating lower-limb amputee gait
Prosthetic shortening	Decrease in prosthetic joint height to increase toe clearance
Single-support time	Duration during which one leg is contacting the ground
Singularity point	Four-bar linkage angular position with coincident link lines
Socket	Carbon fiber prosthetic component worn at the pelvis
Step length	Distance between opposite heel contact points during gait
Stride length	Distance between same-side heel contact points during gait
Transfemoral amputation	Removal of a portion of the leg from the knee downward
Transtibial amputation	Removal of a portion of the leg from the ankle downward
Vaulting	Sound side plantarflexion to boost prosthetic toe clearance
Whipping	Sudden internal or external heel rotation during swing phase

Abbreviations

17-4 PH SS H1025	17-4 Precipitation Hardened Stainless Steel Heat Treated to 1025 °F
17-4 PH SS H900	17-4 Precipitation Hardened Stainless Steel Heat Treated to 900 °F
A-P	Anterior-Posterior
Al 2024-T351	Aluminum 2024-T351
CAD	Computer Aided Design
CAREN	Computer Assisted Rehabilitation Environment
CCW	Counterclockwise
CNC	Computer Numerical Control
COM	Center of Mass
CW	Clockwise
EBS	Ergonomically Balanced Stride
FEA	Finite Element Analysis
GRF	Ground Reaction Force
HD	Hip Disarticulation
HKAFFP	Hip-Knee-Ankle-Foot Prosthesis
HP	Hemipelvectomy
ICR	Instantaneous Center of Rotation
M-L	Medial-Lateral
M2 HSS	M2 High Speed Steel
PLA	Polylactide
PU	Polyurethane
ROM	Range of Motion
RSSR	Revolute-Spherical-Spherical-Revolute
SEA	Series Elastic Actuator
SF	Safety Factor
TF	Transfemoral
TOHRC	The Ottawa Hospital Rehabilitation Center

Acknowledgments

As a Coptic Orthodox Christian, I thank our Lord, God, and Savior Jesus Christ for granting me the health and ability to complete the powered four-bar hip project and this thesis. I also thank the Coptic church community for being a continual spiritual support throughout this journey.

The journey started when Dr. James McDonald, my former Fluid Mechanics professor, encouraged me to pursue a Master of Applied Science in Engineering and informed of graduate scholarships I had previously not known about. I am grateful for his outreach and supportive attitude toward students.

I would also like to extend my gratitude to the administrators who manage graduate scholarship programs. Funding from the Ontario Graduate Scholarship, NSERC Canada Graduate Scholarship, and NSERC Collaborative Research and Training Experience programs have positively contributed to my research and progression as a master's student.

Without a doubt, I owe a momentous appreciation to my co-supervisors Dr. Edward Lemaire and Dr. Natalie Baddour. I, among many, have faced the challenge of progressing as a graduate student during the COVID-19 pandemic. Although the pandemic was a troubling time, it has taught me to be resilient when overcoming difficulties. I thank my supervisors for aiding in my resiliency with their patience, guidance, and open ears during our weekly meetings. My supervisors were an integral part in my development of professionalism as an engineer. Notably, they have encouraged my participation in the 2022 British Columbia Orthotics Prosthetics Canada National conference to present my powered four-bar hip design. The conference was an unforgettable networking experience.

A special mention goes to Dr. Fred Afagh and Dr. Marc Doumit who were my thesis examiners during my oral defense. I appreciate the time they have put into reading my thesis, attending my presentation, and giving me valuable feedback. Their input has allowed me to improve the scientific soundness of my thesis and better my understanding of the practical implications of my project.

Furthermore, I had the opportunity to engage with other students working on other powered hip designs or other aspects of powered hip development. I am thankful for their thoughtfulness and helping hands as the project progressed. Teamwork makes the dream work! Yousef Bader, Kelly Lynn Hill Brannen, Lucas Cho, Amir Fanous, Farshad Golshan, Mahir Hossain, and Sarah Mroz – wishing you all the best!

The University of Ottawa Makerspace, Machine Shop, and Brunsfield Centre have provided most of the necessary tools and equipment for creating powered hip prototypes. I met many professionals who I thank for helping me with prototype construction. A special thanks goes to Stanley Weedmark for machining extra components to increase prototype robustness.

Most prototype components required precise machining. I thank the professionals at Star Rapid and Megatech for accurately machining these components. Job well done!

Össur was the company partner for the powered four-bar hip project. David Langlois, New Product Development lead at Össur, also deserves an enormous thank you! He has been a great engineering mentor throughout the design and prototyping stages of the project. I admire his calm, cool, and collected personality, even when I presented him with various engineering dilemmas I faced. He always seemed to have an answer for everything. Interacting with him has taught me to engage in any kind of discussion with positivity and a solutions-oriented approach.

I am grateful for having had the chance to complete a three-month internship at the Össur headquarters in Iceland. I am also extending my appreciation to the professionals I have met at Össur for assisting me with prototyping and structural testing. There are too many names to list here, but they are names of individuals to whom I greatly esteem. Well, I will mention one, Aron Ingi Ingvarson, because he has coordinated with me and taken multiple weeks out of his schedule to run compression tests on the powered hip, even after I returned to Canada from Iceland. Össur has been a valuable learning experience that has informed me of exciting future career opportunities in prosthetic device development.

Hossein Gholizadeh is a humble but professional prosthetist who offered valuable information related to prosthetic joint motion and alignment. In fact, he heavily inspired the central design concept of the powered four-bar hip. He also took care of preparing the equipment and facilities needed for powered hip walking tests. Hossein was very understanding and accommodating when arranging gait training and powered hip testing sessions which ran over the span of several months. I am glad he was still encouraging me to keep trying to walk with the hip-knee-ankle-foot prosthesis simulator, despite seeing my many struggles while learning to walk with it! The prosthesis simulator has provided the team and me a great appreciation of the positive contributions that the powered hip project has had on prosthetic technology research.

Last but not least, I am extending a warm thank you to my family. My parents Mouris Botros and Ragaa Botros have showed great care for my progression toward the master's degree. They have reminded me of the importance of maintaining a healthy work-life balance and have given me a lot of emotional support during the most difficult times of the project. In addition, my brother, Joseph Botros, is an exemplary engineer who has offered his expertise at various stages of the project. He encouraged me to keep setting goals and has kept me accountable – all the way to project and thesis completion!

Chapter 1: Introduction

Amputations that remove a person's entire leg include hip disarticulation (HD, amputation at the hip joint) and hemipelvectomy (HP, amputation that removes part of the pelvis) [1], [2], [3], [4]. This level of amputation requires a hip-knee-ankle-foot prosthesis (HKAfp), a wearable assistive device that contains mechanical hip, knee, and ankle joints to restore an amputee's lost leg [5]. The current state-of-the-art passive HKAfp consists of a four-bar linkage hip joint (e.g., Otto Bock Helix3D [6]), a microprocessor knee (e.g., Otto Bock C-Leg [7], Össur Rheo Knee [8]), and a microprocessor energy return ankle-foot (e.g., Össur Proprio Foot [9]). Some HD or HP amputees may opt for a powered knee (e.g., Össur Power Knee [10]) and/or a powered ankle-foot (e.g., Otto Bock Empower [11], BionX emPOWER [12]). These three prosthetic joints are the only powered joints on the market.

Current prosthetic hip joints on the market are passive. Hip flexion and extension are achieved through pelvic tilt and pelvic rotation, as well as postural adjustment to modify the body's center of mass (COM) location. Passive hip prostheses support weight bearing and allow hip flexion and extension. Hip amputees, fitted with passive prostheses, experience challenges when walking and maintaining lower-limb stability because they lack the joint moments normally provided by the intact limb [13]. Ideally, a powered hip actuator would compensate for this lack of joint moments. Three powered hip prostheses were developed in laboratory settings [14], [15], [16], but currently no clinically viable powered mobility solution is available for hip amputees.

A four-bar linkage has many benefits when used in a prosthetic hip joint. The kinematic and kinetic properties of a four-bar linkage could be customized by choosing appropriate link lengths. Due to the polycentric nature of a four-bar linkage, moment arms will vary with hip flexion/extension angle and, if the linkage is configured properly, large mechanical advantages can be achieved. Additionally, hip instantaneous center of rotation (ICR) locations can be designed so that the prosthetic leg remains stable (i.e., hip, knee, and ankle joints remain extended) in weight bearing. A four-bar linkage would also allow for the hip joint to rotate and translate simultaneously, meaning that the overall joint height could be shortened during swing phase, thereby increasing toe clearance and reducing pelvic obliquity [17], [18]. In the Helix3D hip joint, hip flexion and extension occur outside the sagittal plane to compensate for pelvic rotation [13], [17]. Furthermore, a four-bar linkage transmits motion and power at a distance away from the joint rotation axis. This characteristic is important for the power hip because it allows for comfortable sitting and good cosmesis.

This thesis proposes a novel powered prosthetic hip joint with a four-bar linkage and harmonic drive DC motor as a solution for improving mobility and increasing limb stability during weight

bearing activities in unilateral HD and HP amputees. An optimization algorithm was developed and used to determine link lengths that best satisfy the design criteria. Force and finite element analyses informed component arrangement and component sizes for a safe design. A static compression test evaluated the joint's structural strength using the ISO 15032 standard for hip prostheses. Functional tests demonstrated that walking could be achieved with the powered hip joint integrated into a hip-knee-ankle-foot prosthesis simulator.

1.1 Rationale

Out of all lower-limb amputees, HD and HP amputees have the most difficulty returning to walking because HD and HP are the most severe lower-limb amputations [1], [3]. HD and HP amputees using a HKAfp require more than double the metabolic cost [1], [14], [19], [20], [21], [22], [23], [24] and walk at approximately half the speed compared to able-bodied people [14], [19], [24], [25]. A lack of muscle power at the hip, knee, and ankle results in a slow cadence [1], [26].

The average comfortable movement speed of wheelchair locomotion is more than double the speed of walking with a HKAfp, and oxygen consumption is significantly lower with a wheelchair [21]. For these reasons, HD amputees tend to select a wheelchair as their primary assistive device [21]. In general, the higher the level of lower-limb amputation, the more likely the amputee is to use a wheelchair over a prosthesis [27]. However, lower-limb amputees using a wheelchair have difficulty with activities of daily living that require them to stand and/or access everything in their environment. A functional prosthesis allows them to participate in these activities more actively.

Many people who use a lower-limb prosthesis have gait asymmetries and movement impairments that may result in abnormal tissue loading and lower back pain [28], [29], [30], [31], [32]. Lower back pain is one of the leading causes of disability [28], [33]. General back pain has been reported to affect 52% to 89.6% of lower-limb amputees [28], [29], [34]. Improvements to lower-limb prosthetic technology would result in better ambulation, reduced pain and thus, a better quality of life.

HD and HP amputees are limited by available hip prostheses that do not provide optimal gait [14], [35] and less than 50% of them use a prosthesis in everyday life [13]. Reportedly, 43% of HD amputees abandon their prostheses at about 20 months after fitting with the difficulty of ambulation being one of the major reasons [14], [36], [37].

Lower-limb amputees have an increased risk of falling during ambulation compared to the general population [38], [39]. Falls in people with an amputation could be devastating, especially in elderly and frail populations [38], [40]. HD and HP amputees experience limited stability control during weight acceptance [13], [41] and a less symmetrical gait than knee or ankle amputees [1], [20]. Therefore, out of all lower-limb amputees, HD and HP amputees have the greatest risk of falling.

The use of a prosthesis after HP improves balance (and thus, decreases the risk of falling), decreases the need for a gait aid (e.g., crutches), helps maintain muscle strength/tone and functional mobility, and improves cardiovascular health [25]. Hip motion assistance with a hip exoskeleton improved walking speed, cadence, stride length, other spatiotemporal gait parameters [42], and metabolic cost [43].

Passive hip joints rely on proper alignment and proper ambulation technique for stable weight bearing and walking. This ambulation technique often results in slow and inefficient gait [13]. When HD and HP amputees walk with passive hip joints (e.g., Otto Bock 7E7 [44] and Otto Bock Helix3D [6]), they experience lower hip extension range and lower hip flexion velocity than able-bodied people [13], [45]. Powered hip prostheses provide joint moments that are hypothesized to provide better stability and faster, more efficient gait with a greater range of hip motion.

Deviations from normal gait are unavoidable in unilateral lower-limb amputees due to the loss of physiological joint and muscle functions [46], [47], [48], [49], [50], [51], [52]. For unilateral amputees, gait is slower and more asymmetric at higher amputations levels [46], [49], [52], [53], [54], [55], [56]. Preferably, a unilateral lower-limb amputee walks as close to normal gait as possible. However, when making improvements to current prosthetic hip joints, a reasonable starting point is to assume that the new hip joint would allow a unilateral HD or a HP amputee to walk like a unilateral transfemoral (TF) amputee, because both groups require a prosthetic knee, ankle, and foot.

To walk like unilateral TF amputees, unilateral HD or HP amputees must match unilateral TF amputee walking kinematics. Kinetics between hip-level and TF amputees will likely differ due to the different prosthetic configurations that each level of amputation presents. The kinetically worst-case scenario in either able-bodied or lower-limb amputee gait is single-support, when the entire body weight is supported on one leg. The novel hip joint presented in this thesis was designed to withstand this worst-case scenario.

In able-bodied gait, the hip joint moment reaches approximately 1 N-m/kg [57]. In unilateral TF amputee gait, the hip joint moment reaches approximately 0.8 N-m/kg on the residual leg [58], [59]. The Helix3D hip joint is designed to support a body weight of up to 100 kg [6], [17], [60]. A hip joint moment of at least 80 N-m is required for a person of this body weight. An actuator would need to be powerful and relatively large compared to the rest of the prosthetic joint to provide 80 N-m of torque. If a large actuator were placed directly at the hip joint center (i.e., on the socket), the user would face challenges in sitting activities and donning/doffing clothing.

With a four-bar linkage prosthetic hip joint, the actuator could be mounted away from the socket to facilitate sitting, fitting under clothing, and enhancing cosmesis. When configured properly,

a four-bar linkage can improve lower-limb stability and toe clearance and increase the hip joint's mechanical advantage.

All lower-limb amputees form an estimated 0.055-0.13% of the world's population [14], [61], [62]. A HD prosthesis is used in less than 2% of lower-limb amputees [14], [62], [63]. The recruitment of HD or HP amputees for walking trials can be difficult due to the low number of hip-level amputees. A HD prosthesis simulator is a device that consists of a wearable socket fastened to a HKAfp. By configuring the HKAfp to be slightly longer than the sound leg, able-bodied people can wear the device to experience how a HD amputee would walk with the hip joint integrated into the HKAfp. Sensors placed on various parts of the simulator would provide information as to how well the overall prosthesis mimics TF amputee kinematics. The simulator enabled walking trials to be conducted with able-bodied people. Able-bodied HD prosthesis simulator results were useful in verifying powered hip function and safety before progressing to future research with HD or HP amputees.

1.2 Objectives

This thesis has the following objectives:

1. Design a powered prosthetic hip joint for a unilateral HP or HD amputee.
2. Manufacture a hip joint prototype.
3. Determine if the hip joint is structurally safe for use based on ISO 15032.
4. Demonstrate hip joint function by integrating the joint into a HKAfp simulator and walking with the device.

1.3 Project Scope

In this thesis, the powered four-bar hip refers to the powertrain that generates hip flexion/extension: the four-bar linkage, torque transmission linkage, DC motor, and motor housing. The chassis refers to the mechanical structure housing the battery and electrical components. The powered hip unit contains both the powertrain and chassis. This thesis details the design, prototype, and evaluation of the powertrain only. Work on the chassis, electronics, and control system has been carried out by other graduate students. The DC motor and battery have been developed by Össur.

1.4 Thesis Contributions

1. The project resulted in the first viable powered four-bar hip joint that enables people with hip-level amputations to walk. This is an advancement from the passive hips on the market due to its potential to reduce gait compensation and thereby, gait energy expenditure. The prototype integrates a modified Össur Power Knee motor into a prosthetic thigh to generate hip moments through linkage power transmission.
2. The project also resulted in a novel gait testing technique that emulates hip amputee gait with an able-bodied person by using a HKAFP simulator. This technique provides a low-risk method of performing a preliminary evaluation of hip joint function, and a testing alternative when hip amputee recruitment is difficult. Gait testing with hip-level amputees can then be done with more confidence since operational safety was verified with the simulator.

1.5 Thesis Outline

This thesis has ten chapters. Chapter 2 provides a review of literature covering types of hip amputations, challenges faced by hip amputee populations, previously developed hip prosthetic technology, four-bar linkages, biomechanics of TF amputee gait, biomechanics of gait with a state-of-the-art passive HKAFP, and powered prosthetic technology. Chapter 3 outlines the design criteria for the powered four-bar hip. Chapter 4 presents the powered four-bar hip design and describes the four-bar link length optimization process. Chapter 5 details powered hip force analysis. Chapter 6 details stress analysis. Chapter 7 details bearing analysis. Chapter 8 showcases the powered hip prototype, its components, fabrication process, and manufacturing feasibility. Chapter 9 evaluates the powered hip's structural strength with static compression testing, and its functional capability during walking trials with able-bodied participants using a HKAFP simulator. Chapter 10 concludes the thesis while highlighting powered hip performance, thesis contributions, and future work for the powered four-bar hip project.

Chapter 2: Literature Review

This literature review first outlines different kinds of lower-limb amputation and lower-limb prosthetic technology, and then details the benefits of four-bar linkages in lower-limb prostheses. The review continues with gait analysis for different levels of lower-limb amputation and then ends with details regarding powered prosthetic legs that improve gait performance in comparison to passive prosthetic legs.

2.1 Hip-Level Amputations

HD and HP are the most proximal lower limb amputations (Figure 2-1). A HD is performed by severing the leg through the hip joint space, where separation occurs between the head of the femur and the acetabulum [1], [2], [3], [4]. A HP removes the entire hip joint along with a section of the pelvis on the same side [1], [2], [3], [4].

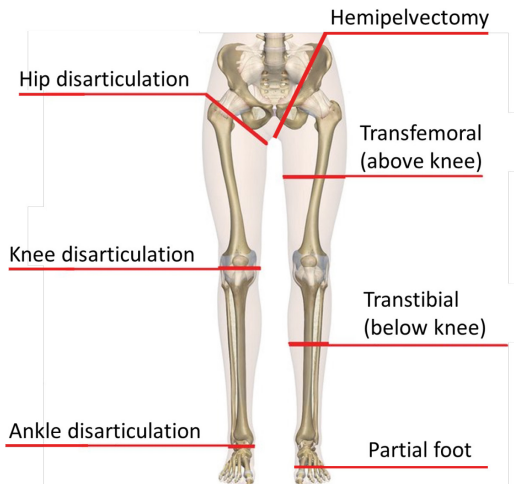


Figure 2-1: Types of lower limb amputations. Adapted from [64], [65].

The most common reason to undergo HD or HP amputation is a malignant tumor in the hip joint or pelvis region [1], [3], [4], [66]. Other causes include severe trauma, vascular insufficiency, or femoral osteomyelitis (inflammation and swelling due to infection or injury) [1], [3], [4], [66], [67].

HD amputees account for less than 2% of all lower-limb amputees [14], [62], [63] and have the largest loss of functional mobility and independence of lower-limb amputees [4]. Depression, anxiety, social phobia, and a general decrease in quality of life are common among all lower-limb amputees [68], [69]. Out of all lower-limb amputees, HD and HP amputees experience the most trouble in activities of daily living such as walking, sit-to-stand, stand-to-sit, and stair ambulation [1], [3], [4].

2.2 Hip-Knee-Ankle-Foot Prostheses with Single-Axis Hip Joints

2.2.1 Early Hip Disarticulation Prostheses

During World War I, a hip-level prosthesis was simply a willow pole attached to a socket made of leather, steel, or willow [70]. The prosthetic leg was heavy and thus cumbersome to use [70].

In 1926, the tilting-table prosthesis was introduced and was made entirely out of metal [70]. The lock in the hip joint engaged when the user was walking and disengaged when the user was sitting [70]. Due to the hip joint being placed below the socket, the user experienced what they felt was a tiresome raise or tilt when seated [70]. Although this prosthesis was lighter than the willow prosthesis, users considered it noisy in comparison [70].

In the early 1950s, the saucer-type prosthesis was introduced. Both the saucer-type prosthesis and tilting-table prosthesis were commonly used by HD amputees [1], [71], [72]. Both types of prostheses had lockable hip and knee joints [1], [71] and for this reason, increased transverse pelvic rotation and vaulting gait (excessive sound ankle plantarflexion) were required to achieve adequate toe clearance on the prosthetic side in swing phase [1], [71], [72], [73]. HD amputee gait with both types of prostheses was observed as jerky and tiring [72], [73].

The saucer-type prosthesis consisted of a prosthetic shank and thigh with a saucer-shaped socket (a socket with the negative shape of the pelvic residuum) on top of the thigh (Figure 2-2) [72].

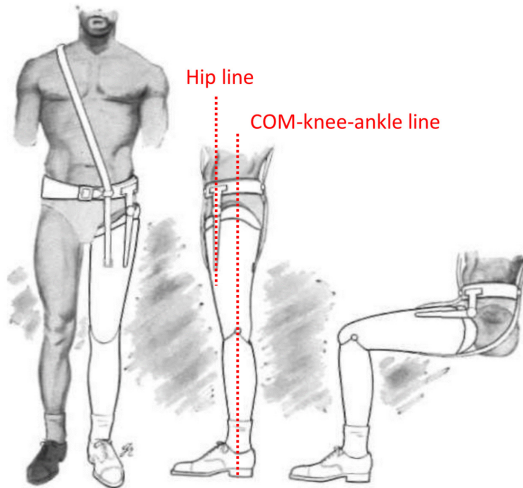


Figure 2-2: Frontal view (left) and sagittal views (right) of the saucer-type prosthesis. Hip joint stability shown by the hip line being anterior to the center of mass (COM)-knee-ankle line. Adapted from [72].

The shank and thigh components were usually made of wood covered with rawhide and the socket was usually made of a plastic laminate core surrounded by two layers of leather [72]. Suspension was achieved with a single axis hip joint, a pelvic band, and a strap passing over the shoulder [72]. The hip joint was placed anterior to the body's COM and knee and ankle joints to provide some measure

of stability (i.e., the ability of the prosthesis to stay erect under the person's body weight and not buckle) [72]. In a HKAfp with this hip joint placement, the amputee's weight kept the hip in extension [72]. At full hip extension, a semiautomatic lock engaged to lock the hip joint and disengaged to free the hip joint for sitting [72]. The lock provided postural stability but offered mechanical difficulties due to all of the loads being transferred through a small hip joint [72]. Aluminum alloys, monel (an alloy of copper and nickel), and steel were common materials for the hip joint and locking mechanism [72].

Figure 2-3 illustrates the tilting-table prosthesis that consisted of a leather socket shaped around the stump and attached by a belt around the pelvis and often with a strap over the shoulder [72], [73]. The socket articulated with the thigh section using a single-axis metal hip joint lateral to the socket [72], [73]. The hip joint lateral placement resulted in high stresses under the person's body weight [73]. The tilting-table prosthesis also had a semiautomatic lock that functioned in the same way as the lock in the saucer-type prosthesis [72], [73]. Materials for this kind of prosthesis were similar to those for the saucer-type prosthesis [72]. The tilting-table prosthesis differed from the saucer-type prosthesis because the total body (COM) and hip, knee, and ankle joints are nearly aligned [72]. However, the tilting-table prosthesis had additional contact between the socket and the medial edge of the thigh section to aid with weight bearing [72].

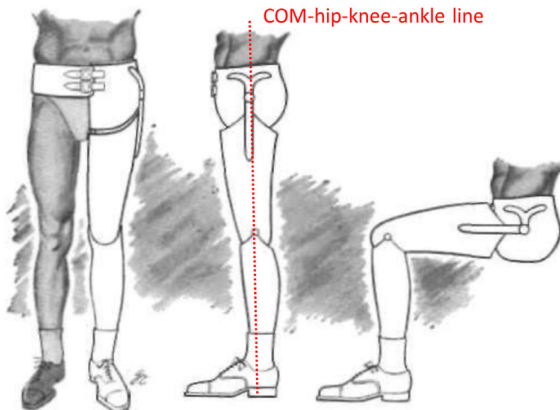


Figure 2-3: Frontal view (left) and sagittal views (right) of the tilting-table prosthesis. The center of mass (COM), and hip, knee, and ankle joints are aligned. Adapted from [72].

2.2.2 Canadian-Type Hip Disarticulation Prostheses

Colin McLaurin further developed the tilting-table concept and, in 1957, he invented the Canadian-type prosthesis (Figure 2-4) [72]. This prosthesis contained single-axis (monocentric) hip, knee, and ankle joints that could freely rotate in the sagittal plane (i.e., flexion/extension) [70], [72], [74], [75]. The hip joint, being a full-width hinge, was placed anterior to the socket (anterior to the

ischial tuberosity) below the anatomical hip joint and was rigidly fixed in the frontal plane to provide lateral stability [70], [72], [74], [76]. The full-width hip joint provided a strong structural connection between the socket and thigh [75]. Since the hip joint was anterior to the knee joint, amputees with some gait training were able to achieve adequate stance phase stability without the use of joint locks (i.e., without restrictions to joint motion in swing phase) [19], [72], [77]. For this reason, the Canadian-type configuration is the standard for prosthetic fitting worldwide [19].

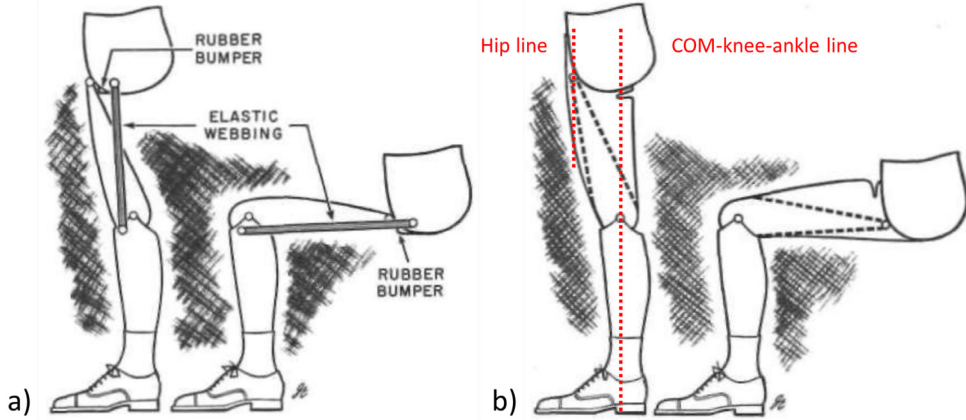


Figure 2-4: Canadian hip disarticulation prosthesis a) without cosmetic cover, b) with cosmetic cover. Hip joint stability shown by the hip line being anterior to the center of mass (COM)-knee-ankle line. Adapted from [72].

Manual locking hip joints were also available at the time; however, amputees found their use to be inconvenient because locked joint required one hand to unlock the mechanism during sitting [77]. More importantly, a locked hip joint was placing the amputee in a risk of a head injury during a backwards fall [77] since, due to the lock preventing hip flexion, the amputee could not brace a fall by falling on their buttocks first [77].

The Canadian-type HD prosthesis did not contain small components with highly concentrated stress as did previous HD prostheses [72]. Relative to previous prostheses, amputees required more effort to initiate swing, but they were able to easily achieve a full stride [72]. The prosthetic socket was a bucket-type seat that fit snugly around the pelvis and minimized stump or socket movement [74]. The socket and waistband were constructed of reinforced plastic in one continuous piece [70]. Amputees comfortably fit into the socket and sat without obstructions from prosthetic components [72]. Due to the hip joint being placed at the anterodistal end of the socket, a shorter thigh component was required for convenient sitting [77]. A shoulder strap prevented the socket from dropping down in swing phase [72]. Suspension included two points at both lateral regions of the pelvis (a broad leather belt provided lateral support [72]) and one directly below the ischium on the prosthetic side [70], [75]. A rubber stop at the bottom of the socket prevented hip hyperextension [72], [74]. An extension bias (e.g., an elastic webbing from the socket to the proximal end of the shank) restrained hip flexion so

that strides were not too long and/or too slow [72], [74], [75], [77]. As a result, an amputee walking on level ground would experience about 15° of relative motion between the socket and the thigh [75].

From its introduction in 1957 all the way to the late twentieth century, the prosthesis has changed very little [74]. Minor modifications have been made to the socket and hip joint, but the core principles of the design have remained the same [74].

Although there were variations in the Canadian-type prosthesis, HD amputees using this type of prosthesis experience similar gait patterns to each other. As the prosthetic leg swings forward in preparation for foot strike, the extension bias limits hip flexion to about 15°-20° [70], [75]. At full hip flexion, the amputee uses their sound leg to propel themselves forward over the prosthesis and then places the heel of the prosthetic foot on the ground [75]. In midstance, the amputee rolls over the extended prosthesis and knee security increases as the weight-bearing line moves anteriorly [75]. During this stage, the sound leg is in swing phase. The amputee continues riding forward with the socket balanced on a free hip joint until the hip joint rear end contacts the rubber bumper on the socket [75]. The hip extends rapidly in stance phase due to low joint friction (i.e., resistance). Full extension is reached at 10-15% of the gait cycle [76]. However, joint alignment provides full stability under weight-bearing and the ground reaction force (GRF) keeps the knee secure [75]. Push-off is initiated during the compression of the rubber bumper [75]. Elastic energy from the bumper provides a rotational moment about the hip, eventually propagating to the knee, and flexing the knee into swing phase [75]. A backward pelvic tilt provides some momentum to swing the prosthetic leg [76]. During prosthetic leg swing phase, the thigh segment remains vertical until the shank segment contacts the knee stop [77]. Hip flexion is initiated from the shank's forward momentum [77]. Like earlier HD prostheses, amputees wearing the Canadian-type prosthesis need to vault (i.e., increase plantarflexion in the sound foot) and hip hike (i.e., raise the pelvis on the sound side) to achieve sufficient toe clearance [76]. The extension assist slows down prosthetic leg movement near the end of swing phase.

2.2.3 Modern Single-Axis Hip Joints

Up until the 1980s, the most commonly used HD prosthesis was the Canadian-type prosthesis [66]. More recently, Otto Bock's 7E series single-axis hip joints are being used due to its lighter weight, improved cosmesis, and the ability to use interchangeable and adjustable components [66]. Figure 2-5 displays all of Otto Bock's single-axis hip joints from oldest to newest.

Hip joints 7E4 and 7E5 are similar modular designs [78], [79], [80]. These three-bar linkage joints have a superior link attached to a plate screwed to the socket, an anterior link extending the entire length of the thigh, and a rectangular bar posterior link [78], [79], [80]. The superior link contains two pin joints, one at each end, where the anterior and posterior links connect [78], [79], [80]. In the 7E4

hip joint, the posterior link, kept in place by a latch-roller mechanism, slides along the anterior link as the hip flexes and extends [78], [80]. A dual latex band extension-assist is connected to the posterior link and the pylon so that hip motion causes the bands to stretch and relax, limiting the range of hip flexion and bringing the hip back to extension [78], [80]. In the 7E5 hip joint, the posterior link and latch mechanism also exist, but instead, the posterior link can act as a lock that can be engaged with a lever [79], [80]. In both hip joints, the anterior link (i.e., pylon) contains a rubber stop that contacts the posterior link to limit hip extension [78], [79], [80]. When either hip joint flexes or extends, the posterior link is not rigidly connected to the anterior link; therefore, the hip is a single-axis joint with the rotation axis being the anterior link's anterior pin [78], [79], [80].

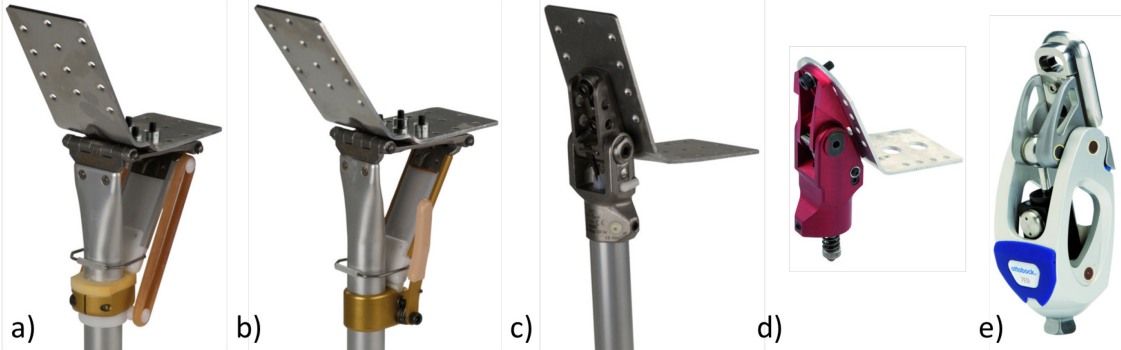


Figure 2-5: Otto Bock's single-axis hip joints from oldest to newest: a) 7E4 [78], b) 7E5 [79], c) 7E7 [44], d) 7E8 [81], e) 7E9 [82].

The 7E7 hip joint is a two-piece structure with a constant-friction pin joint in between (i.e., a simple hinge with its center of rotation at the pin joint) [13], [44], [83]. The top piece is screwed onto the lamination plate and the bottom piece is screw-tightened onto a pylon [44], [83]. The hip joint does not interfere with sitting due to the small structural height of the top piece [44], [83]. Furthermore, the hip joint has abduction/adduction adjustability and interior/exterior rotation adjustability of $\pm 5^\circ$ from neutral [44], [83]. The range of hip flexion/extension can be adjusted by tightening or loosening an internal extension assist spring between the top and bottom pieces [13], [44], [83].

The 7E4, 7E5, and 7E7 hip joints have a fatigue life of two million load cycles [78], [79] and can support a maximum body weight of 100 kg [44], [78], [79], [80], [83]. The 7E4 and 7E5 hip joints are made of aluminum [78], [79], whereas the 7E7 hip joint is made of titanium [44].

The 7E8 hip is a pediatric version of the 7E7 hip joint and is also made of aluminum but has a maximum lifetime of two years [84] and can support a maximum body weight of 45 kg [81], [84]. The 7E8 hip is monocentric and has a 125° flexion/extension range [84]. The 7E8 hip joint is structurally and operationally the same as the 7E7 hip joint [81], [84].

The 7E9 hip joint is a monocentric joint with a hydraulic tube for stance and swing phase control [82], [85], [86]. The hydraulics provide hip joint extension damping after foot strike and results

in a reduction of backward pelvic tilt and hyperlordosis compared to non-hydraulic hip joints [82], [85], [86]. Movement resistances in stance and swing can be individually adjusted independent of each other by turning screws connected to the hydraulic tube [86]. Step length is divided into two ranges: low hip flexion angles where there is no damping and higher flexion angles where swing phase damping is adjustable [85]. The hydraulic hip joint results in a smoother, more controlled roller-over under full load compared to non-hydraulic hip joints [82]. Like the 7E7 and 7E8 hip joints, this hip joint has a small structural height and a maximum hip flexion angle of 130° resulting in comfortable sitting [82], [85], [86], and this hip joint provides adjustability for interior/exterior rotation and abduction/adduction [85]. The 7E9 hip joint, made of aluminum, has a fatigue life of two million load cycles [85] can support a maximum body weight of 125 kg [82], [85], [86].

2.3 Four-bar Linkages in Lower-Limb Prostheses

A four-bar linkage is a mechanism consisting of four rigid bodies (i.e., links) connected in a closed loop [87], [88]. A four-bar linkage that moves in one plane uses parallel revolute joints (i.e., pins) to connect adjacent links [87]. A four-bar linkage that moves out of the plane uses one or more joints with multiple degrees of freedom and/or one or more non-parallel pins [76].

In lower-limb prostheses, four-bar linkages connect two adjacent leg segments together and help guide limb motion [89], [90]. Four-bar linkages are employed to enhance stance phase stability (i.e., limb's tendency to remain straight while supporting the person's body weight) and to achieve good prosthetic cosmesis [6], [60], [76], [89], [90], [91], [92], [93], [94], [95]. They can change lengths within their range of motion and thereby, provide limb-shortening in swing phase to increase toe clearance [18], [25], [90], [91], [94], [95]. In addition, four-bar linkages can offer out-of-plane motion to provide a smoother gait that better mimics human walking than in-plane prosthetic joints [6], [17], [76], [96]. This out-of-plane motion also reduces loading on the prosthetic leg and the upper body [96]. Furthermore, when coupled with an actuator (e.g., a DC motor), a four-bar linkage can be configured to optimize a varying mechanical advantage for prosthetic joint activation. This is an important design challenge of the novel hip joint. A four-bar linkage provides a method of placing an actuator away from the anatomical location of the joint, which can greatly improve prosthesis cosmesis and comfort.

2.3.1 Four-Bar Linkages in Prosthetic Knee Joints

Four-bar linkages are used extensively in prosthetic knee joints because a four-bar linkage has a varying ICR throughout its ROM [89], [95]. A rigid body's ICR is the fixed point on the body around which the body rotates at a given instant of time [97], [98]. A rigid body's ICR is determined by finding the velocity vectors of two points on the body, drawing two lines, each perpendicular to a distinct

velocity vector, and finding the intersection point of these lines [97], [98]. In a four-bar linkage, two velocity perpendiculars are the anterior link's longitudinal axis and the posterior link's longitudinal axis; therefore, the ICR of a four-bar linkage (as a whole) is determined by finding the intersection point between these two lines [13], [91], [94]. The ICR can be located outside the knee joint [91], [99]. The line that passes through the ICR and is parallel to the axes of the link pin joints is the linkage effective axis of rotation [13], [91]. The ICR moves in space based on joint angle [99] and; therefore, there are an infinite number of hip joint rotation axes in a single stride. Thus, a prosthetic four-bar joint is termed as ‘polycentric’ (i.e., many centers) [13], [89], [91]. A ‘centrode’ of a prosthetic joint is the ICR’s path in space as joint angle changes [90], [93].

A TF amputee can voluntarily control knee stability in stance phase by exerting varying amounts of hip flexion and extension moments with their residual musculature [89], [91], [93], [94]. Exerting a hip extension moment in early stance phase shifts the load line anterior to the prosthetic knee joint [91], [93], [94]. Exerting a hip flexion moment in late stance shifts the load line posterior to the prosthetic knee joint [91], [93], [94]. In either case, knee stability is achieved by positioning the ICR so that the GRF pushes the knee into extension [91], [93], [94]. Figure 2-6 illustrates this phenomenon with a stability zone in which the ICR should lie throughout stance phase for the knee joint to remain stable.

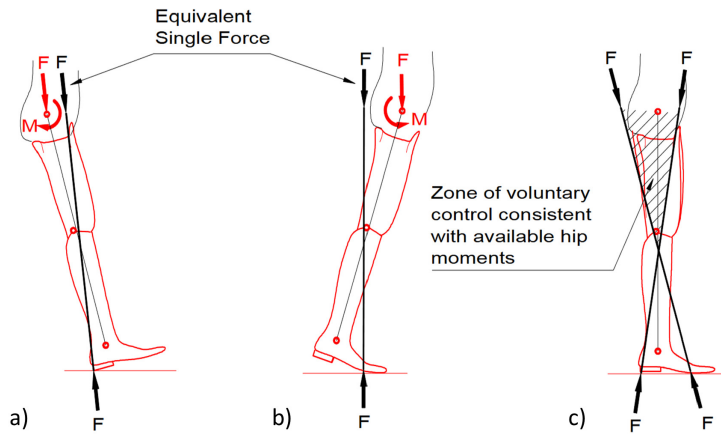


Figure 2-6: Load line (black), joint loads (red), joint centers (red), and limb segments (red) at different parts of stance phase: a) foot strike, b) push-off, c) early and late stance phase superimposed with knee stability zone (black cross hatching). F is ground reaction force and M is the prosthetic side hip flexion-extension moment exerted by the transfemoral amputee. Adapted from [93].

A TF amputee’s ability to exert hip flexion and extension moments is essential for single-axis prosthetic knee stability when bearing weight [91]. If a TF amputee, using a single-axis knee joint, has weak hip musculature and/or too small of a residuum, they would not be able to walk without a knee brake or lock [89], [91]. Four-bar knee prostheses help mitigate a weak hip by positioning the ICR near

or within the stability zone throughout stance phase so that little to no hip flexor and extensor action is required to keep the knee stable [91], [94], [100], [101]. Four-bar knees do not typically incorporate a brake mechanism [90]. The higher the ICR location within the stability zone, the less hip effort is required during early prosthetic leg stance ($\sim 15^\circ$ knee flexion) and during early prosthetic leg swing [90], [95]. This behaviour is due to the GRF's horizontal component acting to provide stability [92]. Figure 2-7 illustrates hip, knee and ankle joint center alignment to reduce the required hip effort in stance and swing phase. The required hip moment is directly proportional to X/Y [89], [90], [94].

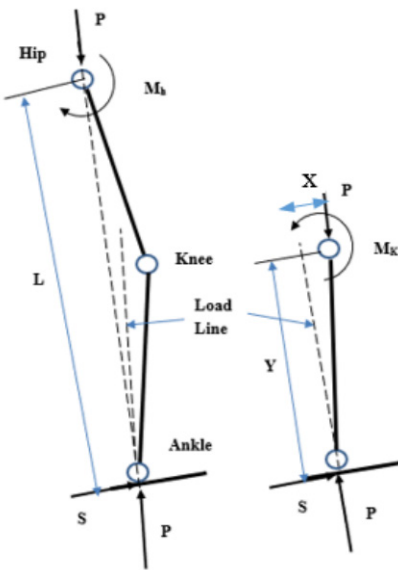


Figure 2-7: Alignment of hip, knee, and ankle joint centers to reduce required hip moment for knee stability. P is ground reaction force. M_h and M_k are hip and knee flexion-extension moments [90].

An ideal linkage configuration for a four-bar knee provides knee kinematic motion and positions the load line in a way that allows the voluntary control of knee stability [90], [91], [94]. Two examples of voluntary control four-bar knees are the University of California Biomechanics Laboratory four-bar knee and the Hosmer four bar knee (Figure 2-8) [91]. A voluntary control four-bar joint elevates the knee ICR to a third up the thigh length [91]. As knee flexion increases, the knee ICR gradually descends in a circular clockwise (CW) path [91]. The change in knee ICR position is not sensitive to changes in knee flexion angle and the ICR path covers a small vertical height compared to other four-bar knee configurations [91]. Therefore, a TF amputee, slightly exerting their hip muscles, can control knee stability during stance phase and early swing phase [91], [95], [102]. This control allows the amputee to react to an event that can disturb knee stability when bearing weight (e.g., stumbling) [91]. A voluntary control four-bar knee that is designed correctly places the ICR well behind the load line during initial stance and creates a centrode that remains behind the load line for about 15° to 20° knee flexion [90].

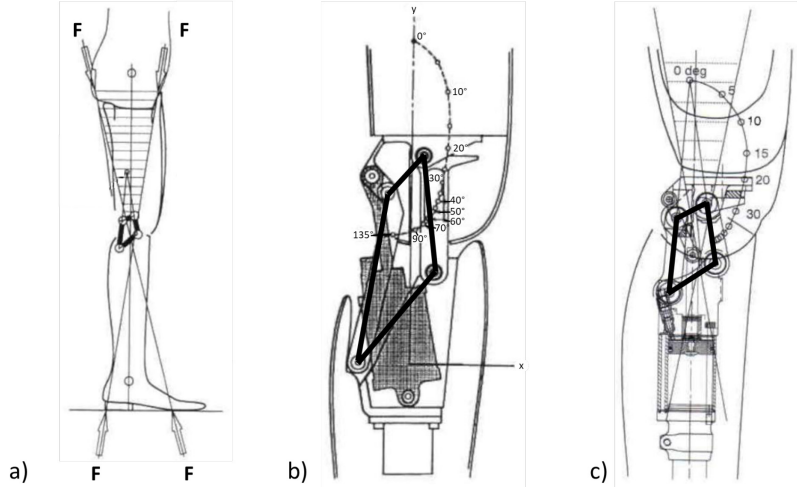


Figure 2-8: Voluntary control four-bar knee prostheses: a) linkage configuration and resulting load lines, b) University of California Biomechanics Laboratory four-bar knee with centrode, c) Hosmer four-bar knee with centrode. Adapted from [91].

Other advantages of a voluntary control four-bar knee are ease of slope and stair descent, increased range of knee flexion (up to approximately 130°), and increased toe clearance during swing phase [91]. Compared to single-axis knees, four-bar knees require less effort to initiate limb motion and control the motion in swing phase due to the voluntary control offered by the changing position of the knee ICR [90].

Polycentric knees are generally preferred for sitting from a cosmetic point of view due to the minimized protrusion at the distal end of the socket at 90° knee flexion [93], [99], [103]. A four-bar knee is also generally used to maximize toe clearance during swing by shortening as the knee passes from flexion to extension [90], [94], [95], [103], [104]. Amputees use energy to increase toe clearance with compensatory gait movements; therefore, the shortening effect of the knee (and thus the prosthesis) results in minimization of energy consumed during walking [90], [99], [105], [106], [107], [108]. Improved toe clearance also reduces the risk of stumbling, asymmetrical gait, musculoskeletal pain and joint degeneration [94], [99].

Shank length is the distance between the knee and ankle. For a TF prosthesis with a four-bar knee, the amount of shank shortening is the difference between the full-length shank and the shank length with a shortened linkage. Linkage shortening occurs when the distance between the lower and upper pins decreases when a prosthetic joint flexes or extends. Toe clearance is the minimum height of the toe above the ground, which occurs at 23° hip flexion and 49° knee flexion in normal gait [90], [94], [99], [109]. Compared to monocentric knees, polycentric knees have shown greater toe clearance [99], [103], [105]. Figure 2-9 showcases fourteen prosthetic knee joints that are popular on the market and the amount of shank shortening and toe clearance at 25° hip flexion [99]. Of these knee joints, the

Otto Bock 3R46/3R55 four-bar knee exhibits the most shank shortening (14.7 mm, SD = 0.0 mm) and the Otto Bock 3R60 exhibits the largest toe clearance (24.4 mm, SD = 0.0 mm) [99]. However, not all polycentric knees shorten appreciably during swing phase [99]. A monocentric knee with an optimized prosthetic alignment and a well designed control system can generate a larger toe clearance compared to a polycentric joint [99].

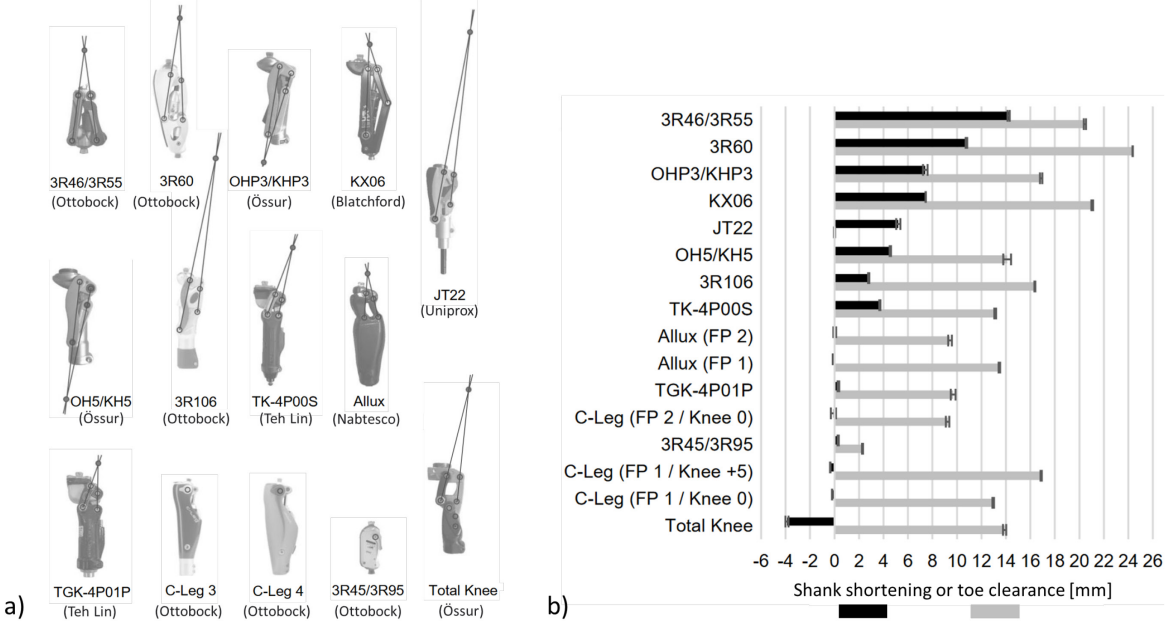


Figure 2-9: a) Monocentric and polycentric prosthetic knee joints with instantaneous centers of rotation labelled with a grey dot, b) millimeter lengths of shank shortening (black) and toe clearance (grey) of prosthetic knee joints. ‘FP 1’, ‘FP 2’, ‘Knee 0’ and ‘Knee+5’ refer to knee alignment positions. Adapted from [99].

Four-bar knees optimally designed for stability and toe clearance place the ICR between 10 cm and 40 cm above the uppermost pin joint of the linkage [90]. These optimal four-bar knees have a superior link that is shorter than its inferior link and link lengths varying from approximately 3 cm to 7 cm [90]. Criteria for optimizing novel four-bar knees include knee stability at foot strike, stabilizing moment at push-off, stable knee flexion range, maximum knee flexion, and maximum toe-clearance at mid-swing [94]. Compared to monocentric knees, polycentric knees generally provide better gait symmetry, balance, and toe clearance [95], [105], [110], [111], [112].

Polycentric knees are often combined with passive mechanical damping components such as hydraulic or pneumatic cylinders [95]. These damping elements provide stance and swing control to help compensate for a TF amputee’s missing musculature [95], [113]. From Figure 2-9, examples of hydraulic four-bar knees include the 3R46 [114], 3R60 [115], KX06 [116], OH5 [117], Allux [118] and the Total Knee [119]. Examples of pneumatic four-bar knees include the OHP3 [120], 3R106 [121], TK-4P00S [122], and TGK-4P01P [123]. Microprocessor controlled prosthetic knees provide

changing hydraulic or pneumatic swing control through mounted sensors and electronic signal processing [25], [95], [124], [125], [126].

Although four-bar prosthetic knees, compared to single-axis knee joints, provide a voluntary control of stability [90], [91], [94] and increased toe clearance [90], [94], [95], [103], [104], state-of-the-art knee prostheses such as the Otto Bock C-Leg and the Össur Rheo Knee are single axis joints. State-of-the-art knees control knee motion by a microprocessor combined with sensors that detect movements and loads on the prosthesis. The microprocessor adjusts damping elements to provide the necessary knee joint resistance at any instant of gait [127]. The C-Leg dampens with a hydraulic cylinder [127], [128] and the Rheo Knee dampens using magnetorheological fluid (fluid viscosity varies with a changing magnetic field) [127], [129]. Microprocessors can use various models and approaches to control gait as an alternative to the purely mechanical gait control provided by a four-bar linkage.

TF amputees require adequate hip flexor and extensor strength to voluntarily control knee stability [89], [91]. HD and HP amputees lack hip musculature and therefore require an active hip joint to contribute to prosthetic knee stability. The novel powered hip provides an augmenting hip torque that could provide equivalent prosthetic knee stability to TF amputees.

2.3.2 Prosthetic Four-Bar Knee Joints Mounted in Reverse at the Hip

In 1982, Peter Tuil proposed the use of a four-bar knee disarticulation joint (the Otto Bock 3R21) mounted in reverse (i.e., front to back and back to front) in place of the hip joint as demonstrated in Figure 2-10 [1], [19], [77]. Benefits were similar to those seen when four-bar linkage was used at the knee: increased toe clearance during swing phase due to the linkage inherently shortening in mid-swing and enhanced stability at foot strike [1], [19], [77]. Amputees observed that the four-bar knee used at the hip provided smooth deceleration and good appearance while sitting [1], [19].

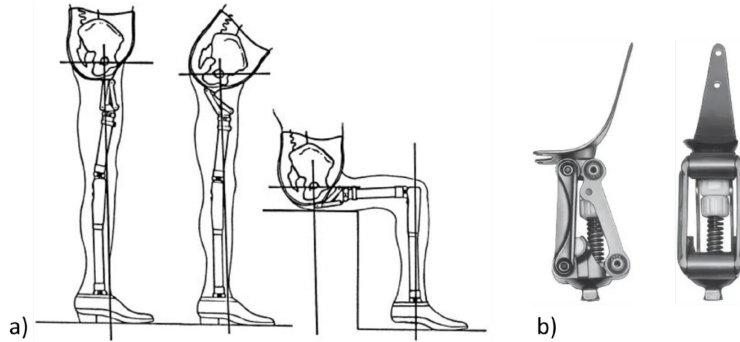


Figure 2-10: a) Sagittal views of different hip flexion angles with a hip-knee-ankle-foot prosthesis containing the 3R21 knee joint at the hip (adopted from [19]), b) sagittal view (left) and frontal view (right) of the 3R21 knee joint (adapted from [130]).

A more modern four-bar knee that can be mounted in reverse at the hip is the Otto Bock Ergonomically Balanced Strike (EBS) knee joint, also known as the Otto Bock 3R60 [131]. Unlike conventional four-bar knees, the 3R60 knee joint contains an additional pivot (i.e., a fifth pivot) at the distal end of the posterior link (Figure 2-11) [132]. Combined with the mounted hydraulic cylinder and elastomer bumper (or spring-hydraulic unit), the fifth pivot serves as an additional anchor point for stance phase flexion damping in conjunction to the existing swing phase damping [131], [132]. Knee flexion and extension resistance increases with increasing walking speed [132] and this resistance is individually adjustable [133]. A pyramid adapter tilted posteriorly by 10° is installed on the proximal end of the 3R60 knee joint to increase the range of hip extension [131], [132]. When used as a four-bar hip, the centrodre moves from its posterosuperior position at full hip extension to its posteroinferior position at 140° hip flexion [132].

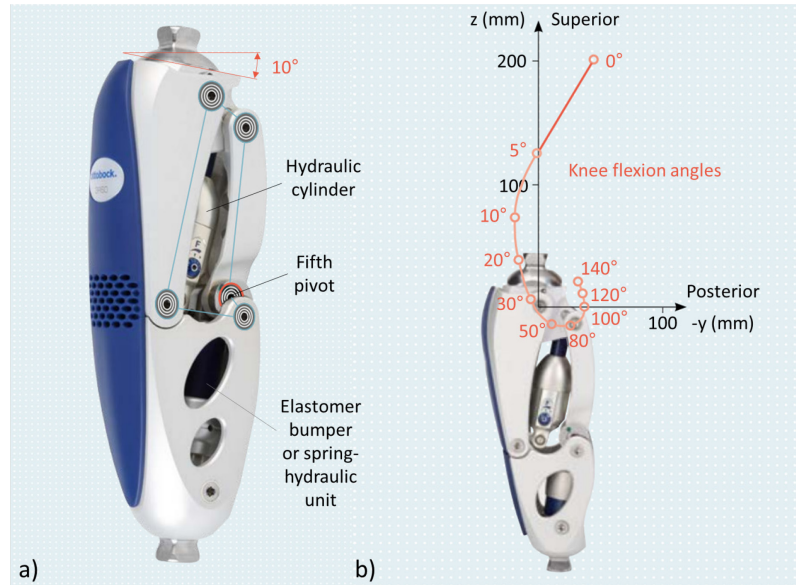


Figure 2-11: a) EBS (3R60) knee joint for hip disarticulation or hemipelvectomy, b) EBS knee joint centrodre when mounted at the hip from 0° to 140° flexion. Adapted from [132].

When mounted at the hip, the 3R60 knee joint can achieve 175° hip flexion [131], [132], [133]. The aluminum joint, being made of aluminum, weighs 880 g, supports 125 kg body weight [131], [132], [133], and has three million load cycle fatigue life [133].

2.3.3 Helix3D (7E10) Hip Joint

The Otto Bock Helix3D (7E10) is currently the state-of-the-art prosthetic hip joint [76], available in the market since 2008 [13]. As presented in Figure 2-12, this joint is a spatial four-bar revolute-spherical-spherical-revolute mechanism (RSSR), containing two pin joints and two ball joints [76]. The ball joints are placed at the ends of the anterior link [76]. All joint axes are perpendicular to

the sagittal plane except the posteroinferior joint axis which is tilted by 26° in the frontal plane relative to the horizontal [76].

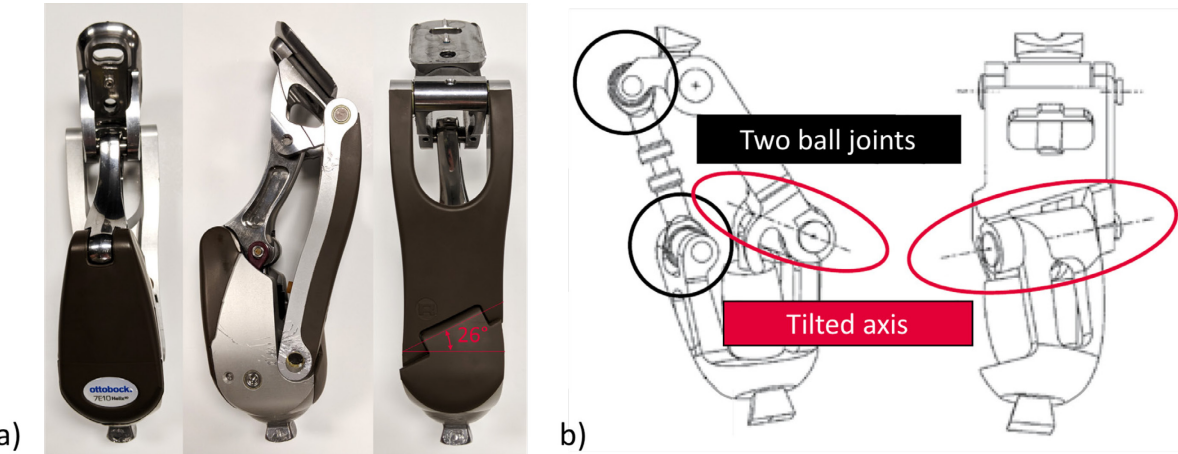


Figure 2-12: a) Otto Bock Helix3D (7E10) hip joint for right leg prosthesis – anterior, medial, and posterior views from left to right, b) principle of the RSSR four-bar linkage with an axis tilted relative to the sagittal plane, medial view (left) and posterior view (right), adapted from [76].

The tilted axis and the ball joints allow mechanism to rotate in the sagittal, frontal, and transverse planes simultaneously, thus mimicking normal 3D movement (i.e., flexion/extension, abduction/adduction, and internal/external rotation) seen in the biological pelvis and hip joint [1], [6], [17], [18], [60], [76]. Hip flexion/extension is the principal movement required for walking and other activities of daily living. The Helix3D hip joint provides up to 130° hip flexion and a low structural height which allow for comfortable sitting [6], [25], [60].

Sagittal plane alignment from the Canadian-type HD prosthesis is maintained in HD and HP prosthesis containing the Helix3D hip joint (Figure 2-13a) [60], [76]. The hip is fastened to the socket at a location far in front of the load line and the knee is 30 ± 10 mm behind the load line [60]. Researchers have found this alignment to be optimal for stability [60]. The Helix3D hip extension range depends on the amputee's limb proportions and the HKAFFP adjustments required to obtain this kind of alignment. HD and HP amputees typically experience up to 15° hip extension when walking at self-selected speeds [13], [76].

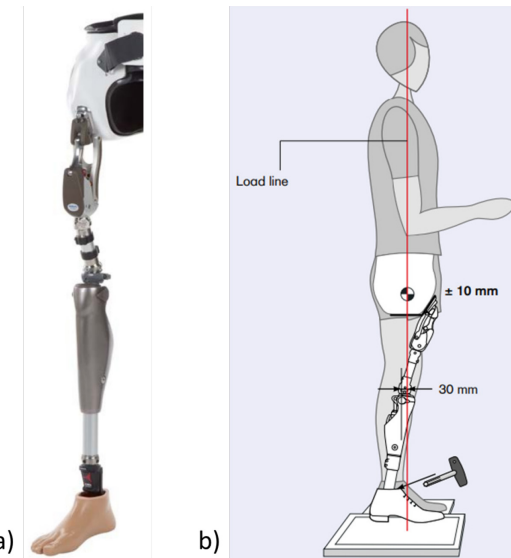


Figure 2-13: a) Hip-knee-ankle-foot prosthesis containing the Helix3D hip joint and the C-Leg knee [60]. b) Prosthetic leg alignment with the Helix 3D hip joint positioned anterior to the load line and the knee positioned 30 ± 10 mm posterior to the load line (adapted from [60]).

The Helix3D hip joint also provides adjustments for frontal plane alignment, as seen in Figure 2-14 [60]. The prosthetist can tighten the screw in any position within the curved screw slot to achieve slight abduction or adduction, helping achieve sagittal plane symmetry [60].



Figure 2-14: Frontal plane alignment adjustment for the Helix3D hip joint [60].

The main reason for the progression of the single-axis hydraulic hip joint (7E9) to the four-bar hydraulic hip joint (7E10) was to compensate for the 6° of pelvic rotation that occurs naturally in walking (Figure 2-15) [6], [17], [76], [96]. The hip joint's transverse movement promotes a symmetrical and natural gait by keeping prosthetic foot loading within the sagittal plane [6], [17]. Furthermore, this compensatory rotation reduces torsion on prosthetic components, the pelvis, and the spine [96]. Although the hip joint experiences motion outside of the sagittal plane, transverse movement depends on the sagittal movement (i.e., only one set of interior/exterior rotation angles for one set of flexion/extension angles) [76], [96].

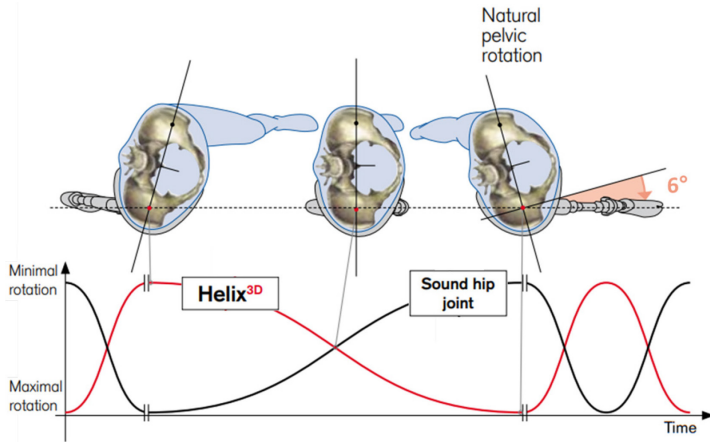


Figure 2-15: Helix3D transverse hip motion to compensate for natural pelvic rotation - interior/exterior rotation versus time. Adapted from [17].

Another reason that Otto Bock implemented a four-bar linkage into their hip joint is to achieve thigh shortening (i.e., linkage shortening) in mid-swing to increase toe clearance and reduce the chance of stumbling while walking [18], [25], [60], [76], [96]. Thigh shortening and toe clearance distances for a HKAFP with Helix3D have not been reported in literature.

Helix3D is polycentric, with the ICR moving in space as a person progresses through the gait cycle (Figure 2-16) [13], [76], [96]. The posterior link length is 10.8 cm, inferior link length is 5.6 cm, anterior link length is 6.7 cm, and superior link length is 2.7 cm. As the Helix3D hip joint flexes and extends, its ICR remains anterior and superior to the acetabulum. As a result, the GRF favors hip extension (i.e., stability) during stance phase.

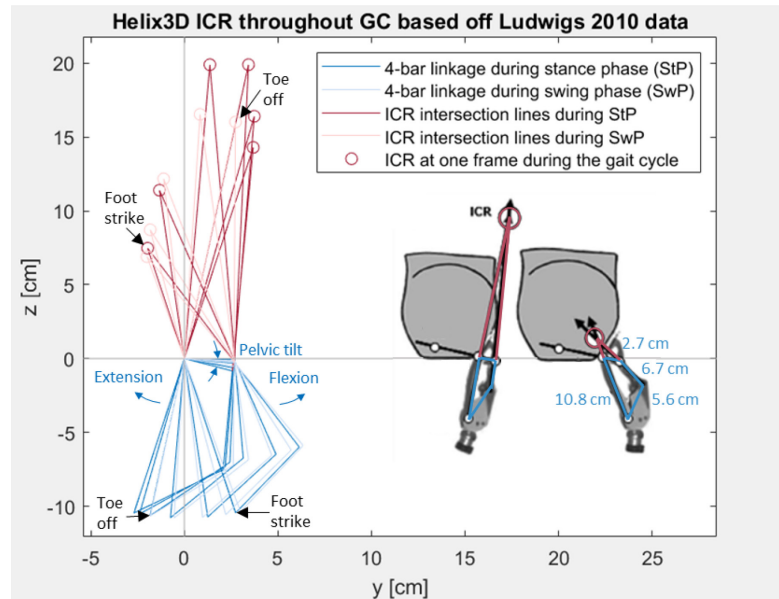


Figure 2-16: Location of the Helix3D hip joint's instantaneous center of rotation (ICR) throughout the gait cycle based on hip flexion/extension. Adapted from [76].

The Helix3D hip joint is mechanically passive and does not contain a microprocessor [13], [76]. As shown in Figure 2-17, the hip joint achieves some stance and swing phase control by means of a polyurethane (PU) component and a hydraulic system [1], [13], [18], [76], [96], [134]. Similar to the 7E9 hip joint, the Helix3D hip joint provides a damped stride, promoting reduced hyperlordosis and a smooth roll-over on the prosthesis under an amputee's full body weight [6], [17], [25], [60], [76], [96]. The 7E9 and 7E10 hip joints extend during stance phase but more slowly and with less trunk movements due to hydraulic damping [96]. Two stretchable PU bands (also referred to as expansion springs) are held at the inferior end of the anterior link and the bottom of the hip on the inside [17], [60], [76]. The PU bands help with swing initiation and prosthetic leg forward acceleration; therefore, hip flexion in swing no longer depends on the knee contacting its extension stop (as was the case with the Canadian-type prosthesis) [6], [17], [25], [60], [76], [96]. The hydraulic system offers three adjustable parameters: stance phase resistance (ST), free-swing range (FSW), and swing phase resistance (SW) [25], [60], [76]. These parameters control fluid flow in the hydraulic piston connected to the anterior link. Piston behavior (i.e., when it experiences resistance and how much resistance) determines how much the hip joint will flex and extend during a gait cycle.

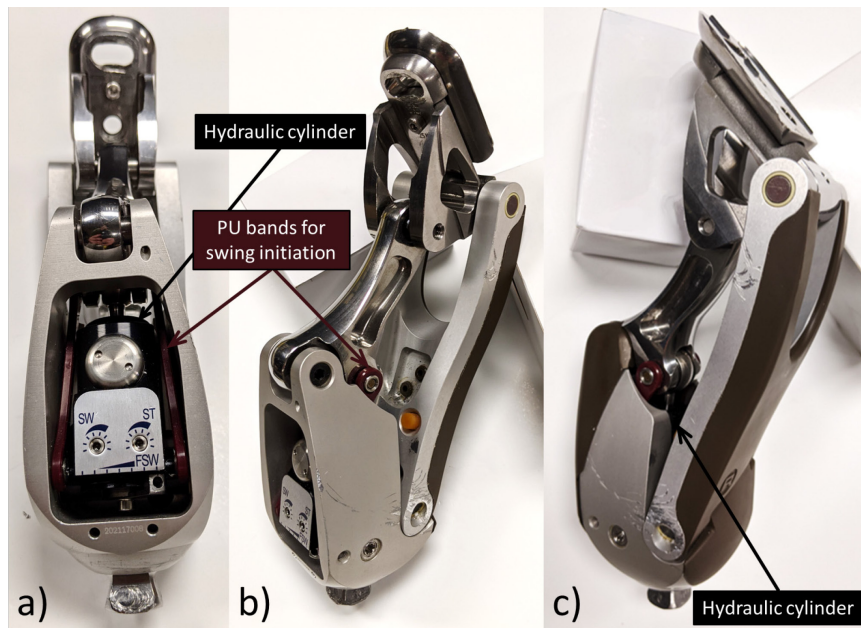


Figure 2-17: a) Helix3D anterior view showing hydraulic stride control parameters stance phase resistance (ST), free-swing range (FSW), swing phase resistance (SW), and two PU bands for swing initiation; b) medioanterior view showing the PU element location on the anterior link; c) medioposterior view showing the hydraulic cylinder connected to the anterior link.

The user can increase hip extension resistance in early stance by increasing the ST parameter [60], [76]. Figure 2-18 shows time to extension stop for different ST settings. An optimal ST setting allows the person to reach full hip extension at approximately 45% of the gait cycle [76].

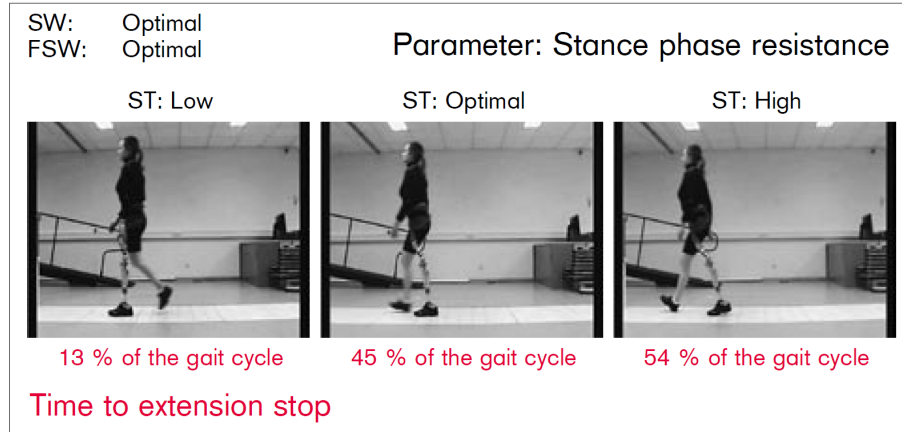


Figure 2-18: Effects of stance phase resistance (ST) on the time (expressed as percent gait cycle) to reach the hip extension stop [76].

FSW and SW adjustments are primarily used to adjust step length [76]. FSW allows a certain stride length within which the hip flexes without resistance [60]. SW determines how much hip flexion resistance acts on the hip joint past the hip flexion range without resistance [60]. Results for step length are represented in Figure 2-19 for different SW settings. An optimal SW setting provides approximately 0.69 m step length [76].

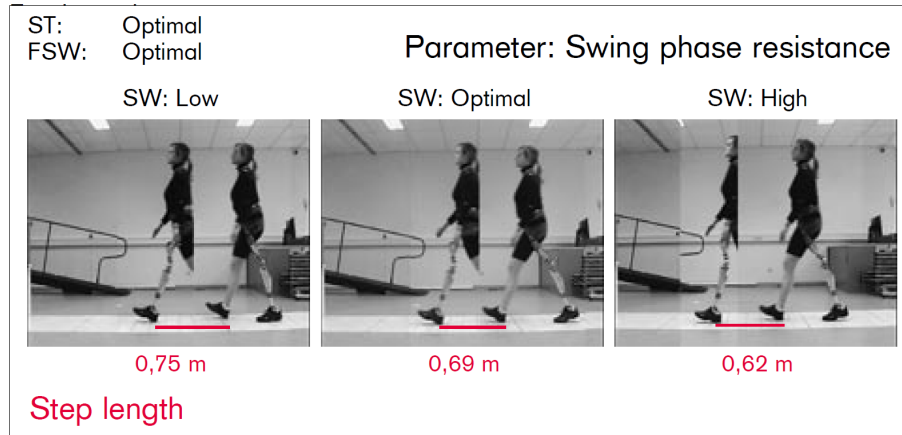


Figure 2-19: Effects of swing phase resistance (SW) on step length [76].

The Helix3D hip joint, being made of aluminum and weighing 990 g [6], [60], can bear a person weighing 100 kg body weight and has a fatigue life of two million cycles [6], [17], [60]. Unlike the hip flexion bias system, a HKAFFP becomes unstable in weight bearing when polycentric knee joints are used in combination with the Helix3D hip joint [76]. For best stability, microprocessor controlled

knee joints such as the Otto Bock C-Leg and the Otto Bock Genium are preferable in a HKAFP containing Helix3D [6], [17], [60].

Studies have compared gait with the Helix3D or 7E7 hip joint when combined with the C-Leg knee joint [13], [18], [76], [134], [135]. Walking speed and prosthetic side step length were similar with the two hip joints [13]. Figure 2-20 shows differences in hip joint angle and moment patterns [13]. On average, motion was much more rapid and abrupt with the 7E7 hip joint than the Helix3D hip joint, especially in early stance and early swing phases, because the Helix3D hydraulic cylinder provided more damping than the 7E7 constant-friction pin joint [13], [76]. As a result, hip amputees experienced approximately double the amount of stabilizing hip extension moment with the Helix3D hip joint compared to the 7E7 hip joint [13]. The polycentric nature of the Helix3D increased stance phase stability [13]. Furthermore, the range of pelvic tilt was much smaller with Helix3D than with the 7E7 hip joint, which could help alleviate spinal pain [13]. Natural hip angle and angular velocity were better reproduced with the Helix3D than other hip joints [13], [25], [136], [137], [138].

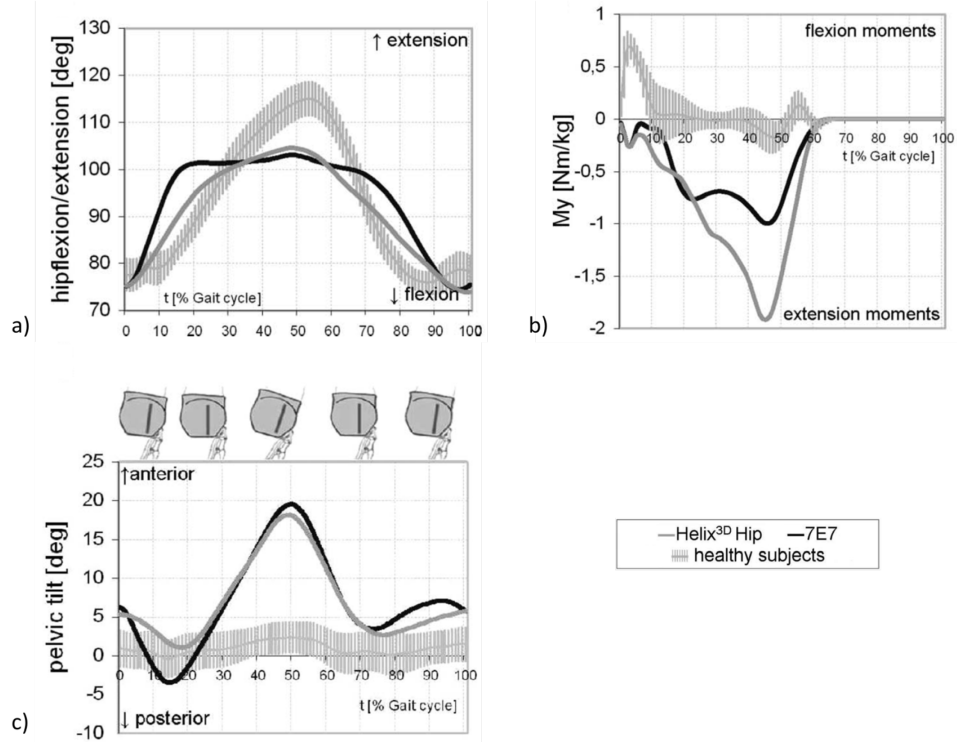


Figure 2-20: Mean gait data with the Helix3D and 7E7 hip joints in comparison to able-bodied gait (± 1 standard deviation): a) flexion/extension moments, b) flexion/extension angles, c) pelvic tilt angle [13].

Functional outcomes were also investigated with these two hip joints [18], [134], [135]. One study described a hip amputee who completed the timed up and go and 2-minute walk tests 1.7 to 1.9 times faster with Helix3D than the 7E7 hip joint, after fifteen weeks of training [18]. Another study showed improvements in speed and mobility when completing various functional activities such as

walking down a ramp or staircase with Helix3D versus the 7E7 joint [135]. However, a study with three people indicated that the amputees abandoned the Helix3D hip joint in favor of their previous hip joints due to comfort problems [134].

2.4 Overview of Prosthetic Hip Joint Specifications

Table 2-1 lists the specifications for various hip joints from Otto Bock. ‘EBS’ refers to Otto Bock’s EBS knee mounted in reverse at the hip. All hip joints listed in Table 2-1 are made of aluminum, except the 7E7 hip joint which is made of titanium. The 7E8 hip joint is paediatric. Some quantities are unavailable and thus, are unlisted.

Table 2-1: Specifications for Otto Bock's 7E series hip joints and EBS knee joint mounted at the hip.

Specifications	7E4	7E5	7E7	7E8	7E9	7E10	EBS
Max body weight	100 kg	100 kg	100 kg	45 kg	125 kg	100 kg	125 kg
Device weight	-	-	-	-	-	0.99 kg	0.88 kg
Fatigue life (# of cycles)	2 million	3 million					
Max hip flexion	-	-	-	125°	130°	130°	175°
Max hip extension	-	-	-	-	-	15°	10°

2.5 Lower-Limb Amputee Gait

Ideally, a lower-limb prosthesis would restore gait to the performance seen in able-bodied individuals. However, this restoration becomes increasingly difficult with more superior levels of amputation. Rather than attempting to design a prosthetic hip that restores gait to able-bodied performance, a more reasonable approach is to design a prosthetic hip that restores gait to TF amputee performance.

2.5.1 Gait Compensation Mechanisms and Gait Deviations

The more superior level of lower-limb amputation, the more difficult it is for the amputee to ambulate due to the greater loss of biological joints and musculoskeletal structure [46], [47], [48], [49], [50], [51], [52]. For unilateral lower-limb amputees, a more severe amputation generally results in a slower and more asymmetrical gait [46], [49], [52], [53], [54], [55], [56], [139]. Gait deviations occur because lower-limb amputees employ different muscles to achieve a smooth gait pattern than able-bodied people [47], [125], [140], [141]. A lower-limb amputee requires greater compensation by the trunk, hip, and sound leg muscles to achieve postural stability and movement throughout the gait cycle; therefore, a lower-limb amputee consumes more energy when they walk [52], [58], [140], [142], [143].

Gait compensation mechanisms in TF amputees include vaulting [19], [99], [144], hip hiking [99], [140], [145], circumduction [99], [144], whipping (i.e., sudden internal or external rotation of the heel during swing) [19], [144], increased abduction [19], [146], [147], lateral trunk bending [19], [52], [144], [146], [147], anterior trunk bending [144], [146], [147], and lumbar lordosis [19], [146], [147]. These compensatory movements result in gait deviations including prolonged prosthetic knee extension during stance phase [140], [142], greater loading bearing on the sound limb than the prosthetic limb [46], [58], [140], [148], [149], shorter prosthetic limb stride than sound limb stride [144], shorter prosthetic limb stance time than sound limb stance time [46], [52], [144], increased step width [19], [46], [144], increased pelvis and sound limb hip and knee movement [52], [58], [140], [148], [150], decreased walking speed [46], [58], [143], [151], [152], [153], and decreased cadence [46].

Gait compensation mechanisms and gait deviations seen in TF amputees have also been reported for HD and HP amputee gait including hip hiking, pelvic rotation, circumduction, whipping, lumbar lordosis, and increased sound limb hip and knee movement [1], [19], [45], [46], [71], [72], [73], [76], [77]. Gait compensation and gait deviation are generally more severe for hip-level amputees due to the higher level of amputation [46]. As a result, an average unilateral HD or HP amputee requires 1.6 to 2.5 times more energy for level walking than able-bodied individuals [23] and more than 1.68 to 2 times more energy than an average unilateral TF amputee [140], [142].

2.5.2 Hip and Knee Joint Kinematics and Kinetics

Figure 2-21 illustrates sagittal plane kinematic and kinetic curves for the prosthetic hip joint for unilateral HD/HP and unilateral TF amputees, and the dominant hip for able-bodied individuals. Figure 2-22 presents knee kinematics and kinetics. Curves were plotted with the ‘LiteraturePlot.m’ MATLAB program (Appendix B.3). HD/HP amputee gait data were obtained from six unilateral HD amputees walking on level-ground at 1.08 ± 0.21 m/s with the Helix3D hip joint [13]. No joint power data for HD/HP amputees were available in literature. TF amputee gait data were obtained from eight individuals who walked at 1.11 ± 0.10 m/s with the C-Leg knee [149]. Able-bodied gait data were obtained from 22 individuals who walked at 1.17 ± 0.21 m/s [154]. These data were selected for presentation because they are comprehensive, cover a wide range of genders, ages, and bodyweights, have been collected in a well-controlled experimental environment, and reflect the use of state-of-the-art prosthetic technology.

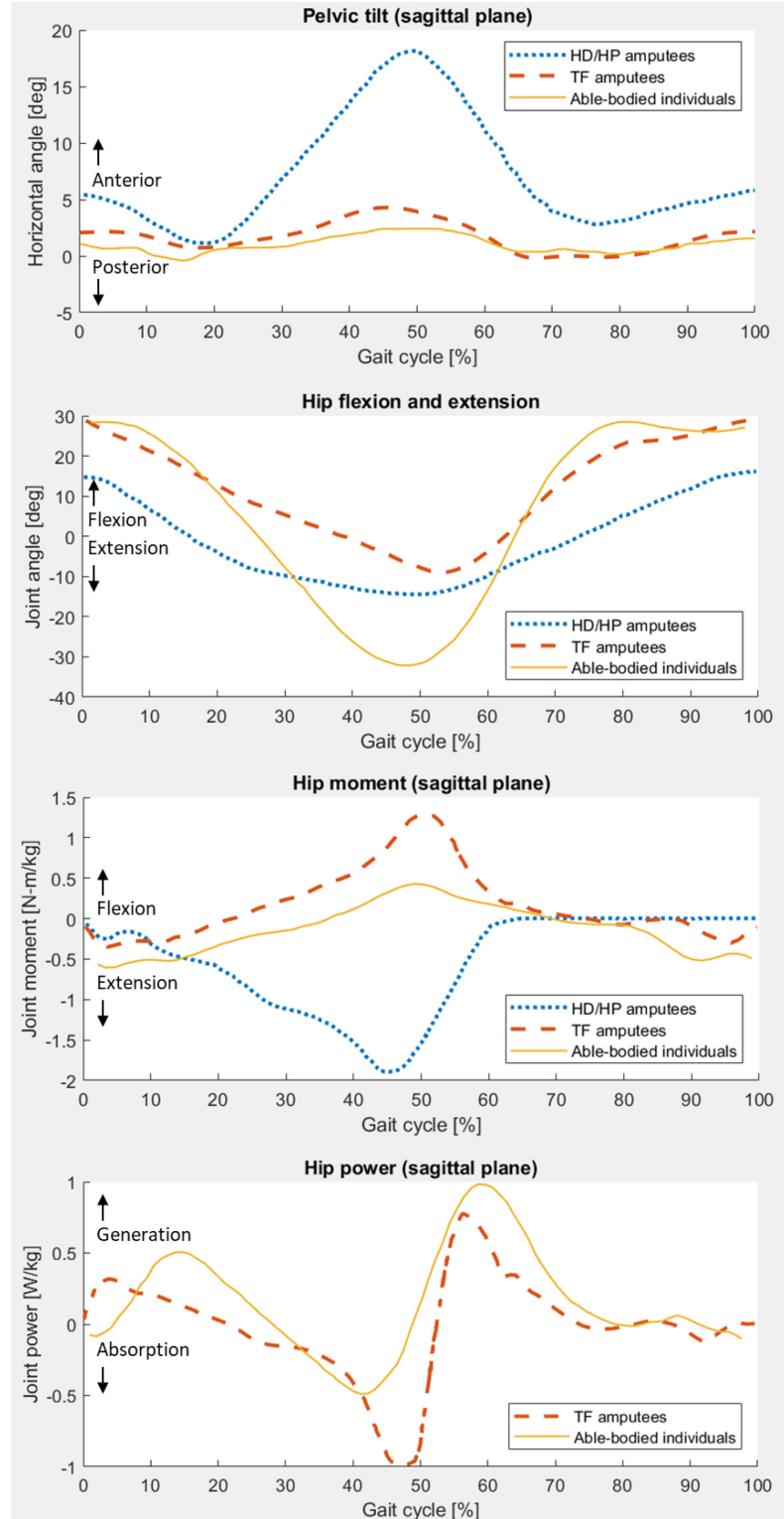


Figure 2-21: Sagittal plane prosthetic hip joint kinematics and kinetics over one level-ground gait cycle for different levels of lower-limb amputation. HD/HP amputee data obtained from [13]. Mean curves shown starting from foot strike. Pelvic tilt data obtained from The Ottawa Hospital Rehabilitation Center. Other TF amputee data obtained from [149]. Able-bodied data obtained from [13], [154].

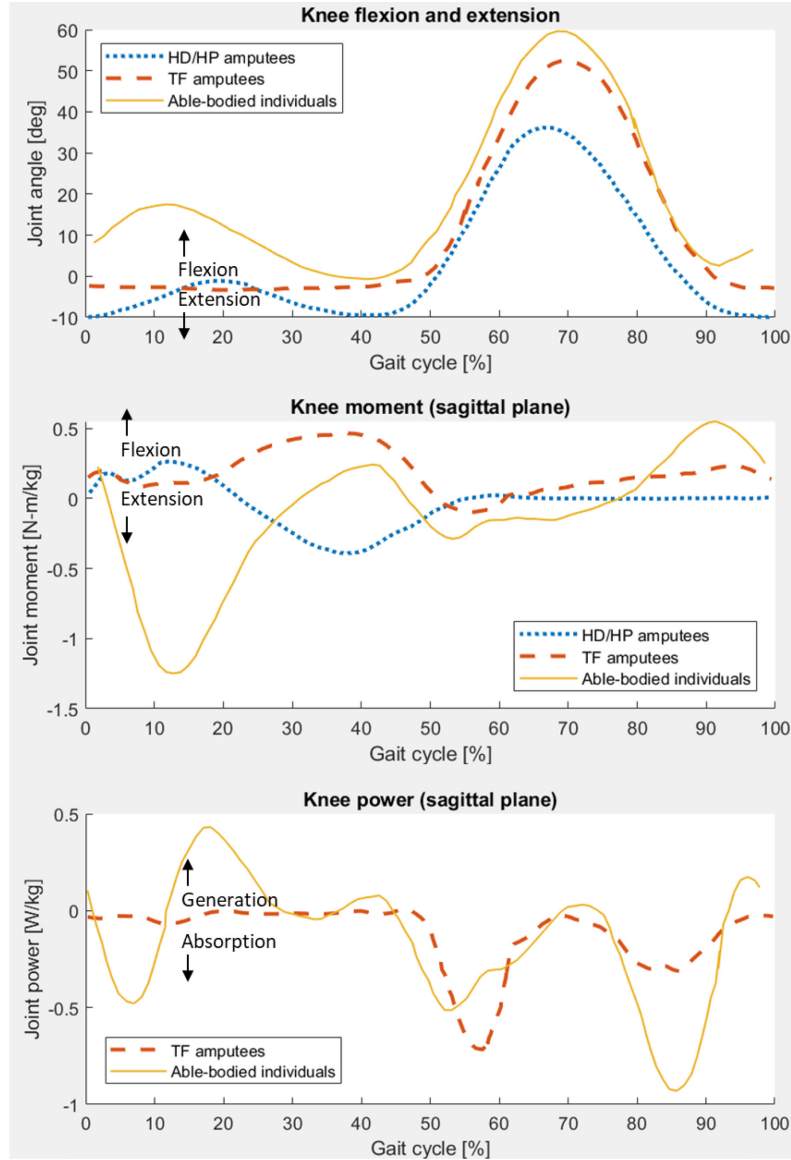


Figure 2-22: Sagittal plane prosthetic knee joint kinematics and kinetics over one level-ground gait cycle for different levels of lower-limb amputation. Mean curves shown. HD/HP amputee data obtained from [13]. TF amputee data obtained from [149]. Able-bodied data obtained from [154].

Both HD/HP and TF amputees walk with less prosthetic hip and knee motion than what is expected for able-bodied gait [13], [149], [154]. Individuals with more severe amputations exhibit lower walking speeds that correspond to lower joint motion ranges [13], [149], [154]. HD/HP amputees experience both reduced hip flexion and reduced hip extension, whereas TF amputees experience reduced hip extension only [13], [149], [154]. During weight acceptance, able-bodied individuals flex their knees slightly, whereas HD/HP and TF amputees maintain full knee extension during stance phase [13], [149]. Both HD/HP and TF amputees initiate swing phase later in the gait cycle than able-bodied individuals [13], [149], [154].

To compensate for the loss of hip flexor and extensor muscles, HD/HP amputees swing their pelvis back and forth to give momentum to the hip [13]. This pelvic tilt is greatly exaggerated in HD/HP amputees compared to TF amputees and able-bodied individuals [13], [149], [154]. HD/HP amputees walk with an anteriorly tilted pelvis and have the greatest pelvic tilt just before push-off [13].

Non-amputees exert a concentric hip extension moment in early stance to accelerate the leg backward while preventing hip flexion [154]. In late stance, non-amputees exert an eccentric hip flexion moment to slow down the backward motion of the leg and then bring the leg forward into swing phase [154]. Concentric hip flexion follows to continue leg forward progression during swing [154].

TF amputee hip moment patterns are similar to non-amputees; however, TF amputees experience less concentric hip extension and more eccentric hip flexion [149]. As discussed in Section 2.3.1, TF amputees achieve prosthetic knee stability in early stance by exerting a hip extension moment to shift the load line anterior to the knee center, and in late stance by exerting a hip flexion moment to shift the load line posterior to the knee center [91], [93], [94]. TF amputee power generation occurs much earlier than in non-amputees, which indicates that in early stance phase foot contact is less gradual and hip extension is faster and less controlled [149]. As a result, more power absorption is required to slow down hip extension and later flex the hip into swing phase. [149] TF amputees generate less power just before swing phase than non-amputees [149].

HD/HP amputee hip moment patterns differ significantly than TF amputees and non-amputees [13]. HD/HP amputees experience a hip extension moment throughout stance phase without any instances of a hip flexion moment [13]. HD/HP amputees lack the musculature to move the hip [13]. Due to the forward placement of the hip center relative to the knee center, the hip is forced into extension upon foot contact to prevent buckling [13]. The Helix3D hip joint contains hydraulic damping to slow down hip extension during stance phase [13]. HD/HP amputees exert a sound side hip extension moment during stance phase to push the sound leg backward into the ground, resulting in a forward GRF on the body and a forward momentum on the prosthetic leg [155]. Compared to TF amputees and non-amputees, HD/HP amputees experience a slow transition from hip extension to hip flexion from late stance to early swing due to the time taken for momentum to be transmitted from the sound leg to the prosthetic leg [155]. Furthermore, HD/HP amputees rely on moving their trunk and pelvis backward to generate prosthetic leg forward momentum [13], [155]. This pelvic tilt is a tiresome gait compensation that reduces gait efficiency. The motor within the novel powered hip would provide hip moments where required and reduce the need for HD/HP amputees to tilt their pelvis to generate prosthetic leg momentum.

Non-amputees exert a knee extension moment to prevent the knee from buckling during weight acceptance [154]. A slight knee flexion moment occurs during push-off and in terminal swing phase

to slow the knee down for the next stride [154]. Knee power absorption occurs during weight acceptance, during push-off and in terminal swing phase [154]. Knee power generation occurs during midstance while the leg is kept straight as it moves backward [154].

Both TF and HD/HP amputee knee moment patterns are much different than non-amputee knee moment patterns [13], [149], [154]. TF amputees do not experience a knee extension moment in early stance phase but rather a knee flexion moment during mid-stance [149]. TF amputees walk with almost no knee power from early to late stance when their knee remains in full extension [149]. It is hypothesized that this knee flexion moment occurs due to knee pressing against its extension stop. TF amputees experience a slight knee extension moment during push-off to maintain knee stability and a slight knee flexion moment during swing phase to bend the knee for adequate swing phase toe clearance [149]. TF amputee knee power absorption occurs in early and mid swing phases [149]. HD/HP amputees experience a knee extension moment during mid-stance to late stance to keep the knee stable [13].

2.6 Powered Prostheses

Powered prostheses contain an actuator that provides augmenting moments that compensate for an amputee's missing musculature. Compared to passive prostheses, powered prostheses are reported to facilitate gait activities and increase gait symmetry [113], [115], [156], [157], [158], [159], [160], [161], [162], [163], [164], [165], [166], [167]. Most powered lower-limb prostheses are for transfemoral or transtibial amputees. The Össur Power Knee, released in 2007, is the only powered knee joint on the market for transfemoral amputees [10], [139], [158], [168]. There is no viable power hip currently on the market. In this thesis, the Össur Power Knee motor was utilized in conjunction with a four-bar linkage. The varying mechanical advantage of the linkage provides higher torque at points in the gait cycle where the HD or HP amputee is prone to limb instability. The linkage's mechanical advantage varies with the ICR location.

2.6.1 Össur Power Knee 2

The Össur Power Knee 2 contains a brushless DC motor that is connected to a harmonic drive (Figure 2-23) [158]. A harmonic drive contains a wave generator, flex spline, and circular spline [169], [170], [171], [172]. The wave generator, being an ellipse fitted with a ball bearing, is the transmission's driving element [169], [170], [171], [172]. The flex spline is a high-strength, torsionally stiff, and radially flexible component with external teeth. The circular spline is a rigid ring with internal teeth [169], [170], [171], [172]. The circular spline, having an inner diameter slightly larger than the flex spline outer diameter, contains two more teeth than the flex spline and is fixed relative to the motor

[169], [170], [171], [172]. When the wave generator rotates inside the flex spline, the flex spline radially deforms and assumes an elliptical shape [169], [170], [171], [172]. This deformation leads to meshing the flex spline at opposite ends along the ellipse's major axis [169], [170], [171], [172]. The flex spline rotates relative to the circular spline due to the mismatching number of teeth [169], [170], [171], [172]. For every full rotation of the wave generator, the flex spline teeth are advanced by two teeth relative to the circular spline [169], [170], [171], [172]. Output torque is transmitted through the flex spline while it rotates inside the circular spline [172]. Advantages of a harmonic drive include a high gear ratio (80:1 in the Össur Power Knee 2 DC motor), zero backlash between mating teeth (i.e., high positional accuracy), and a compact, lightweight design [169], [170], [171], [172].



Figure 2-23: a) Össur Power Knee with a brushless DC motor at the proximal end [10], b) harmonic drive implemented in the Össur Power Knee brushless DC motor (adapted from [169]), c) harmonic drive operation (adapted from [170]).

Table 2-2 lists specifications for the Össur's Power Knee 2 motor and battery to be implemented in the novel power hip.

Table 2-2: Össur's Power Knee 2 and chosen battery specifications.

Specification	Value
Motor mass	1.43 kg
Motor torque capacity	96 N·m
Motor length	8.0 cm
Motor diameter	7.7 cm
Battery mass	0.49 kg
Battery capacity	95.0 W·h

Össur's Power Knee 2 provides active assistance for level-ground walking and ascending/descending stairs or ramps [10], [173], [174]. In the Power Knee 2, the DC motor is connected to a series elastic actuator (SEA), which is a metal strip attached to the motor and a pulley at the distal end of the knee [139], [175]. As the motor rotates, the SEA pulls or pushes on the distal end of the knee to provide knee flexion or extension [175]. The Power Knee 2 contains sensors to accurately detect user movements and inform the microprocessor. Within the microprocessor are imbedded algorithms that interpret these movements and enable the knee to reproduce natural gait and symmetrical weight distribution [10], [139], [173], [174].

Many non-commercial powered prosthetic knee joints are being developed and/or clinically tested [139]. DC motors, brushless DC motors, linear stepper motors, servomotors, pneumatic tubes, and hydraulic tubes are the power transmissions elements that have been used in power knees [113], [139], [168], [175], [176], [177], [178], [179], [180]. Stiff actuators, SEAs, parallel springs, pneumatic muscles, and variable stiffness actuators are powered knee actuation strategies [139], [168], [175], [179], [180], [181].

Brushless DC motor alternatives to the Össur Power Knee 2 motor have been considered for use in the novel power hip. Table 2-3 compares the Power Knee 2 motor to brushless DC motors of a similar torque, mass and/or size, manufactured by Hathaway Emoteq Inc [182]. The Power Knee 2 motor has a much higher torque to mass ratio than any Emoteq motor and is much smaller than the two Emoteq motors with torque capacities similar to the Power Knee 2 motor [182]. For these reasons, the Power Knee 2 motor has been developed for use in the novel power hip.

Table 2-3: Comparison of the Össur Power Knee 2 brushless DC motor to three Hathaway Emoteq Inc. High Torque (HT) series brushless DC motors. Lengths and diameters include the motor housing. Hathaway Emoteq specifications obtained from [182].

Motor Specifications	Power Knee 2	HT07001	HT07000	HT02305
Torque capacity (N·m)	96.0	140.6	57.2	12.9
Mass (kg)	1.43	9.90	7.10	1.38
Length (cm)	8.0	9.6	7.9	8.9
Diameter (cm)	7.7	19.7	19.7	7.1

2.6.2 Powered Hip Prostheses

In 2013, Össur patented a powered hip prosthesis, the Power Hip, which is a slight modification of the Power Knee 2 mounted with the anterior face of the knee facing backwards (Figure 2-24) [16], [23], [183]. Össur's motivation for developing the Power Hip was to provide additional energy for HD and HP amputees [23], [183]. The Power Hip was tested on one bilateral amputee with the left leg being a hip disarticulation and the right leg being a TF amputation [23], [183]. The amputee used three setups for their left leg [23], [183]. The control HKAFP setup consisted of the Otto Bock Helix3D hip and the Otto Bock Genium X2 knee [23], [183]. The two test HKAFP setups included the Össur Power Hip and the Otto Bock Genium X2 knee (a passive microprocessor knee), and the Össur Power Hip and the Össur Power Knee 2 [23], [183]. The participant used the Otto Bock Genium X2 knee for their right leg [23], [183]. All setups provided a maximum hip flexion of 122° and a maximum hip extension of 23° [23]. The Power Hip weighed 3.2 kg and provided up to 96 N·m of torque with a maximum angular speed of 300°/s [23].

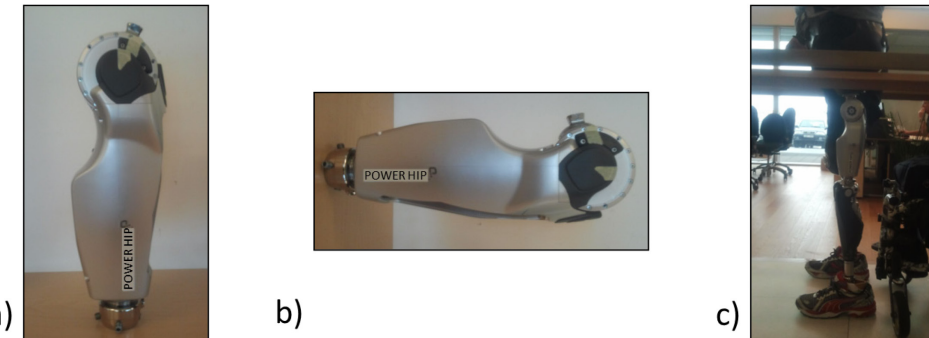


Figure 2-24: Össur Power Hip – a) fully extended (23°), b) fully flexed (122°), c) user with Power Hip and Genium X2 setup. Adapted from [183].

The amputee experienced comfortable and stable standing with the Power Hip [183]. A hip flexion bias of approximately 2° was used to ensure that the prosthesis did not go into extension unexpectedly [183]. This bias reduced balance and the ability to initiate stance phase [183]. However, the Power Hip would be problematic for sitting because the motor was fixed directly below the socket, resulting in an uncomfortable sitting posture with a tilted pelvis.

During level walking with the test setup containing the Genium X2 knee, the hip tended to jerk toward the defined hip flexion bias position. This jerking affected hip extension, causing gait deviations [183]. Motor power was sent to the hip when joint stiffness was required [183]. Foot strike was properly supported by ensuring the hip was stiffened just before contact [183]. In late stance, the hip joint stiffened to stop the shank's backwards momentum and force the knee into flexion [183]. Motor power was also sent to the hip to propel the HKAFP forward during swing [183]. No mechanical dissipation

was required at the hip because the hip moved much more slowly and thus had less momentum than the knee in level walking [183].

During the 2-minute level-ground walk test, the person covered 10% more distance with the Power Hip/Genium X2 knee setup (88 m) than with the Helix3D/Genium X2 knee setup (80 m) [23], [183]. The amputee felt that much less energy was required when walking with the Power Hip than with the Helix3D hip joint [183]. The Power Hip and Power Knee 2 combination appeared to give the best results without needing to make significant changes to device parameters [183]. In all setups, hip flexion was taking place too quickly because the Power Knee 2's firmware (with rapid joint motion) was maintained for all powered prostheses used in the setups [183]. Nevertheless, the amputee felt that the double powered prosthesis setup was the most stable setup [183].

Other power hip prostheses were reported in literature; however, they were still undergoing prototyping or benchmark testing and had not yet reached the clinical testing stage [14], [15], [167]. Figure 2-25 illustrates three powered hip designs that have been disseminated from 2020 to 2022 [14], [15], [167]. Ueyama et al. [14] developed a powered hip containing two DC motors connected to harmonic gearing and a pulley system. Song et al. [15] designed a powered hip containing two rods connected to one prismatic and one revolute joint, and one rod connected to two revolute joints (i.e., a 2-UPR/URR powered hip). Fan et al. [167] developed a powered hip with a brushless DC motor connected to a ball screw powering a remote center mechanism; these authors demonstrated that the remote center hip provides variable stiffness and gait symmetry improvements. The Ueyama and Fan designs appeared to present problems for sitting and being fit underneath clothing due to the bulkiness of the designs near the socket. No prototype of the Song design was presented in literature.

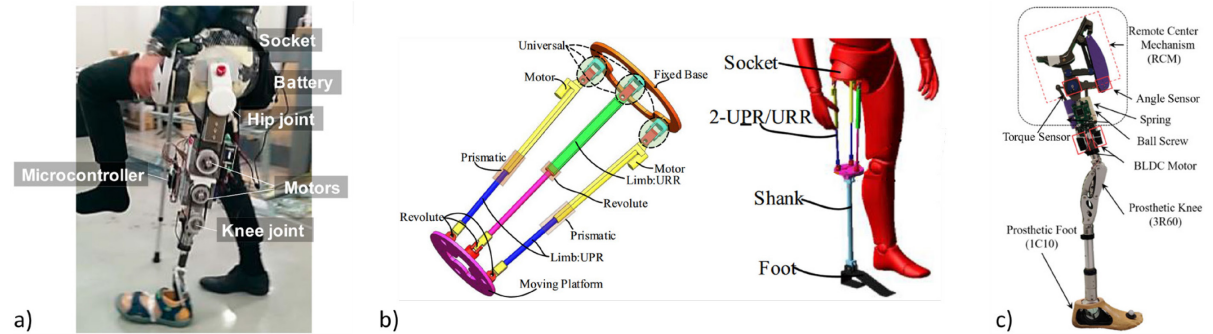


Figure 2-25: Powered hip joints not on the market: a) dual DC motor harmonic drive pulley system by Ueyama et al. (adapted from [14]), b) 2-UPR/URR joint by Song et al. (adapted from [15]), c) remote center mechanism by Fan et al. (adapted from [167]).

2.7 Summary

Of lower-limb amputations, HD and HP are the most severe, leading to the most pronounced gait compensation mechanisms and gait deviations. A four-bar power hip has been designed with the goal of achieving TF amputee gait performance.

The Canadian-type HD prosthesis places a single-axis hip joint anterior to its knee and ankle joints so that the hip remains stable (i.e., remains in extension) during stance. When this prosthesis was first introduced, a major problem was inadequate toe clearance, resulting in vaulting and hip hiking and overly rapid extension in stance phase. Other hip prostheses were developed, but they all maintained the same anterior hip joint alignment.

The Otto Bock Helix3D (7E10) hip joint is the current state-of-the-art. The Helix3D contains a hydraulic cylinder to provide extension damping in stance phase and polyurethane bands to help with swing phase initiation. The Helix3D is a four-bar linkage that has a moving rotation center throughout its ROM. When used in lower-limb prostheses, four-bar linkages can increase joint stability, provide a shortening effect to increase toe clearance, provide out-of-plane motion to better mimic human walking (as is the case with the Helix3D), and offer a varying mechanical advantage.

A powered prosthetic hip provides augmented hip flexion-extension moments to overcome energy-consuming gait compensation and increase lower-limb stability. A motor combined with a four-bar linkage has varying output torques due to the four-bar linkage's varying mechanical advantage. The Össur Power Knee 2 harmonic drive DC motor is appropriate for prosthetic applications due to its high torque to mass ratio.

Literature presents three designs for interfacing an actuator to a prosthetic hip joint. Powered hip prototyping and testing was completed in one paper with one able-bodied participant [14], and in another paper with one hip-level amputee [167]. These powered hip prototypes had poor cosmesis and presented difficulties in sitting. The thesis addresses these gaps in research by detailing the design, prototyping, and testing of the novel powered hip.

Chapter 3: Design Criteria

This chapter presents the power hip design criteria. The goal of the power hip is to provide level-ground walking with active hip joint assistance for HD and HP amputees. This thesis presents the powertrain design only. The powertrain integrates with a separately designed chassis containing the battery and circuit boards.

3.1 Range of Motion

Available specifications from Otto Bock indicate that their prosthetic hip joints offer a maximum of 10°-15° extension and a maximum of 125°-175° flexion [6], [13], [25], [60], [76], [82], [84], [85], [86], [131], [132], [133]. The Össur Power Hip prototype (Power Knee 2 mounted in reverse at the hip) provided 23° maximum extension and 122° maximum flexion [23]. Prosthetic hip ROM for HD/HP amputee walking is 14°-16° extension to 16°-23° flexion [13], [76]. Prosthetic hip ROM for TF amputee walking has been reported to be 9° extension to 28° flexion [149]. The Ottawa Hospital Rehabilitation Center (TOHRC) collected hip ROM data from ten TF amputees using state-of-the-art knee prostheses, reporting average hip ROM between 16° extension and 26° flexion. Able-bodied hip ROM during walking is 32° extension and 28° flexion [154].

4.3 demonstrates that hip extension beyond 20° results in a joint that is much longer and heavier than a joint with 20° hip extension. Activities requiring the most hip flexion are sitting and squatting which require between 80° and 130° hip flexion [184], [185]. Therefore, the design criterion for powered hip ROM is 20° extension to 130° flexion.

3.2 Body Weight

Otto Bock's adult prosthetic hips support maximum body weights between 100 kg to 125 kg [44], [78], [79], [80], [82], [83], [85], [86]. Helix3D supports up to 100 kg. In the ISO 15032:2000 standard for HD/HP prosthesis design [186], the largest body weight category is A100 for people weighing 100 kg [186] and corresponds to a 75th percentile male in the United States from the years 2007–2010 [187]. Therefore, the body weight design criterion is 100 kg.

3.3 Device Weight

Otto Bock's Helix3D weighs 0.99 kg [6], [60] and Otto Bock's EBS weighs 0.88 kg [131], [132], [133]. The additional weight of an actuator in powered prostheses makes the joints heavier than

passive joints on the market. The Össur Power Hip prototype weighed 3.2 kg [23]. The novel power hip should be at most 3.2 kg with motor and battery included.

3.4 Actuator Specifications

Selecting an appropriate actuator is a design challenge for powered prostheses [168]. Underestimating actuator power can impede a person's ability to execute high-power activities [168]. Overestimating actuator power can result in a heavier prosthesis that amputees generally find more tiring to walk with than a lighter prosthesis [168].

Powered hip actuator selection was based on TF amputee hip joint kinetics during walking. For TF amputee level-ground walking, the maximum hip moment ranges from 0.8 N·m/kg to 1.3 N·m/kg, and the maximum hip angular speed ranges from 118°/s to 143°/s [58], [59], [149]. Maximum hip joint power generation in TF amputee level-ground walking was 0.82 W/kg and maximum hip joint power absorption was 0.99 W/kg [149].

The Össur Power Knee 2 DC motor provides 96 N·m maximum torque, 300°/s maximum hip angular velocity, and 503 W maximum power [23]. Össur motor torque would be within the range of hip moments experienced by a 100 kg TF amputee walking on level-ground (i.e., the motor could provide at least 80 N·m of torque). Össur motor power exceeds required hip powers for TF amputee gait performance. With a torque capacity of 96 N·m and a mass of 1.43 kg, the motor has a much higher torque to mass ratio compared to other competitive DC motors on the market. For these reasons, the Össur Power Knee 2 DC motor is appropriate for the novel powered hip.

3.5 Mechanical Loading

The power hip must withstand three kinds of threshold loads: body weight compression, actuator torque, and body weight compression plus actuator torque combined.

The ISO 15032:2000 A100 condition specifies a 3360 N maximum static compression for a prosthesis made of a ductile material, including a 3.43 safety factor [186]. Since the ISO standard assumes that no external power is being provided to the prosthesis, the 3360 N load includes body weight compression only [186].

When a 100 kg HD/HP amputee walks on level-ground, the power hip experiences the person's body weight and the torque required to keep the hip stable at various hip ROM positions. Literature recommends a safety factor of 1.5 to 2 for well-known materials under reasonably constant environmental conditions, subjected to loads and stresses that can be determined readily [188], [189]. For average materials and ordinary but less certain environmental conditions, the recommended safety factor range becomes 2 to 2.5 [188], [189]. Chapter 4 explains that the powered hip is made of

engineering materials that are well-known in industry and are being used extensively by Össur in prosthetic devices. However, environmental conditions can vary depending on the climate of where the user lives. Thus, a safety factor of 2 was selected for the body weight plus torque loading scenario.

The selected power hip actuator provides a 96 N·m maximum torque and thus should not yield under this torque at any position within its ROM. A motor-only loading scenario does not include the weight of a 100 kg person and assumes that the prosthesis body is fixed, and the motor is operating at full torque. A torque load safety factor of 1 has been selected because motor torque can be controlled, and it is impossible to exceed the 96 N·m torque.

3.6 Size and Cosmesis

For the power hip to have an appropriate cosmesis and fit under clothing, the power hip should have similar dimensions to a physiological thigh, or slightly smaller. Due to the supported body weight criterion corresponding to the 75th percentile male, analogous benchmarks were selected for the power hip upper size limits. In the United States, from the years 2007–2010, the 75th percentile male had a thigh length of approximately 42 cm [187]. From the anthropometric data provided in NASA-STD-3000 Man-System Integration Standards, it can be inferred that the 75th percentile American male, in the year 2000, had a thigh diameter of approximately 17 cm [190]. The Helix3D has a 17 cm height from its posterosuperior pivot to the bottom. The Power Knee 2 motor has a 7.7 cm diameter and an 8 cm length.

To reflect anatomical dimensions, the power hip, from below the socket, would, ideally, be no larger than a 17 cm x 17 cm x 17 cm box. A shorter hip joint would accommodate HD/HP amputees of lower percentile heights. Motor dimensions are well within the volume requirement, leaving adequate space for the four-bar linkage. The power hip would be installed above the electronics chassis, leaving a chassis height of up to 25 cm for a maximum desired thigh length of 42 cm.

Power hip designs reported in literature did not fit under clothing and were not appropriate for sitting because the designs had large protrusions below and in front of the socket [14], [167]. The power hip motor must be placed within the prosthetic thigh to keep protrusions away from the socket and therefore, provide good cosmesis under clothing and comfortable sitting. Furthermore, the power hip should be anteriorly mounted on the socket to enhance stability, and not interfere with sitting.

Protrusions near the socket may exist even with the motor placed away from the socket. How much a prosthetic hip sticks out anteriorly when the person is standing depends on prosthetic alignment. For the Helix3D, this anterior protrusion is likely to be approximately 2 cm (Figure 3-1) [134]. Ideally, the powered hip would not stick out more than 2 cm when the person is standing. Expected user thigh diameter is 17 cm, so the powered hip should protrude upward more than 17 cm

when the person is sitting. Moreover, the powered hip bottom surface should be flush with or above the socket bottom surface when the user is sitting.



Figure 3-1: Helix3D hip joint anteriorly mounted on the socket with an anterior protrusion of 2 cm. Adapted from [134].

3.7 Prosthetic Shortening

Most four-bar prosthetic knees shorten during mid-swing to increase toe clearance and reduce the likelihood of stumbling, but some do not shorten appreciably and some lengthen during mid-swing [99]. The powered four-bar hip should shorten by greater than 0 mm during mid-swing.

3.8 Lifespan

Otto Bock's 7E series prosthetic hips are designed to withstand 2 million load cycles (i.e., 2 million strides) before needing to be serviced or replaced [60], [80], [83], [84], [85]. One load cycle is equivalent to one stride or two steps. Otto Bock estimates that a fatigue life of 2 million load cycles corresponds to two to three years of use by a HD/HP amputee [60], [80], [83], [84], [85]. A 7E series prosthetic hip would last two years if the user walked approximately 5500 steps per day and three years if the user walked approximately 3650 steps per day. A healthy adult takes at least 4000 steps per day [191]. Therefore, 2 million load cycles would support a reasonable amount of HD/HP amputee activity for two to three years. To reflect the fatigue life of current prosthetic hips, the power hip should also be able to withstand at least 2 million load cycles.

3.9 Summary

Table 3-1 summarizes previously discussed power hip design criteria.

Table 3-1: Power hip design requirements and criteria.

Requirements	Criteria
Range of motion	20° extension to 130° flexion
Supported body weight	Minimum of 100 kg
Device weight	Maximum of 3.2 kg
Motor torque	At least 80 N-m
Motor angular velocity	At least 143 °/s
Motor power	At least 99 W
Strength	Withstand three kinds of loads: <ul style="list-style-type: none"> • ISO 15032:2000 A100 static compression (3360 N) • Combined body weight and torque loading (100 kg user and required torque for hip stability) with a safety factor of 2 • Maximum motor torque (96 N-m) with no body weight
Size	Length, width, and height less than 17 cm at neutral position (i.e., standing)
Cosmesis	<ul style="list-style-type: none"> • Hip joint anteriorly mounted onto the socket with the motor placed within the prosthetic thigh • Maximum anterior protrusion of 2 cm in the standing position • Maximum superior protrusion of 17 cm in the sitting position • No protrusion below the bottom surface of the socket in the sitting position
Prosthetic shortening	Prosthesis length shortens at mid-swing
Fatigue life	2 million load cycles

Chapter 4: Powered Hip Design

This chapter presents the final powered four-bar hip design and details supporting engineering analysis. The analysis demonstrates appropriate hip joint function and movement and justifies major design decisions. Candidate designs and reasons for their elimination are discussed in Appendix A. Appendix B contains the engineering analysis MATLAB code.

4.1 Design Overview

The powered hip unit weighs 4.337 kg and can be used in a HKAFP (Figure 4-1). The motor is placed between the two inferior revolute joints. The motor housing acts as the inferior link in a closed loop kinematic chain. Figure 4-1 shows the full prosthetic thigh with the powertrain, chassis, battery, and electronics. The scope of this thesis covers the powertrain only.

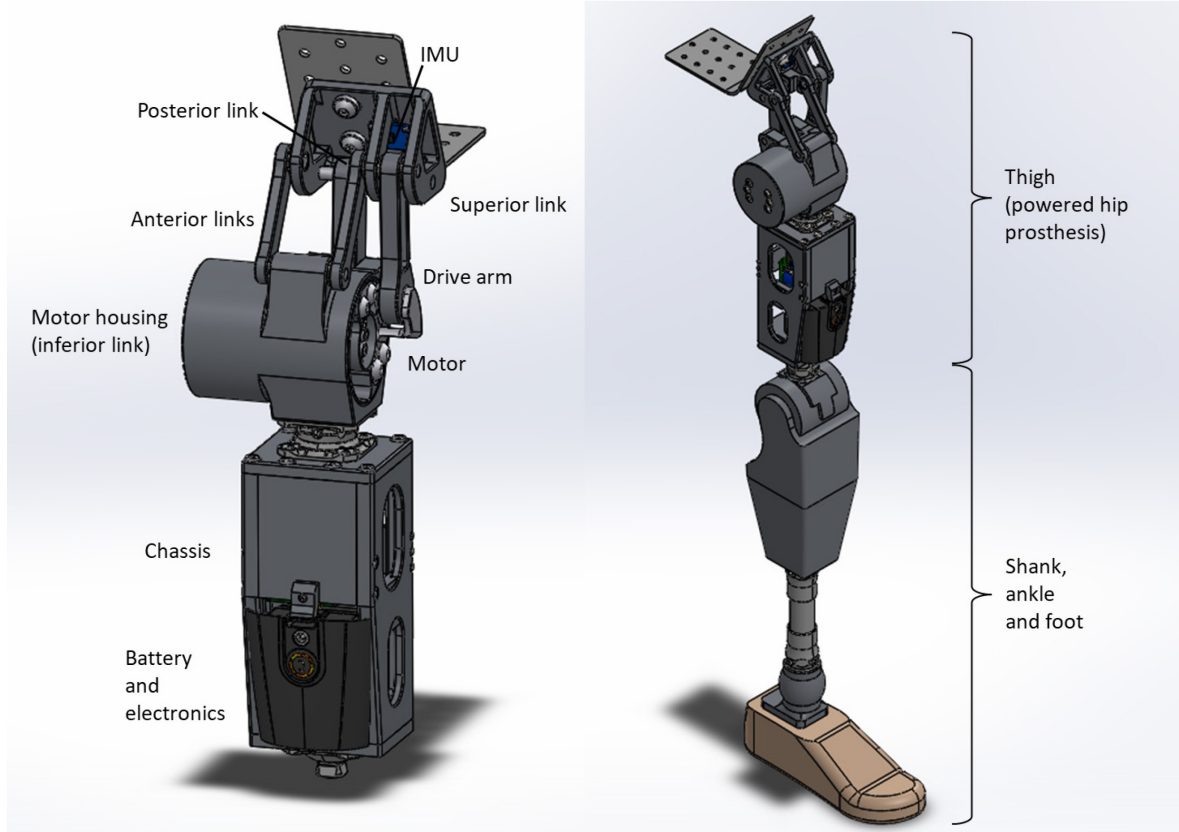


Figure 4-1: Powered four-bar hip joint (left) for use in a right-leg prosthesis (right).

Figure 4-2 illustrates powered hip components and operation. The lateral end of the motor is fixed to the motor housing with screws that fasten into the threaded holes of the lateral motor cover. The motor applies torque to rotate the medial drive flange. A double-supported drive arm shaft is screwed onto the drive flange and a drive arm is mounted onto the shaft. When the drive flange rotates,

the shaft pushes or pulls on the drive arm which pushes or pulls on the superior link. From Newton's third law of action-reaction, an upward push of the drive arm on the superior link (due to counterclockwise (CCW) motor torque when viewing from the medial perspective) results in a downward push on the inferior link to generate hip extension. Similarly, a downward pull of the drive arm on the superior link (due to CW motor torque when viewing from the medial perspective) results in an upward pull on the inferior link to generate hip flexion.

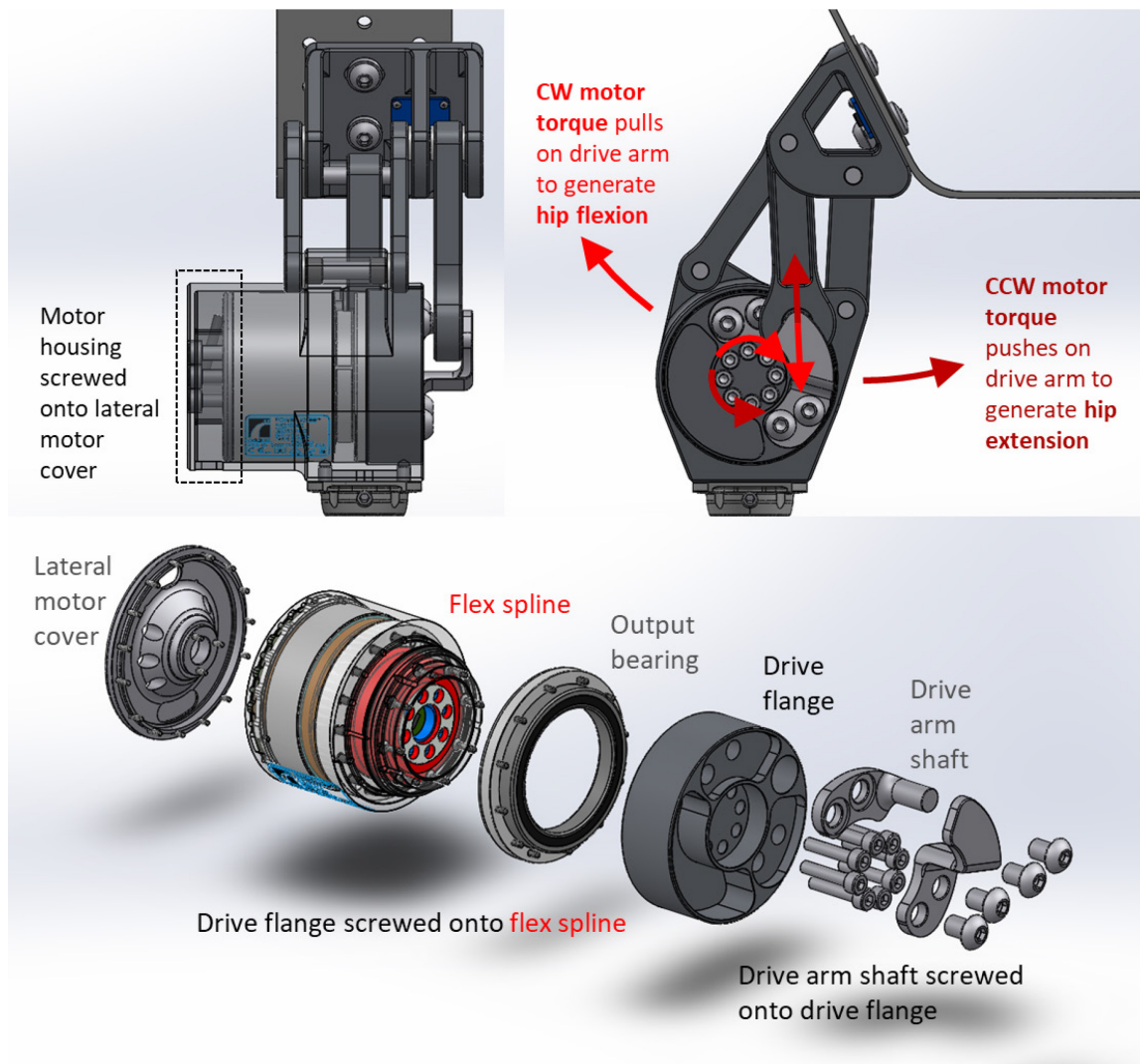


Figure 4-2: Powered four-bar hip joint operation, and motor components.

4.2 Range of Motion and Average Mechanical Advantage

Figure 4-3 shows the ROM from 20° hip extension to 100° hip flexion. Hip extension is limited by posterior link contact on an angled superior link surface. Neutral position occurs when the prosthetic thigh is vertical. Changes in motor angle are indicated by changes in the angle between the bottom

edge of the motor housing and the line connecting the motor center to the drive arm shaft center (i.e., the motor line). Like candidate designs, motor torque is converted to a hip flexion-extension moment that acts at the linkage ICR.

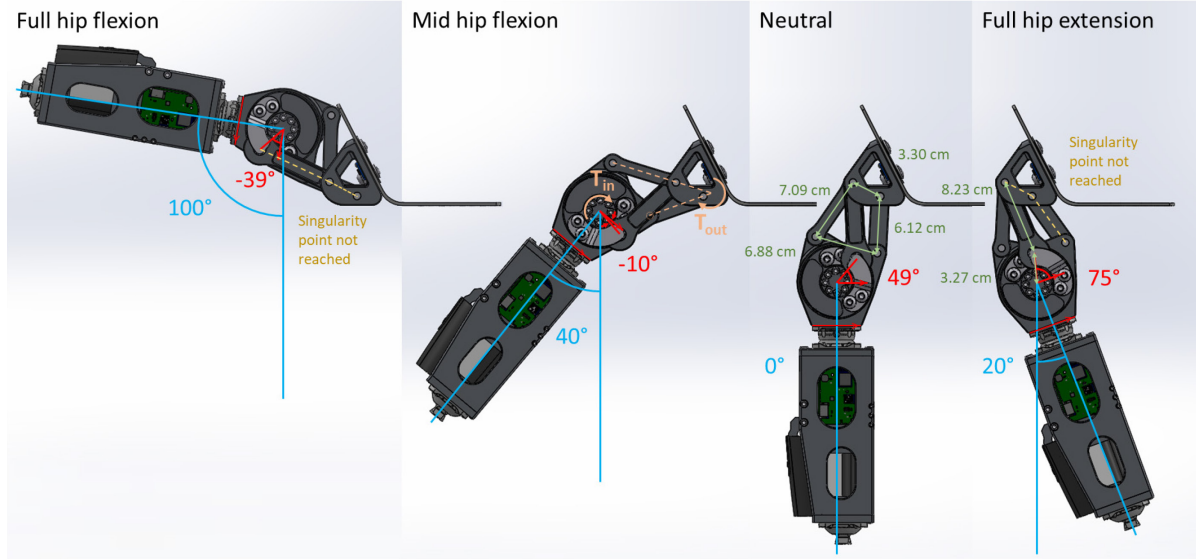


Figure 4-3: Chosen design range of motion. Hip flexion-extension angle is in blue, motor angle is in red, and link dimensions are in green.

Posterior link length is 6.12 cm, inferior link length is 6.88 cm, anterior link length is 7.09 cm, and superior link length is 3.30 cm. Drive arm length is 8.23 cm and the distance from motor center to drive arm shaft center is 3.27 cm. These dimensions were selected through a trial-and-error process detailed in Section 4.3. The selected lengths resulted in a linkage that balances different design criteria.

Unlike the candidate designs, the chosen design also contains a motor linkage (consisting of the drive flange and the drive arm) that transfers torque to drive the four-bar linkage (instead of the motor directly driving the four-bar linkage). Like the candidate designs, the four-bar linkage contains two ROM singularity points that occur when the posterior and superior links are collinear. In addition, the motor linkage contains two ROM singularity points, one when the drive arm and motor line are collinear and the other when the drive arm and superior link are collinear. Figure 4-3 demonstrates that hip flexion and extension singularity points occur slightly beyond their respective physical limits, which guarantees that the linkage will not become jammed due to crossing a ROM singularity point.

When the drive arm and motor line are collinear, the drive arm force line of action passes through the motor center since the drive arm is a two-force member. The motor generates no hip moment because there is no moment arm between the drive arm and the motor center. When the drive arm and superior link are collinear, the drive arm force line of action passes through both superior link pivots. Again, the motor generates no hip moment because there is no moment arm between the drive arm and any of the superior link pivots.

Section 4.3 shows that the powered hip extension singularity point occurs when the posterior link and superior links are collinear and that the powered hip flexion singularity point occurs when the drive arm and superior link are collinear. Figure 4-3 demonstrates that hip flexion and extension singularity points occur slightly beyond their respective physical limits.

The design has an unrestricted hip flexion-extension ROM of 120°. The angle between the drive arm and the motor line changes from 75° to -39° (i.e., motor rotates 114° CW) when the hip moves from full extension to full flexion.

For the powered hip, mechanical advantage (MA) is defined as

$$MA = \frac{T_{out}}{T_{in}} \quad (4-1)$$

where T_{out} is output torque, and T_{in} is input torque. Assuming that energy is conserved throughout power hip operation, rotational power remains constant, i.e., output rotational power equals input rotational power:

$$T_{out}\omega_{out} = T_{in}\omega_{in} \quad (4-2)$$

where ω_{out} is output angular velocity, and ω_{in} is input angular velocity. After combining Eq. (4-1) and (4-2), mechanical advantage can be rewritten as

$$MA = \frac{\omega_{in}}{\omega_{out}} \quad (4-3)$$

or

$$MA = \frac{\frac{d\theta_{in}}{dt}}{\frac{d\theta_{out}}{dt}} \quad (4-4)$$

where $d\theta_{in}$ is the infinitesimal change in input angle, $d\theta_{out}$ is the infinitesimal change in output angle, and dt is the infinitesimal change in time.

For the powered hip, the input angle is motor angle, and the output angle is hip angle. After simplifying Eq. (4-4), the average mechanical advantage throughout the powered hip ROM can be approximated as

$$(MA)_{average} = \frac{\Delta\theta_{motor}}{\Delta\theta_{hip}} \quad (4-5)$$

where $\Delta\theta_{motor}$ is the change in motor angle between ROM extremities, and $\Delta\theta_{hip}$ is the change in hip flexion-extension angle between ROM extremities.

Substituting $\Delta\theta_{motor} = 114^\circ$ and $\Delta\theta_{hip} = 120^\circ$ in Eq. (4-5) yields $(MA)_{average} = 0.95$ for the powered hip. Although the chosen design's average mechanical advantage throughout hip ROM is less than 1, mechanical advantage exceeds 1 from full hip extension to approximately 40° hip flexion, as demonstrated by the change in hip motor angle being larger than the change in hip angle in this hip

flexion-extension range (Figure 4-3). Walking is within this range; therefore, the prosthetic hip will always experience a boost in torque during walking. Designing the hip optimally for walking is one of the main goals of the project. Although the chosen design has a 100° maximum hip flexion (less than the target 130° hip flexion), the increased average mechanical advantage increases the likelihood of hip stability in weight bearing.

4.3 Linkage Optimization

Linkage optimization determined appropriate link geometry (i.e., link lengths and sagittal plane angles between pin joints) for fulfillment of the design criteria. The optimization process consisted of repeated iterations, each of which was evaluated in up to five steps as demonstrated in Figure 4-4. Step 1 was iterative linkage geometry calculations: substitute input lengths and angles, solve the geometric relationships derived in Appendix C for output link lengths and protrusion parameters, and compare the resulting four-bar hip ROM, size, and protrusion to the design requirements. Step 1 was repeated if improvements could be made. Steps 2-4 (involving drive arm force, mechanical advantage, and CAD model checks) were carried out only if step 1 yielded satisfactory outputs. The completion of a few iterations (step 1 done a few times with different guesses for inputs) allowed for a step 5 which was trend observation and the modification of inputs. Most linkage optimization iterations consisted of performing steps 1 and 5. A few promising iterations moved on to steps 2-4. If any of these steps yielded results that were too distant from design requirements, the iteration was ended and the next iteration restarted at step 1.

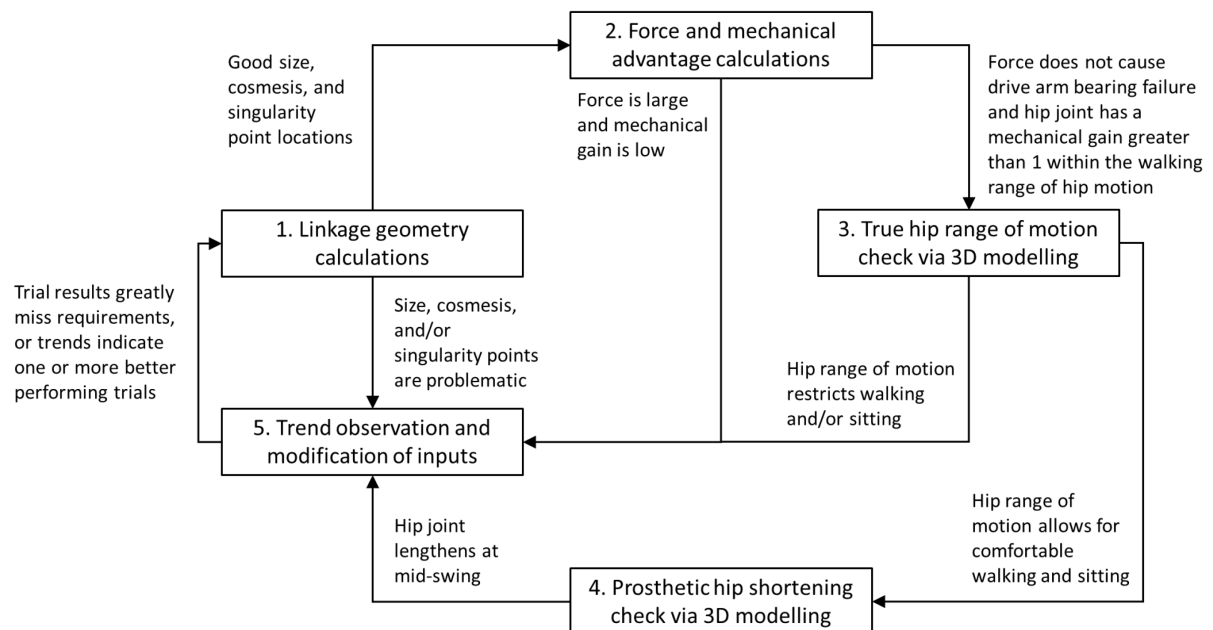


Figure 4-4: Linkage optimization steps for each iteration.

Figure 4-5 shows iteration inputs and outputs of linkage geometry calculations. Inputs that were kept constant for most iterations (i.e., fixed inputs) were lengths r_c , r_2 and r_4 , and angles α , β and θ_4 . Inputs that changed between iterations were angles at hip flexion and extension singularity points: $\theta_{ext_{max}}$, $\theta_{flex_{max}}$, $\theta_{m_{ext}}$, and $\theta_{m_{flex}}$. Outputs were lengths r_1 , r_3 , r_a , r_m , l , h and Δz , and a ‘yes’ or ‘no’ answer to whether the hip crosses a singularity point between $\theta_{ext_{max}}$ and $\theta_{flex_{max}}$.

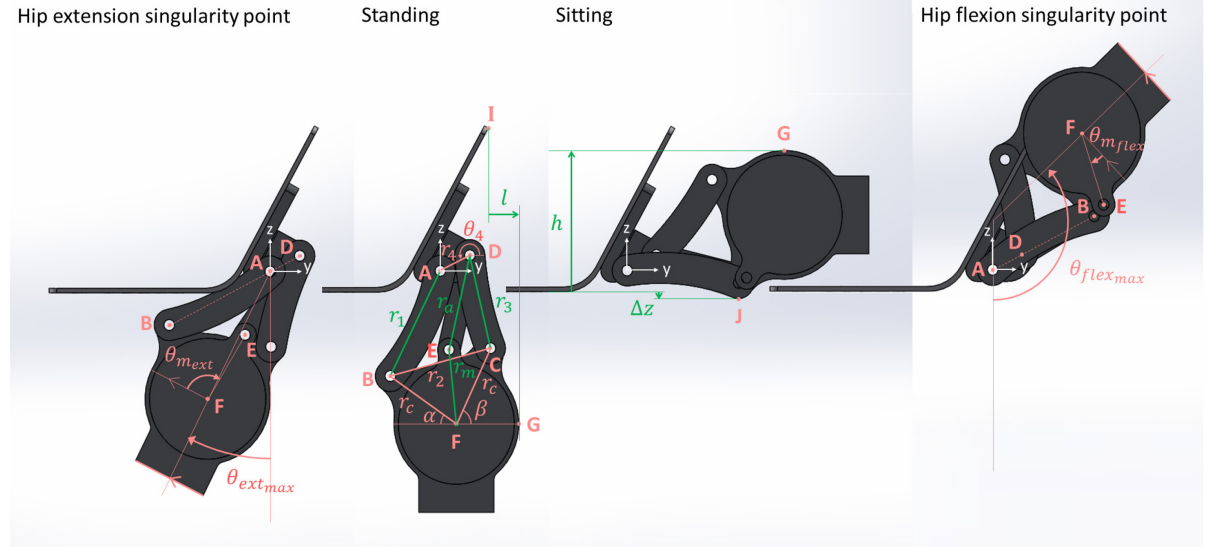


Figure 4-5: Inputs (pink) and outputs (green) of powered hip geometry calculations at four-bar linkage singularity points and standing and sitting positions. Lateral view shown. Dimensions shown on an earlier powered hip model with the motor protruding medially. Origin at point A. Positive y is anterior and positive z is superior.

Table 4-1 lists ranges of input and output values for a hypothetical iteration that satisfies all design requirements simultaneously. To allow design flexibility, no constraints were directly applied on fixed inputs r_c , r_2 and r_4 , and angles α , β and θ_4 . An implicit constraint on r_c , r_2 and r_4 were that they were small enough to satisfy the protrusion constraints l , h and Δz . An implicit constraint on all dimensions was allowing enough distance between components for appropriate motion. Thus, links were made to be as short as possible (i.e., have as little mass as possible) without them mechanically interfering with each other. A positive Δz value meant that point J (Figure 4-5) was above the bottom edge of the socket and vice versa for a negative Δz value (i.e., inferior protrusion).

Table 4-1: Geometric inputs and outputs for an ideal linkage optimization iteration.

Inputs ($^{\circ}$)			Outputs (cm)						
$\theta_{ext_{max}}$	$\theta_{flex_{max}}$	$\theta_{m_{ext}} - \theta_{m_{flex}}$	r_1	r_3	r_a	r_m	l	h	Δz
> 21.0	> 131.0	> 152.0	< 9.30	< 9.30	< 9.30	> 2.15 and < 3.37	< 2.00	< 17.00	≥ 0.00

If such a case were possible, the powered hip would perform to the specifications in Table 4-2. A 6648 N drive arm force would result in a 2 million load cycle fatigue life for the drive arm bearing analyzed in Section 7.1.

Table 4-2: Performance specifications for ideal linkage optimization.

Hip ROM	Size	Max drive arm force	Average mech. adv.	Swing phase shortening
$\geq 20^\circ$ extension and $\geq 130^\circ$ flexion	$\leq 17 \times 17 \times 17$ cm	≤ 6648 N	≥ 1	> 0 cm

An attempt at achieving an ideal case consisted of selecting dimensional inputs satisfying Table 4-1, and performing linkage geometry calculations to obtain the dimensional outputs. No attempt yielded dimensional outputs satisfying Table 4-1. Many attempts yielded a hip joint with singularity points disrupting hip ROM and/or physical interference of components. Therefore, compromises to some performance aspects were made to achieve a design that performs well enough to produce stable level-ground walking for a hip amputee (despite the design not fully satisfying the design requirements). The inputs and outputs in Table 4-1 were adjusted to those in Table 4-3 which would yield a slightly compromised, yet effective design. The ranges of values in Table 4-3 became the linkage geometry optimization constraints. An iteration satisfying these constraints passed step 1.

Table 4-3: Target geometric inputs and outputs for a linkage optimization iteration.

Inputs ($^\circ$)			Outputs (cm)						
$\theta_{ext_{max}}$	$\theta_{flex_{max}}$	$\theta_{m_{ext}} - \theta_{m_{flex}}$	r_1	r_3	r_a	r_m	l	h	Δz
> 21.0	> 101.0	> 122.0	< 9.30	< 9.30	< 9.30	> 2.15 and < 3.37	> 7.00	< 17.00	≥ 0.00

Steps 2-4 were evaluated based on how the iteration compared to the performance specifications in Table 4-4. A 10077 N drive arm force would result in a 500000-cycle fatigue life for the drive arm bearing analyzed in Section 7.1. Mechanical advantage was prioritized within the walking ROM (20° extension to 40° flexion) even if lower mechanical advantages occurred at larger hip flexion angles.

Table 4-4: Target performance specifications for linkage optimization.

Hip ROM	Size	Max drive arm force	Mech. advantage	Swing phase shortening
$\geq 20^\circ$ extension and $\geq 100^\circ$ flexion	$\leq 17 \times 17 \times 17$ cm	≤ 10077 N	≥ 1 within walking ROM	> 0 cm

In no predetermined order, 184 optimization iterations were carried out with linkage geometry calculations in the MATLAB code ‘OptimizeLinkage8.m’ (Appendix B.4). The results of each iteration were recorded in Table D-1 to Table D-40 (Appendix D). Some inputs were modified between

iterations based on results of previous iterations. Table 4-5 shows the results for optimization iteration 179 which was chosen for the powered hip design. Table 4-6 shows the fixed inputs corresponding to iteration 179. Initial fixed inputs were selected through a trial-and-error SolidWorks modelling process. Fixed inputs were modified far less frequently than iteration inputs.

Table 4-5: Linkage optimization iteration 179 chosen for powered hip design.

Iteration	Inputs (°)				Outputs (cm)							
	$\theta_{ext_{max}}$	$\theta_{flex_{max}}$	$\theta_{m_{ext}}$	$\theta_{m_{flex}}$	r_1	r_3	r_a	r_m	l	h	Δz	Sing.
179	36.5	109.5	89.1	-39.0	6.1224	7.0854	8.2285	3.2739	6.0667	11.5240	1.9915	Yes

Table 4-6: Fixed inputs for linkage optimization iteration 179.

Fixed Inputs	r_c	r_2	r_4	α	β	θ_4
Values	5.35 cm	6.88 cm	3.30 cm	35.0°	65.0°	207.0°

In early iterations, output lengths were calculated with angles α and β set to 0. This geometry resulted in link lengths substantially longer than Helix3D link lengths, and anterior protrusion l values that were much longer than Helix3D's anterior protrusion.

Changing angles α and β to $\alpha = 35^\circ$ and $\beta = 65^\circ$, resulted in a more compact geometry. Following iterations with these α and β values resulted in link lengths that were generally shorter than Helix3D links. Inputting hip flexion-extension angle boundaries and motor rotation boundaries implies inputting an average mechanical advantage over the maximum allowable hip ROM (see Eq. (4-5)). Inputting a larger motor rotation often resulted in longer drive arm lengths (r_a values), shorter motor arm lengths (r_m values), and a higher average mechanical advantage.

Increasing the hip extension singularity angle ($\theta_{ext_{max}}$) while keeping all other inputs constant generally decreased posterior link length r_1 , anterior link length r_3 , drive arm length r_a and inferior protrusion Δz (i.e., Δz values were more positive), and increased motor arm length r_m , anterior protrusion l , and superior protrusion h .

Increasing the hip flexion singularity angle ($\theta_{flex_{max}}$) while keeping all other inputs constant generally decreased posterior link length r_1 , anterior link length r_3 , drive arm length r_a and superior protrusion h , and increased motor arm length r_m , anterior protrusion l , and inferior protrusion Δz (i.e., Δz values were more negative).

$\theta_{ext_{max}}$ and $\theta_{flex_{max}}$ are not to be confused with physical hip flexion/extension limits ($\theta_{ext_{allow}}$ and $\theta_{flex_{allow}}$). $\theta_{ext_{max}}$ and $\theta_{flex_{max}}$ values were selected to be slightly beyond the targeted

$\theta_{extallow}$ and $\theta_{flexallow}$ values to give room for play before reaching singularity points and to reduce the drive arm force at maximum hip extension.

Section 5.4 demonstrates that the drive arm force for a set motor torque increases as hip extension angle increases, with the maximum drive arm force being at the maximum allowable hip extension. The maximum force that the drive arm can withstand equals the drive arm bearing static load capacity of 11.8 kN (see Section 6.3 for more information on bearing selection). The drive arm has a 1 million cycle fatigue life at 90% reliability at its bearing dynamic load capacity of 8.18 kN. The powered hip is required to achieve a minimum hip extension of 20°. While many iterations satisfied the ROM and cosmesis requirements, they did not satisfy the torque handling requirement because the drive arm force under the 96 N-m maximum motor torque greatly exceeded the 11.8 kN limit at 20° hip extension.

Designing the powered hip to physically extend past 20° was not considered due to the difficulties in achieving a reasonable drive arm force at 20°. To maintain structural integrity at hip extension angles beyond 20°, motor linkage components would need to be larger and/or made of stronger materials to handle the larger drive arm force and therefore, device weight would increase. Also, longer links may be required to bring the motor housing further away from the socket as to not cause interference with the socket well before the desired hip flexion or extension angles are reached (and thereby, well before the hip flexion and extension singularity positions are reached).

Increasing motor rotation while keeping all other inputs constant increased the average mechanical advantage but also increased the drive arm force at 20° hip extension. The optimization process was improved by including drive arm force and average mechanical advantage calculations after linkage geometry calculations were carried out.

Shifting the hip ROM more towards extension while keeping the same amount of motor rotation (i.e., increasing θ_{extmax} and decreasing $\theta_{flexmax}$, and keeping the difference between $\theta_{m_{ext}}$ and $\theta_{m_{flex}}$ the same) reduces the drive arm force at 20° hip extension while maintaining the average mechanical advantage. This reduction in drive arm force occurs due to the hip flexion singularity being moved further away from 20° hip extension, which in turn, increases the moment arm between the drive arm and hip ICR. However, this ROM shift resulted in the motor linkage hip flexion singularity point occurring at a smaller hip flexion angle and/or in the motor housing contacting the socket at a smaller hip flexion angle, thereby reducing the hip flexion range.

Motor housing geometry was kept constant for most iterations. However, experimenting with different α and β values provided valuable information on how motor housing geometry affects drive arm force and mechanical advantage. Section 5.3 shows that high motor torques are required during hip extension; therefore, average mechanical advantage values from full hip extension to neutral were

examined. For most iterations, $\alpha = 35^\circ$, $\beta = 65^\circ$, $\theta_4 \cong 207^\circ$, and $r_4 = 2.20\text{ cm}$. Other link lengths in Table 4-7 show how changing α and β influenced powered hip performance. Extension mechanical advantage values were not calculated when the change in α and β values resulted in an increased drive arm force because these iterations were eliminated since the goal was to decrease drive arm force.

Table 4-7: Changes in powered hip performance with changes to α and β relative to $\alpha = 35^\circ$ and $\beta = 65^\circ$, $\theta_4 \cong 207^\circ$, $r_c = 5.35\text{ cm}$, and $r_4 = 2.20\text{ cm}$. Approximate increases and decreases are provided.

α	β	Change in drive arm force at 20° hip extension	Change in average mechanical advantage from 20° hip extension to neutral
40°	65°	30% decrease	10% decrease
30°	65°	189% increase	-
35°	75°	345% increase	-
35°	60°	32% decrease	16% decrease
40°	60°	46% decrease	14% decrease
30°	70°	575% increase	-

The largest decrease in drive arm force at 20° hip extension occurred when $\alpha = 40^\circ$ and $\beta = 60^\circ$, but the iteration was suboptimal due to the accompanying decrease in average mechanical advantage from 20° hip extension to neutral.

Motor housing geometry could have also been modified by changing r_c , the distance between the motor center and the motor housing pivots. However, a smaller r_c would have been difficult to achieve due to anterior or posterior link interference with the motor housing (whose minimum size is governed by the motor diameter). A larger r_c would have increased the overall size and weight of the hip and would have potentially reduced the hip flexion range due to the anterosuperior portion of the motor housing contacting the socket sooner. Therefore, the optimization process leading up to the selection of iteration 179 for the design did not experiment with different r_c values.

Superior link length r_4 was kept constant for most iterations. However, modifying r_4 provided valuable information on how superior link length affects drive arm force, mechanical advantage, and overall hip ROM (limited by the hip extension stop and the socket at full hip flexion). The optimization process was expanded to calculate mechanical advantage over the hip flexion-extension angles seen in TF amputee walking which range from approximately 20° hip extension to 40° hip flexion. Table 4-8 shows how changing r_4 influenced powered hip performance.

Table 4-8: Changes in powered hip performance with changes in r_4 relative to $\alpha = 35^\circ$ and $\beta = 65^\circ$, $\theta_4 \approx 207^\circ$, $r_c = 5.35\text{ cm}$, and $r_4 = 2.20\text{ cm}$. Approximate increases and decreases are provided.

r_4	Change in drive arm force at 20° hip extension	Change in average mechanical advantage for walking hip range of motion	Change in hip flexion range
3.0 cm	8% increase	17% increase	3° increase
3.3 cm	11% decrease	29% increase	2° increase
3.5 cm	21% decrease	40% increase	7° decrease

A superior link length (r_4) of 3.3 cm provides benefits to device function without sacrificing any other functional aspects. Other values of r_4 meant increasing the drive arm force or decreasing the hip flexion range. At this optimization stage, mechanical advantage and hip ROM were prioritized over drive arm force so long as the drive arm force was well below 11.8 kN (i.e., prosthesis function was prioritized over prosthesis longevity during the first prototype stage of the project). Therefore, subsequent iterations were carried out with $r_4 = 3.3\text{ cm}$.

In later iterations, cosmesis parameters l and h became lesser priorities so that options that potentially provide better hip function could be examined. For iteration 179, anterior protrusion l was calculated to be 6.07 cm; however, superior link anterior protrusion was slightly increased, thereby increasing l to 6.68 cm and increasing the hip flexion range from 98.5° to 100°. Inferior protrusion Δz remained a high priority because it determined user comfort in sitting. In addition, motor arm length r_m was examined more closely. To avoid design complications, the originality of the drive flange (an existing part in the Össur Power Knee 2 motor) was preserved as much as possible. Therefore, r_m was chosen such that the drive arm shaft lied within the unused portion of the drive flange and such that the drive flange outer diameter remained approximately equal to the 7.70 cm motor outer diameter. Figure 4-6 illustrates that the ideal r_m range was 2.15 cm to 3.37 cm.

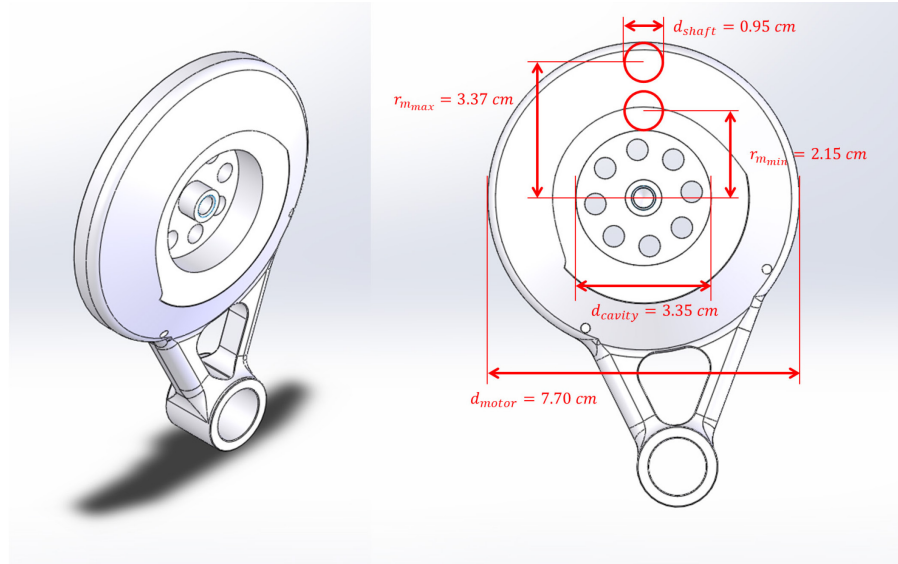


Figure 4-6: Drive flange motor arm design region. The drive arm shaft should lie between the circle of diameter d_{cavity} and the circle of diameter d_{motor} . Original drive flange from the Össur Power Knee 2 motor shown.

Iteration 179 resulted in a 9599 N maximum drive arm force and a 1.40 average mechanical advantage within the walking hip ROM (20° extension to 40° flexion). The drive arm length (r_m) of 3.27 cm is within the drive flange motor arm design region. Furthermore, cosmesis parameters h and Δz fulfilled design requirements. However, anterior protrusion ($l = 6.07 \text{ cm}$) exceeded the target $l = 2.00 \text{ cm}$. The larger than desired l value did not pose any major inconvenience during walk tests (Section 9.2).

To confirm that iteration 179 was appropriate, true hip ROM was determined by checking singularity point locations relative to the physical limits of hip flexion and extension (Figure 4-7).

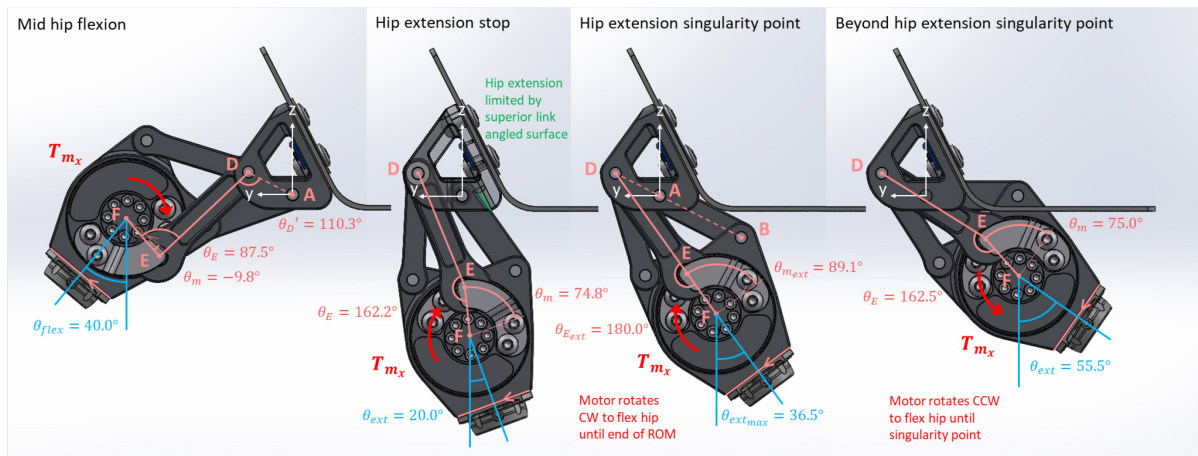


Figure 4-7: Powered hip extension singularity points and motor linkage configuration that produces hip flexion with clockwise motor rotation from hip extension singularity point. Medial view shown. Positive y is anterior and positive z is superior.

Both the four-bar linkage hip extension singularity position (with points A, B and D being collinear), and the motor linkage singularity position (with points D, E and F being collinear) occur simultaneously at 36.5° hip extension (i.e., there is one hip extension singularity point at 36.5° hip extension). Iterations show that mechanical advantage is greater the closer these singularity positions are to each other; thus, the simultaneousness of singularity positions is ideal. Hip extension is physically limited by a stop, an angled surface on the superior link that the posterior link contacts at 20° hip extension. The true range of hip extension is indeed 20° because both the hip extension singularity position and the motor linkage singularity position occur beyond 20° hip extension.

Supposing the hip to be far into extension and θ_m to be acute, the motor rotates CCW to flex the hip until it reaches its extension singularity point (Figure 4-7). To continue flexing the hip from the hip extension singularity point, the motor switches to CW rotation (Figure 4-7) or continues with CCW rotation (Figure 4-8). Both motor rotation directions are possible due to there being two motor linkage configurations for each θ_E value.

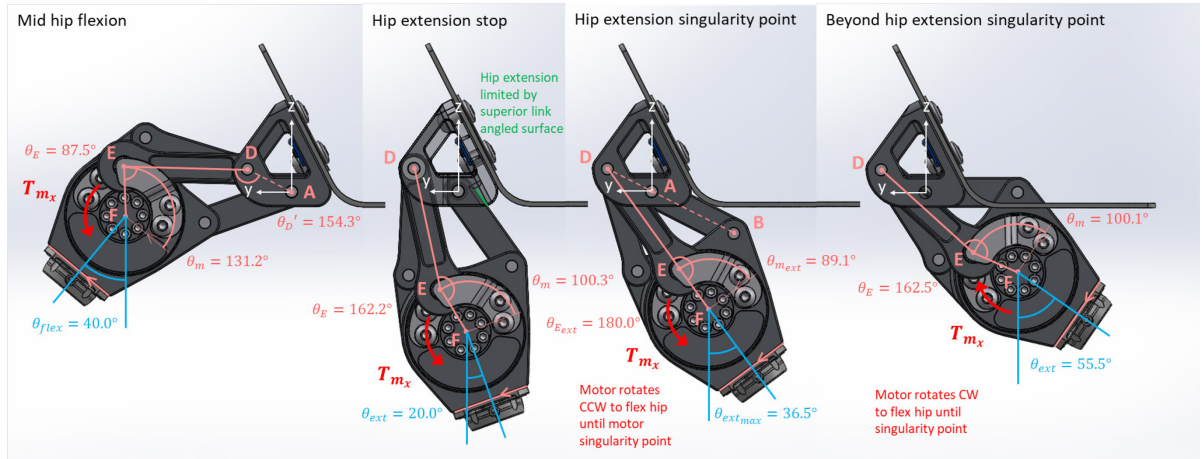


Figure 4-8: Powered hip extension singularity points and motor linkage configuration that produces hip flexion with counterclockwise motor rotation from hip extension singularity point. Medial view shown. Positive y is anterior and positive z is superior.

The motor appeared to switch rotation directions if the motor linkage hip extension singularity position occurred at a smaller hip extension angle than the four-bar linkage hip extension singularity position (e.g., due to the input θ_{mext} being too large). In each optimization iteration, the motor linkage hip extension singularity point was found by examining the change in θ_E . θ_E is the principal angle between the motor and drive arms. With either motor linkage configuration (Figure 4-7 or Figure 4-8), θ_E increased as the hip flexed from beyond its extension singularity point, and then decreased once the hip crossed its extension singularity point. If the four-bar linkage hip extension singularity position occurred at a smaller hip extension angle than the motor linkage hip extension singularity position, the

motor would appear to be rotating in one direction only and θ_E would be monotonically decreasing. Therefore, if θ_E increased at all while the hip flexed, the hip would contain a motor linkage hip extension singularity point within the inputted hip ROM (i.e., within the range of inputted θ_{extmax} and $\theta_{flexmax}$ values).

The powered hip was assembled with the motor linkage configuration in Figure 4-7 because this configuration provided a much greater average mechanical advantage for walking (20° hip extension to 40° hip flexion). Applying Eq. (4-5) to both configurations yields an average mechanical advantage for walking of 1.410 for the motor linkage configuration in Figure 4-7, and 0.515 for the motor linkage configuration in Figure 4-8. Furthermore, angle θ_D' (Figure 4-8) is nearly 180° at 40° hip flexion, meaning that the motor linkage hip flexion singularity point is not far beyond 40° hip flexion (greatly restricting hip flexion).

In each optimization iteration, the motor linkage hip flexion singularity point was found by examining the change in θ_D' (Figure 4-9). The powered hip flexion range is limited by contact with the socket at 100° . If the hip were able to flex beyond 100° , it would reach its motor linkage hip flexion singularity point at 101.5° and its four-bar linkage hip flexion singularity point at 109.5° . θ_D' increased as the hip approached full flexion and started to decrease after crossing the motor linkage hip flexion singularity point. Therefore, if θ_D' decreased at all while the hip flexed, the hip would contain a motor linkage hip flexion singularity point within the inputted hip ROM, as seen in iteration 179. However, iteration 179 reached its physical limit for hip flexion before it ever could reach that point.

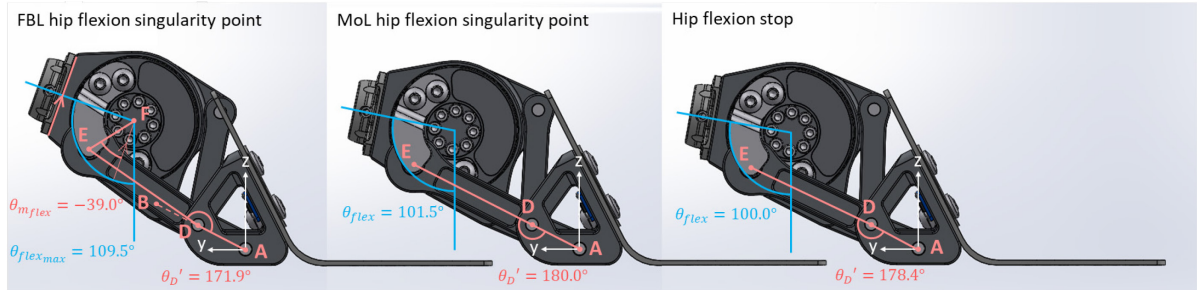


Figure 4-9: Powered hip flexion singularity points and motor linkage configuration that produces hip flexion with counterclockwise motor rotation from hip extension. ‘FBL’ designates ‘four-bar linkage’ and ‘MoL’ designates ‘motor linkage’.

The powered hip ROM of 20° extension to 100° flexion does not include any linkage singularity points, so there is no risk of jamming during operation.

The link length optimization MATLAB code may assume one motor linkage configuration (e.g., Figure 4-7) and then switch to the other (e.g., Figure 4-8) after the hip extension motor singularity point is crossed. In this case, motor linkage singularity points become more difficult to detect due to a potential false detection of θ_E monotonically decreasing. Therefore, the occurrence of motor linkage

singularity points was also checked with a sagittal plane linkage motion plot (Figure 4-10), and a hip rotation versus motor rotation plot (Figure 4-11). Figure 4-10 shows hip ROM motion between its four-bar linkage singularity points. Motion linkage singularity points occur within this ROM if the drive arm is parallel to the motor arm or the superior link. Figure 4-11 would show a zigzag in its curve if the motor were to change direction within the hip ROM. For iteration 179, these plots demonstrated proper hip function while not crossing any four-bar linkage or motor linkage singularity points within its physical ROM (20° extension to 100° flexion).

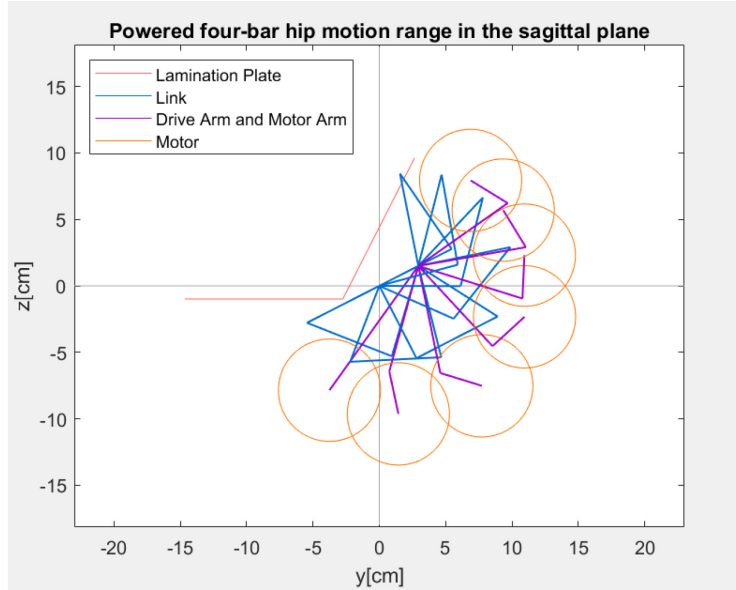


Figure 4-10: Powered hip sagittal plane motion from the four-bar linkage hip extension singularity position to the four-bar linkage hip flexion singularity position.

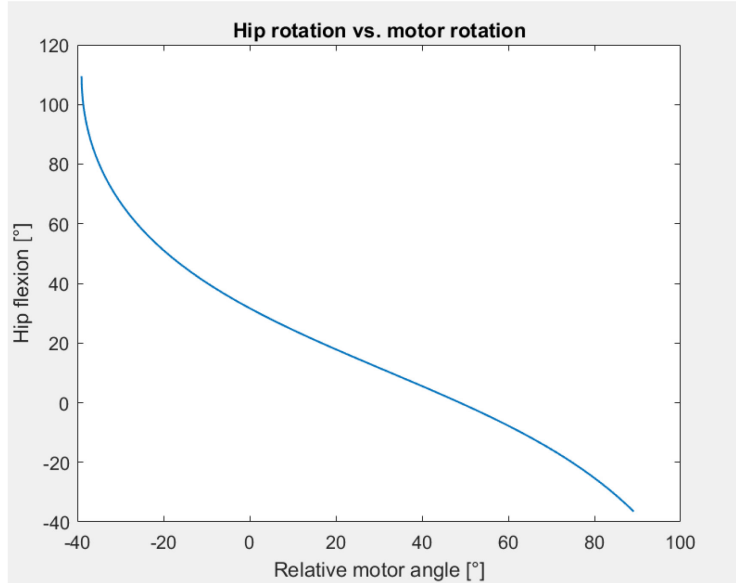


Figure 4-11: Hip flexion angle θ_{flex} ($^{\circ}$) versus relative motor angle θ_m ($^{\circ}$).

If configured properly, a four-bar linkage shortens to increase toe clearance during mid-swing. Toe clearance occurs at approximately 23° hip flexion in normal walking [90], [94], [99], [109]. Prosthetic hip shortening is how much thigh length decreases as the hip flexes from late stance at the full 20° extension to mid swing at 23° flexion as defined by Eq. (4-6).

$$\text{Prosthetic hip shortening} = (l_{\text{thigh}})_{20^\circ \text{ hip extension}} - (l_{\text{thigh}})_{23^\circ \text{ hip flexion}} \quad (4-6)$$

Thigh length was taken to be the distance between two points fixed relative to the thigh: the anterosuperior pin center and the knee center (Figure 4-12). Hip ICR was not taken as one of the reference points because ICR location could vary greatly with changing hip flexion-extension angle (as demonstrated in Section 2.3.3). The goal was to determine the change in physical prosthetic thigh length. Applying Eq. (4-6) to the powered hip (iteration 179) gives a prosthetic hip shortening of 23.8 mm, which satisfies the design requirement because any amount of prosthetic shortening increases toe clearance and reduces the risk of tripping and falling. In an optimization iteration, prosthetic shortening was examined last because it was a lower priority than core functional aspects such as torque handling and ROM. Prosthetic lengthening was not observed in any of the iterations tested.

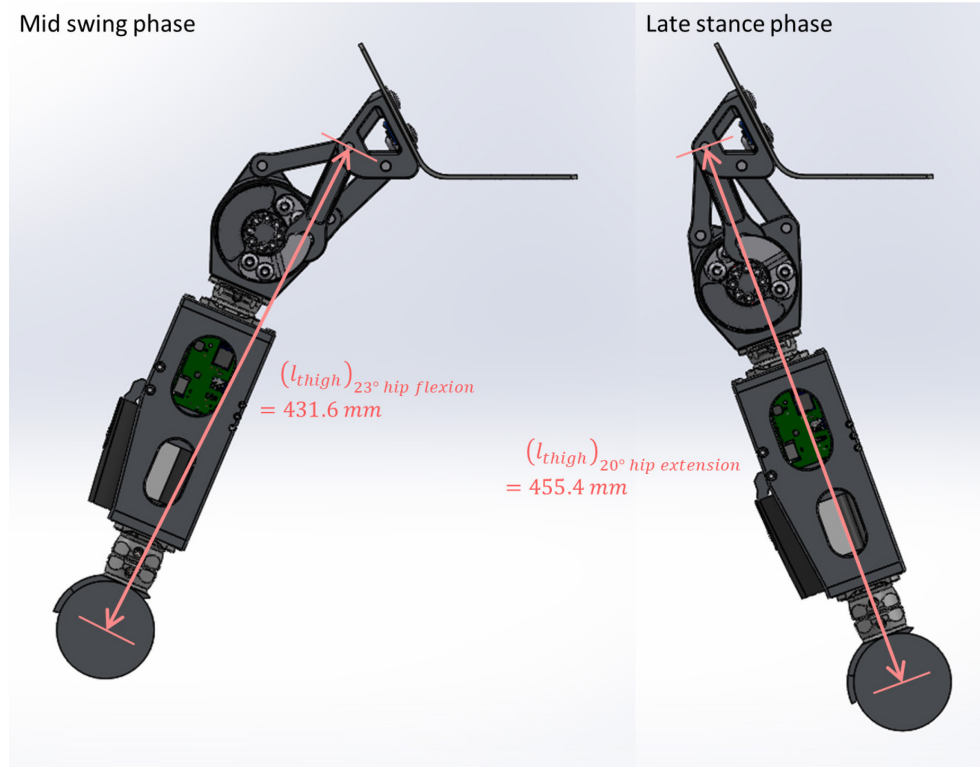


Figure 4-12: Change in prosthetic thigh length from late stance phase to mid swing phase. Powered hip shortening of 23.8 mm at mid swing.

Table 4-9 summarizes the theoretical performance of the design chosen based on linkage optimization iteration 179. Out of the 184 iterations conducted, iteration 179 was the only one that fulfilled the target performance specifications (Table 4-4). Therefore, iteration 179 was appropriate for a first prototype that would enable stable hip amputee gait and sustain a 96 N·m torque. Beyond the design conception stage, prototype testing could reveal strengths and weaknesses to inform possible modifications to the design concept, target performance specifications, and the optimization process itself. Thus, future linkage optimization would likely result a device that is more versatile and robust over the long term. However, during the design conception phase preceding the first prototype, there was no obvious method of improving the outcomes of iteration 179 with the information known at the time. Size was estimated to be at most a box whose dimensions equalled the motor diameter (7.7 cm) plus the longest link length (8.2 cm).

Table 4-9: Performance specifications for linkage optimization iteration 179.

Hip ROM	Size	Max drive arm force	Mech. advantage	Swing phase shortening
20° extension to 100° flexion	≤ 15.9 x 15.9 x 15.9 cm	9599 N	1.40 average within walking ROM	2.38 cm

Chapter 5: Force Analysis

Force analysis under motor torque only with no body weight (Section 5.4) yielded maximum drive arm forces that informed appropriate link lengths. A more detailed analysis was carried out to determine forces acting on individual powered hip components after link length optimization was complete. The MATLAB program ‘Forces.m’ (Appendix B.6) was used for the analysis.

5.1 ISO 15032:2000

The only available engineering standard for prosthetic hip joint strength requirements is ‘ISO 15032:2000 – Structural Testing of Hip Joints’ [186]. The standard details different loading scenarios and load magnitudes that the hip would need to sustain for user weights up to 100 kg [186]. A100 loads (i.e., 100 kg user loads) were selected as the most conservative design approach. ISO 15032 has been published for passive hip joints only. For the powered four-bar hip, ISO 15032 loads are purely structural strength requirements. They are the loads the hip must sustain purely due to the user putting their entire body weight on the hip. ISO 15032 loads do not consider how strong the hip needs to be if subjected to both user body weight and motor torque simultaneously. However, to ensure design robustness, the standard has been taken as one of the powered hip strength requirements.

Three static compression loading scenarios are outlined in the standard (Figure 5-1). These scenarios are ultimately to be physically tested on a prosthetic hip prototype, so the standard refers to these loading scenarios as test conditions. The anterior-posterior (A-P) extension test loading condition refers to sagittal plane compression (force with y and z components only) on the hip when it is locked in full extension. The A-P flexion test loading condition refers to sagittal plane compression when it is locked in full flexion. The medial-lateral (M-L) test loading condition refers to frontal plane compression (force with x and z components only) on the hip when it is locked in full extension.

ISO 15032 outlines a torsional test loading condition, but this was not considered for the project. Össur, the company partner for the project, did not recommend carrying out torsional tests because they expected that the 50 N-m twisting torque suggested by the standard would induce far less stress on components than the large A-P and M-L compression loads.

For each compression loading condition, the upper end attachment was isolated as a free body (Figures 5-2 to 5-4). Applying static equilibrium (sum of forces and moments equal to zero) yielded hip reactions F_{hx} , F_{hy} , F_{hz} , M_{hx} , and M_{hy} which act at the hip ICR. The end attachment weights were neglected. The hip and knee centers were not vertically aligned when the hip was fully extended or fully flexed. Eq. (5-1) notates the rotation angle as $\theta_{f'u'}$ meaning either $(\theta_{f'u'})_{AP\ ext}$ or $(\theta_{f'u'})_{AP\ flex}$,

rotations of the ISO 15032 coordinate system (f' , u') relative to the biomechanics coordinate system (y , z) in the A-P extension or A-P flexion positions.

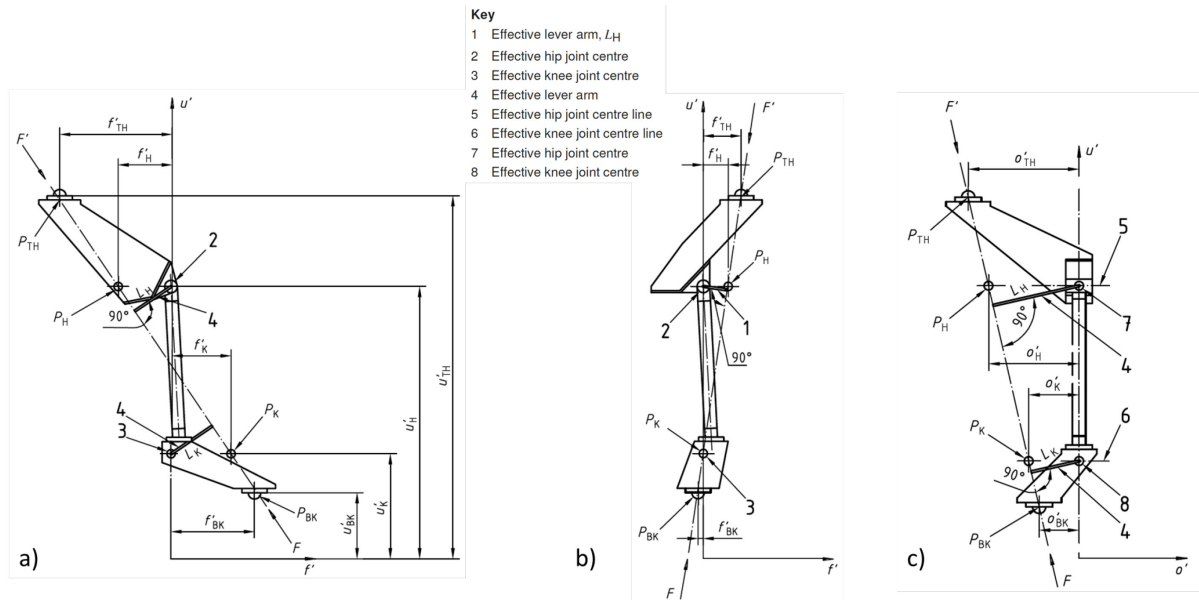


Figure 5-1: ISO 15032:2000 compression: a) A-P extension, b) A-P flexion, c) M-L. The u' axis passes through the effective hip and knee joint centers (points 2 and 3). Equal and opposite forces F' and F act on the proximal and distal end attachments of the prosthetic thigh. Adapted from [186].

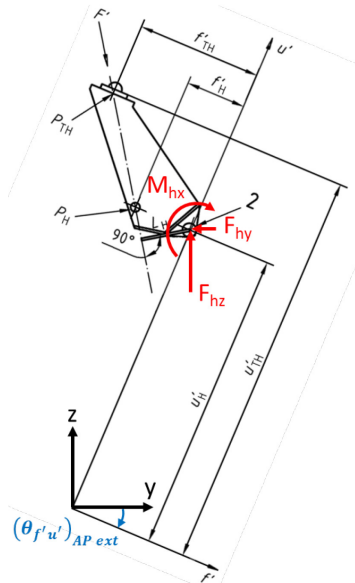


Figure 5-2: ISO 15032 A-P extension end attachment free body diagrams. Adapted from [186].

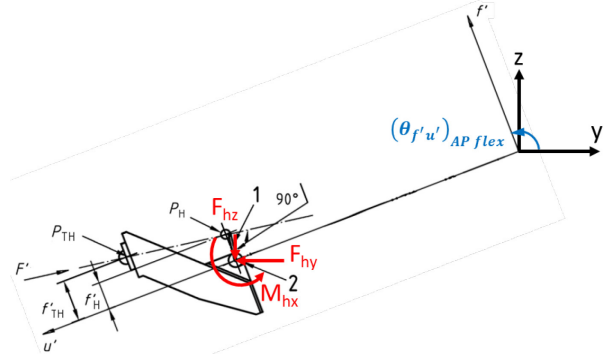


Figure 5-3: ISO 15032 A-P flexion end attachment free body diagrams. Adapted from [186].

$$\begin{bmatrix} -F_{hy} \\ F_{hz} \end{bmatrix} = \frac{F'}{\sqrt{(f'_{TH} - f'_H)^2 + (u'_{TH} - u'_H)^2}} \begin{bmatrix} \cos \theta_{f'u'} & -\sin \theta_{f'u'} \\ \sin \theta_{f'u'} & \cos \theta_{f'u'} \end{bmatrix} \begin{bmatrix} f'_{TH} - f'_H \\ u'_{TH} - u'_H \end{bmatrix} \quad (5-1)$$

$$M_{hx} = \frac{F'(u'_{TH} - u'_H)|f'_H|}{\sqrt{(f'_{TH} - f'_H)^2 + (u'_{TH} - u'_H)^2}} \quad (5-2)$$

Eq. (5-1) yielded reactions F_{hy} , and F_{hz} with respect to the y-z coordinate axes with right and up being positive. To match the direction of F_{hy} assumed in Figures 5-2 and 5-3, F_{hy} was multiplied by -1 in both the A-P extension and A-P flexion loading cases.

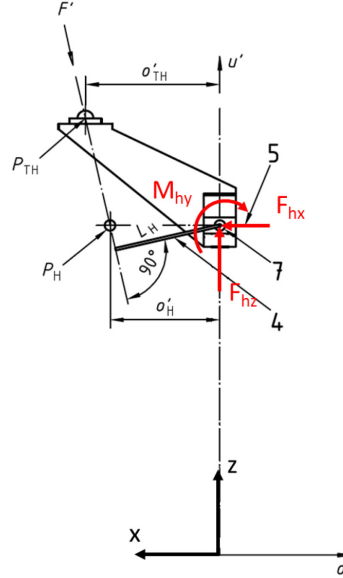


Figure 5-4: ISO 15032 M-L end attachment free body diagrams. Adapted from [186].

$$\begin{bmatrix} F_{hx} \\ F_{hz} \end{bmatrix} = \frac{F'}{\sqrt{(o'_{TH} - o'_H)^2 + (u'_{TH} - u'_H)^2}} \begin{bmatrix} |o'_{TH} - o'_H| \\ u'_{TH} - u'_H \end{bmatrix} \quad (5-3)$$

$$M_{hy} = \frac{F'(u'_{TH} - u'_H)|o'_H|}{\sqrt{(o'_{TH} - o'_H)^2 + (u'_{TH} - u'_H)^2}} \quad (5-4)$$

Reactions F_{hy} , F_{hz} , and M_{hx} from Eq. (5-1) and (5-2) were transferred in opposite directions (Newton's Third Law) to the powered hip isolated as a free-body in the A-P extension and A-P flexion positions (Figure 5-5). The powered hip was then dismembered into its components, also represented as individual free bodies. Gravity and friction were neglected at this stage, and the hip was assumed to be for a right leg prosthesis. The anterior link force was multiplied by 2 to represent two anterior links with assumed equal loads. No forces acted on the drive arm or motor because the motor was turned off during ISO 15032:2000 compression tests. Lamination plate screw loads were absorbed into hip reaction loads F_{hy} , F_{hz} , and M_{hx} .

Table 5-1 lists the static failure test force, moment arms, and axis rotation angle for the ISO 15032:2000 A100 A-P extension, A-P flexion, and M-L loading conditions.

Table 5-1: Parameters for ISO 15032:2000 A100 A-P and M-L loading conditions.

Parameter	A-P extension value	A-P flexion value	M-L value
F'	3360 N	3360 N	3360 N
f'_{TH}	-159 mm	43 mm	-
f'_H	-83 mm	29 mm	-
$u'_{TH} - u'_H$	200 mm	200 mm	200 mm
o'_{TH}	-	-	-106 mm
o'_H	-	-	-83 mm
$\theta_{f'u'}$	-19.1°	106.1°	-

Figure 5-5 shows the powered hip at an arbitrary hip flexion angle. ISO 15032 requires the hip to be at full extension or full flexion. Link angles at full extension ($\theta_{ext} = 20^\circ$) and full flexion ($\theta_{flex} = 100^\circ$) were calculated with Eq. (C-3), (C-27), and (C-30).

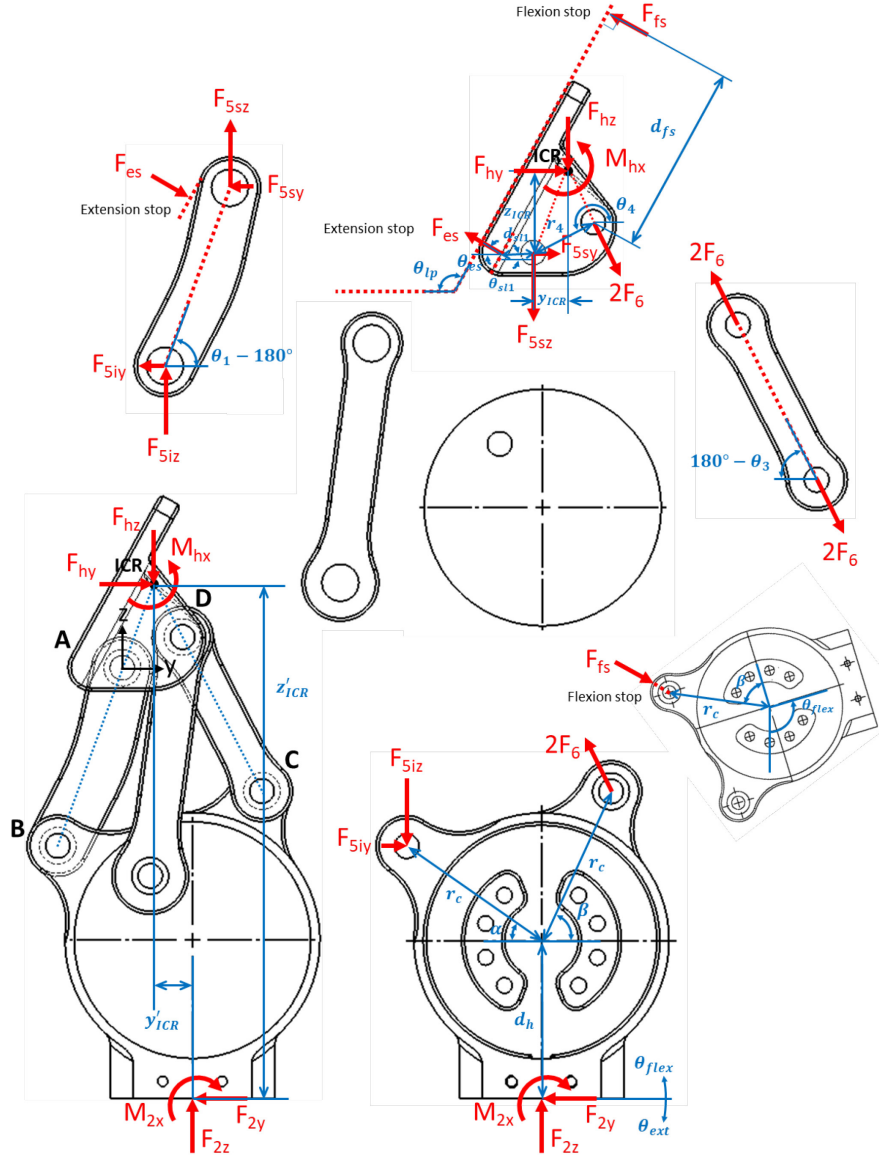


Figure 5-5: Powered hip free body diagrams for the ISO 15032:2000 A-P compression conditions. Motor turned off. Lateral view of older powered hip model shown at an arbitrary hip flexion angle.

Applying static equilibrium to the non-dismantled powered hip provided reactions F_{2y} , F_{2z} , and M_{2x} . Eq. (5-5) and (5-6) can be applied to either the A-P extension or A-P flexion positions so long as the corresponding y'_{ICR} and z'_{ICR} distances are used.

$$\begin{bmatrix} F_{2y} \\ F_{2z} \end{bmatrix} = \begin{bmatrix} F_{hy} \\ F_{hz} \end{bmatrix} \quad (5-5)$$

$$M_{2x} = -F_{2y}z'_{ICR} + F_{2z}y'_{ICR} + M_{hx} \quad (5-6)$$

Motor housing static equilibrium is expressed by Eq. (5-7), (5-8), and (5-9):

$$-F_{2y} + F_{5iy} - 2F_6 \cos(180^\circ - \theta_3) + F_{fs} \cos(\theta_{lp} - 90^\circ) = 0 \quad (5-7)$$

$$F_{2z} - F_{5iz} + 2F_6 \sin(180^\circ - \theta_3) - F_{fs} \sin(\theta_{lp} - 90^\circ) = 0 \quad (5-8)$$

$$\begin{aligned} & -M_{2x} - F_{5iy}r_c \sin(\alpha - \theta_{flex}) + F_{5iz}r_c \cos(\alpha - \theta_{flex}) \\ & + 2F_6 \cos(180^\circ - \theta_3) r_c \sin(\beta + \theta_{flex}) \\ & + 2F_6 \sin(180^\circ - \theta_3) r_c \cos(\beta + \theta_{flex}) - F_{2y}d_h \cos \theta_{flex} \\ & + F_{2z}d_h \sin \theta_{flex} - F_{fs} \cos(\theta_{lp} - 90^\circ) r_c \sin(180^\circ - \beta - \theta_{flex}) \\ & + F_{fs} \sin(\theta_{lp} - 90^\circ) r_c \cos(180^\circ - \beta - \theta_{flex}) = 0 \end{aligned} \quad (5-9)$$

Superior link static equilibrium is expressed by Eq. (5-10), (5-11), and (5-12):

$$F_{5sy} + 2F_6 \cos(180^\circ - \theta_3) + F_{hy} - F_{es} \cos \theta_{es} - F_{fs} \cos(\theta_{lp} - 90^\circ) = 0 \quad (5-10)$$

$$-F_{5sz} - 2F_6 \sin(180^\circ - \theta_3) - F_{hz} + F_{es} \sin \theta_{es} + F_{fs} \sin(\theta_{lp} - 90^\circ) = 0 \quad (5-11)$$

$$\begin{aligned} & M_{hx} + F_{5sy}z_{ICR} + F_{5sz}y_{ICR} - F_{es} \cos \theta_{es} (d_{sl1} \sin \theta_{sl1} + z_{ICR}) \\ & - F_{es} \sin \theta_{es} (d_{sl1} \cos \theta_{sl1} + y_{ICR}) + F_{fs}d_{fs} = 0 \end{aligned} \quad (5-12)$$

At A-P extension, force F_{es} prevents further hip extension and F_{fs} is zero. At A-P extension, force F_{fs} prevents further hip flexion and F_{es} is zero. Posterior link forces F_{5iy} , F_{5iz} , F_{5sy} and F_{5sz} , anterior link force F_6 , extension stop force F_{es} , and flexion stop force F_{fs} were determined by solving the system of six static equilibrium equations (Eq. (5-7) to (5-12)) simultaneously for the A-P extension and A-P flexion loading conditions.

Reactions F_{hx} , F_{hz} , and M_{hy} from Eq. (5-3) and (5-4) were transferred in opposite directions (Newton's Third Law) to the powered hip upper portion isolated as a free-body (Figure 5-6). This upper portion consisted of the posterior, anterior and superior links, and the drive arm. Anterior link forces were not assumed equal due to medial-lateral loading. Medial-lateral force F_{hx} , pointing medially, was assumed by the posterior and lateral anterior links only because medial-lateral force distribution can be controlled with part tolerancing. Like the A-P loading cases, no force acted on the drive arm because the motor was off during testing. Lamination plate screw moment M_{10x} could have been represented as a hip moment M_{hx} acting at the hip ICR, but for clearer presentation, M_{10x} was represented as a moment acting at the centroid of lamination plate screw.

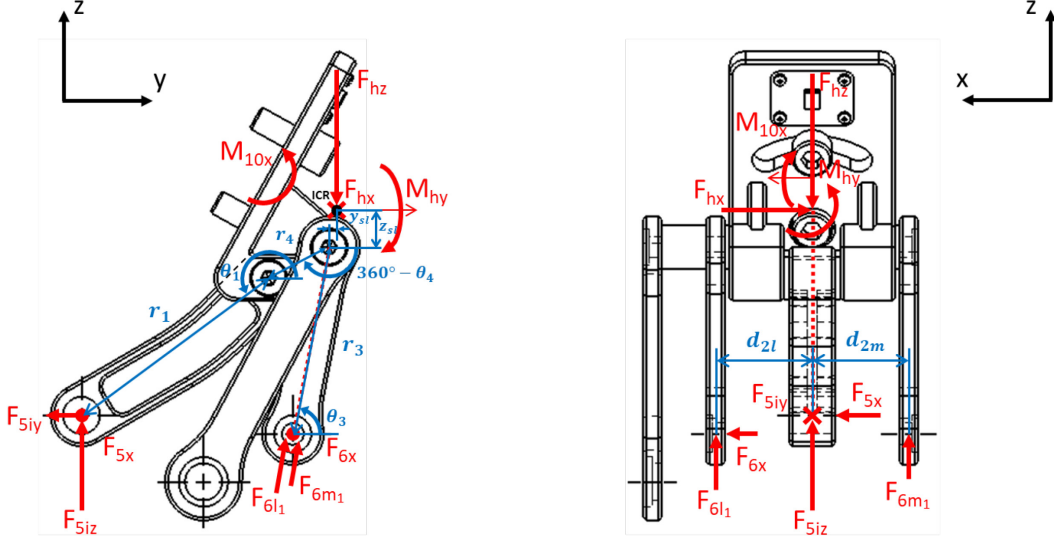


Figure 5-6: Powered hip upper portion free-body diagram for the ISO 15032:2000 M-L compression condition. Older powered hip model shown. No forces are shown on the drive arm or the motor because the motor is turned off during ISO 15032:2000 compression tests.

ISO 15032:2000 suggests that during M-L compression testing, an A-P offset ($l_{AP\ offset}$) of up to 10 mm may be used to ensure the hip remains fully extended during the test. For the ISO 15032:2000 M-L compression force analysis, it is assumed that the hip remains extended with a 10 mm moment arm between the hip and knee joints. The reaction moment M_{10x} at the centroid of the lamination plate screws is therefore given by Eq. (5-13).

$$M_{10x} = F_{hz} l_{AP\ offset} \quad (5-13)$$

Posterior link forces F_{5x} , F_{5y} and F_{5z} , and anterior link forces F_{6x} , F_{6l_1} and F_{6m_1} are determined by solving the powered hip upper portion static equilibrium equations simultaneously.

$$F_{5x} + F_{6x} - F_{hx} = 0 \quad (5-14)$$

$$-F_{5iy} + (F_{6l_1} + F_{6m_1}) \cos \theta_3 = 0 \quad (5-15)$$

$$F_{5iz} + (F_{6l_1} + F_{6m_1}) \sin \theta_3 - F_{hz} = 0 \quad (5-16)$$

$$\begin{aligned} & M_{10x} - F_{5iy} [r_1 \sin(\theta_1 - 180^\circ) + r_4 \sin(\theta_4 - 180^\circ)] \\ & - F_{5iz} [r_1 \cos(\theta_1 - 180^\circ) + r_4 \cos(\theta_4 - 180^\circ)] - F_{hz} y_{sl1} = 0 \end{aligned} \quad (5-17)$$

$$\begin{aligned} & M_{hy} - F_{5x} [r_1 \sin(\theta_1 - 180^\circ) + r_4 \sin(\theta_4 - 180^\circ)] - F_{6x} r_3 \sin \theta_3 - F_{6l_1} \sin \theta_3 d_{2l} \\ & + F_{6m_1} \sin \theta_3 d_{2m} - F_{hx} z_{sl} = 0 \end{aligned} \quad (5-18)$$

$$F_{5x}[r_1 \sin(\theta_1 - 180^\circ) + r_4 \sin(\theta_4 - 180^\circ)] + F_{6x}r_3 \cos \theta_3 + F_{6l_1} \cos \theta_3 d_{2l} - F_{6m_1} \cos \theta_3 d_{2m} - F_{hx}y_{sl} = 0 \quad (5-19)$$

Table 5-2 lists distance and angle values used for the ISO 15032:2000 static equilibrium analysis. Some of these values have also been used for the gait cycle dynamic equilibrium analysis (Section 5.3) and the motor-only static equilibrium analysis (Section 5.4).

Table 5-2: Free-body diagram distances and angles used for ISO 15032:2000 static equilibrium analyses.

Parameter	Value (cm)	Parameter	Value (cm or °)
d_{2l}	3.04	y_{sl}	-0.12
d_{2m}	1.32	z_{sl}	2.44
d_{fs}	6.46	α	35.0
d_h	4.65	β	65.0
d_{sl1}	1.56	θ_{ext}	20.0
r_1	6.12	θ_{flex}	100.0
r_3	7.09	θ_{tilt}	0.0
r_4	3.30	θ_1	234.4
r_c	5.35	θ_3	92.8
$(y_{ICR})_{AP\ ext}$	2.82	θ_4	207.0
$(z_{ICR})_{AP\ flex}$	3.94	θ_{es}	35.6
$(y_{ICR}')_{AP\ ext}$	-4.94	θ_{lp}	117.0
$(z_{ICR}')_{AP\ flex}$	17.66	θ_{sl1}	14.6

5.2 Powered Hip Instantaneous Center of Rotation

Hip ICR was an important design consideration because hip ICR location in space determines hip joint stance phase stability, loads and stresses on hip joint components, and mechanical advantage. MATLAB program ‘ICRLinkages.m’ (Appendix B.5) calculates and plots hip ICR location in the sagittal plane throughout the gait cycle.

Linkage pivot point locations in space were calculated throughout the TF amputee gait cycle using Eq. (C-21), (C-22), (C-31), (C-32), (C-33), (C-34), and (C-38).

Hip ICR location in space throughout the TF amputee gait cycle (Figure 5-7) was calculated by finding the intersection points of the posterior and anterior link lines simultaneously (i.e., by solving Eq. (5-20) and (5-21) simultaneously for coordinates (y, z)). Eq. (5-20) and (5-21) are slope-intercept forms of line equations in the y - z plane.

$$z = m_{post}y + b_{post} = \frac{z_B}{y_B}y \quad (5-20)$$

$$z = m_{ant}y + b_{ant} = \frac{z_C - z_D}{y_C - y_D}y + \frac{y_Cz_D - z_Cy_D}{y_C - y_D} \quad (5-21)$$

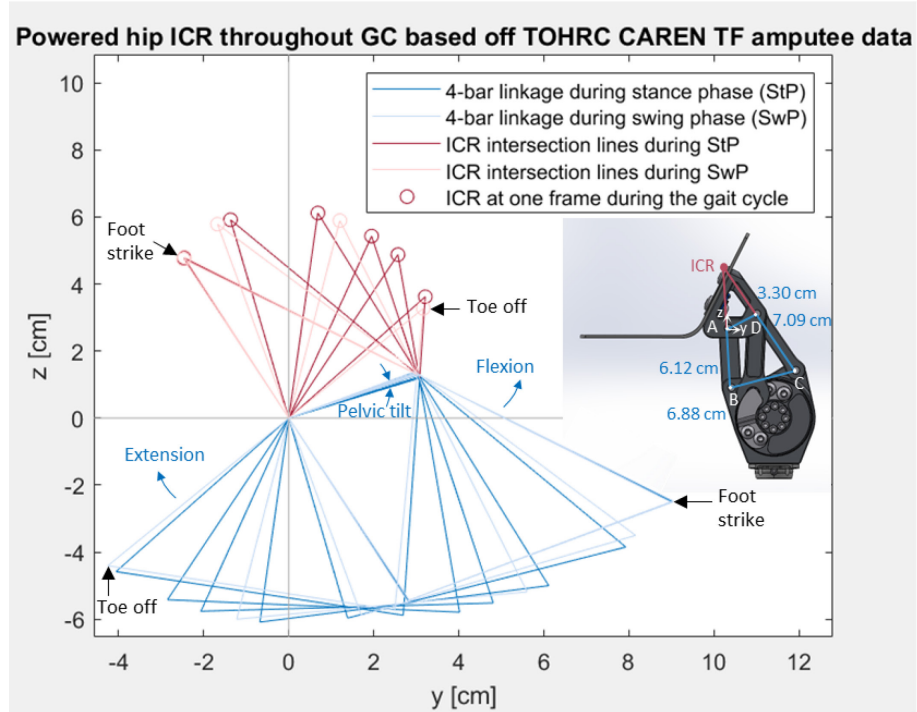


Figure 5-7: Location of the powered hip joint's instantaneous center of rotation throughout the TF amputee gait cycle. Plot created with TOHRC Computer-Assisted Rehabilitation Environment (CAREN) data.

Throughout the TF amputee gait cycle, the powered hip's ICR remains within approximately 2.5 cm behind and 3.6 cm in front of the origin, and within approximately 3.3 to 6.1 cm above the origin. The Helix3D's ICR (Figure 2-16), moves within approximately 2 cm behind and 3.7 cm in front of the origin, and within approximately 6.9 to 19.9 cm above the origin. The powered hip's ICR remains anterior to the origin throughout most of stance phase, thereby promoting prosthetic limb stability. Furthermore, the powered hip's ICR remains much closer to the superior link than Helix3D's ICR which is advantageous for reducing effective moment arms between the GRF and hip joint, thereby reducing hip joint loads and stress on hip joint components. Horizontal movement of the powered hip ICR is slightly greater than the Helix3D which means that, on average, there is more

horizontal distance between the drive arm force line of action (parallel to the drive arm) and the hip ICR. The increase in this horizontal distance allows the drive arm to induce a larger moment on the superior link when the drive arm pushes or pulls on the superior link. If the same motor torque generates a larger moment, mechanical advantage is increased, which has been observed for the powered hip at flexion-extension angles expected during walking.

5.3 Link Forces Throughout the Gait Cycle

ISO 15032:2000 does not provide hip joint strength guidelines for when the hip is subjected to both actuator torque and body weight simultaneously. This section describes the analysis done to determine link forces and required motor torque for the powered hip to operate at unilateral TF amputee level walking performance while supporting a 100 kg person. Static equilibrium of a right HKAfp was assumed at 51 equally spaced instances from 0% gait cycle to 100% gait cycle (i.e., 2% gait cycle between instances). The HKAfp was assumed to contain the powered hip, Össur Power Knee 2, and Össur Proflex LP Torsion Foot. This HKAfp model had a mass of $m_{leg} = 8.44 \text{ kg}$.

The powered hip was assumed to provide unilateral TF gait performance if it could provide the same hip flexion-extension angle, pelvic tilt angle, and hip flexion-extension moment curves expected in TF gait. Unilateral TF amputee level walking data was collected in 2014 in TOHRC CAREN. The data included all walking trials at self-selected speeds ($0.89 \pm 0.22 \text{ m/s}$) from five participants $174.4 \pm 11.7 \text{ cm}$ tall, weighing $86.28 \pm 10.99 \text{ kg}$. Measured quantities included hip flexion-extension angle, anterior-posterior pelvic tilt angle, GRF, and hip flexion-extension moment (Figure 5-8). This data was selected for design purposes because it was more comprehensive than literature data and was recently collected in a well-controlled environment. Gait data were plotted with the ‘TFdata6.m’ MATLAB program (Appendix B.2).

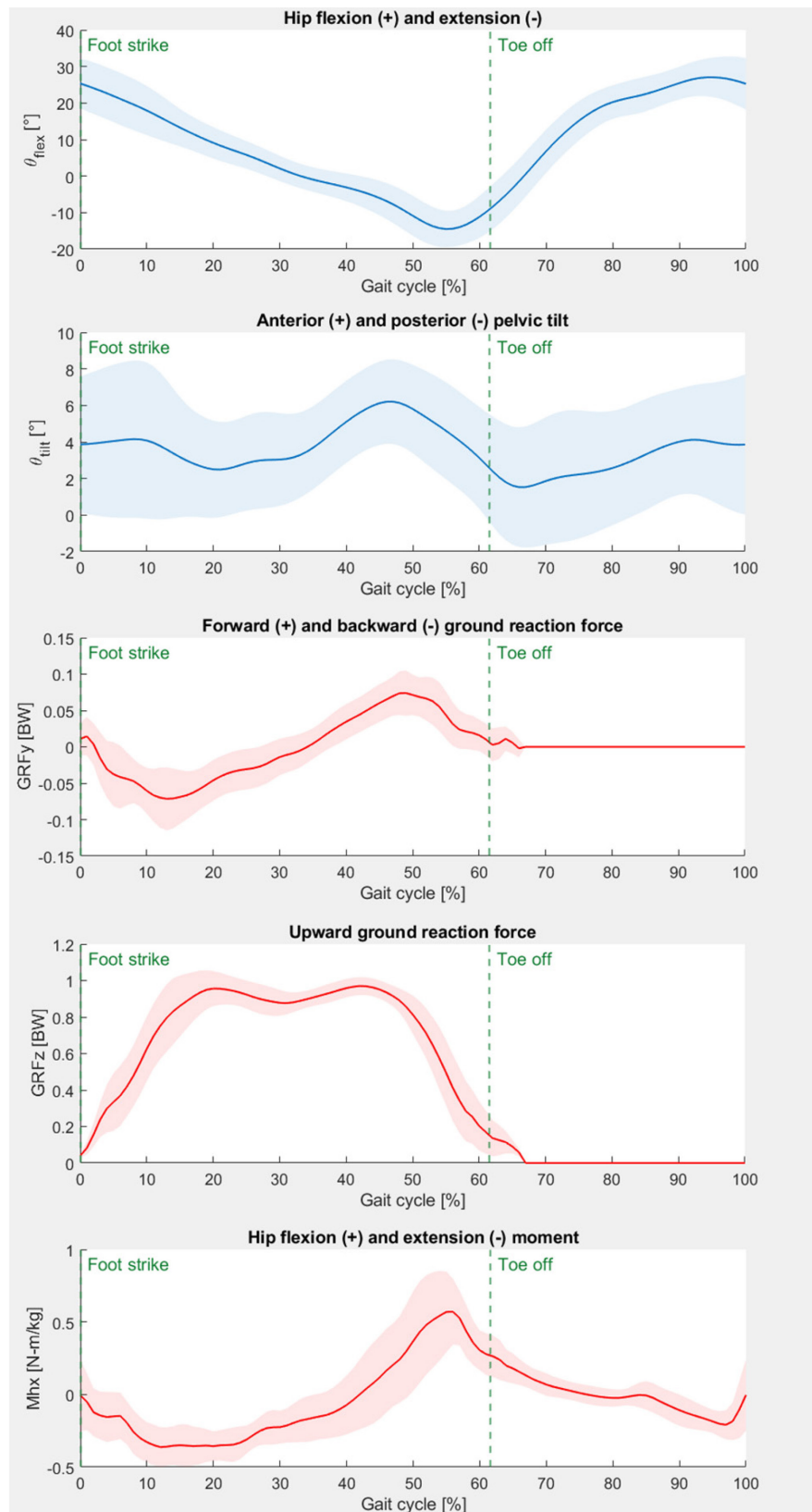


Figure 5-8: Mean plus-minus one standard deviation of unilateral transfemoral amputee level-ground gait kinematics and kinetics. Data collected at TOHRC CAREN.

Normalized GRFs (fraction of body weight (BW)) and normalized hip moments (N-m/kg) were converted into 100 kg person data by multiplying by the corresponding mass (m_{design}) or body weight ($m_{design}g$), where g is the 9.81 m/s acceleration due to gravity.

$$(GRF_y)_{100\ kg} = (GRF_y)_{data}m_{design}g \quad (5-22)$$

$$(GRF_z)_{100\ kg} = (GRF_z)_{data}m_{design}g \quad (5-23)$$

$$(M_{hx})_{100\ kg} = (M_{hx})_{data}m_{design} \quad (5-24)$$

Figure 5-9 isolates the entire prosthetic leg as a free body. The leg was assumed to be one rigid rod with a point-mass at the leg's COM.

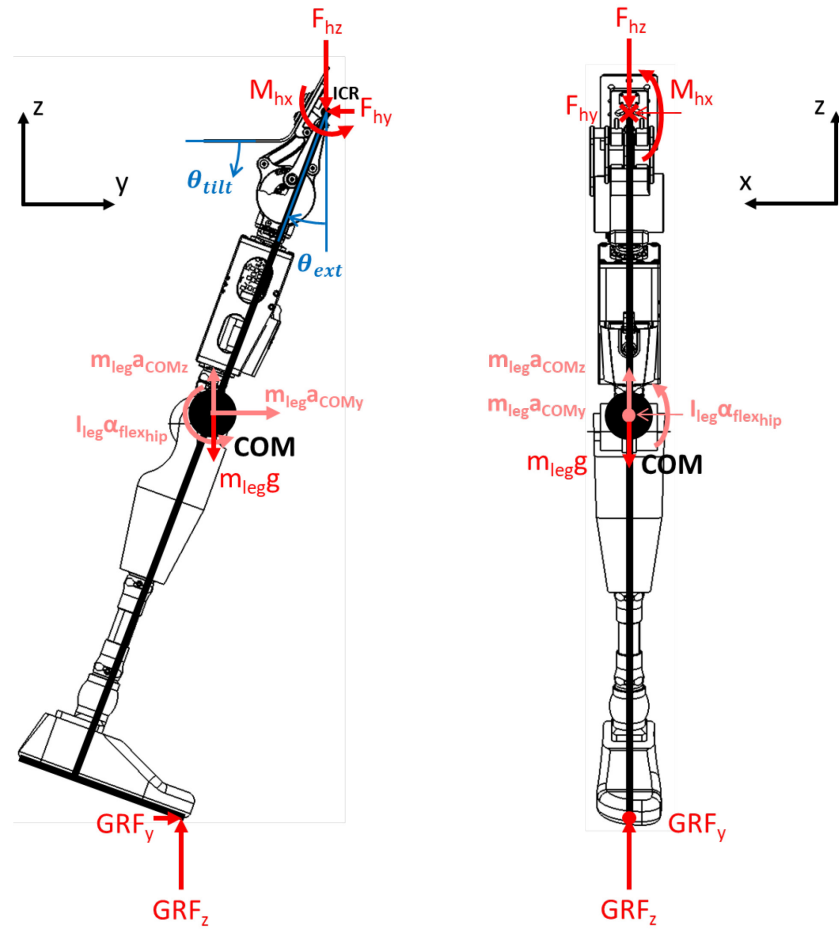


Figure 5-9: Hip-knee-ankle-foot prosthesis free-body diagram. Older powered hip model shown.

Applying dynamic equilibrium to the prosthetic leg yields hip joint forces F_{hy} and F_{hz} . M_{hx} values came from the data collected from TOHRC CAREN (Figure 5-8).

$$F_{hy} = (GRF_y)_{100\text{ kg}} - m_{leg} a_{COMy} \quad (5-25)$$

$$F_{hz} = (GRF_z)_{100\text{ kg}} - m_{leg}(a_{COMz} + g) \quad (5-26)$$

The linear COM acceleration components a_{COMy} and a_{COMz} were determined by expressing the COM position (y_{COM}, z_{COM}) relative to origin (0,0) at point A (Figure 5-10) as a function of time t , and taking the second derivative of the COM position with respect to t . Hip flexion (θ_{flex}), hip extension (θ_{ext}), and pelvic tilt (θ_{tilt}), which vary during the gait cycle, are functions of t . The distance between point D and the COM (l_{COM_D}) was estimated to be an average of 0.38 m. While this distance changes with changing hip flexion angle due to the hip's polycentric nature, l_{COM_D} was assumed constant at 0.38 m.

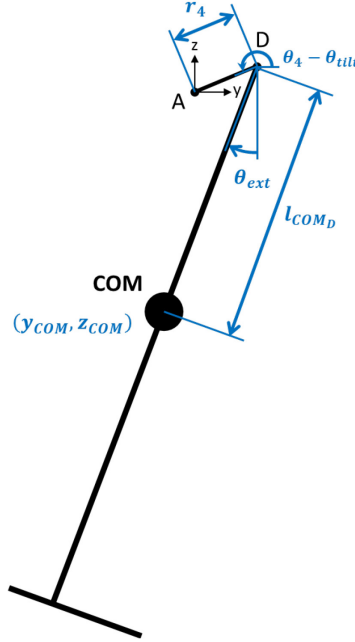


Figure 5-10: Prosthetic leg COM position relative to the origin at point A.

$$y_{COM} = r_4 \cos(\theta_4 - \theta_{tilt}(t) - 180^\circ) - l_{COM_D} \sin \theta_{ext}(t) \quad (5-27)$$

$$z_{COM} = r_4 \sin(\theta_4 - \theta_{tilt}(t) - 180^\circ) - l_{COM_D} \cos \theta_{ext}(t) \quad (5-28)$$

$$\theta_{ext}(t) = -\theta_{flex}(t) \quad (5-29)$$

$$\begin{bmatrix} a_{COMy} \\ a_{COMz} \end{bmatrix} = \begin{bmatrix} \frac{d^2 y_{COM}}{dt^2} \\ \frac{d^2 z_{COM}}{dt^2} \end{bmatrix} \quad (5-30)$$

Eq. (5-30) yielded an expression for prosthetic leg COM acceleration in terms of hip flexion velocity (ω_{flex}), hip flexion acceleration (α_{flex}), pelvic tilt velocity (ω_{tilt}), and pelvic tilt acceleration (α_{tilt}). The angular velocities and accelerations were determined by taking the first and second derivatives of the angle curves in Figure 5-8 with a forward difference approach.

$$\omega = \frac{d\theta}{dt} \approx \frac{\theta(t + \Delta t) - \theta(t)}{\Delta t} \quad (5-31)$$

$$\alpha = \frac{d^2\theta}{dt^2} = \frac{d\omega}{dt} \approx \frac{\omega(t + \Delta t) - \omega(t)}{\Delta t} \quad (5-32)$$

Time interval Δt depended on mean gait cycle time ($\bar{t}_{gait} = 1.25 s$), and the number of datapoints ($n = 101$) from 0% gait cycle to 100% gait cycle.

$$\Delta t = \frac{\bar{t}_{gait}}{n - 1} \quad (5-33)$$

To simplify the analysis, GRF_x was assumed to be zero throughout the gait cycle. GRF_x did not influence required motor torque for stability. GRF_x values were small compared to GRF_z values, so including them in the calculations would have not substantially changed the results. Furthermore, ISO 15032:2000 M-L compression loading results in a horizontal force component that is more than 4.5 times max GRF_x expected for a 100 kg person. Therefore, additional medial-lateral loading design metrics were not necessary.

Another simplifying assumption was that hip flexion-extension and pelvic tilt were the only hip motions during gait. Gait was assumed to be without pelvic obliquity or pelvic rotation. Powered hip gait cycle force analysis was in the sagittal plane in which the gross motion of the leg occurs. In addition, the hip was assumed to not come in contact with either the flexion or extension stop during gait (i.e., $F_{es} = 0$ and $F_{fes} = 0$).

Fifty-one equally spaced instances throughout the gait cycle were chosen for force analysis. Link angles at each of these instances were calculated with Eq. (C-3), (C-19), (C-20), (C-27), and (C-30). Figure 5-11 shows the powered hip at an arbitrary hip flexion angle and dismembers the powered hip into individual free bodies. Unlike the ISO 15032 loading conditions, the gait cycle force analysis examines the powered hip with motor operation. All motor torque is assumed to be transmitted

through the drive arm with force F_7 . Furthermore, individual component weights and inertial loads were neglected because they were much smaller compared to body weight and motor torque.

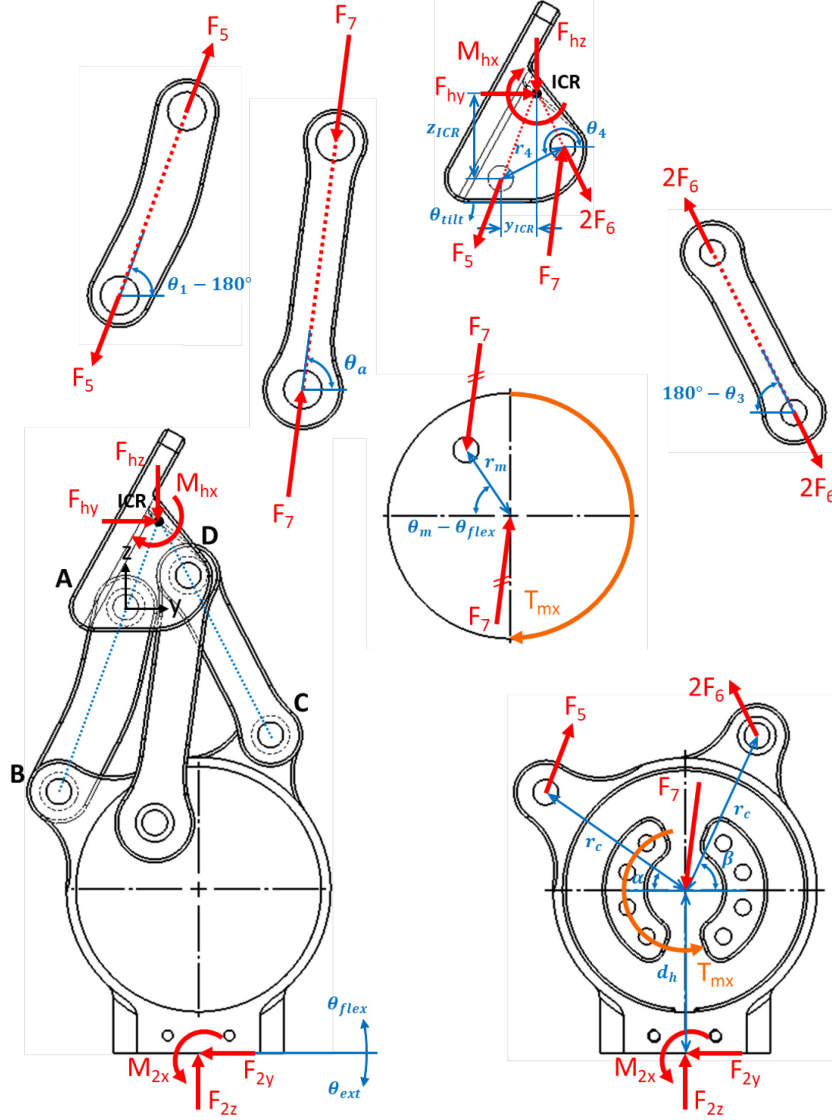


Figure 5-11: Powered hip free body diagrams at an instance of the gait cycle. Motor provides the required torque for stable gait at each gait cycle instance. Lateral view of older powered hip model shown at an arbitrary hip flexion angle.

Applying sum of moments on the motor in static equilibrium gave an expression for drive arm force F_7 in terms of motor torque T_{mx} and motor moment arm ($r_m = 3.27 \text{ cm}$).

$$F_7 = \frac{T_{mx}}{r_m [\cos \theta_a \sin(\theta_m - \theta_{flex}) + \sin \theta_a \cos(\theta_m - \theta_{flex})]} \quad (5-34)$$

Taking the sum of moments on the superior link in static equilibrium at the hip ICR gave an expression for hip moment M_{hx} in terms of drive arm force F_7 .

$$M_{hx} = F_7[\cos \theta_a (z_{ICR} - r_4 \sin(\theta_4 - \theta_{tilt} - 180^\circ)) + \sin \theta_a (r_4 \cos(\theta_4 - \theta_{tilt} - 180^\circ) - y_{ICR})] \quad (5-35)$$

Eq. (5-36) defined mechanical advantage for the powered hip.

$$MA = \frac{M_{hx}}{T_{mx}} \quad (5-36)$$

Combining Eq. (5-34), (5-35), and (5-36) gave an expression for mechanical advantage in terms of known link lengths, link angles, and joint angles. Mechanical advantage values throughout the gait cycle were found by substituting known quantities in Eq. (5-37) at each gait cycle instance.

$$MA = \frac{\cos \theta_a (z_{ICR} - r_4 \sin(\theta_4 - \theta_{tilt} - 180^\circ)) + \sin \theta_a (r_4 \cos(\theta_4 - \theta_{tilt} - 180^\circ) - y_{ICR})}{r_m [\cos \theta_a \sin(\theta_m - \theta_{flex}) + \sin \theta_a \cos(\theta_m - \theta_{flex})]} \quad (5-37)$$

The required motor torque T_{mx} for static equilibrium throughout the gait cycle was determined by substituting the known TOHRC CAREN M_{hx} data and the calculated mechanical advantage values in Eq. (5-36). The motor torque required for stable level-ground gait was at most 64.51 N-m for a 100 kg person. The torque profile throughout the gait cycle is presented in Section 5.3.

Applying sum of forces on the superior link in static equilibrium gave a system of two equations that were solved simultaneously for posterior link force F_5 , and anterior link force F_6 throughout the gait cycle.

$$-F_5 \cos(\theta_1 - 180^\circ) + 2F_6 \cos(180^\circ - \theta_3) + F_7 \cos \theta_a + F_{hy} = 0 \quad (5-38)$$

$$-F_5 \sin(\theta_1 - 180^\circ) - 2F_6 \sin(180^\circ - \theta_3) + F_7 \sin \theta_a - F_{hz} = 0 \quad (5-39)$$

Motor housing bottom surface reactions F_{2y} , F_{2z} , and M_{2x} were calculated by applying static equilibrium on the motor housing. Equations and values for F_{2y} , F_{2z} , and M_{2x} are not presented in this thesis because they were not used for stress analysis (Chapter 6).

5.4 Motor-Only Analysis

The 64.51 N-m motor torque required for stable level-ground walking is well below the motor torque capacity of 96 N-m. Compared to level walking, other ambulation activities such as sloped ascent or descent, stair ascent or descent, and sit-to-stand or stand-to-sit require a larger hip moment, thus requiring a greater motor torque than predicted for level walking [154], [185], [192], [193]. The scope of this project was to design the powered hip for walking. However, it was important to consider the loads and stresses on powered hip components if the motor were to reach its full torque capacity.

This kind of analysis informed whether powered hip structural components are strong enough to handle full motor torque. The analysis also provided some insight on whether the hip can be used for activities more rigorous than level walking.

The motor-only force analysis presented in this section assumed that the powered hip moved through 61 instances from full extension to full flexion without pelvic obliquity or pelvic tilt. In each instance, static equilibrium was assumed with the superior link and motor housing fixed, and the motor outputting its full 96 N-m torque. In all the examined instances, the powered hip was assumed to not support any body weight (i.e., only torque loads were considered).

As with previous parts of the force analysis, the powered hip was isolated as a free body and dismembered into individual free bodies (Figure 5-12).

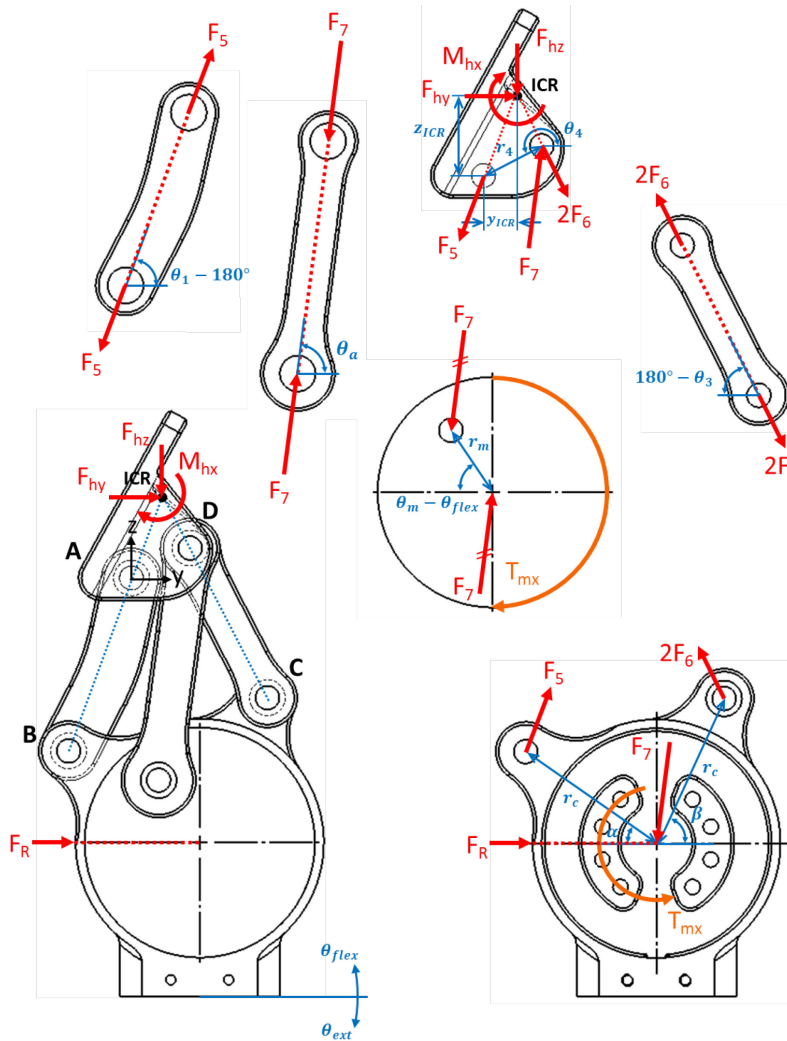


Figure 5-12: Powered hip free body diagrams when subjected to motor torque only. Motor assumed to provide its full 96 N-m torque at each instance of the powered hip range of motion. Lateral view of older powered hip model shown at an arbitrary hip flexion angle.

The powered hip was assumed to experience loads at two points: the ICR and the anterior posterior surface of the motor housing. Hip joint loads F_{hy} , F_{hz} , and M_{hx} kept the superior link fixed. Reaction force F_R kept the motor housing fixed. F_R was assumed to always pass through the motor center while remaining parallel to the motor housing bottom surface. This scenario would be physically encountered if the motor housing were clamped in a vice and the superior link were screwed onto rigid wall that is rotatable through the hip flexion-extension range. If the motor were to apply its maximum torque in the other direction, F_R would act in the opposite direction on the opposite side of the motor housing. The direction of motor torque was assumed to be the same as in gait cycle force analysis, but motor direction only determined link force signs and did not influence link force magnitudes. As before, motor torque was assumed to be transmitted to the upper portion of the powered hip entirely through the drive arm.

Link angles throughout the powered hip ROM were found using Eq. (C-3), (C-19), (C-20), (C-27), and (C-30). Hip ICR locations in the sagittal plane were found using Eq. (5-20) and (5-21).

Substituting $T_{mx} = 96 \text{ Nm}$ in Eq. (5-34) yielded drive arm force (F_7) values throughout powered hip ROM. The maximum F_7 value was used to determine the feasibility of each link length optimization loop.

F_7 values were substituted in Eq. (5-35) to determine the resulting hip moment M_{hx} throughout powered hip ROM. The resulting M_{hx} values and the known constant T_{mx} were substituted in Eq. (5-36) to determine mechanical advantage values throughout powered hip ROM. These mechanical advantage values were examined in each link length optimization loop.

Posterior link force F_5 and anterior link force F_6 were determined by solving the motor housing static force equilibrium equations simultaneously.

$$F_5 \cos(\theta_1 - 180^\circ) - 2F_6 \cos(180^\circ - \theta_3) - F_7 \cos \theta_a + F_R \cos \theta_{flex} = 0 \quad (5-40)$$

$$F_5 \sin(\theta_1 - 180^\circ) + 2F_6 \sin(180^\circ - \theta_3) - F_7 \sin \theta_a + F_R \sin \theta_{flex} = 0 \quad (5-41)$$

$$\begin{aligned} T_{mx} - F_5 \cos(\theta_1 - 180^\circ) r_c \sin(\alpha - \theta_{flex}) - F_5 \sin(\theta_1 - 180^\circ) r_c \cos(\alpha - \theta_{flex}) \\ + 2F_6 \cos(180^\circ - \theta_3) r_c \sin(\beta + \theta_{flex}) \\ + 2F_6 \sin(180^\circ - \theta_3) \cos(\beta + \theta_{flex}) = 0 \end{aligned} \quad (5-42)$$

Hip joint forces F_{hy} and F_{hz} were calculated by applying static equilibrium on the superior link. Equations and values for F_{hy} , and F_{hz} are not presented in this thesis because they were not used for stress analysis (Chapter 6).

5.5 Results

Table 5-3 presents powertrain link forces under the ISO 15032:2000 A100 A-P extension and A-P flexion loading conditions.

Table 5-3: ISO 15032:2000 A100 A-P extension and A-P flexion link forces.

Force	F_{5iy}	F_{5iz}	F_{5sy}	F_{5sz}	F_6	F_7	F_{es}	F_{fs}
Extension (N)	125	-3893	-9777	3191	268	0	12175	0
Flexion (N)	1266	2072	1266	2072	-824	0	0	799

Table 5-4 presents powered hip loads under the ISO 15032:2000 A100 M-L loading condition.

Table 5-4: ISO 15032:2000 A100 M-L link forces.

Force	F_{5iy}	F_{5iz}	F_{5sy}	F_{5sz}	F_{6l1}	F_{6m1}
Value (N)	196	-130	-706	138	6697	-4056

Figure 5-13 illustrates the hip moment, required motor torque for hip joint stability, and mechanical advantage throughout the gait cycle. The 50 N-m maximum hip extension moment occurs during early mid-stance from 12% to 16% gait cycle. Maximum required early mid-stance motor torque is 32.2 N-m at 12% gait cycle. The 85.2 N-m maximum hip flexion moment occurs during pre-swing at 54% gait cycle. Maximum required motor torque pre-swing motor torque is 64.5 N-m at 54% gait cycle. Mechanical advantage varies from 1.30 to 1.64 throughout the gait cycle. Mechanical advantage is maximal during the mid-stance and early-swing phases and is minimal during the pre-swing and late-swing phases. Maximizing mechanical advantage during pre-swing would mean shifting the hip extension singularity point further in extension. During the link length optimization process, this shift was observed to reduce hip ROM, average mechanical advantage, and peak mechanical advantage. Although the powered hip does not maximize mechanical advantage during pre-swing, it maintains a mechanical advantage well above one during the gait cycle. Maximizing mechanical advantage during mid-stance reduces the required motor torque to prevent the hip from buckling (i.e., uncontrolled hip flexion), thereby increasing user safety. Meeting the torque requirement near pre-swing is not as crucial for safety due to the powered hip's extension stop stabilizing the hip at 20° extension. However, a well controlled system would ideally provide enough torque to stabilize the hip before it reaches the extension stop.

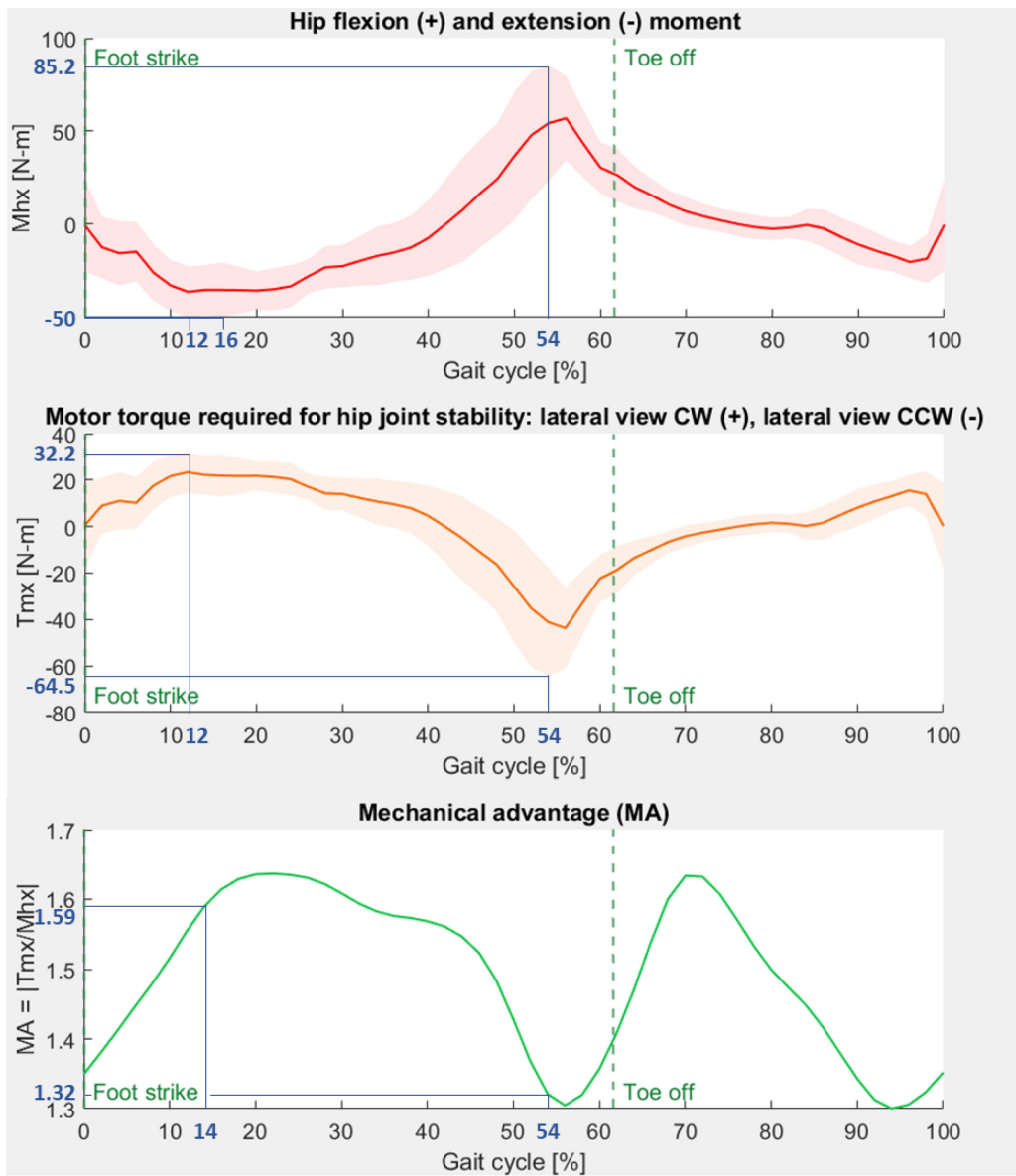


Figure 5-13: Powered hip moment, stabilizing motor torque, and mechanical advantage throughout the gait cycle. Mean plus-minus one standard deviation curves are shown. Approximate local maxima and minima are in blue.

Figure 5-14 shows the link force profiles throughout the gait cycle. Force magnitudes are generally largest during pre-swing at 54% gait cycle when the hip is almost fully extended (much larger than in early mid-stance). Maximum posterior link force is 3849 N in compression and maximum drive arm force is 3822 N in tension. The corresponding anterior link force is 370 N. Maximum link forces occur when stabilizing motor torque is also at its maximum.

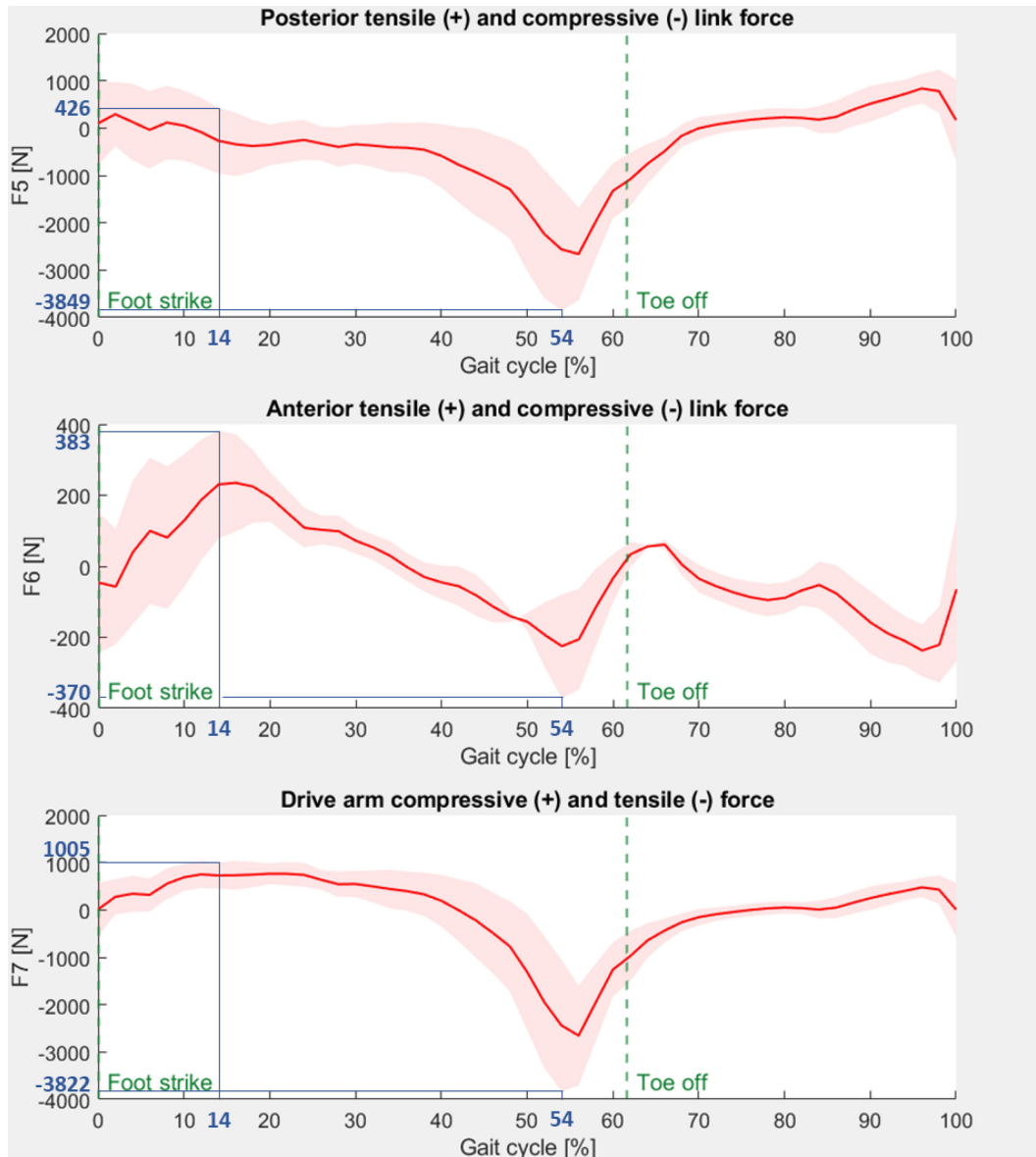


Figure 5-14: Posterior link, anterior link, and drive arm forces throughout the gait cycle. Mean plus-minus one standard deviation curves are shown. Approximate local maxima and minima are in blue.

Mechanical advantage for the motor-only analysis has been plotted as a function of hip flexion angle in Figure 5-15. The 1.64 maximum mechanical advantage occurs at 10° hip flexion. Mechanical advantage tapers off as the hip flexes or extends towards the ROM extremities. Mechanical advantage remains above 1 from 20° hip extension to 40° hip flexion, which is approximately the hip ROM expected in walking. Mechanical advantage decreases dramatically at hip flexion angles beyond 40° meaning that motor torque would drastically increase to sustain weight bearing activities requiring large hip flexion (e.g., uphill walking, stair ascent, sit-to-stand, and stand-to-sit).

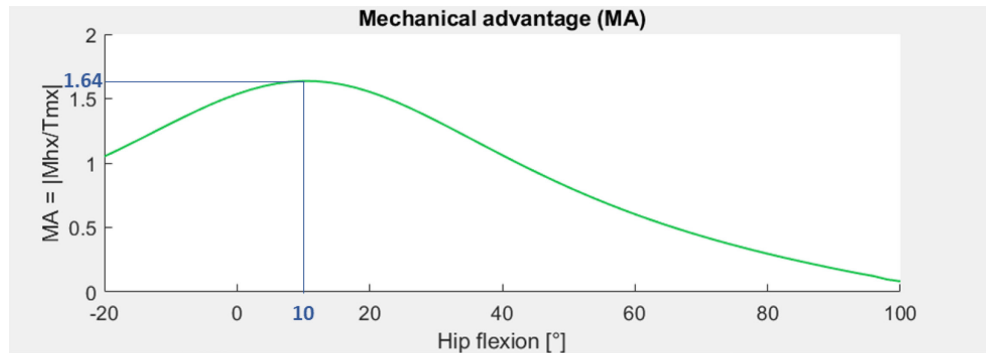


Figure 5-15: Powered hip mechanical advantage throughout its range of motion. Maximum mechanical advantage and its corresponding hip flexion angle are in blue.

Mechanical advantage, as defined by Eq. (4-3), indicates that the input angular velocity (i.e., the motor angular velocity) to produce a set torque is highest when mechanical advantage is largest. The rated maximum motor angular velocity is $300^\circ/\text{s}$, and the maximum expected hip angular velocity during gait is $143^\circ/\text{s}$. Maximum required motor angular velocity (ω_m)_{max} for TF amputee gait performance can be estimated as the product of maximum mechanical advantage and maximum hip angular velocity (ω_h)_{max}.

$$(\omega_m)_{\text{max}} = (MA)_{\text{max}} \cdot (\omega_h)_{\text{max}} = 1.64 \cdot (143^\circ/\text{s}) = 235^\circ/\text{s} \quad (5-43)$$

Therefore, the motor can rotate quickly enough to provide the required gait performance. In reality, the required motor angular velocity is likely to be lower because the maximum required hip angular velocity does not necessarily occur at 10° hip flexion as suggested by Figure 5-15. Nevertheless, the angular velocity criterion has been met.

Link force magnitudes as a function of hip flexion angle when the motor operates at its full 96 N-m torque have been plotted in Figure 5-16. Link forces are highest at the 20° full hip extension and decreases exponentially with deceleration with increasing hip flexion angle. Maximum posterior link force F_5 is 5533 N, maximum anterior link force F_6 is 2310 N and maximum drive arm force F_7 is 9599 N. The drive arm force (i.e., input force) magnitude dictates the magnitudes of the other link forces. Link forces are higher in hip extension because relative motor angle θ_m increases to approach 90° as the hip reaches full extension. As θ_m approaches 90° the moment arm between the drive arm and motor center decreases, thereby increasing the required drive arm force to transmit the same motor torque. From full hip extension, link forces decay exponentially with increasing hip flexion angle due to the drive arm becoming more perpendicular to the motor arm (i.e., the drive flange radial line) at large hip flexion angles. Drive arm force F_7 decreases with increasing hip flexion angle until 30° hip flexion and remains constant at approximately 3000 N (corresponding to the drive arm force acting at

the full motor moment arm of 3.27 cm). Posterior link force F_5 and anterior link force F_6 have similar trends to drive arm force F_7 but with different force magnitudes.

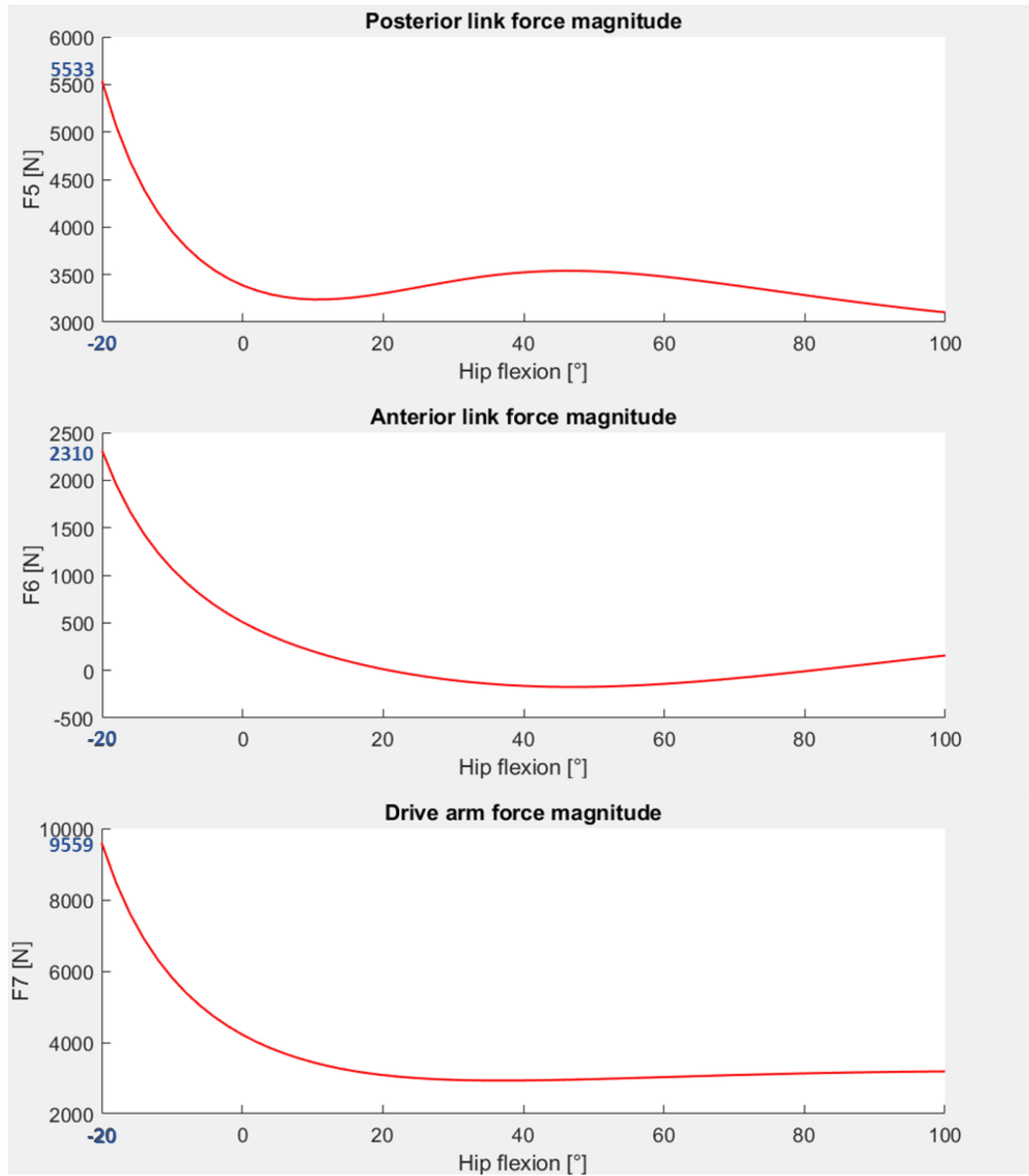


Figure 5-16: Link force magnitudes throughout powered hip range of motion. Maximum link forces and the corresponding hip flexion angle are in blue.

5.6 Chosen Load Case Scenarios for Further Analysis

Out of the examined loading scenarios, the ISO 15032:2000 A100 A-P extension loading condition is the only one that considers loading on the superior link extension stop surface. The ISO 15032:2000 A100 M-L loading condition is the only one that considers medial-lateral loading and is the scenario that results in the largest anterior link forces. Therefore, both loading conditions were

selected for further analysis. The ISO 15032:2000 A100 A-P flexion loading condition resulted in link forces that were much smaller in magnitude compared to other loading conditions. The A-P flexion scenario is also unlikely to occur in a practical setting because it is unlikely that the user would fully bend over (with the hip joint contacting the socket) while simultaneously putting their full body weight on the prosthetic leg. Thus, the A-P flexion case was not considered for further analysis.

The gait cycle force analysis showed that link force magnitudes are maximal during pre-swing and much larger than in other gait stages. The governing gait cycle loading scenario would thus be loading at 54% gait cycle.

However, the motor-only force analysis showed that the maximum drive arm force under the full motor torque (at 20° hip extension) is about 250% greater than the drive arm force at 54% gait cycle. Although it would be unlikely for walking to require the full 96 N-m motor torque, mechanical advantage was found to be below 1 at 40° hip flexion and further decrease with increasing hip flexion angle. Uphill walking, stair ascent, sit-to-stand, and stand-to-sit are weight bearing activities that require large hip flexion angles and hip moments [154], [185], [192], [193]. Although the project scope did not investigate these additional weight bearing activities, the motor would likely need to provide additional torque for weight bearing activities beyond walking. To ensure the motor does not cause the powered hip to self-destruct, the motor-only loading scenario at 20° hip extension was selected for further analysis instead of the 54% gait cycle loading scenario. This selection applied a safety factor of 1.44 to F_5 , 6.24 to F_6 , 2.50 to F_7 in the 54% gait cycle loading scenario. Although it appeared that posterior link force F_5 was being underestimated (safety factor below 2), the A-P extension loading scenario placed a calculated 10284 N on the proximal end of the posterior link (safety factor of 2.67). Considering both the motor-only and ISO static compression loading scenarios, 2.50 was the governing safety factor applied to the motor-only loading scenario at 20° hip extension.

Table 5-5 summarizes the loading scenarios chosen for the stress, deflection, and bearing analyses described in following sections. Only forces used for further analysis are listed. Angles are listed for forces that are not parallel to the link. Extension stop force F_{es} was not calculated in the ISO 15032 M-L position because the A-P extension loading condition had a much greater A-P offset than the M-L loading condition, thereby resulting in a much larger M_{hx} and F_{es} .

Table 5-5: Governing load cases for powered hip design. Signs are with respect to assumed force directions in the free-body diagrams for each load case.

Force	ISO 15032 A-P extension		ISO 15032 M-L		Motor-only at $\theta_{ext} = 20^\circ$
F_{5x}	0 N		196 N		0 N
F_5	10284 N $\angle 18.1^\circ$ (proximal link end)	3895 N $\angle 88.2^\circ$ (distal link end)	717 N $\angle 79.6^\circ$ (distal link end)		5533 N (both link ends)
F_{6x}	0 N		138 N		0 N
F_6	268 N		-4056 N (medial link)	6697 N (lateral link)	2310 N
F_7	0 N		0 N		9599 N
F_{es}	12175 N		-		0 N

Chapter 6: Stress Analysis

Powered hip component thicknesses and diameters were determined by iteratively assigning required dimensions, calculating mechanical stresses based on previously determined loads, comparing these stresses to component material strengths, and making dimensional adjustments to ensure that component stresses remain below their respective strengths. MATLAB program ‘Stresses.m’ contains all computations from this section and can be found in Appendix B.7.

6.1 Failure Criteria

The failure criteria used to determine if a mechanical component breaks under a load depends on whether the material is brittle or ductile. Ductile metals were selected for the power hip because they provide a balance of tensile strength and fatigue life. Failure criteria also depend on if material properties vary with direction. Metals are generally isotropic [194].

Failure theories for ductile isotropic materials assign a benchmark stress value by comparing stress, strain, or strain energy in a three-dimensional stress state to the stress, strain, or strain energy in a yielding uniaxial tensile stress state [195]. Several failure theories for ductile isotropic materials depend on the loading rate, surrounding temperature and chemical environment, and the material’s shape or form [195]. The Tresca (maximum shear stress) yield criterion and the von Mises (distortion energy) yield criterion are two commonly used yielding theories for ductile materials [195]. Experiments have shown that the von Mises yield criterion provides better agreement with observed fracture behaviour than the Tresca yield criterion [195], [196]. Therefore, the von Mises yield criterion was selected for powered hip stress analysis [195].

The von Mises yield criterion states that a material will yield if the energy distorting a volume of material (i.e., distortion energy) in a three-dimensional stress state (Figure 6-1) equals or exceeds the distortion energy when the same material with the same volume yields in uniaxial tension [195].

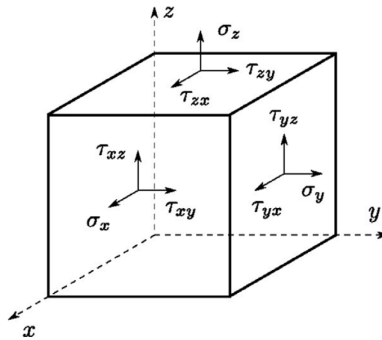


Figure 6-1: Three-dimensional stress state [197].

Comparing distortion energies leads to Eq. (6-1) which compares a stress value in the three-dimensional stress state to the yield stress in the uniaxial tensile stress state [195]. The left-hand side of Eq. (6-1) is the von Mises stress (σ_v). Ideally, the von Mises stress does not exceed the material yield strength (σ_Y).

$$\sigma_v = \sqrt{\frac{1}{2}[(\sigma_x - \sigma_y)^2 + (\sigma_y - \sigma_z)^2 + (\sigma_z - \sigma_x)^2] + 3[\tau_{xy}^2 + \tau_{yz}^2 + \tau_{zx}^2]} \leq \sigma_Y \quad (6-1)$$

Failure also depends on the type of loading. The previously discussed failure criteria assumed static loading. Materials will fail at lower stresses under cyclic loading like weight bearing during gait. The distortion energy theory still holds true but compares von Mises stress (σ_v) to fatigue strength (σ_F) as shown in Eq. (6-2).

$$\sigma_v \leq \sigma_F \quad (6-2)$$

6.2 Powered Hip Materials

Table 6-1 lists engineering material properties considered at the design and prototyping stages of the powered hip project. The 17-4 PH SS H1025 mass density was not explicitly estimated from [198] but was estimated to be equal to the H1075 mass density. Two-million cycle fatigue strength was not available for 17-4 PH SS H1025 but was available for 17-4 PH SS H1150, which is weaker than the H1025 condition [198]. Therefore, the H1025 fatigue strength can be assumed to be greater than the H1150 fatigue strength.

Table 6-1: Engineering materials considered for powered hip project. R is the ratio of the minimum load to the maximum load during fatigue loading.

Material	Mass density	Rockwell hardness	Elastic modulus	Yield strength	2-million cycle fatigue strength
Al 2024-T351 or T4	2780 kg/m ³ [199]	B75 [199]	73.1 GPa [199]	310 MPa [199]	248 MPa (R = 0.1) [199]
17-4 PH SS H1025	7810 kg/m ³ [198]	C35 [200]	201 GPa [198]	1000 MPa [200]	> 752 MPa (R = 0.1) [201]
17-4 PH SS H900	7800 kg/m ³ [198]	C40 [200]	200 GPa [198]	1172 MPa [200]	959 MPa (R = 0.1) [201]
M2 high speed steel	8160 kg/m ³ [202]	C62 [202]	200 GPa [202]	3250 MPa [202]	697 MPa (R = -1) [203]

At the start of the project, Össur recommended two commonly used engineering materials for the powered hip: aluminum (Al) 2024-T351 or T4 (both alloys are almost identical), and 17-4 precipitation hardened stainless steel heat treated at 1025 °F (17-4 PH SS H1025).

Al 2024-T351 was selected for most powertrain components (e.g., the superior link, posterior link, anterior links, drive arm, drive flange, and motor housing) due to its high strength-to-weight ratio, and small differences between its yield strength and 2-million cycle fatigue strength compared to other metals. Powertrain components that needed a material stronger than Al 2024-T351 (i.e., the linkage shafts, drive arm screw-on and motor cover) were initially selected to be 17-4 PH SS H1025. This grade of steel was selected due to its yield strength being high while still being moderately ductile and hard. The initial rationale was that the selected materials would exhibit ductile fractures, thereby avoiding situations in which the prosthesis breaks unexpectedly while in use. Furthermore, machining time and cost would be greatly reduced with softer materials.

The finite element analysis (FEA) carried out in Section 6.5 assumes that Al 2024-T351 and 17-4 PH SS H1025 are the only two materials used in the powered hip. However, the FEA informed that stresses on the drive arm shaft (assumed to be made of 17-4 PH SS H1025) are not far below its yield strength, thereby compromising the fatigue life requirement of 2 million cycles.

17-4 PH SS H1025 was mostly replaced with 17-4 PH SS H900 (heat treated at 900°) because the latter material has a higher yield strength and 2-million cycle fatigue strength while having a similar mass density. 17-4 PH SS H900 is harder and more difficult to machine than 17-4 PH SS H1025, but the long-term benefit in prosthetic performance outweighs the slight increase in manufacturing time and cost. Linkage shafts (revolute joints) which were assumed to previously be made of 17-4 PH SS H1025, are now made of M2 high speed steel (HSS). This kind of steel is much stronger and harder than 17-4 PH SS H1025. Despite the brittleness of M2 HSS relative to other steels, linkage shafts are the components that experience the largest loads and therefore, require the strongest material possible. Furthermore, drawn cup needle bearings were inserted into the powertrain links. Needle rollers are constantly under high loads while being in contact with the shafts. The increased hardness of M2 HSS ensures that the shafts do not deform under the bearing rolling elements, ensuring that linkage motion remains smooth. Smooth linkage motion is also ideal for bearing life because there would not be instances where loading is increased due to irregular motion. The only drawback with M2 HSS is need of specialized laser cutter to cut a M2 HSS cylinder into shafts of correct lengths.

The only exception is the upper and lower drive arm shafts which are made of 17-4 PH SS H900, a material machinable with standard equipment. The lower drive arm shaft is not a straight cylinder (as are all other linkage shafts) but rather a portion of the drive arm screw-on (a component with a shaft merging into a flange as shown in Figure 4-2). The drive arm screw-on component would not be machinable with the hard M2 HSS. For mechanical symmetry, the portion of the upper drive arm shaft in contact with the upper drive arm bearing is also made of 17-4 PH SS H900. The upper

shaft consists of long hard M2 HSS cylinder with a short 17-4 PH SS H900 bushing that slide fits onto the cylinder. The tool steel portion of the shaft supports the anterior link.

6.3 Link Thicknesses

Powertrain links need to be thick enough to house bearings that are strong enough to support previously calculated forces. Drawn cup needle roller bearings were selected for the powertrain links because this bearing type has a high strength to size ratio and a high strength to mass ratio. Table 6-2 compares the maximum radial link loads to the radial static load capacities of the selected link bearings and lists the medial-lateral bearing thicknesses.

Table 6-2: Maximum radial link loads and bearing thicknesses, and radial static load capacities.

Component	Max radial load	Bearing	Thickness	Radial static load capacity
Posterior link	10284 N	INA HN0808 [204] (two at each end)	16 mm [204]	13400 N [204]
Anterior link	6697 N	INA HN0808 [204] (one at each end)	8 mm [204]	6700 N [204]
Drive arm	9599 N	Koyo B-68 [205] (one at each end)	12.7 mm [205]	11788 N [205]

Medial-lateral link thicknesses were initially set to be uniform and equal to the thicknesses in Table 6-2. For the loading scenarios listed in Table 5-5, links were sectioned at cross-sections where internal shear and bending loads are largest (Figures 6-2 and 6-3). A drive arm section is not shown because its governing loading scenario is uniaxial tension that is uniform along the drive arm length (Figure 6-4) with its von Mises stress given by Eq. (6-16). Static equilibrium equations (Eq. (6-3), (6-4), (6-5), (6-12), and (6-13)) were used to determine these internal loads, which informed general stress states at cross-sectional points where stresses were expected to be largest. Points on the outside edges of the cross-section were only subject to normal stress in one direction, which simplified the von Mises stress to be equal this normal stress (Eq. (6-6) and (6-14)). Points in the middle of the cross-section were only subject to shear stress in one direction, which simplified the von Mises stress to be equal to this shear stress multiplied by $\sqrt{3}$ (Eq. (6-9)).

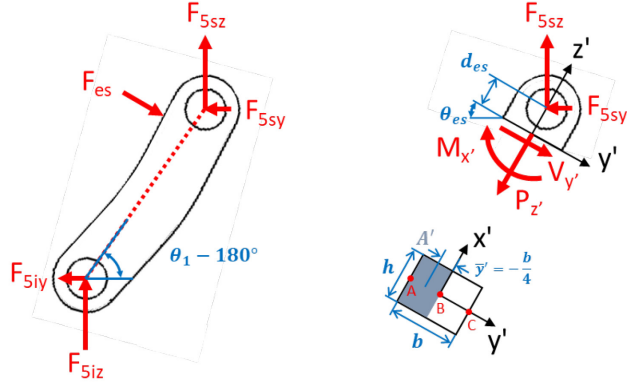


Figure 6-2: Posterior link free-body diagram with a cross-section at extension stop force application point. Older model shown.

$$V_{y'} = F_{5sy} \cos \theta_{es} + F_{5sz} \cos(90^\circ - \theta_{es}) \quad (6-3)$$

$$P_{z'} = -F_{5sy} \sin \theta_{es} + F_{5sz} \sin(90^\circ - \theta_{es}) \quad (6-4)$$

$$M_{x'} = F_{5sy} d_{es} \cos \theta_{es} + F_{5sz} d_{es} \cos(90^\circ - \theta_{es}) \quad (6-5)$$

The von Mises stress at point A or C is the magnitude of the sum of respective normal and bending stresses at these points.

$$(\sigma_v)_C^A = |(\sigma_{z'})_C^A| = \left| \frac{P_{z'}}{A} \mp \frac{M_{x'} y'}{I_{x'}} \right| \quad (6-6)$$

A is the cross-sectional area, y' is the distance from the neutral axis to the point A or C, and $I_{x'}$ is the second moment of area about the x' axis. A , and $I_{x'}$ were calculated as follows.

$$A = bh \quad (6-7)$$

$$I_{x'} = \frac{hb^3}{12} \quad (6-8)$$

The von Mises stress at point B is simply one shear stress term.

$$(\sigma_v)_B = \sqrt{3} \left| (\tau_{z'y'})_B \right| = \sqrt{3} \left| \frac{V_{y'} Q_{x'}}{I_{x'} t_{x'}} \right| \quad (6-9)$$

$Q_{x'}$ is the first moment of area about the x' axis, and $t_{x'}$ is the cross-sectional thickness along the x' axis (i.e., height h). $Q_{x'}$ was calculated as follows.

$$Q_{x'} = \bar{y}' A' \quad (6-10)$$

\bar{y}' is the distance between the neutral axis and the centroid of A' , the area behind the neutral axis on the tail end of internal shear $V_{y'}$. A' was calculated as follows with $b = 20 \text{ mm}$ and $h = 16 \text{ mm}$.

$$A' = h \left(\frac{b}{2} \right) \quad (6-11)$$

The governing cross-sectional von Mises stress was the maximum of $(\sigma_v)_A$, $(\sigma_v)_B$, and $(\sigma_v)_C$.

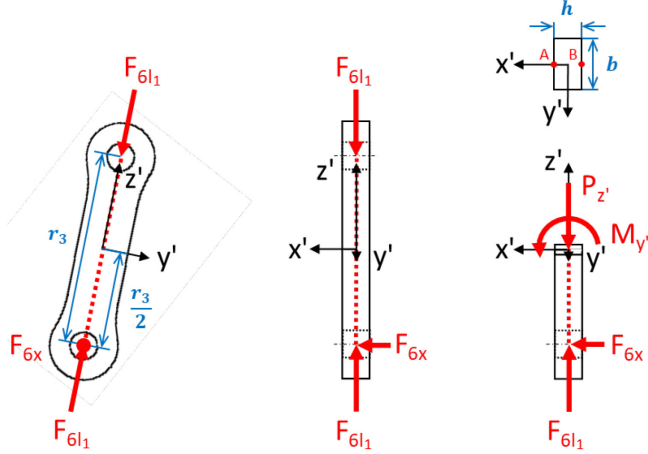


Figure 6-3: Anterior link free-body diagram with a cross-section at middle of its length. Older model shown.

$$P_{z'} = F_{6l1} \quad (6-12)$$

$$M_{y'} = F_{6x} \left(\frac{r_3}{2} \right) \quad (6-13)$$

The von Mises stress at point A or B was calculated in a similar way as the outer edge points on the posterior link cross-section. The governing cross-sectional von Mises stress was the larger of $(\sigma_v)_A$ and $(\sigma_v)_B$.

$$(\sigma_v)_B^A = (\sigma_{z'})_B^A = \left| -\frac{P_{z'}}{A} \mp \frac{M_{y'} x'}{I_{y'}} \right| \quad (6-14)$$

x' is the distance from the neutral axis to the point A or B. $I_{y'}$ was calculated as follows with $b = 15 \text{ mm}$ and $h = 8 \text{ mm}$.

$$I_{y'} = \frac{bh^3}{12} \quad (6-15)$$

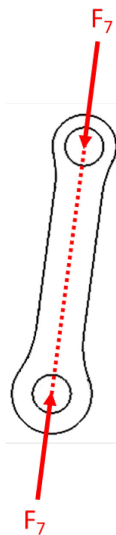


Figure 6-4: Drive arm free-body diagram. Older model shown.

The drive arm governing von Mises normal stress equalled the cross-section's uniform tensile normal stress over area A with $b = 20 \text{ mm}$ and $h = 12.7 \text{ mm}$.

$$\sigma_v = \frac{F_7}{A} \quad (6-16)$$

Table 6-3 lists governing von Mises stresses for powertrain links and the cross-sectional points at which they occur. These stresses are well below the Al 2024-T351 yield strength of 310 MPa, which suggests that link weights can be reduced while still being able to support the required loads. Link weight reduction was analyzed in Section 6.5.

Table 6-3: Governing von Mises link stresses with cross-sectional locations.

Component	von Mises stress	Point
Posterior link	129.2 MPa	A
Anterior link	86.5 MPa	B
Drive arm	37.8 MPa	N/A (uniform stress)

6.4 Shaft Diameters

Shaft diameters were set equal to link bearing bore diameters. The compatibility of the selected bearings with the powered hip also depends on if these diameters are large enough for the shafts to support required loads. Table 6-4 compares maximum radial loads on link bearings to their respective bore diameters.

Table 6-4: Maximum radial loads on link bearings and bearing bore diameters.

Component	Max radial load	Bearing	Bore (shaft) diameter
Posterior link	10284 N	INA HN0808 (two at each end)	8.000 mm
Anterior link	6697 N	INA HN0808 (one at each end)	8.000 mm
Drive arm	9599 N	Koyo B-68 (one at each end)	9.525 mm

The governing scenario is the posterosuperior shaft with a maximum radial load of 10284 N and a diameter of 8 mm. The posterosuperior shaft was isolated as a free body (Figure 6-5). Axes x'' , y'' , and z'' are the biomechanics axes rotated about the x -axis so that the direction of the z'' -axis matches that of the posterior link force F_{5s} .

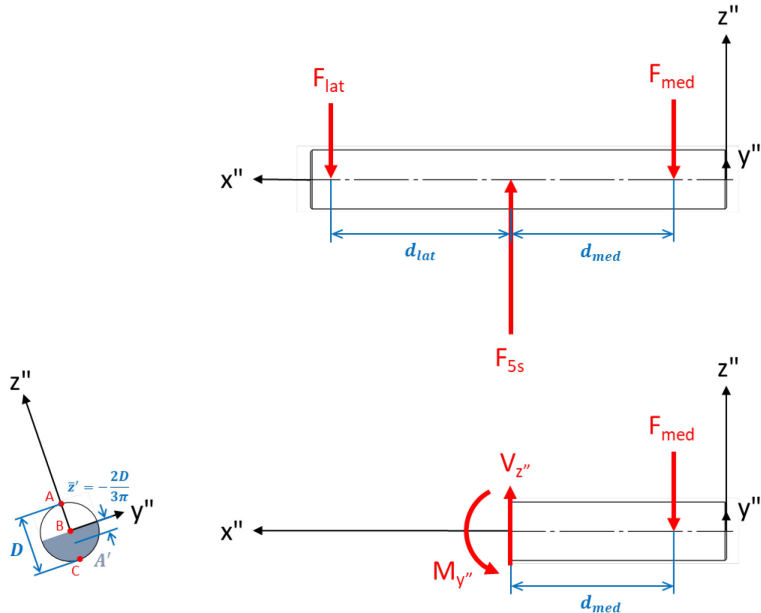


Figure 6-5: Posterosuperior shaft free-body diagram with a cross-section at the posterior link superior force F_{5s} application point.

Lateral and medial posterosuperior shaft forces F_{lat} and F_{med} were determined taking the entire shaft in static equilibrium and solving the system of equations.

$$-F_{lat} + F_{5s} - F_{med} = 0 \quad (6-17)$$

$$F_{lat}d_{lat} - F_{med}d_{med} = 0 \quad (6-18)$$

Internal loads $V_{z''}$ and $M_{y''}$ were found by taking the shaft medial half in static equilibrium.

$$V_{z''} = F_{med} \quad (6-19)$$

$$M_{y''} = F_{med} d_{med} \quad (6-20)$$

The von Mises stress at points A and C equals the bending stress magnitude at these points.

$$(\sigma_v)_C^A = |(\sigma_{x''})_C^A| = \left| \frac{M_{y''} z''}{I_{y''}} \right| \quad (6-21)$$

z'' is the distance between the neutral axis and points A or C. $I_{y''}$ is the second moment of area about y'' . $I_{y''}$ was calculated as follows.

$$I_{y''} = \frac{\pi D^4}{64} \quad (6-22)$$

The von Mises stress at point B equals the shear stress magnitude at this point times $\sqrt{3}$.

$$(\sigma_v)_B = \sqrt{3}|(\tau_{x''z''})_B| = \sqrt{3} \left| \frac{V_{z''} Q_{y''}}{I_{y''} t_{y''}} \right| \quad (6-23)$$

$Q_{y''}$ is the first moment of area about the y'' axis, and $t_{y''}$ is the cross-sectional thickness along y'' (i.e., shaft diameter D). $Q_{y''}$ was calculated as follows.

$$Q_{y''} = \bar{z}' A' \quad (6-24)$$

\bar{z}' is the distance between the neutral axis and the centroid of A' , the area behind the neutral axis on the tail end of internal shear $V_{z''}$. A' was calculated as follows.

$$A' = \frac{\pi D^2}{8} \quad (6-25)$$

The maximum cross-sectional von Mises stress was 2241.6 MPa at points A and C. This stress was well below the 3250 MPa yield strength of M2 HSS, which meant that shafts met load requirements and were compatible with selected bearings so long as they were made of M2 HSS. The drive arm screw-on containing the inferior drive arm shaft has a complex shape and therefore, has been analyzed with FEA (Section 6.5).

6.5 Finite Element Analysis

Static equilibrium, when applied to a three-dimensional stress state (Figure 6-1), is expressed as follows where the b terms are body forces such as gravity [206].

$$\frac{\partial \sigma_x}{\partial x} + \frac{\partial \tau_{yx}}{\partial y} + \frac{\partial \tau_{zx}}{\partial z} + b_x = 0 \quad (6-26)$$

$$\frac{\partial \tau_{xy}}{\partial x} + \frac{\partial \sigma_y}{\partial y} + \frac{\partial \tau_{zy}}{\partial z} + b_y = 0 \quad (6-27)$$

$$\frac{\partial \tau_{xz}}{\partial x} + \frac{\partial \tau_{yz}}{\partial y} + \frac{\partial \sigma_z}{\partial z} + b_z = 0 \quad (6-28)$$

$$\tau_{xy} = \tau_{yx} \quad (6-29)$$

$$\tau_{xz} = \tau_{zx} \quad (6-30)$$

$$\tau_{zy} = \tau_{yz} \quad (6-31)$$

Simplified forms of static equilibrium equations can be used to determine stresses on cross-sections with simple shapes, as was done in Sections 6.3 and 6.4. However, mechanical parts with complex cross-sections (possibly containing stress concentrators) require solving the general form of static equilibrium (Eq. (6-26) through (6-31)).

The hip was separated into an upper unit and a motor unit (Figure 6-6). FEA was performed on each unit independently with previously solved link forces (Table 5-5). SolidWorks' FFEPlus iterative solver was used for upper unit FEA and SolidWorks' Intel Direct Sparse solver was used for motor unit FEA. The lamination plate and the bottom of the motor housing were assumed to be fixed to the socket. All chamfers were removed.

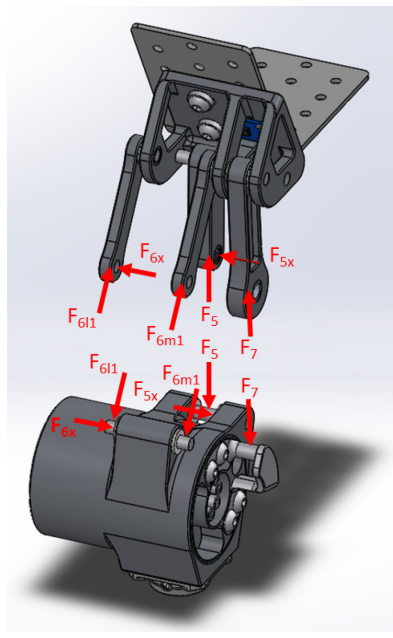


Figure 6-6: Powered hip motor and upper FEA units. ISO 15032 M-L loading case shown. Drive arm force shown for example only.

FEA constraints included pin, bearing, and screw connections. All FEA pins and washers were assumed to be made of 17-4 PH SS H1025. All FEA screws were assumed to be made of class 12.9 alloy steel. All other FEA parts were assumed to be made of Al 2024-T351. Superior, lateral, and medial screw connections (Figure 6-7) were specified by thread engagement lengths and preload torques. Thread engagement lengths (i.e., screw lengths and threaded hole lengths) were chosen such that screw yielding occurred at a lower stress than thread stripping (Appendix E). Preload torques were chosen such that there was enough static friction between fastened surfaces to prevent movement under input loads (Appendix F).

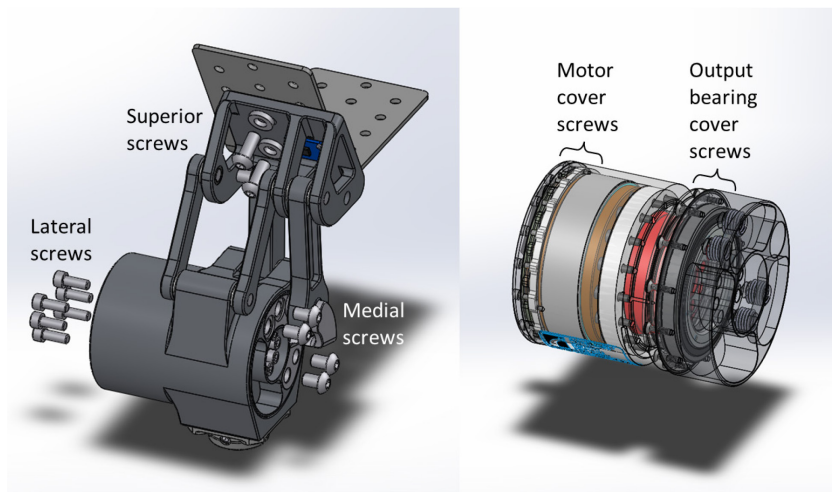


Figure 6-7: Screw connections for powered hip finite element analysis.

Table 6-5 lists selected properties for powered hip FEA screw connections.

Table 6-5: Thread engagement lengths and preload torques for powered hip FEA screw connections.

Connection	Thread engagement length (mm)	Preload torque (N-m)
Superior screws	10.00	19.0
Medial screws	8.00	14.1
Lateral screws	3.25	7.1
Output bearing cover screws	4.30	1.15
Motor cover screws	3.10	1.00

Upper unit FEA would have not been accurate with the lamination plate being the only component above the superior link. The lamination plate would have brought the fixed surface constraint too close to the superior link (introducing local stresses that do not exist on the superior link) and would have overestimated stresses on the lamination plate itself since it would have been the only component above the powered hip absorbing the link loads.

A mock pelvis and a mock socket were modelled to more accurately represent how loads are absorbed by the upper unit (Figure 6-8). Mock pelvis dimensions were those of the American male between the 75th and 95th percentiles in the year 2000 [187], [190]. For simplicity, the mock pelvis was assumed to be made entirely of cortical bone, which is the main contributor to biological pelvis compressive strength. Assumed cortical bone properties are mass density = 1800 kg/m³ [207], elastic modulus = 15 GPa [207], [208], [209], and yield strength = 120 MPa [208]. The mock socket was assumed to be entirely of Al 2024-T351 because the pelvic socket contains a combination of aluminum and carbon fiber. Assuming uniformity with aluminum was the more conservative approach.

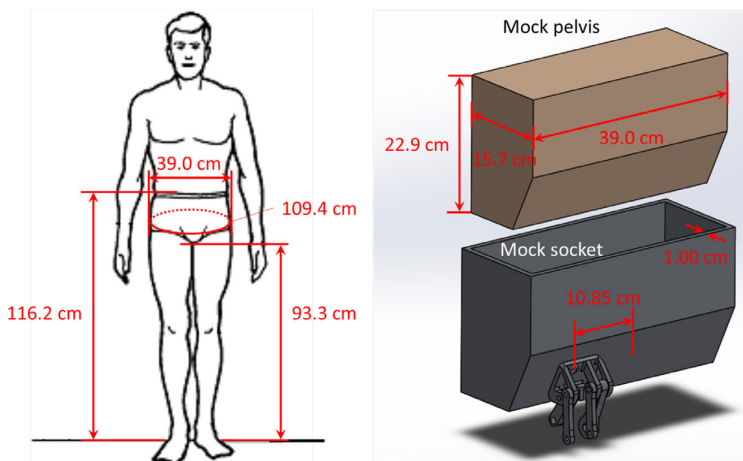


Figure 6-8: Powered hip upper unit with a mock pelvic and a mock socket. Mock pelvis dimensions determined from [187], [190]. Hip joint distance from the midline determined from [210].

Minor simplifications of the linkage portion of the upper unit were performed: removal of chamfers and removal of the superior link rectangular IMU slot. Figures 6-9 to 6-11 illustrate the motor unit medial-lateral cross-section at various levels of simplicity.

Performing FEA on the non-simplified motor unit with many internal components with complex geometry (Figure 6-9) would have resulted in unreasonably large simulation times and an increased likelihood of mathematical inconsistencies.

Össur designed the motor and its internal components to support up to 96 N-m of torque on the knee joint. Initially, the motor was treated as a black box that can support 96 N-m regardless of geometry and method of torque transmission. Therefore, the motor was simplified to a cylinder with a circular cover on the lateral end and the drive flange on the medial end (Figure 6-10).

However, it was later determined that the motor unit in Figure 6-10 was an oversimplification for the load case with the motor turned on. The Össur Power Knee 2 transfers torque with medial-lateral symmetry to the shank because its motor is centered with the shank. When placed in the powered hip, the motor pushes or pulls on the drive arm. The drive arm reaction force then pulls or pushes on the drive arm shaft which is connected to motor internal components. The drive arm is medially offset to the motor output bearing and the motor is laterally offset to the thigh. These offsets increase the moment arm between the drive arm force and the motor's internal components. Therefore, there was more bending stress to be expected in the powered hip motor unit than the Össur Power Knee 2 motor unit and some internal components needed to be reintroduced into the motor unit, as was done in Figure 6-11. Reintroduced components were re-evaluated for structural integrity with powered hip offsets taken into consideration.

The fully simplified motor unit (Figure 6-10) was acceptable for the ISO 15032 A-P extension and M-L cases because they assumed the motor was turned off. The semi-simplified motor unit (Figure 6-11) was used for the scenario with the motor operating at full torque (Figure 6-11). This semi-simplified motor unit included two additional screw sets: the motor covered screws (torqued at 1 N-m) and the output bearing cover screws (torqued at 1.15 N-m). For increased thread strength, all motor units included helicoils in the threaded holes for the drive arm screw-on button head screws.

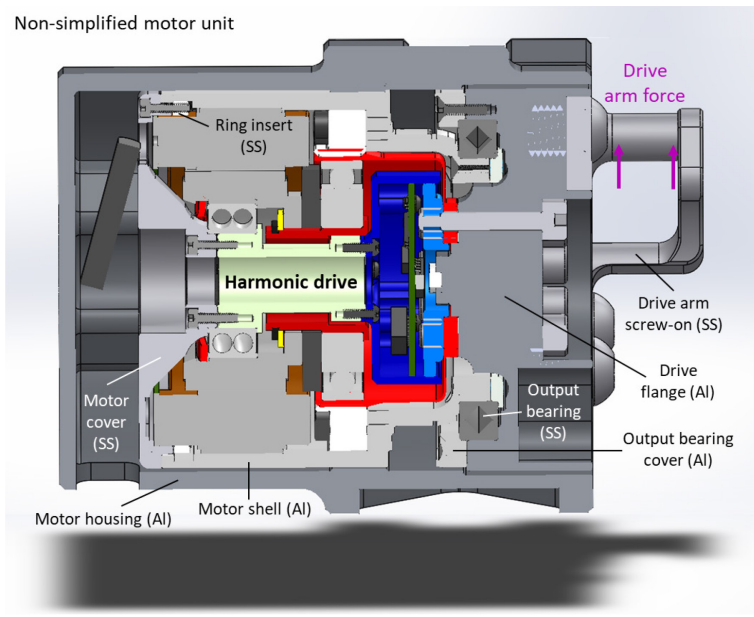


Figure 6-9: Non-simplified powered hip motor unit containing all motor internal components.

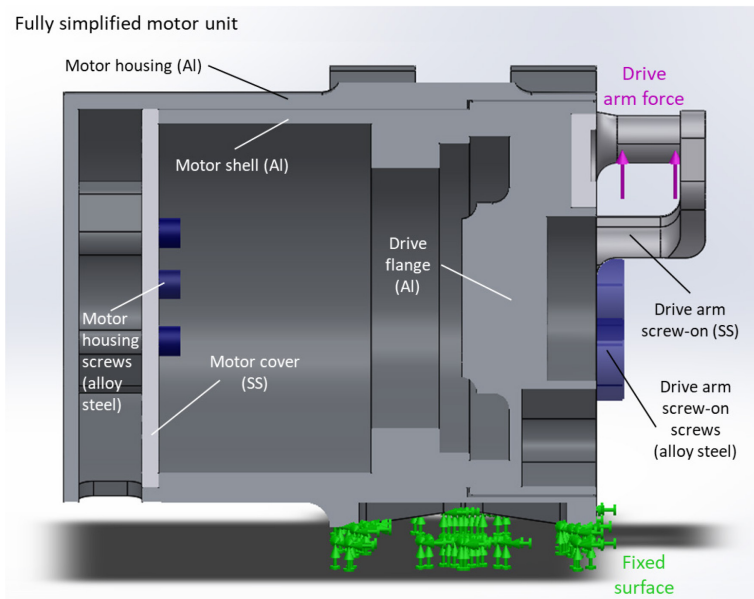


Figure 6-10: Fully simplified powered hip motor unit with all internal components removed.

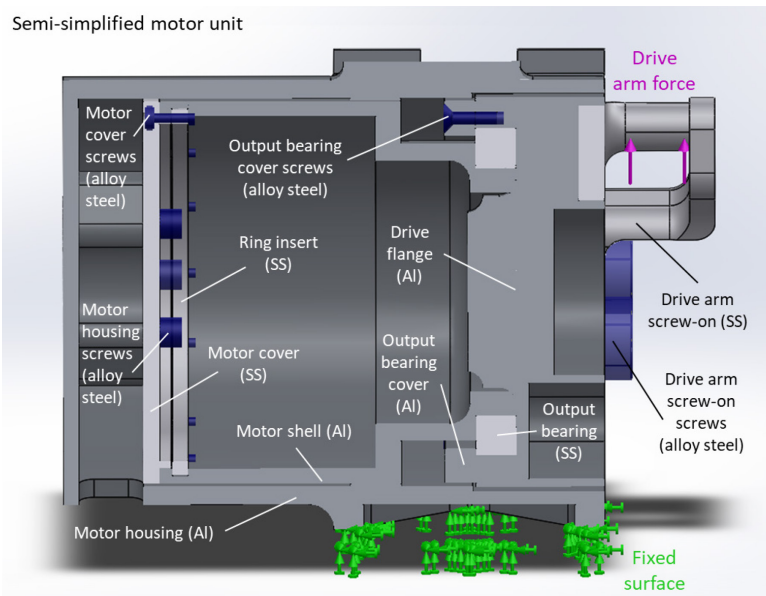


Figure 6-11: Semi-simplified powered hip motor unit with most internal components removed. Ring insert and output bearing included.

Figures 6-12 to 6-14 illustrate the SolidWorks-generated curvature-based meshes for the upper unit, motor unit, and three drive arms with different weight reduction features. Meshing properties are listed in Table 6-6.

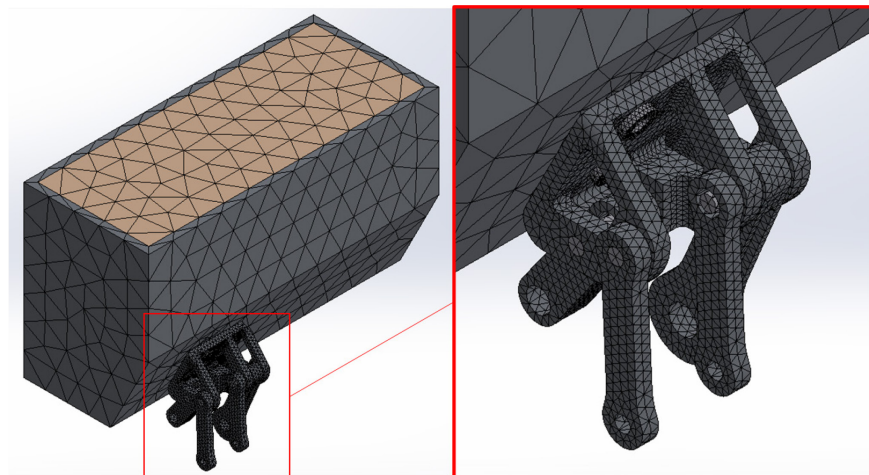


Figure 6-12: Upper unit FEA mesh. Large elements assigned to pelvic components. Small elements assigned to powered hip components.

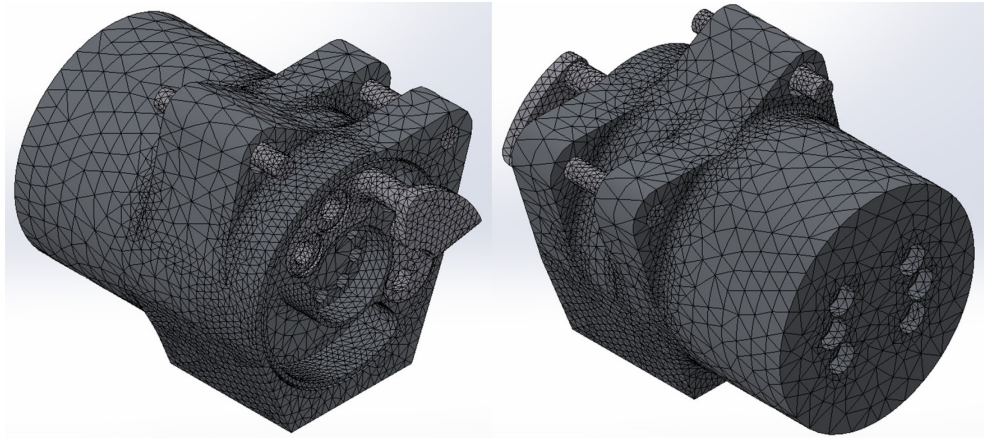


Figure 6-13: Motor unit FEA mesh. Large elements assigned to thick, geometrically simple regions, and low stress magnitude regions. Small elements assigned to thin, geometrically more complex regions, and high stress magnitude regions.



Figure 6-14: FEA meshes for drive arms 1 (left), 2 (middle), and 3 (right). Mostly uniform meshing.

Table 6-6: FEA meshing properties.

Assembly or component	No. elements	Maximum element size (cm)	Minimum element size (cm)	Percentage of elements with aspect ratio < 3	Percentage of elements with Jacobian ratio < 10	Portion of distorted elements
Upper unit	33688	3.49	0.0811	96.6	99.997	0%
Motor unit	157000	2.77	0.555	95.6	99.974	0%
Drive arm 1	9845	0.276	0.0921	99.4	100.000	0%
Drive arm 2	8706	0.276	0.0921	99.9	100.000	0%
Drive arm 3	10927	0.276	0.0921	99.9	100.000	0%

Ideally, all tetrahedral elements have equal edge lengths (i.e., an aspect ratio of 1) [211]. Higher aspect ratios result in stretched tetrahedral elements that cause results to be less accurate due to inconsistent spacing between nodes [211]. Furthermore, each element's Jacobian ratio should be as

close to 1 as possible [211]. The Jacobian ratio measures each element's deviation in shape relative to the ideal shape with an aspect ratio of 1 [211]. The Jacobian ratio is an indication of distorted elements because near sharp and/or curved geometry, the Jacobian ratio increases and the likelihood of element edges crossing each other (resulting in a negative Jacobian ratio) increases [211].

SolidWorks developers recommend that at least 90% of elements have an aspect ratio of 5 or less and a Jacobian ratio of 10 or less [211]. Furthermore, the mesh should have no distorted elements [211]. Finer meshes generally result in lower element aspect ratios. All FEA assemblies and components had high quality meshes since they greatly exceeded the criteria for mesh quality, thereby providing high result reliability. Many FEA iterations were performed, but only the most recent iterations, most accurately reflecting the current powered hip design, are presented in this thesis.

Figure 6-15 illustrates the upper unit von Mises stress distribution for the ISO 15032:2000 A-P extension loading scenario. Results are shown for three versions of the posterior link. Initially, posterior link weight was reduced by removing material from the anterior and posterior surfaces with the idea that material on the medial and lateral surfaces would remain to support medial-lateral bending. However, posterior link contact with the superior link at full hip extension creates a stress concentration on the posterior link along the contact surface bottom edge. Posterior link weight reduction features introduce thin geometry near this stress concentration further increasing stresses in nearby elements. The posterior link without weight reduction is approximately 20 g heavier but has a maximum von Mises stress that is at least 102.8 MPa lower than weight reduced posterior links. Although the maximum von Mises stress is below the 310 MPa yield strength of Al 2024-T351 when any one of the three posterior links are used, the solid posterior link was chosen for the design because it resulted in a large reduction in stress for a 0.75% increase in the total powered hip weight (considering the powered hip without the chassis weighs about 2.7 kg).

Safety factor (SF) is expressed in terms of maximum von Mises stress $(\sigma_v)_{max}$. Eq. (6-32) is used when failure is governed by yielding. Eq. (6-33) is used when failure is governed by fatigue.

$$SF = \frac{\sigma_y}{(\sigma_v)_{max}} \quad (6-32)$$

$$SF = \frac{\sigma_f}{(\sigma_v)_{max}} \quad (6-33)$$

From Eq. (6-32), the design safety factor for compression under the ISO 15032:2000 A-P extension condition is 1.80, indicating that the upper unit is strong enough for this loading condition.

Shaft stresses under this loading condition are much smaller than predicted in Section 6.4 because pin connectors were used to model the FEA. Pin connectors assume a rigid pin between

selected cylindrical surfaces. Pin connectors are intended to examine the stresses on parts adjacent to pins rather than the stress distribution of the pins themselves [212]. Implemented pin connectors also served the purpose of locking rotation and translation of shafts relative to the superior link (as a representation of shaft-superior link press fits), and the purpose of locking link translation relative to the shafts. Even though pin connectors are meant to replace pin models [212], the upper unit FEA used pin connectors in conjunction with pin models (i.e., physical shafts) because pin models provide mounting locations for link bearing connectors (which were assumed and set to be rigid) [212]. Bearing connectors were placed in the gaps between pin models and link bearing slots. Some shaft stress was absorbed into the rigidity of each pin connector, and some was absorbed into each pin model. Furthermore, Section 6.4 assumed that the pin fixed ends had infinite stiffness. However, the superior link was modelled to be aluminium and to have weight reduction features that rendered the piece more elastic than the 17-4 PH SS H1025 pins themselves and therefore, much of the stress was absorbed by superior link elastic deformation.

No motor unit analysis was performed for ISO 15032:2000 A-P extension loading because link force magnitudes for this load scenario are well below force magnitudes in the other loading scenarios analyzed. FEA for the ISO 15032:2000 A-P extension loading scenario was intended to confirm that yielding would not occur near the extension stop.

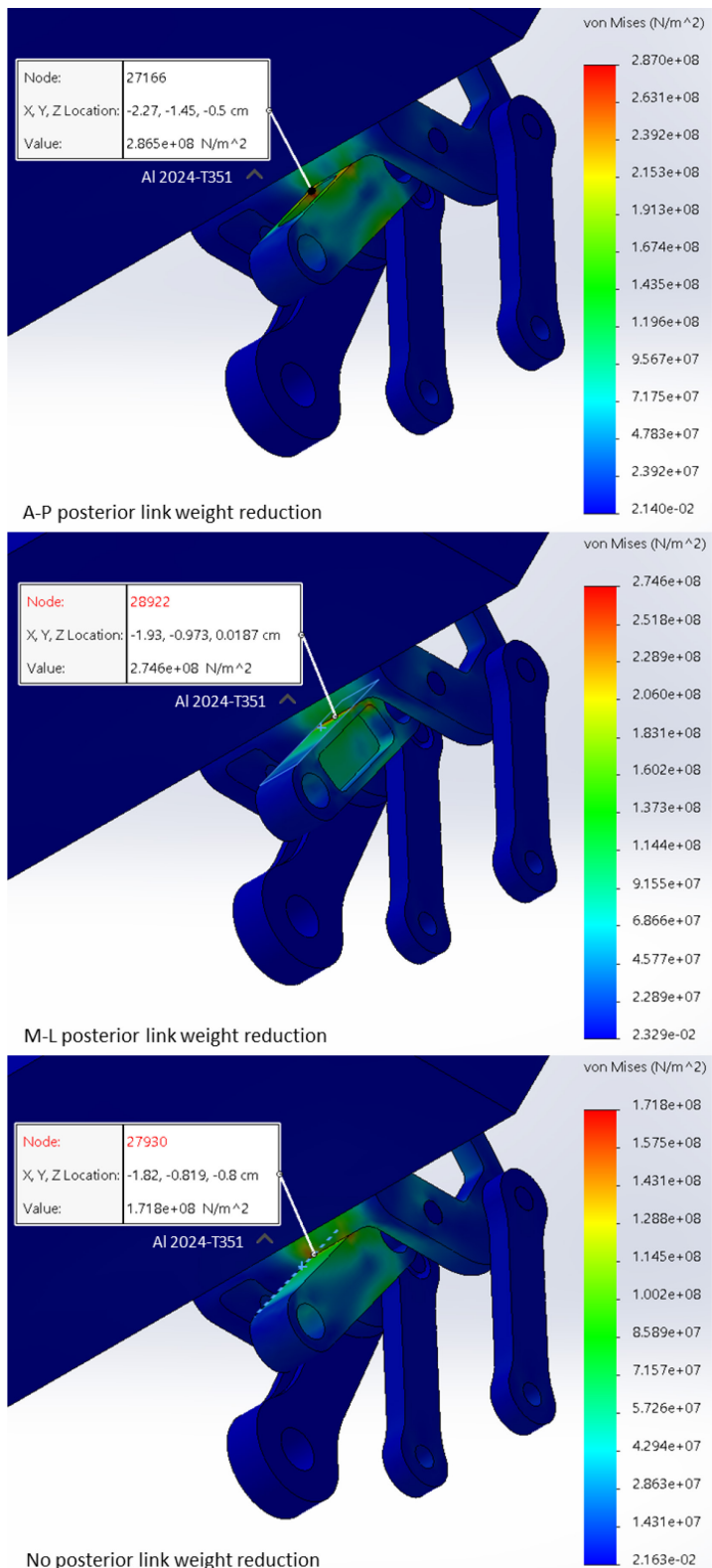


Figure 6-15: Upper unit FEA with ISO 15032:2000 A-P extension loading: posterior link force $F_5 = 3895 \text{ N}$ at 88.5° (compression), anterior link force $F_6 = 268 \text{ N}$ (tension), drive arm force $F_7 = 0 \text{ N}$. Maximum von Mises stresses shown for various levels of posterior link weight reduction.

Figures 6-16 and 6-17 show upper unit and motor unit FEA results for the ISO 15032:2000 M-L loading scenario. In this scenario, the upper unit is resisting compression and clockwise bending simultaneously (when viewed from the front). This combined loading places the majority of the stress on the lateral side of the upper unit. A right leg prosthesis undergoing compression with a lateral offset has been assumed. If a left leg prosthesis or compression with a medial offset were assumed, the majority of the stress would be taken by the medial lateral link and the middle superior link rib. All superior links are of equal thicknesses. The middle rib is slightly wider to accommodate loading from both the anterior link and drive arm simultaneously. The more conservative approach was therefore to assume that the majority of the load was on the smaller lateral rib.

In earlier computer-aided design (CAD) models, superior link ribs were solid. FEA iterations for earlier CAD models indicated low stresses on rib central regions and high stresses near linkage shafts. Creating rib trapezoidal windows resulted in a more balanced stress distribution throughout each rib and a 43 g (1.6%) overall weight reduction.

The maximum von Mises stress on upper unit parts made of Al 2024-T351 is 178.6 MPa (Figure 6-16), which occurs on the anterior portion of the superior link along the outside edge of the lateral weight reduction feature. The maximum von Mises stress on upper unit parts made of 17-4 PH SS H1025 is 325.2 MPa (Figure 6-16), which occurs on the lateral portion of the superior washer along its inner edge. From Eq. (6-32), the yielding safety factor for upper unit aluminum parts is 1.74, and the yielding safety factor for upper unit 17-4 PH SS H1025 parts is 2.84. Thus, the upper unit can handle ISO 15032:2000 M-L compression.

Under this loading condition, motor unit stresses are highest on the anterior portion. The motor housing anterior curvature contains two bearings, assumed to be rigid. Bearing rigidity provides a hard surface for anterior shaft bending. As a result, the anteroinferior shaft absorbs most of the medial-lateral loading and a small portion of the load is transferred to the motor housing anterior portion.

The maximum von Mises stress on motor unit parts made of Al 2024-T351 is 124.1 MPa (Figure 6-17), occurring on the lateral edge of the motor housing anterior curvature. The maximum von Mises stress on motor unit parts made of 1717-4 PH SS H1025 is 920.7 MPa (Figure 6-17), occurring on the lateral-posterior portion of the anteroinferior shaft. From Eq. (6-32), the yielding safety factor for motor unit aluminum parts is 2.50, and the yielding safety for motor unit 17-4 PH SS H1025 parts is 1.09. Thus, the motor unit can also support ISO 15032:2000 M-L compression.

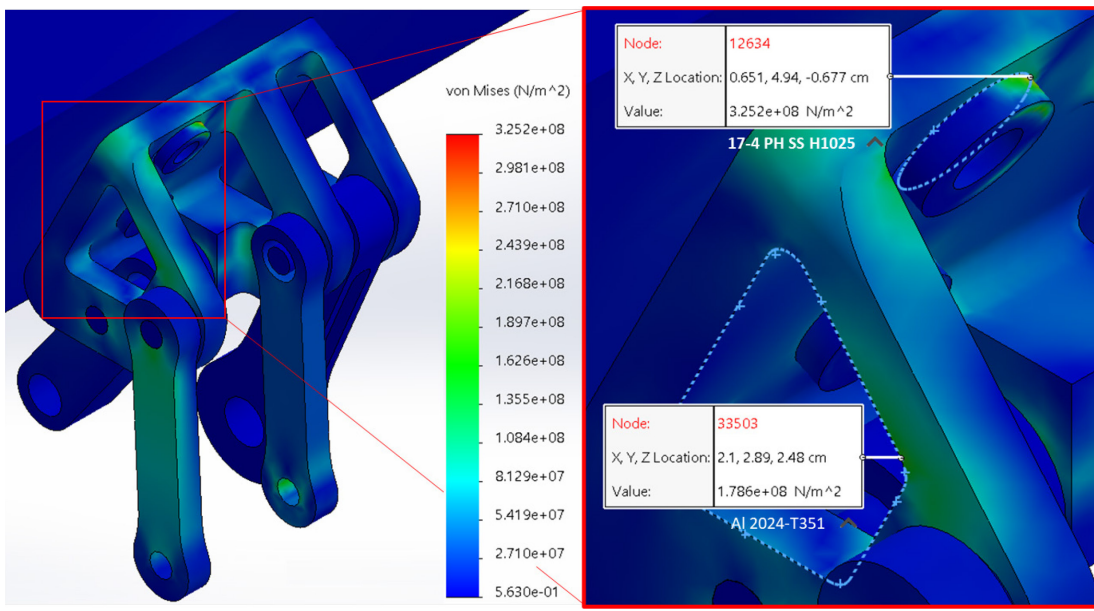


Figure 6-16: Upper unit FEA with ISO 15032:2000 M-L extension loading: posterior link forces $F_5 = 717 \text{ N}$ at 79.6° , $F_{5x} = 196 \text{ N}$ (outward), anterior link forces $F_{6m1} = 4056 \text{ N}$ (tension), $F_{6l1} = 6697 \text{ N}$ (compression), $F_{6x} = 138 \text{ N}$ (outward on lateral link), drive arm force $F_7 = 0 \text{ N}$. Maximum von Mises stresses shown for each material.

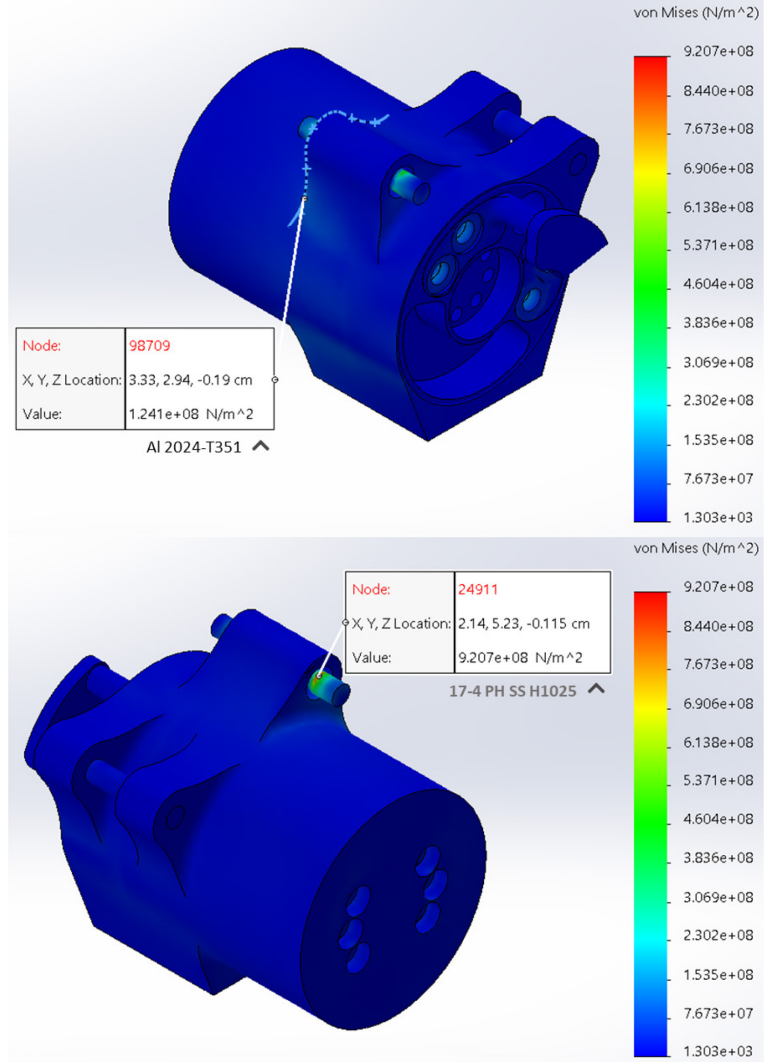


Figure 6-17: Motor unit FEA with ISO 15032:2000 M-L extension loading: posterior link forces $F_5 = 717 \text{ N}$ at 79.6° , $F_{5x} = 196 \text{ N}$ (outward), anterior link forces $F_{6m1} = 4056 \text{ N}$ (tension), $F_{6l1} = 6697 \text{ N}$ (compression), $F_{6x} = 138 \text{ N}$ (outward on lateral link), drive arm force $F_7 = 0 \text{ N}$. Maximum von Mises stresses shown for each material.

Figures 6-18 to 6-20 show upper unit and motor unit FEA results for the motor-only loading case (at the maximum torque of 96 N-m). For this loading case, the motor was assumed to apply a CW torque (when viewing the hip medially) to prevent further hip extension (since motor counteracted hip extension near push off at which drive arm force is largest). Therefore, the posterior and anterior links were in compression and the drive arm was in tension.

Section 6.3 shows that the drive arm cross-section, without weight reduction features, can easily support the maximum motor torque. For FEA, drive arm material was initially removed from the anterior and posterior faces with the rationale that material would be left on the medial and lateral faces to support medial-lateral loads. However, FEA on the drive arm with material removed from the

medial and lateral faces showed a 15.7 MPa decrease in maximum von Mises stress (occurring on the inner surface of the lower hole at the 3 o'clock and 9 o'clock positions (Figure 6-18)) and a 3 g decrease in mass. The decrease in stress and mass simultaneously occurred because the remaining material on the anterior and posterior faces redirected stress flow lines to be further away from the inferior hole stress concentrators at the anterior and posterior ends of the hole. Furthermore, the maximum von Mises stress on the drive arm with medial-lateral weight reduction (171 MPa (Figure 6-18b), well below the 2-million cycle fatigue strength at 248 MPa) was only 3.4 MPa higher than the solid drive arm which weighed 20 g more. Therefore, the drive arm with medial-lateral weight reduction was integrated into the powered hip.

The motor-only loading scenario placed most of the stress on the posterior link, drive arm, and superior link middle rib. Since the middle rib supports loads from the posterior link, the lateral anterior link, and the drive arm simultaneously, it was designed to be larger than the medial and lateral ribs. Fillet radii are stress concentrators and were thus chosen to be large enough to keep peak von Mises stresses within the design criteria.

The maximum von Mises stress on upper unit parts made of Al 2024-T351 was 203.8 MPa (Figure 6-19), which occurred directly below the superior washer along the screw slot edge. This stress value was well below the Al 2024-T351 2-million cycle fatigue strength of 248 MPa. Fatigue was taken as the governing failure mode for the motor-only loading scenario as a conservative way to represent ambulatory activities that may result, though unlikely, in consistent 96 N-m torque loading. From Eq. (6-33), the 2-million cycle fatigue safety factor on upper unit parts made of Al 2024-T351 was 1.22. The maximum von Mises stress on upper unit parts made of 17-4 PH SS H1025 was 385.5 MPa (Figure 6-19), which occurred on the superior washer out edge. Similarly, this stress value was below the 17-4 PH SS H1025 2-million cycle fatigue strength of at least 752 MPa. From Eq. (6-33), the fatigue safety factor on upper unit parts made of 17-4 PH SS H1025 was at least 1.95. Thus, the upper unit is strong enough to support the 96 N-m maximum motor torque at full hip extension and at all other places within the ROM.

The majority of the motor unit stress is absorbed by the posteroinferior shaft and the drive arm screw-on. The 17-4 PH SS H1025 drive arm screw-on contains an inside half with a shaft integrated into a plate that is screwed onto the drive flange, and an outside half with a L-bracket that is also screwed onto the drive flange (Figure 4-2). Both halves of the screw-on served as an elastic component that supports the drive arm medially and laterally and deforms elastically to absorb the large stresses induced by the drive arm resisting maximum motor torque. In earlier CAD models, the screw-on was only one part containing cantilever shaft. Although the part was made of 17-4 PH SS H1025, this previous approach resulted in fracture under maximum motor torque. FEA iterations informed

appropriate thicknesses and screw sizes for the two-part drive arm screw-on which distributed stresses in a more balanced way than the one-part drive arm screw-on. Thicknesses were chosen such that the screw-on was strong enough to avoid yielding but be not too stiff as to transfer too much stress to the drive flange, potentially causing it to yield.

The external maximum von Mises stress on motor unit parts made of Al 2024-T351 was 217.5 MPa (Figure 6-20), which occurred on the motor housing lateral face near the posteroinferior counterbore, resulting in a 2-million cycle fatigue safety factor of 1.14. The corresponding von Mises stress on motor unit parts made of 17-4 PH SS H1025 was 704.3 MPa (Figure 6-20), which occurred on the drive arm screw-on medial fillet nearest to the drive flange center, resulting in a 2-million cycle fatigue safety factor of at least 1.07.

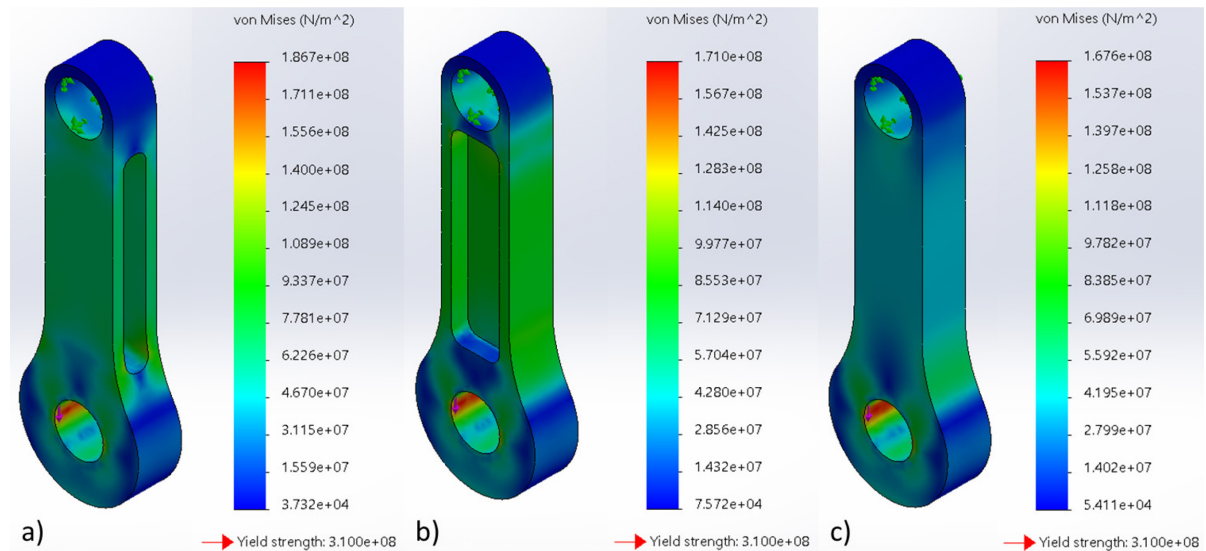


Figure 6-18: Drive arm under the motor only loading case ($F_7 = 9599 \text{ N}$ (tension)): a) anterior-posterior weight reduction, b) medial-lateral weight reduction, c) no weight reduction.

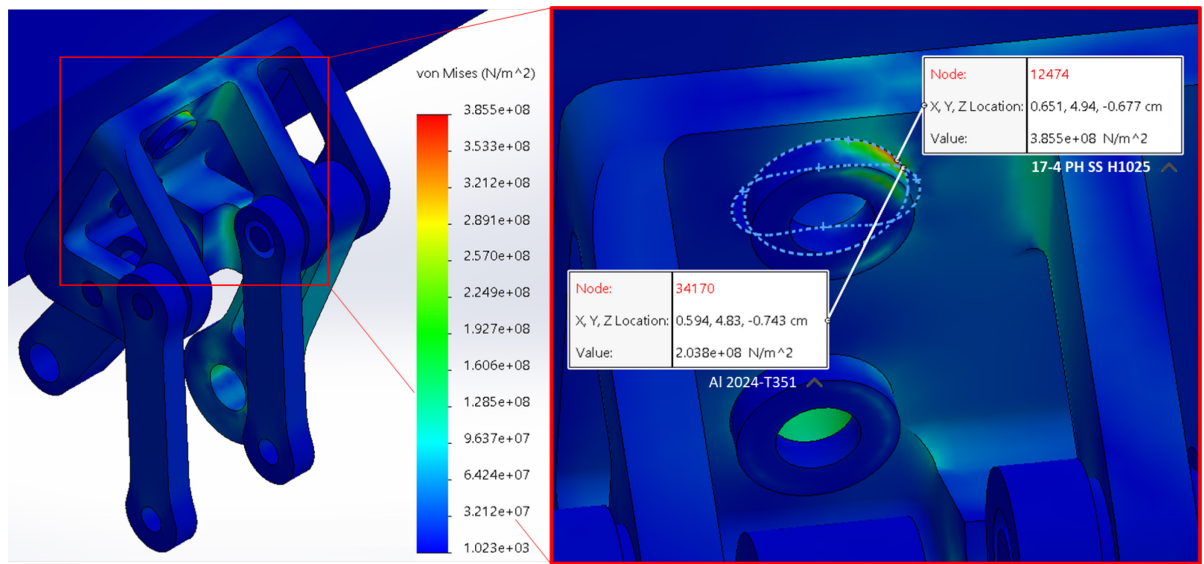


Figure 6-19: Upper unit FEA with motor-only loading: posterior link forces $F_5 = 5533\text{ N}$ (compression), anterior link force $F_6 = 2310\text{ N}$ (compression), drive arm force $F_7 = 9599\text{ N}$ (tension). Maximum von Mises stresses shown for each material.

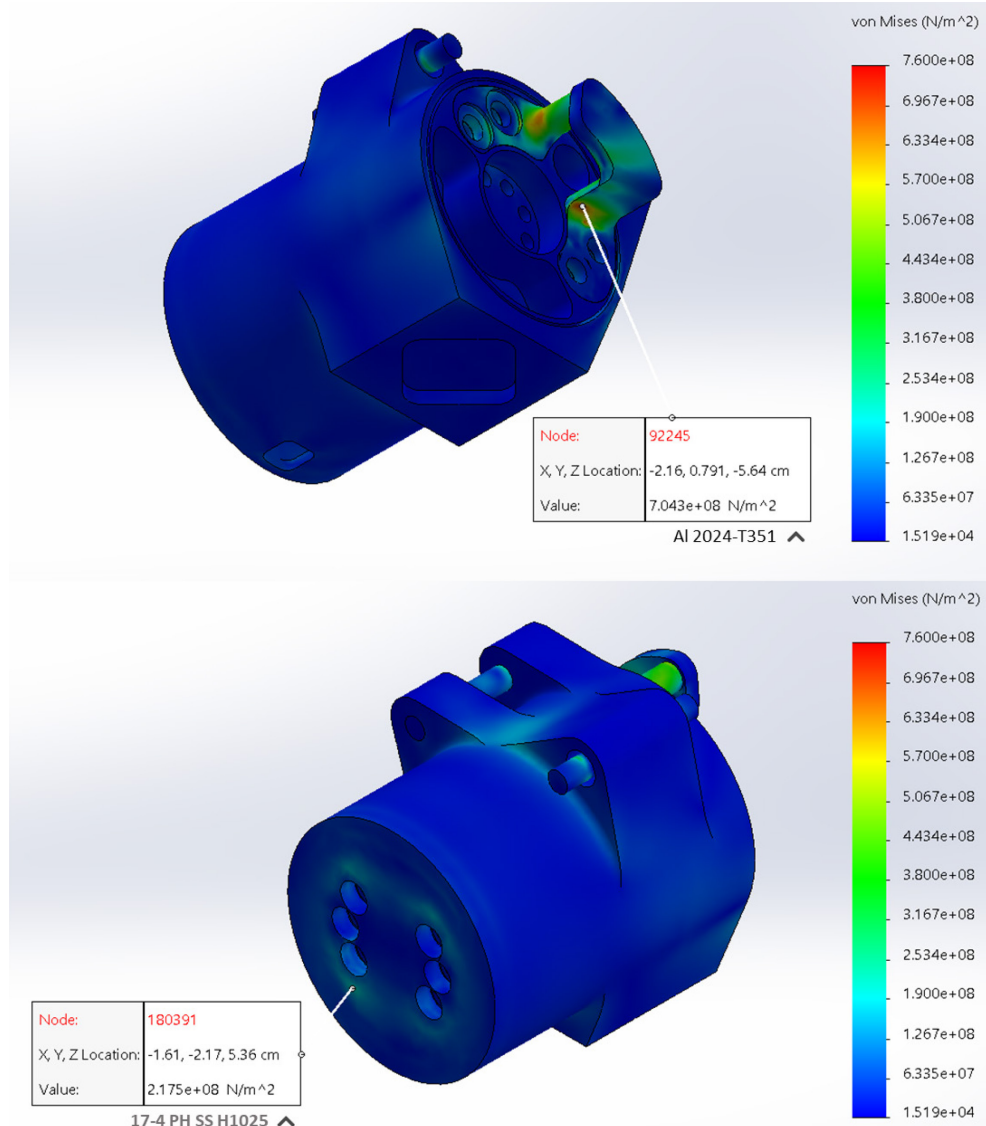


Figure 6-20: Motor unit FEA with motor-only loading: posterior link forces $F_5 = 5533 \text{ N}$ (compression), anterior link force $F_6 = 2310 \text{ N}$ (compression), drive arm force $F_7 = 9599 \text{ N}$ (tension). External maximum von Mises stresses shown for each material.

Posteroinferior shaft and drive arm screw-on loads are transferred to the motor housing when the motor shell contacts the motor housing (Figure 6-21). The medial-lateral location of the contact point was determined by a tighter motor housing inner diameter along the longitudinal axis. FEA iterations informed the contact point to be optimally placed near external features that thickened the motor housing A-P cross-sectional area. This contact point is approximately in the middle of the motor housing medial-lateral length. FEA iterations also informed that a minimum motor housing thickness of 2.6 mm is appropriate for supporting the motor torque load.

The motor acts as a cantilever beam fixed at the motor housing lateral inner surface until the motor shell contacts the motor housing. The tighter the contact surface diameter, the lower the drive arm force needs to be before this contact occurs. A tighter contact surface diameter resulted in lower motor cover stresses but higher motor shell stresses. The contact surface diameter was chosen so that stresses are distributed between the motor cover and the motor shell in a way that keeps stresses below fatigue strengths on respective materials. Furthermore, the contact surface diameter was not too tight as to increase assembly difficulty. The Power Knee 2 motor cover is made of aluminum. However, due to the high stresses induced by the large drive arm force acting at a large moment arm, 17-4 PH SS H900 steel was selected as the motor cover material (though the H1025 condition was used for FEA).

The internal maximum von Mises stress on motor unit parts made of Al 2024-T351 was 288.2 MPa (Figure 6-21), which occurred on the motor shell outer surface with the smaller diameter, resulting in a 2-million cycle fatigue safety factor of 0.86. This safety factor becomes 1 at 364863 load cycles [213]. The internal maximum von Mises stress on motor unit parts made of 17-4 PH SS H1025 was 760.0 MPa (Figure 6-21), which occurred inside the motor cover anterior-inferior thread hole, resulting in a 2 million load cycle fatigue safety factor of at least 0.99 (with the H1150 condition assumed). The H1025 condition is likely to have a 2 million load cycle fatigue safety factor above 1 because H1025 has yield and tensile strengths that are approximately halfway in between the H900 and H1150 conditions [198], and 2 million load cycle fatigue strength is higher for slightly lower heat treatment temperatures [201]. Therefore, the motor unit is likely to support 364863 load cycles under the maximum torque load. Governing safety factors are those corresponding to the internal maximum von Mises stresses because they are larger than the external maximum von Mises stresses. Although a 364863-load cycle fatigue life did not meet the 2 million load cycle fatigue life requirement, this lifespan would be more than adequate for early prototype testing.

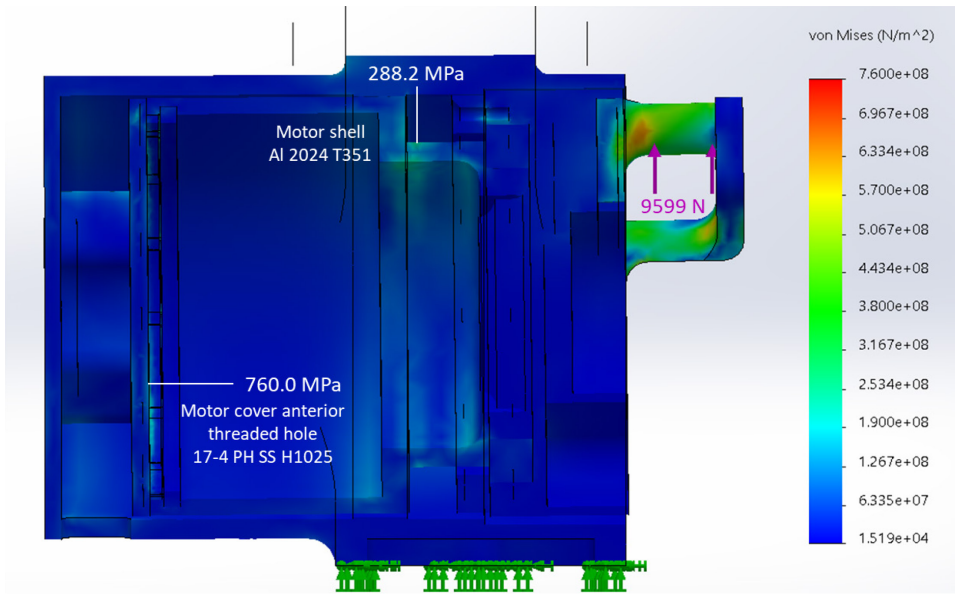


Figure 6-21: Medial-lateral cross-section of motor unit FEA with motor-only loading. Internal maximum von Mises stresses shown for each material.

Table 6-7 lists the governing safety factors for powered hip structural components (not including shafts, bearings, and fasteners). Powered hip structural components are designed to pass ISO 15032:2000 static compression tests and support 364863 strides at maximum motor torque.

Table 6-7: Structural component von Mises stress safety factors for A-P extension, M-L, and motor-only loading.

Load case	Failure mode	Assembly	SF for Al 2024-T351	SF for 17-4 PH SS H1025
A-P extension	Yielding	Upper unit	1.8	-
		Motor unit	-	-
M-L	Yielding	Upper unit	1.74	2.84
		Motor unit	2.50	1.09
Motor-only (2 million cycles)	Fatigue	Upper unit	1.22	≥ 1.95
		Motor unit	0.86	≥ 0.99

Figure 6-22 labels all FEA screw connectors. Table 6-8 lists the governing screw yielding and 1 million load cycle fatigue safety factors which occur in the motor-only load case. The complete table for screw safety factors can be found in Appendix H. Class 12.9 alloy steel screws, with a yield strength of 1100 MPa [214], were implemented in the FEA. High strength screws have a 1 million cycle fatigue strength of at least 825 MPa, 75% of class 12.9 alloy steel yield strength [215]. S-N curves for class 12.9 alloy steel are not available in literature, so exact screw fatigue lives could not be predicted. Nevertheless, all screws are well below yielding.

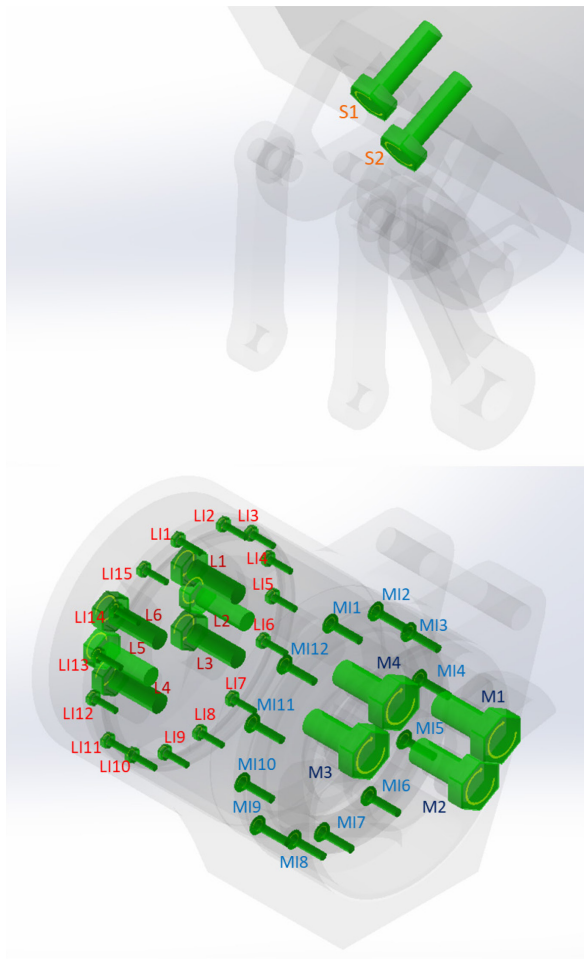


Figure 6-22: Upper unit and motor unit screw connectors: superior screws (S), lateral screws (L), lateral internal screws (LI), medial internal screws (MI), and medial screws (M).

Table 6-8: Screw von Mises stress yielding and 1 million load cycle fatigue safety factors for the governing motor-only load case.

Screw	S1	M4	MI1	LI10	L6
SF (yielding)	4.04	1.22	1.31	1.17	1.45
SF (fatigue)	3.03	0.92	0.98	0.88	1.09

6.6 Deflection Analysis

For uninterrupted motor operation, the drive flange should not contact the motor housing at any point throughout hip motion. The larger the drive arm force (i.e., higher motor torque), the more motor components will bend and the more likely this contact will occur. When the motor is turned off, there is a 0.65 mm gap between the output bearing cover and motor housing, and a 0.90 mm gap between the drive flange and motor housing. At maximum motor torque (i.e., 9599 N drive arm force), these gaps decrease to minimums of 0.21 mm and 0.20 mm, respectively (Figure 6-23) due to the upward displacement of the drive flange relative to the motor housing. Motor housing thicknesses were selected such that gaps between rotating components are approximately the same at maximum motor torque, without taking tolerancing into consideration. The output bearing cover is unmodified from the Power Knee 2 motor and has ± 0.025 mm radial tolerancing. With -0.15 mm radial tolerancing on the drive flange outer radius and +0.15 mm radial tolerancing on the motor housing inner radii (potentially increasing the minimum gaps to 0.51 mm and 0.50 mm), no contact between moving parts is expected between rotating components; thus, the motor, at any torque, is expected to operate without interruption.

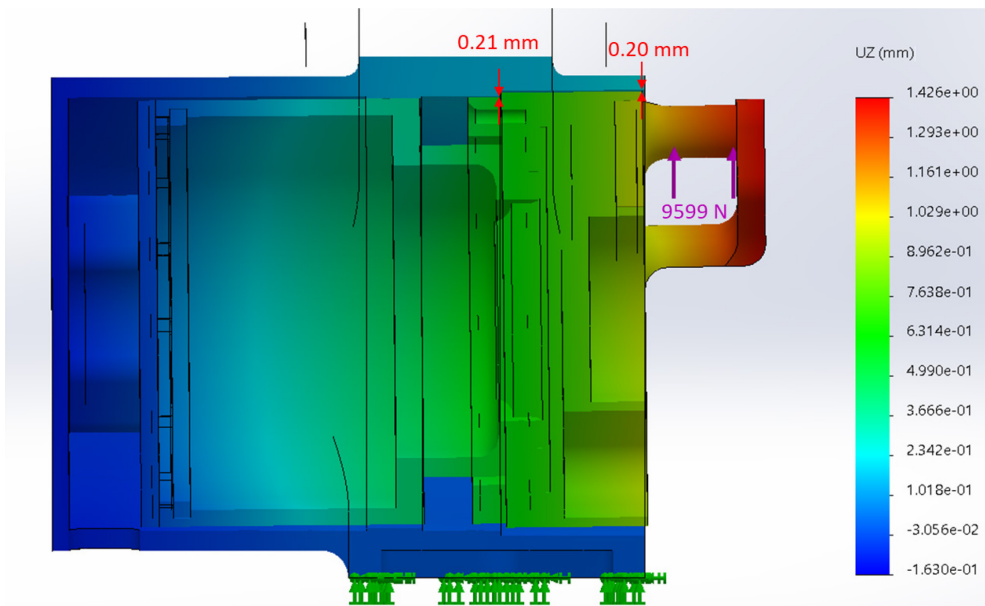


Figure 6-23: Medial-lateral cross-section of motor unit FEA with motor-only loading. Internal upward displacements (UZ) and minimum gaps between rotating parts shown.

The motor unit's maximum upward deflection is 1.426 mm, occurring at the assembly's medial section. The smaller motor housing inner diameter near the middle of the motor medial-lateral length reduces overall motor unit medial deflection because, at a high drive arm force, motor shell contact with the motor housing results in a smaller distance between the bending point and drive arm force (rather than bending point being at the motor cover).

Chapter 7: Bearing Analysis

7.1 Link Bearings

Maximum link bearing radial loads were determined in Chapter 5 and listed in Table 6-2. The bearing static safety factor is defined by Eq. (7-1) and applies to the ISO 15032:2000 compression load cases. C_0 is the radial static load capacity and P_0 is the equivalent radial load.

$$SF = \frac{C_0}{P_0} \quad (7-1)$$

Applying Eq. (7-1) to the previously determined maximum radial loads provides link bearing static safety factors (Table 7-1). All static safety factors are above 1, meaning that the link bearings can support ISO 15032:2000 loading and motor-only loading at max torque.

Table 7-1: Link bearing static safety factors.

Component	Bearing	Rad. stat. load cap.	Max radial load	Static SF
Posterior link	INA HN0808 [204] (two at each end)	13400 N [204]	10284 N	1.30
Anterior link	INA HN0808 [204] (one at each end)	6700 N [204]	6697 N	1.0004
Drive arm	Koyo B-68 [205] (one at each end)	11788 N [205]	9599 N	1.23

Roller bearing life at 90% reliability is defined by Eq. (7-2) and applies to the motor-only load case. C is the radial dynamic load capacity and P is the equivalent dynamic radial load.

$$L = \left(\frac{C}{P}\right)^{\frac{10}{3}} \times 10^6 \text{ rev} \quad (7-2)$$

Applying Eq. (7-2) to the posterior link, anterior link, and drive arm in the motor-only load case provides link bearing lives at 90% reliability Table 7-2).

Table 7-2: Link bearing lives at 90% reliability for the motor-only load case.

Component	Bearing	Radial dynamic load capacity	Radial load at 96 N·m	Life
Posterior link	INA HN0808 [204] (two at each end)	10000 N [204]	5533 N	7191140 cycles
Anterior link	INA HN0808 [204] (one at each end)	5000 N [204]	2310 N	13117772 cycles
Drive arm	Koyo B-68 [205] (one at each end)	8185 N [205]	9599 N	587907 cycles

The governing link bearing fatigue life is the drive arm bearing fatigue life of 587907 cycles under maximum motor torque. This is more than enough load cycles for early prototype testing, despite not meeting the 2 million cycle fatigue life requirement.

7.2 Output Bearing

Initially, the motor was assumed to be a black box with internal components that can handle the full 96 N·m motor torque regardless of geometry or torque transmission method. However, this assumption overlooked the robustness of internal motor components in the powered hip's torque transmission system, different than that of the Össur Power Knee 2. The drive arm's medial offset relative to the output bearing creates a bending moment on the output bearing compromising output bearing integrity under the maximum motor torque (Figure 7-1). The output bearing is an unmodified component inside the Power Knee 2 motor.

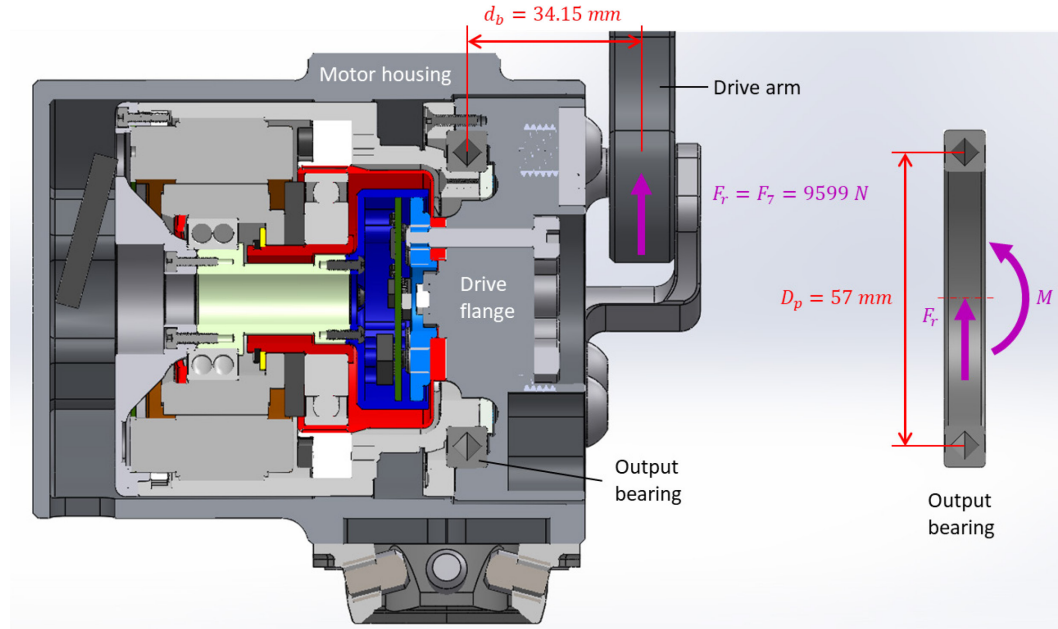


Figure 7-1: Motor unit medial-lateral cross-section demonstrating the drive arm bending effect on the output bearing due to the drive arm force.

The output bearing equivalent static radial load P_0 includes both the drive arm force and the bending moment caused by the drive arm force acting at a distance $d_b = 34.15 \text{ mm}$ (Eq. (7-3)). The bearing has a pitch diameter of $D_p = 57 \text{ mm}$ [216]. X is the dynamic radial factor and Y is the dynamic axial factor [216]. X is set to 1 and Y is set to 0.45 since an axial load of zero was assumed (i.e., $F_a = 0$) [216].

$$P_0 = X \left(F_r + \frac{2M}{D_p} \right) + YF_a \quad (7-3)$$

Bending moment M was calculated as follows.

$$M = F_r d_b \quad (7-4)$$

From Eq. (7-3) and (7-4), M is 328 N-m and P_0 is 21101 N. Applying Eq. (7-1) with a radial static load capacity $C_0 = 7190$ N results in a 0.34 static safety on the output bearing (unsafe).

Output bearing static permissible moment M_0 is given by Eq. (7-5) and was 205 N-m, which is well below the output bearing bending moment at maximum motor torque (unsafe).

$$M_0 = \frac{C_0 D_p}{2} \quad (7-5)$$

To achieve an output bearing static safety factor of 1, equivalent static radial load P_0 cannot exceed the radial static load capacity of 7190 N. Combining Eq. (7-3) and (7-4) and rearranging gives an expression for the output bearing radial load that achieves a static safety factor of 1.

$$F_r = \frac{P_0 D_p}{D_p + 2d_b} \quad (7-6)$$

From Eq. (7-6), the output bearing radial load F_r should not exceed 3271 N.

Output bearing life is defined by Eq. (7-7) [216]. f_T is the temperature factor accounting for decreasing performance at higher temperatures [216]. f_W is the load factor account for decreasing performance at higher levels of impact [216]. f_T was set to 1 because the powered hip operates at room temperature [216]. f_W was set to 1.5, the upper limit recommended for normal motion since repetitive foot strikes during walking constitute loading with moderate impact [216].

$$L = \left(\frac{f_T C}{f_W P} \right)^{\frac{10}{3}} \times 10^6 \text{ rev} \quad (7-7)$$

With a radial dynamic load capacity $C = 5100$ N [216], and $P = 7190$ N, output bearing life is 82382 revolutions. This new governing fatigue life is still adequate for early prototype testing. The motor's full torque ($(T_{mx})_{full}$) is 96 N-m. However, the motor should not output a torque that causes the drive arm force to exceed 3271 N. Maximum allowable motor torque ($T_{mx})_{allow}$, a function of hip flexion angle θ_{flex} , is expressed as follows.

$$(T_{mx})_{allow} = \begin{cases} \frac{(F_r)_{allow}}{F_r(\theta_{flex})} (T_{mx})_{full} & \text{if } F_r > (F_r)_{allow} \\ (T_{mx})_{full} & \text{if } F_r \leq (F_r)_{allow} \end{cases} \quad (7-8)$$

$F_r(\theta_{flex})$, a function of hip flexion angle θ_{flex} , is the resulting output bearing radial load under the full 96 N-m motor torque. Applying Eq. (7-8) to the powered hip gives $(T_{mx})_{allow}$ as a function of θ_{flex} , as illustrated in Figure 7-2.

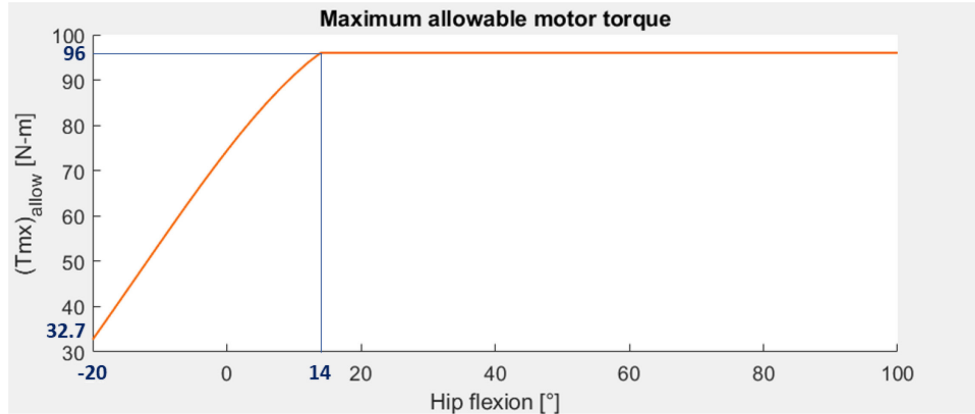


Figure 7-2: Maximum allowable motor torque for safe operation as a function of hip flexion angle.

The motor can operate at its full 96 N-m torque from 14° hip flexion to 100° hip flexion. From 14° hip flexion to the full 20° hip extension, the maximum allowable motor torque decreases approximately linearly until 32.7 N-m at full hip extension.

From Eq. (7-4), the output bearing bending moment M is 127.1 N-m when $(F_r)_{allow}$ is 3271 N. M is far below $M_0 = 205 \text{ Nm}$, indicating that the output bearing will not fail due to bending when the radial load is 3271 N.

This bearing analysis was performed on the assumption that the output bearing translation and rotation are rigidly fixed (i.e., the bearing is locked in place by a surrounding material that is infinitely stiff). A rigid fixed output bearing would absorb 100% of the radial force and bending moment applied to it. However, the output bearing is not surrounded by an infinitely stiff material and is kept in place by an aluminum bearing cover and an aluminum drive flange. Al 2024-T351 is elastic compared to hard metals such as 17-4 PH SS H1025 and M2 HSS. Aluminum's elasticity absorbs some of the equivalent static load applied to the output bearing. Therefore, the load on the output bearing is likely lower than predicted meaning that if motor torque slightly exceeds 32.7 N-m, failure is unlikely.

Chapter 8: Prototype

This chapter presents the powered four-bar hip prototype. An earlier 3D printed prototype is discussed in Appendix G. The 3D printed prototype was not used in walking tests but informed design considerations leading up to the prototype that was used for walking tests.

The powered four-bar hip prototype was constructed based on linkage optimization iteration 179, with link dimensions listed in Table 4-5 and Table 4-6. Assembly drawings are presented in Figures 8-1 to 8-3. Mechanical components are listed in Table 8-1. The posterior, anterior, and superior links, motor housing, drive arm, and drive flange are made of Al 2024-T351, whereas the motor cover and drive arm screw-on pieces are made of 17-4 PH SS H900. Despite its more brittle nature, the H900 condition was used instead of the H1025 assumed in the FEA model due to its higher yield and 2-million cycle fatigue strengths. For the superior link, drive arm screw-on, and output bearing cover screw sets, class 10.9 screws (940 MPa yield strength [214]) were used due to class 12.9 screws (1100 MPa yield strength [214]) not being readily available. This change in screw strength did not affect powered hip performance because fatigue life was governed by the output bearing (82382 load cycles), followed by the motor shell (364863 load cycles).

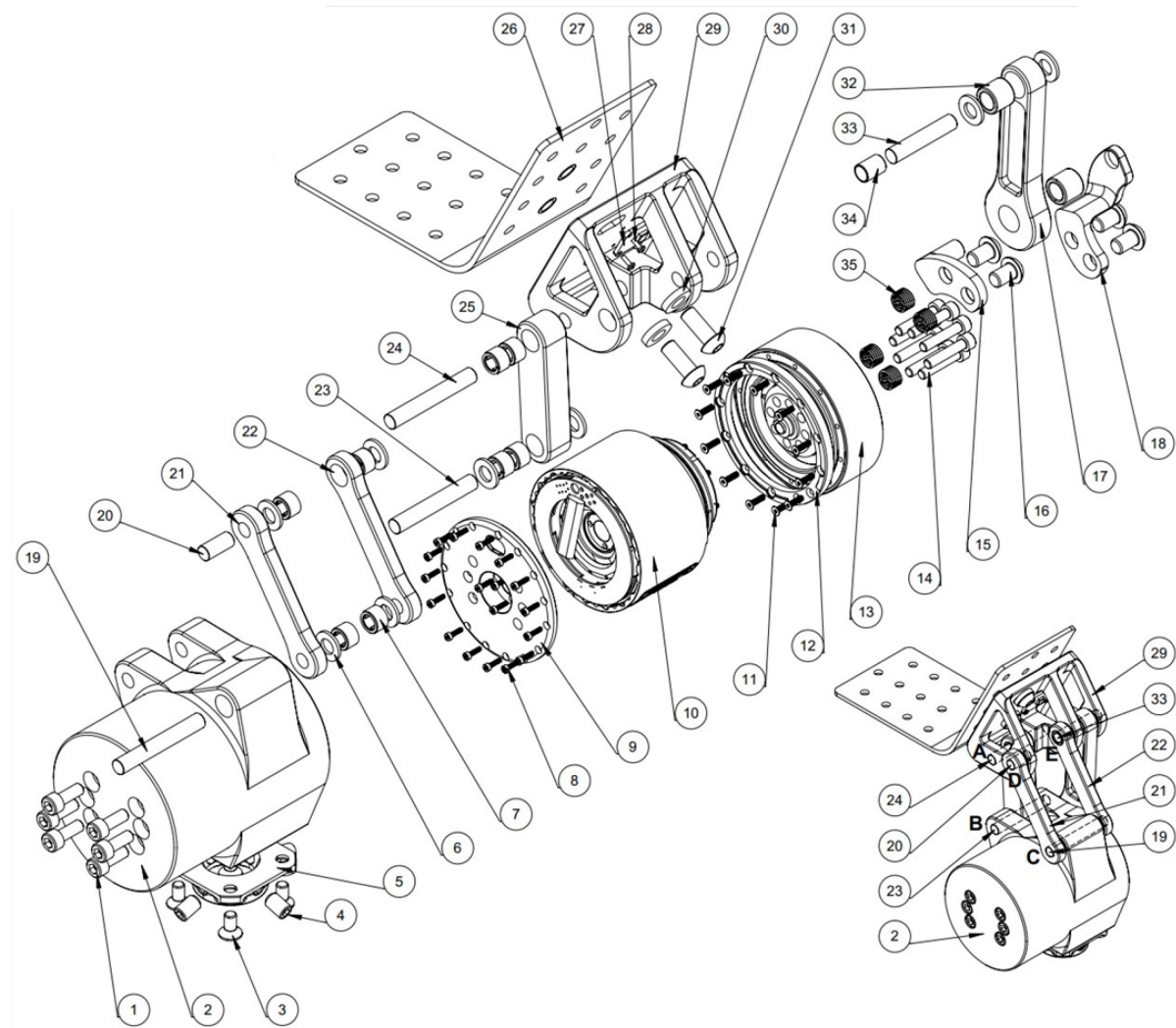


Figure 8-1: Lateral isometric view of powered four-bar hip prototype. Parts are listed in Table 8-1.

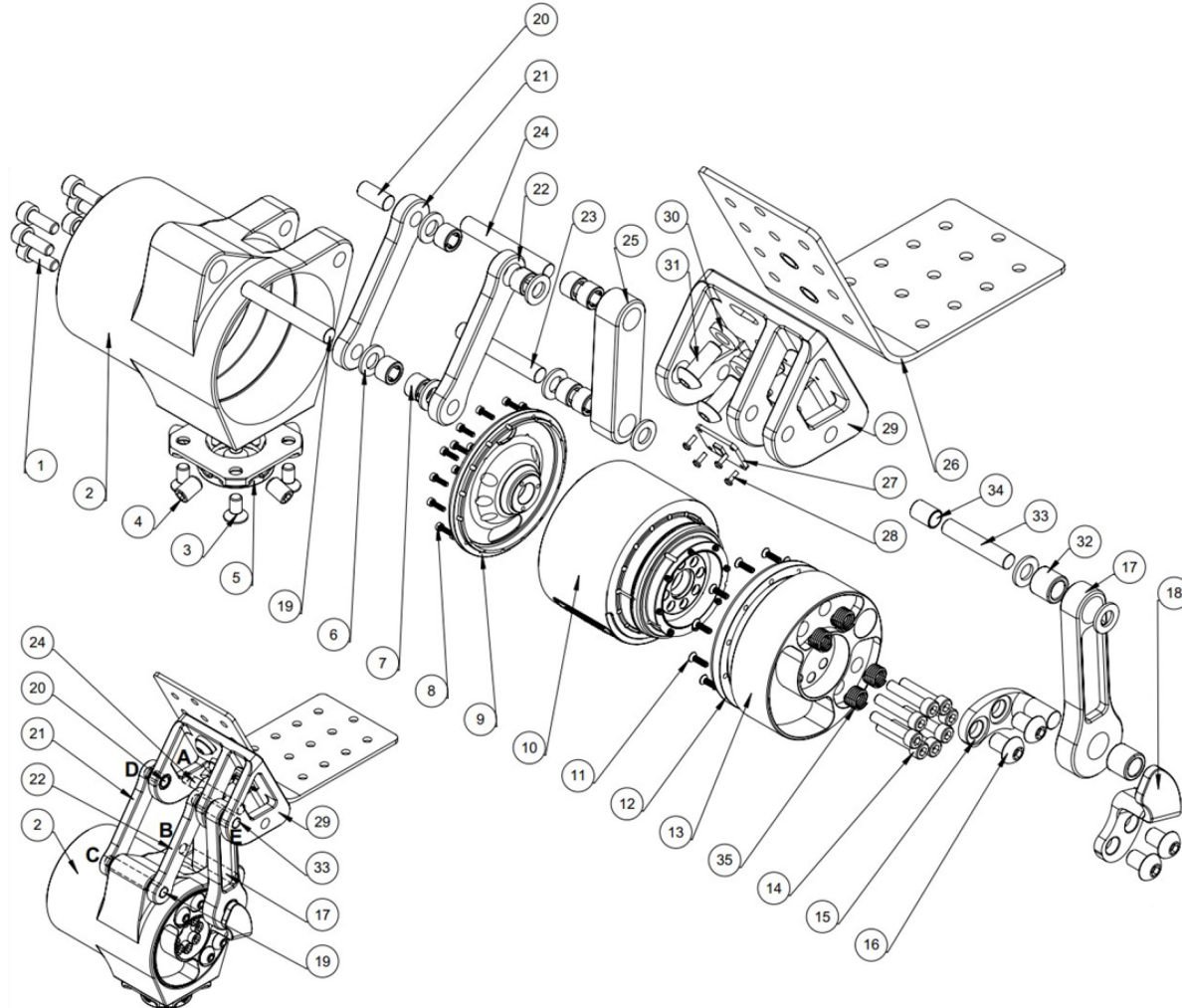


Figure 8-2: Medial isometric view of powered four-bar hip prototype. Parts are listed in Table 8-1.

Table 8-1: List of mechanical components in powered four-bar hip prototype.

Item	Description	Qty
1	Motor housing hex socket head cap screws (M6 x 1.0 x 16)	6
2	Motor housing	1
3	Female adapter flat head socket cap screws (M6 x 1.0 x 12)	4
4	Female adapter flat point set screws (M8 x 1.0 x 12)	4
5	Aluminum female adapter	1
6	M8 flat plastic washer	8
7	INA HN0808 drawn cup needle roller bearing	8
8	Motor cover hex socket head cap screws (M2 x 0.4 x 8)	18
9	Stainless steel motor cover	1
10	Power knee 2 DC motor	1
11	Output bearing cover socket flat head cap screws (M2.5 x 0.45 x 10)	12
12	Output bearing cover	1
13	Drive flange	1
14	Drive flange hex socket head cap screws (M5 x 0.8 x 25)	8
15	Drive arm screw-on inside half	1
16	Hex socket button head cap screws for drive arm screw-on (M8 x 1.25 x 12)	4
17	Drive arm	1
18	Drive arm screw-on outside half	1
19	Anteroinferior shaft	1
20	Lateral anterosuperior shaft	1
21	Lateral anterior link	1
22	Medial anterior link	1
23	Posteroinferior shaft	1
24	Posterosuperior shaft	1
25	Posterior link	1
26	Lamination plate	1
27	IMU BNO055	1
28	IMU Phillips pan head machine screws (M2 x 0.4 x 6)	4
29	Superior link	1
30	M8 flat oversized stainless-steel washer	2
31	Superior link hex socket button head cap screws (M8 x 1.25 x 20)	2
32	Koyo B-68 drawn cup needle roller bearing	2
33	Medial anterosuperior shaft	1
34	Drive arm bushing	1
35	M8 x 1.25 x 8 stainless steel helicoil	4

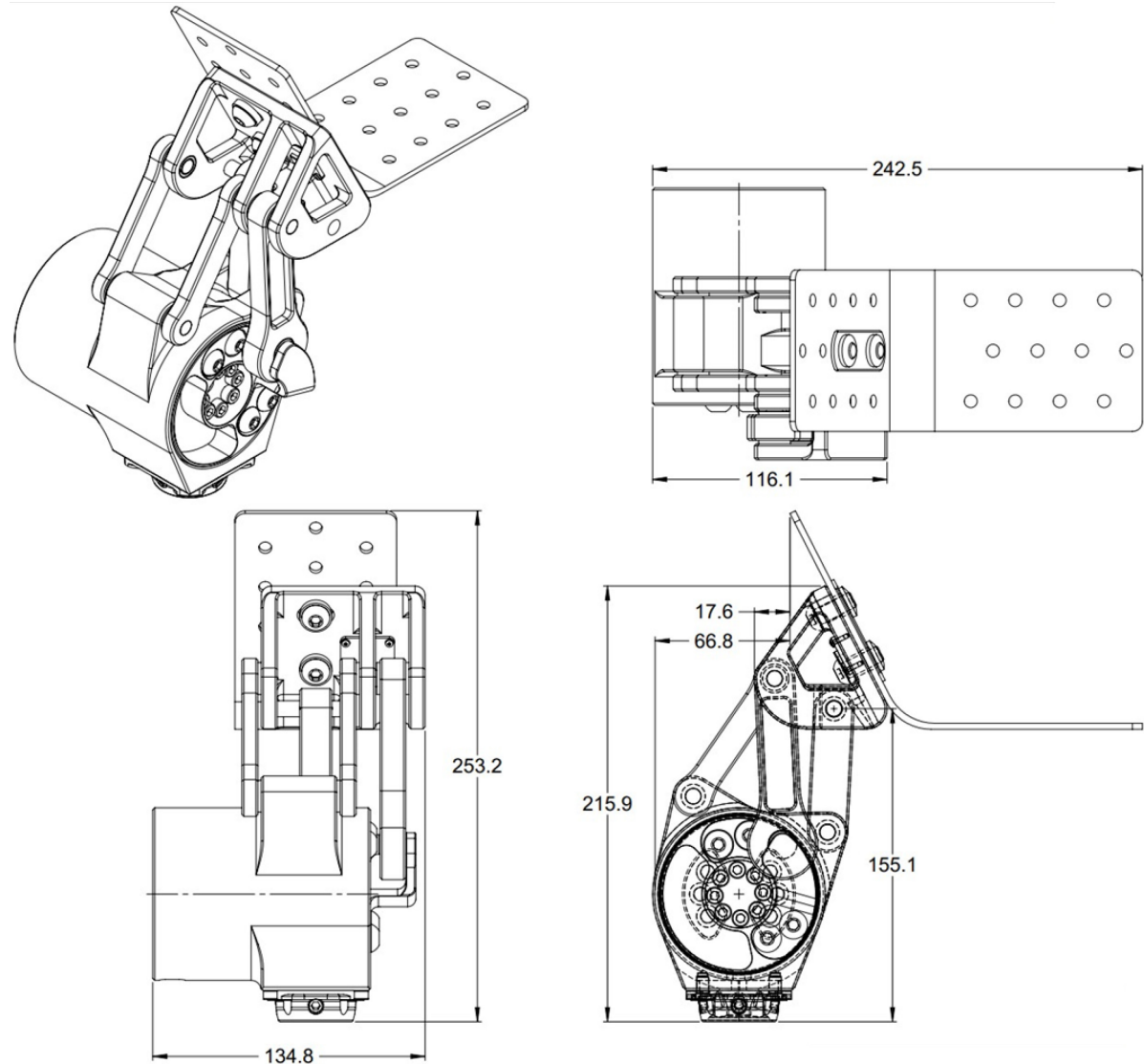


Figure 8-3: Powered four-bar hip prototype orthogonal views in third angle projection. Dimensions in mm.

The powered hip dimensions from below the posterosuperior pivot are 11.61 cm x 13.48 cm x 15.51 cm, meeting the requirement of fitting within a 17 cm x 17 cm x 17 cm box. Sizing of individual components can be found in the complete set of drawings in Appendix I.

Figure 8-4 illustrates the sitting and standing configurations of a HKAFP containing the powered four-bar hip prototype. The prototype has a superior protrusion of 11.51 cm in the sitting position, thereby meeting the cosmetic requirement of not protruding superiorly in the sitting position by more than 17 cm. Furthermore, the prototype allows for normal sitting with no bulge from below the socket causing the user to be uncomfortable in the seat. However, the 6.68 cm anterior protrusion in the standing position does not meet the 2 cm cosmetic requirement for anterior protrusion. HD and

HP amputees may see a slight anterior bulge through their clothing if they were to use the prototype. Future prototypes could improve the anterior cosmesis.

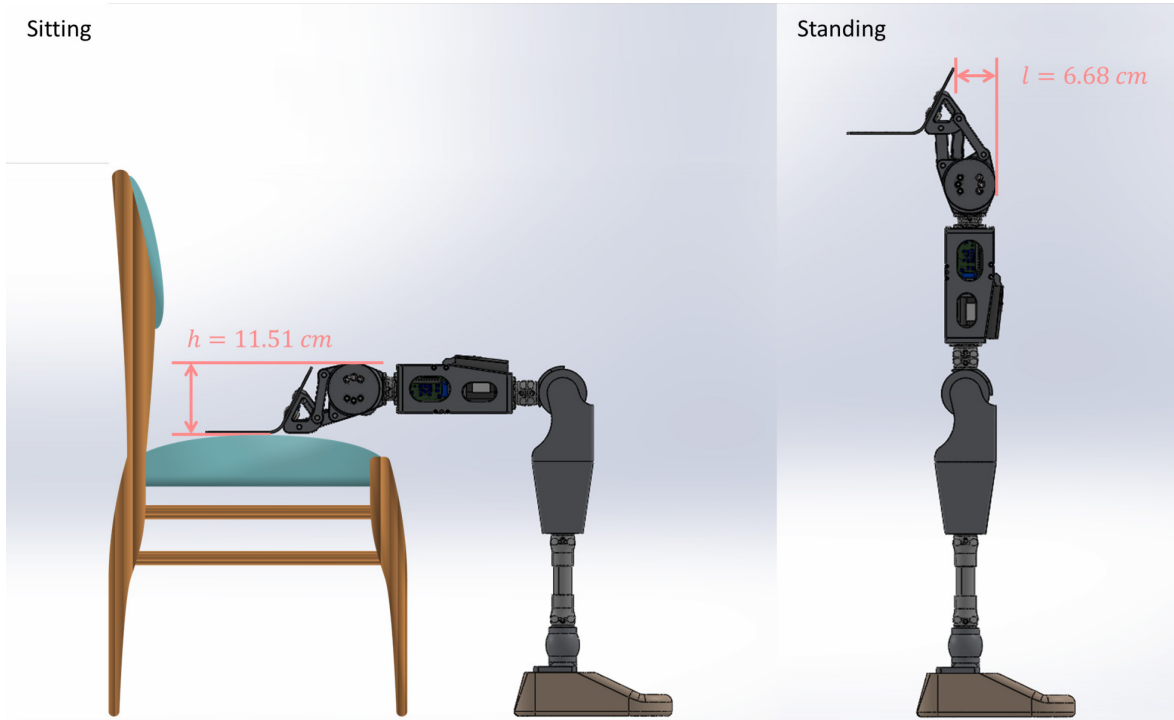


Figure 8-4: Powered four-bar hip protrusions when integrated in a hip-knee-ankle-foot prosthesis. Sitting and standing positions shown. No sitting interference.

Computer numerical control (CNC) machined powered hip components are displayed in Figure 8-5. Most parts were machined from Al 2024-T351 with a B75 Rockwell hardness, easily machinable with a standard CNC drill. Fewer parts were machined from 17-4 PH SS H900 with a C40 Rockwell hardness, more difficult than aluminum to machine with a standard CNC drill but still doable. No parts contained overlapping geometry blocking drill access to part features. Parts were designed to minimize the number of drill orientations required for machining. Most parts required one to three drill orientations. The superior link required six drill orientations due to its more complex geometry. All parts were successfully machined in one attempt.



Figure 8-5: Powered hip CNC machined components. The superior link, drive arm, anterior links, posterior link, drive flange, and motor housing are made of Al 2024-T351. The drive arm screw-on pieces, and motor cover are made of 17-4 PH SS H900.

Dimensional tolerancing costs increase exponentially as tolerances decrease [217]. Össur recommended general fits to be ± 0.3 mm which is 20% of the cost of machining at ± 0.03 mm [217]. Tighter fits were assessed based on ISO 2768-1 for linear and angular dimensions [218], [219], and ISO 286-1 and ISO 286-2 for dimensions pertaining to shafts, holes, and bearings [220], [221].

ISO 2768-1 indicates a medium tolerance of ± 0.3 mm for linear dimensions between 30 mm and 120 mm (range for most powered hip dimensions) [218]. This tolerance aligned with Össur's recommendation, so drawings indicated dimensions with ± 0.3 mm tolerance, unless otherwise indicated. The standard indicates a medium tolerance of ± 0.2 mm for linear dimensions between 6 mm and 30 mm [218]. This tolerance applied to inertial measurement unit (IMU) screw hole locations on the superior link.

ISO 2768-1 indicates a fine tolerance of ± 0.15 mm for linear dimensions between 30 mm and 120 mm [218]. This fine tolerance applied to link lengths because small changes in link lengths resulted in noticeable changes in hip kinematic and kinetic behaviour (as observed during the link length optimization process). The standard indicates a fine tolerance of ± 0.1 mm for linear dimensions of

between 6 mm and 30 mm [218]. Drive arm screw-on dimensions were within this range. This fine tolerance promoted good contact between the screw-on shaft and the screw-on cylindrical cavity, thereby achieving a balanced force distribution between both drive arm screw-on halves.

ISO 2768-1 indicates fine and medium tolerances of 0.5° for shorter angle side lengths of between 10 mm and 50 mm (i.e., most corresponding side lengths) [219]. This angular tolerance applied to angular dimensions indicating screw hole locations.

A P7/h6 shaft-basis interference fit was selected for shafts, bearings, and their respective holes. As per ISO 286-1, the shaft-basis system keeps the shaft diameter fixed and offers various smaller hole diameters that can achieve an engineering fit [220]. Here, the shaft-basis system was chosen because it allows for press-fitting into multiple coaxial holes while ensuring that the shaft does not exceed the bearing's bore diameter. With the selected P7/h6 interference fit, parts can be assembled via cold pressing with small to moderate forces (no need for hot pressing and/or large forces) [222].

A H7/h6 hole-basis clearance fit was selected for the drive arm screw-on pieces and the drive arm bushing. As per ISO 286-1, the hole-basis system keeps the hole diameter fixed and offers various larger shaft diameters to achieve an engineering fit [220]. This clearance fit allows the drive arm screw-on pieces to be easily assembled by hand without a press and adequate contact between cylindrical surfaces for load transfer. This clearance fit also allows the bushing to be easily inserted onto the medial anterosuperior shaft yet have a snug fit onto the shaft. Here, the hole-system was chosen because it guarantees that the screw-on shaft will simultaneously slide into the coaxial drive arm bearing and the screw-on cylindrical slot for the shaft. Furthermore, the hole-basis system is more economical than the shaft-basis system, so the hole-basis system is used unless otherwise necessary [220].

ISO 286-2 provides the tolerance values for the P7/h6 interference fit and H7/h6 clearance fit with respect to diameter ranges [221]. These values are listed in Table 8-2. The drive arm screw-on shaft has a 9.525 mm diameter. All other shafts have an 8 mm diameter. Drawn cup needle roller bearing manufacturers do not provide outer bearing diameter tolerancing. Thus, bearing interference fit was controlled with only the P7 interference fit.

Table 8-2: ISO 286-2 hole and shaft tolerances for 6 to 10 mm and 10 to 18 mm diameter ranges.

Diameter range	Components	Hole tolerance		Shaft/bearing tolerance	
6 to 10 mm	All shafts	P7	-0.024 to -0.009 mm	h6	-0.009 to 0.000 mm
		H7	0.000 to +0.015 mm		
10 to 18 mm	All drawn cup needle roller bearings	P7	-0.011 to -0.029 mm	h6	-0.011 to 0.000 mm

The smallest tolerance value is 9 μm . A 4.5 μm surface roughness average (R_a) reduces a hole's diameter by 9 μm , on average. All metal cutting operations are, on average, able to commonly achieve a surface finish of $R_a = 4.5 \mu\text{m}$ or smoother [223]. Therefore, no additional surface finishing operations were specified for all CNC machined parts.

Following CNC machining, the Power Knee 2 motor was disassembled and reassembled with the new motor cover and new drive flange (Figure 8-6). Medial screws, connecting the drive flange to the harmonic drive, were torqued to 14.1 N-m. The micro-axial cable was connected to the angle sensor embedded within the motor. The signal cable was connected to the motor processing unit that takes commands from a separate circuit board within the chassis. The power wires were connected to the electromagnetic coil within the stator. As indicated in assembly drawings (Figures 8-1 and 8-2), helicoils could have been inserted into the drive flange to provide extra thread strength. However, the drive flange for this prototype did not include helicoils because the motor was controlled to stay well below its torque capacity, thereby removing the need for helicoils.

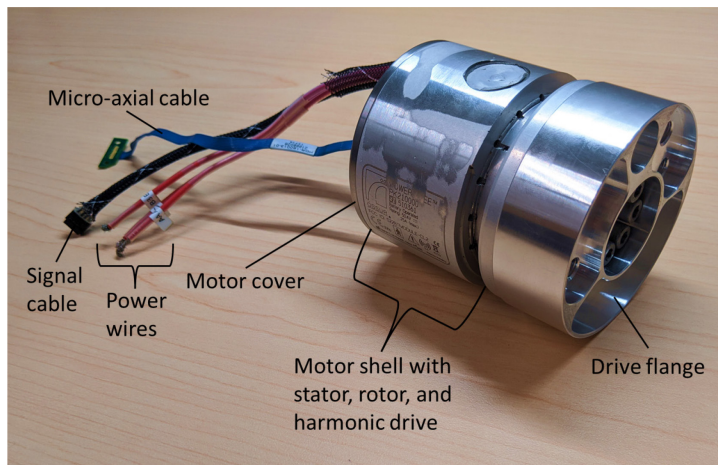


Figure 8-6: Powered hip motor assembly.

The reassembled motor, weighing 1.484 kg, was inserted into the motor housing. Screws were inserted through the lateral side of the motor housing into the thread holes of the motor cover, fastening the motor to the motor housing. These lateral screws were torqued to 7.1 N-m. The drive arm screw-on and drive arm were then simultaneously fastened to the drive flange. Drawn cup needle roller bearings were pressed into their designated locations (Figures 8-1 and 8-2). The anteroinferior shaft was pressed into the anterior link distal ends and motor housing anterosuperior portion simultaneously (locking anterior link translation relative to the motor housing). Then, the posteroinferior shaft was pressed into the posterior link and posterosuperior portion of the motor housing simultaneously (locking posterior link translation relative to the motor housing). Furthermore, the posterosuperior and anterosuperior shafts were pressed through the proximal ends of the anterior links, posterior link, and

drive arm, and through superior link holes simultaneously (locking superior link translation and completing the linkage). A thin 17-4 PH SS H900 bushing was inserted on the M2 HSS medial anterosuperior shaft so that the proximal drive arm bearing can fit snugly onto the shaft. This approach was preferred over machining the shaft out of 17-4 PH SS H900 (too weak) or M2 HSS (too hard). The powered hip joint (Figure 8-7), without the lamination plate, adapters, and associated hardware, has mass of 2.676 kg.



Figure 8-7: Powered four-bar hip joint.

Pressing forces were calculated to assess the feasibility of hand pressing components at room temperature and to determine the friction forces locking medial-lateral translation between components. Each pressing force was required to overcome static friction between mating components. Each press-fit resulted in an interference pressure p acting on components with a diametrical interference δ as defined by Eq. (8-1) [224], [225].

$$p = \frac{\delta}{\frac{D}{E_o} \left(\frac{D_o^2 + D^2}{D_o^2 - D^2} + \nu_o \right) + \frac{D}{E_i} \left(\frac{D^2 + D_i^2}{D^2 + D_i^2} - \nu_i \right)} \quad (8-1)$$

Instead of machining 17-4 PH SS H900 shafts with h6 tolerancing, ready-made M2 HSS shafts with -0.005 to 0.000 mm tolerance were purchased. With P7 hole tolerancing, δ ranged from 0.004 to 0.024 mm. D is the shaft or hole nominal diameter. All shafts had $D = 8 \text{ mm}$. D_o is the outer diameter of material surrounding the shaft (assumed to be the smallest width of material surrounding the shaft if this material did not have a cylindrical form). All surrounding material had $D_o = 20 \text{ mm}$. D_i is the

shaft inner diameter. All shafts were solid ($D_i = 0\text{mm}$). E_o and ν_o are the surrounding material elastic modulus and Poisson ratio. E_i and ν_i are the shaft elastic modulus and Poisson ratio (Table 8-3).

Table 8-3: Elastic moduli and Poisson ratios for interference fit materials.

Material	Elastic modulus	Poisson ratio
Al 2024-T351	73.1 GPa [199]	0.33 [199]
M2 HSS	200 GPa [202]	0.285 [202]

Press forces F_p were required to overcome static friction between components, under the interference pressure p , moving against each other over cylindrical contact area A . l is the interference length along the shaft axis. Coefficient of static friction μ_s between aluminum and steel (dry contact) was taken as the lower end value of 0.45 [226]. This μ_s conservatively estimates the friction force locking component medial-lateral translation after assembly (a lower friction force is a more conservative estimate).

$$A = \pi Dl \quad (8-2)$$

$$F_p = \mu_s p A \quad (8-3)$$

Table 8-4 presents the ranges of required cold pressing forces to insert shafts in their designated locations. Pressing forces ranged from 1676 N to 43008 N. On average, pressing forces were expected to be halfway in between the respective minimums and maximums. All press fits were accomplished at room temperature with a standard arbor press. The minimum 1676 N pressing force exceeded the expected 334 N medial-lateral force component in the ISO 15032-200 M-L loading condition, guaranteeing that the shafts will not translate when structurally tested.

Table 8-4: Ranges of expected pressing forces for powered hip assembly at room temperature.

Shaft	Mating component	Min pressing force	Max pressing force
Posterosuperior	Superior link	5365 N	32193 N
Posteroinferior	Motor housing	7168 N	43008 N
Anteroinferior or lateral anterosuperior	Anterior link	1676 N	10060 N
Medial anterosuperior	Superior link	3353 N	20120 N

Ideally, interference fits should not cause materials to plastically deform. Plastic deformation for an interference fit was assessed by comparing the weaker material's interfacial von Mises stress to the material's yield strength. For interference fits, the weaker material was Al 2024-T351 surrounding

the shaft. At the shaft-hole interface, Al 2024-T351 experiences compressive radial stress σ_r (Eq. (8-4)) and tensile circumferential stress σ_θ (Eq. (8-5)) [224], [225].

$$\sigma_r = -p \quad (8-4)$$

$$\sigma_\theta = p \left(\frac{D_o^2 + D^2}{D_o^2 - D^2} \right) \quad (8-5)$$

An element directly above the shaft, σ_r can be treated as the stress in the vertical direction (σ_z) and σ_θ can be treated as the stress in the horizontal direction (σ_y). Applying Eq. (6-1) to the element gives an expression for the element's von Mises stress (σ_v).

$$\sigma_v = \sqrt{\sigma_r^2 - \sigma_r\sigma_\theta + \sigma_\theta^2} \quad (8-6)$$

Due to variance of diametrical interference, the von Mises stress at each hole interface ranges from 38.8 to 230.2 MPa, well below the Al 2024-T351 yield strength of 310 MPa. Therefore, all press-fitting operations were within the elastic deformation stress range, facilitating prototype disassembly and reassembly if required. Furthermore, remaining within the elastic deformation range guaranteed that no permanent damage was done to components during powered hip assembly.

Figure 8-8 illustrates the full prosthetic thigh unit with the powered four-bar hip and the electronics and battery chassis. The prosthetic thigh weighs 4.337 kg, exceeding the 3.2 kg device mass requirement. The powered four-bar hip was connected to the chassis by male and female pyramid adapters. The motor cables and wires were soldered or plugged into their designated locations on circuits boards enclosed within the chassis. Chassis development is not within the scope of this thesis.



Figure 8-8: Powered four-bar hip with chassis containing the battery and electronics.

A gait cycle motor torque control algorithm (described in Section 9.2) was implemented into the command-processing circuit board contained within the chassis. With the control algorithm, the hip was able to rotate to 100° flexion and 20° extension, matching the 120° ROM prediction in Chapter 4. However, during control system testing, it was observed that the motor, with enough torque, could still rotate CCW beyond the hip extension singularity point, causing the mechanism to stall. It was hypothesized that the gap between the drive flange and the motor housing provided enough space for the motor to be pushed slightly downward, allowing it to pass through the hip extension singularity point. A software stop was implemented so that the motor would not rotate too far CCW.

Chapter 9: Evaluation

This chapter covers the powered hip structural and functional tests carried out to demonstrate that the powered hip can safely support level-ground walking for a 100 kg person. Test results have been parsed with the ‘Evaluation.m’ MATLAB program (Appendix B.8).

9.1 Static Compression Testing

ISO 15032:2000 is the only engineering standard for prosthetic hip joint structural testing. As discussed in Section 5.1, the standard suggests applying a static 3360 N compressive force in different orientations to test hip joint strength in the sagittal and frontal planes. The suggested load applies a 3.43 safety factor for a person weighing 100 kg. Therefore, ISO 15032:2000 static compression tests were performed on the powered hip as a conservative evaluation for powered hip joint strength under body weight only. This evaluation was a prerequisite for walking tests (Section 9.2) in which the powered hip supported body weight and motor torque simultaneously.

The powered hip static compression test procedure was a simplification of the static failure test procedure outlined in ISO 15032:2000 and consisted of the following [186]:

1. Install the prosthetic thigh in the uniaxial mechanical loading machine with appropriate lever arms.
2. Compress the hip to the 50 N stabilizing force.
3. Compress the hip joint to the 1024 N settling force and hold the force for 30 s before off-loading to the 50 N stabilizing force.
4. Compress the hip joint to the ductile failure ultimate test force of 3360 N and as soon as this peak force is reached, off-load the hip to the 50 N stabilizing force.

Figure 9-1 represents the change in force over time during compression testing. Loading and off-loading were carried out at 200 N/s, within the loading rate range of 100 N/s to 250 N/s recommended by the standard [186].

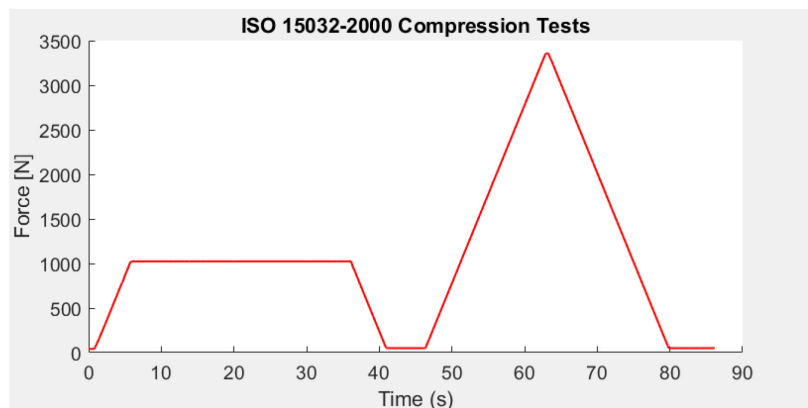


Figure 9-1: Powered hip compression test force-time profile.

Two configurations were tested: A-P extension with the hip fully extended and medial-lateral force alignment with the hip and knee (Figure 9-2), and M-L with the hip fully extended but with a medial-lateral force offset relative to the hip and knee (Figure 9-3). Appropriate hip and knee moment arms L_H and L_K were achieved with end attachments each consisting of two perpendicular cylindrical poles. The poles were tightened at distances specified in Figures 9-2 and 9-3. No battery was included in the chassis because no motor power was required for static compression testing.

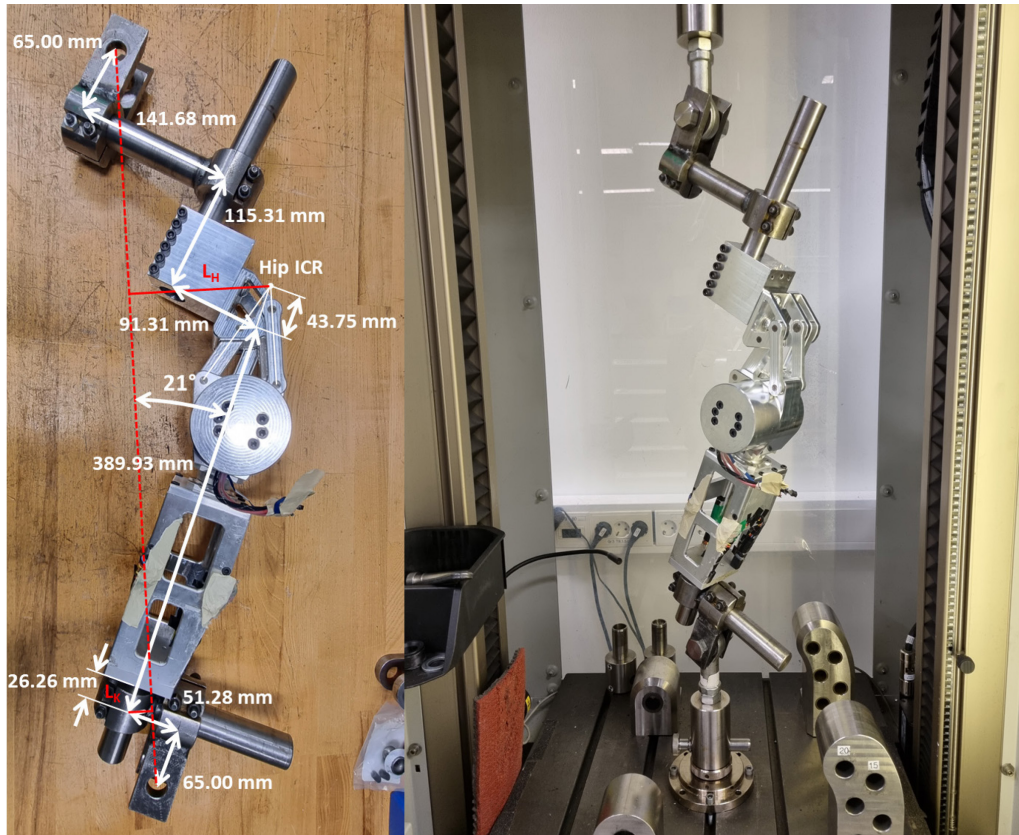


Figure 9-2: Powered hip A-P extension static compression test setup. Setup resulted in hip moment arm $L_H = 134.79 \text{ mm}$ and knee moment arm $L_K = 23.93 \text{ mm}$.

The standard suggests a more gradual approach for applying the compressive force so that relative movement between components due to low friction and deformation of weaker components could be detected well before the ultimate test force is reached [186]. Simplifications to the A-P extension and M-L static failure tests outlined in ISO 15032:2000 were that the prosthetic thigh was not kept at rest for 15 min at zero force after the off-loading of the stabilizing force, and that moment arms L_H and L_K were measured and adjusted only at the beginning of the procedure before any loads were applied (not also after the off-loading of the stabilizing force). These simplifications resulted in scenarios with a more aggressive application of the load to the prosthetic thigh and therefore more conservative structural testing.

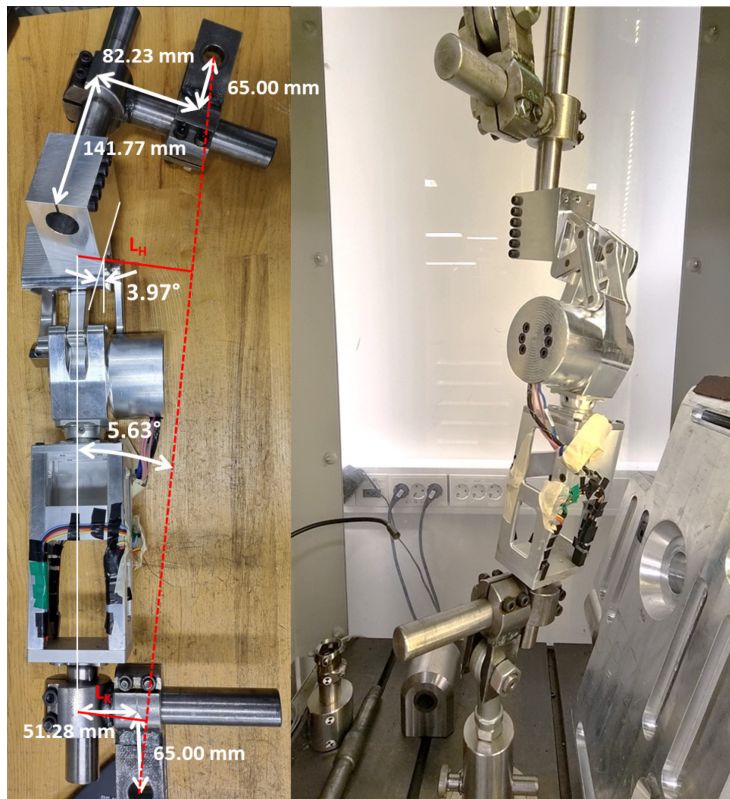


Figure 9-3: Powered hip M-L static compression test setup. Setup resulted in hip moment arm $L_H = 99.96 \text{ mm}$ and knee moment arm $L_K = 57.41 \text{ mm}$.

ISO 15032:2000 recommends moment arms $L_H = 78 \text{ mm}$ and $L_K = 63 \text{ mm}$ for the A-P extension test condition, and moment arms $L_H = 86 \text{ mm}$ and $L_K = 47 \text{ mm}$ [186]. To achieve these moment arms while maintaining the standard-recommended force directions, the thigh needed to be 400 mm long [186]. However, the minimum possible thigh length (length between the hip and knee) that could be achieved with the powered four-bar hip and chassis was 433.68 mm (Figure 9-2). Thus, the powered hip A-P extension and M-L configurations had moment arms that were different than the standard. Both configurations maintained the standard-recommended force directions, but the configurations had larger than recommended L_H values and lower than recommended L_K values. Therefore, these configurations placed larger bending stresses near the powered hip itself and less-so near the bottom of the chassis, thereby making the powered hip structural tests even more conservative. The chassis, by itself, had previously passed separate static compression tests (chassis design and evaluation was carried out by another MSc student in the research group) and was not within the scope of the powered four-bar hip project.

The uniaxial mechanical loading machine applied compression to the prosthetic thigh by keeping the lower attachment fixed and pushing downward on the upper attachment. Force and displacement were measured with sensors integrated in the uniaxial mechanical loading machine.

Force-displacement profiles were plotted for A-P extension compression (Figure 9-4) and M-L compression (Figure 9-5). These profiles include only the rising portion of the compressive force from the 50 N stabilizing force to the 3360 N ultimate test force.

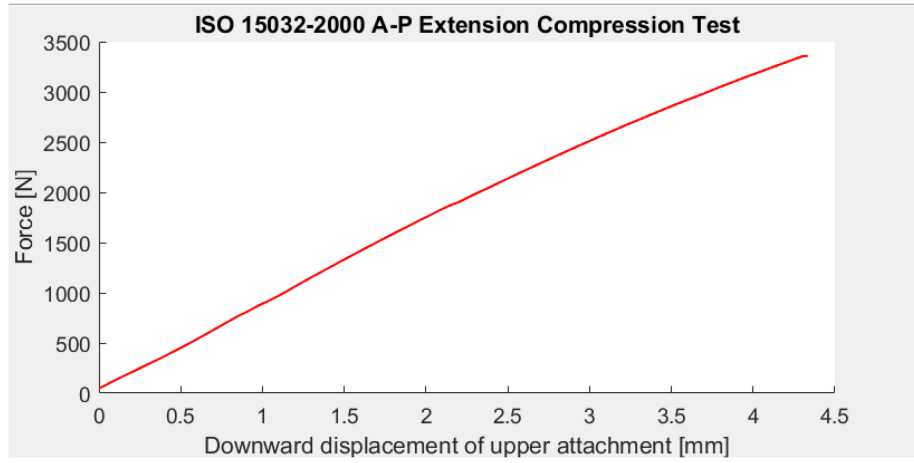


Figure 9-4: Powered hip A-P extension compression test force-displacement profile.

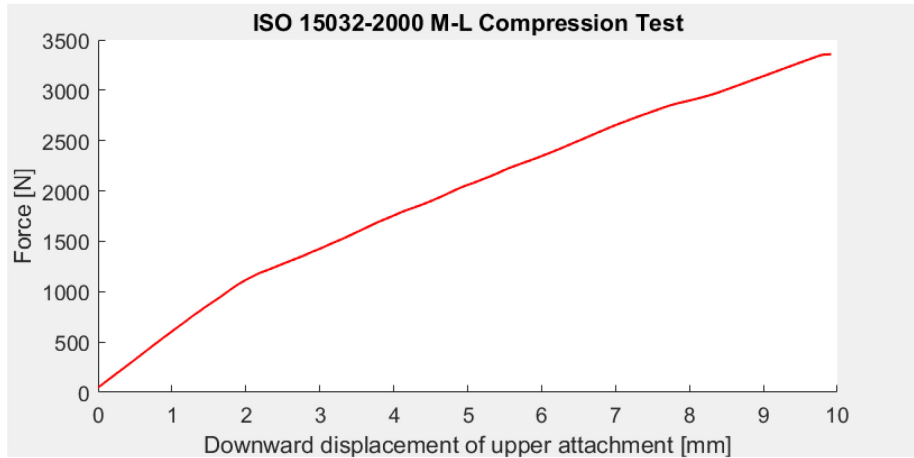


Figure 9-5: Powered hip M-L compression test force-displacement profile.

The prosthetic thigh is mainly composed of Al-2024 T351 and 17-4 PH SS H900, both of which are linear elastic and ductile materials. Figures 9-4 and 9-5 show that the compressive force-displacement profiles remained approximately linear for both the A-P extension and M-L tests. After each test, the powered hip was thoroughly inspected for distorted geometry, newly formed gaps, and cracks, but none were found. Thus, prosthetic thigh did not yield during static compression testing.

The 3360 N compression resulted in a 4.3 mm upper attachment downward displacement for the A-P extension test and a 9.9 mm upper attachment downward displacement for the M-L test. The greater displacement was observed during the M-L test because there was slight frontal plane rotation between the upper attachment and the superior link, and between the powered hip and chassis. This rotation occurred due to insufficient friction between components for them to be held perfectly still

during the tests. An approximate estimate for the displacement strictly due to frontal plane rotation between components is the 5.6 mm difference between the M-L and A-P extension displacements. This extra displacement did not greatly affect the hip and knee moment arms and thus, the M-L test results were still valid for interpretation.

The slight frontal plane rotation between components also resulted in the M-L force-displacement profile to be less linear than the A-P extension force-displacement profile. However, both force-displacement profiles did not contain a portion that tapers off (sharply decreasing in rate of change) as one would expect in a stress-strain curve beyond the yield point. Therefore, it was reasonable to conclude that the prosthetic thigh remained in its elastic region during both the A-P extension and M-L static compression tests, thereby satisfying the ISO 15032:2000 strength requirements for supporting a 100 kg person.

9.2 Functional Testing

Structural tests showed that the powered hip can support 100 kg at full extension without motor power. Functional tests followed to determine if the powered hip can support level walking (ideally for people weighing up to 100 kg).

Walking tests were completed by three male able-bodied participants wearing a HKAFF simulator [227], placing the HKAFF lateral to the person's right leg (Figure 9-6). The participants were 177.7 ± 2.5 cm tall, weighed 96.00 ± 1.73 kg, and averaged 33.3 ± 10.0 years.

The simulator consisted of the Orthomerica Newport 3 hip abduction orthosis [228]; a HKAFF containing the powered four-bar hip, Rheo Knee [8], and Pro-Flex ST foot [229]; an adapter connecting the HKAFF to the hip abduction orthosis; straps holding the body to the orthosis; and a holster to hold a smartphone for collect pelvic motion data collection. A shoe with a thicker midsole was worn on the sound side and the HKAFF was configured to be slightly longer than the biological leg so that the biological leg on the prosthetic side was 4 cm above the ground. This setup allowed for an able-bodied person to walk like a hip-level amputee while achieving prosthetic side single-limb support. A cane was optionally used to aid with medial-lateral balance during prosthetic side single-limb support. This experimentation method has been approved by the University of Ottawa Office of Research Ethics and Integrity (Appendix J).

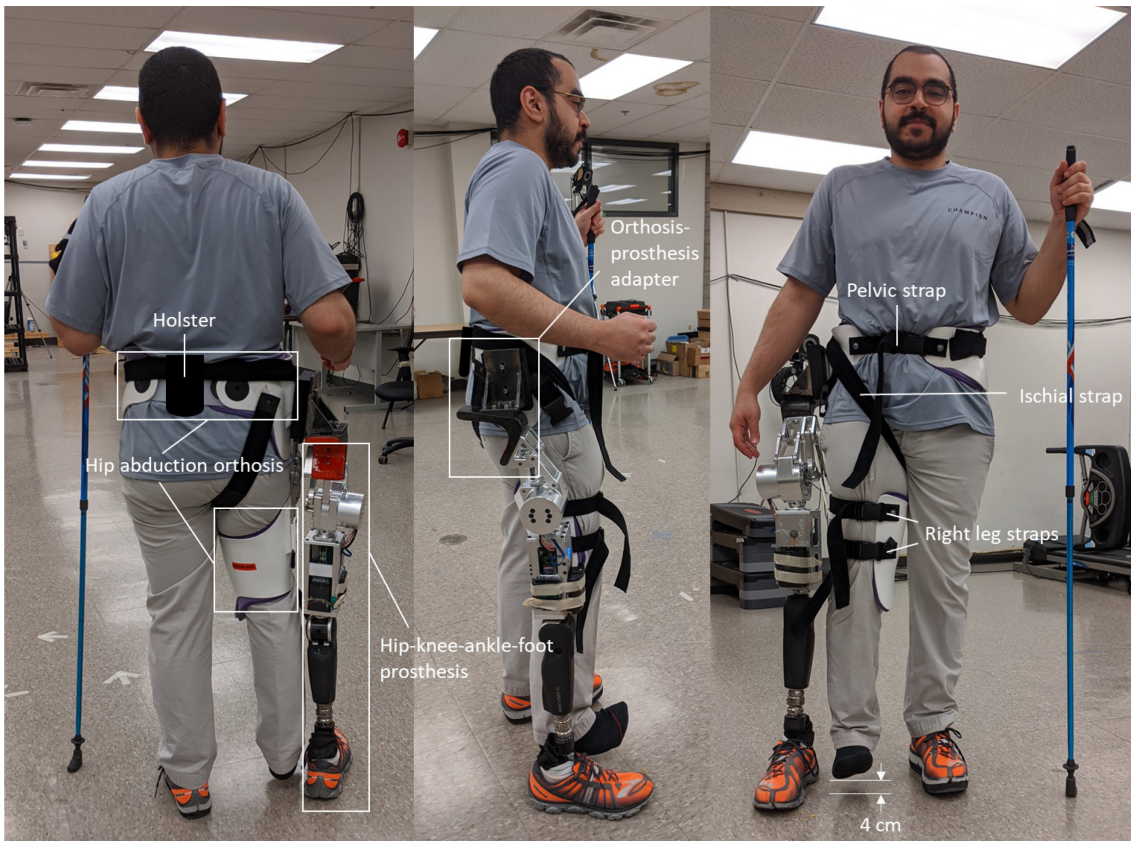


Figure 9-6: Hip disarticulation prosthesis simulator with full lower-limb prosthesis containing the powered four-bar hip.

Each participant completed one walking trial which consisted of walking back and forth in a straight line on a 10-m walkway (i.e., walking 20 m in total). Prior to data collection, participants learned to walk with the HD prosthesis simulator with a preliminary control system implemented into the powered hip. At the start of walking, the control system flexed the hip to the maximum hip flexion angle required for comfortable gait. When the participant touched the ground with the prosthetic leg, the control system extended the powered hip. Powered hip flexion-extension angle and angular velocity during stance were directly proportional to how much body weight was placed on the prosthetic limb and for how long. When the participant removed their body weight from the prosthesis, the control system flexed the hip to initiate swing. Upon the completion of swing, the hip had returned to its fully flexed position in preparation for the next stride. During the gait training process, control system parameters were adjusted to achieve toe off timing and hip flexion-extension velocities that were comfortable for each participant. Control system design and testing were carried out by a PhD student in the research group and were therefore not included in this thesis.

On average, each participant had completed ten hours of gait training on the HD prosthesis simulator before data collection with the powered four-bar hip. Two of the ten hours were spent

learning to walking with the powered four-bar hip. The other eight hours were spent walking with other hip joints including the 7E7, Helix3D, and two other powered hip joints developed by other MSc students in the research group. Participants mentioned that previous gait training with other hip joints had facilitated gait training with the powered four-bar hip.

Pelvic motion was captured with the DataLogger smartphone application, with the smartphone attached to the posterior pelvis. Each walking trial was captured on smartphone video, using a separate phone. For each walking trial, the powered hip angle sensor collected hip motor angle data and the Rheo Knee angle sensor collected knee flexion-extension angle data. The video clips were imported into the Kinovea software to extract spatiotemporal parameters. Kinematic data were taken from the DataLogger and Össur software. Spatiotemporal results are listed in Table 9-1 and prosthetic leg kinematic results are presented in Figure 9-7. All three participants successfully completed 20 strides. Ten steady-state strides were selected for each participant.

Participants employed gait compensation mechanisms while attempting to walk with the HD prosthesis simulator in an energy-efficient way. Gait compensation mechanisms included circumduction, whipping, increased abduction, lateral trunk bending, and anterior trunk bending.

Despite the attempted gait compensations, participants still showed gait asymmetries such as a shorter average prosthetic step length than the average sound step length and a shorter prosthetic side single-support time than sound side single-support time, and decreased walking speed. The average early-stance double-support time was slightly greater than the average late-stance double-support time. The average sound step length was slightly greater than the average prosthetic step length indicating some degree of spatial step symmetry despite the lack of temporal step symmetry.

Of the three participants, participants 1 and 2 had better gait symmetry than participant 3. Participants 1 and 2 had smaller differences between sound and prosthetic side single-limb support times than participant 3. Furthermore, participants 1 and 2 had smaller differences between sound and prosthetic step lengths.

Table 9-1: Spatiotemporal results for powered four-bar hip level-walking tests. Mean plus-minus one standard deviation shown for each participant and for the ensemble.

Participant	Early-stance double-support time (s)	Prosthetic side single-support time (s)	Late-stance double-support time (s)	Sound side single-support time (s)	Sound step length (m)	Prosthetic step length (m)	Cadence (steps/min)	Walking speed (m/s)
1	0.42 ± 0.06	0.23 ± 0.03	0.38 ± 0.05	0.60 ± 0.06	0.43 ± 0.08	0.42 ± 0.04	77 ± 17	0.52 ± 0.05
2	0.46 ± 0.03	0.25 ± 0.03	0.42 ± 0.04	0.56 ± 0.04	0.45 ± 0.07	0.43 ± 0.04	73 ± 12	0.52 ± 0.07
3	0.63 ± 0.13	0.24 ± 0.04	0.56 ± 0.09	0.74 ± 0.07	0.41 ± 0.06	0.28 ± 0.05	59 ± 15	0.32 ± 0.06
Ensemble	0.50 ± 0.12	0.24 ± 0.03	0.46 ± 0.10	0.63 ± 0.10	0.43 ± 0.07	0.38 ± 0.08	69 ± 17	0.45 ± 0.11

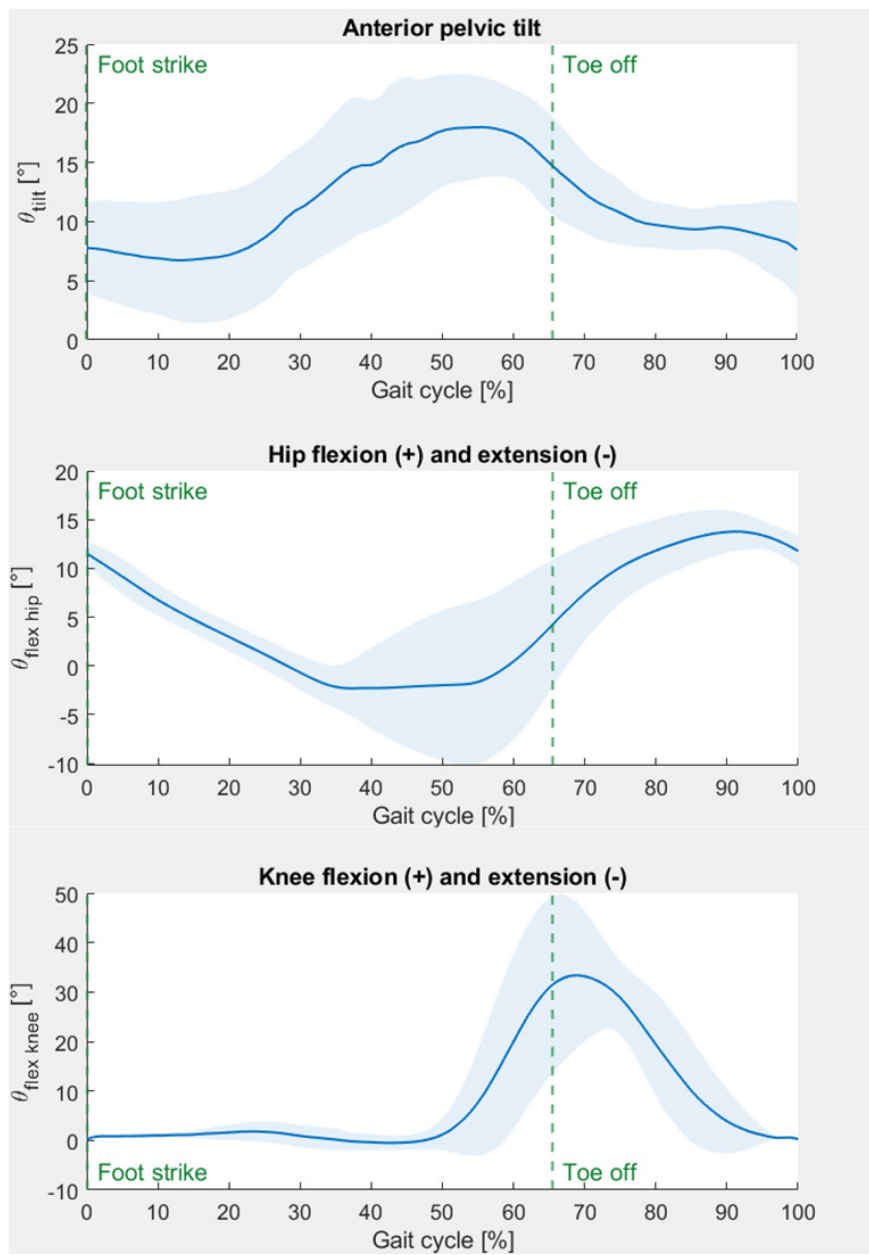


Figure 9-7: Ensemble average across all participants for pelvic tilt, prosthetic side hip and knee flexion-extension angles for level-walking. Mean plus-minus one standard deviation.

On average, participants walked at 0.45 m/s, approximately one third the normal walking speed of 1.39 m/s [230]. It was observed that participants were more comfortable walking with smaller steps (0.4 m on average, 56% the length of a normal 0.72 m step [230]). In addition, the average 69 steps/min cadence was slower than the normal 100 steps/min cadence for moderate intensity walking [231]. These observations were hypothesized to be caused by the lack of gait training with the prosthesis. Amputees may require gait re-training to achieve optimal mobility with the powered hip [232].

Furthermore, a well-fitting prosthesis should provide better device control than the simulator; therefore, better results could be anticipated when evaluating gait with hip-level amputees.

Participants were trained with the powered four-bar hip for only 2 hours prior to their walking trials. Participants learned to walk stably with a passive hip joint by maintaining their COM posterior to the hip and anterior to the knee during early-stance, and posterior to both the hip and knee during late-stance. The larger the prosthetic step, the further in front the knee was relative to the hip, thereby reducing prosthetic limb stability. Ideally, a person using the HD prosthesis simulator containing a powered hip would trust the motor to provide this stability and not feel the need to compensate by bending their trunk and/or tilting their pelvis. However, participants carried their passive hip walking gait compensation habits to their walking trials with the powered four-bar hip, as seen by noticeable trunk and pelvic motions. To reduce the severity of gait compensations (increasing gait smoothness), participants walked with smaller steps and slower cadence (reducing the abruptness of each foot strike).

Smaller step lengths corresponded to smaller changes in joint angles during each stride. On average, the hip rotated between 13.8° flexion and 2.3° extension (16.1° total rotation), and the knee rotated between 33.4° flexion and 0.5° extension (33.9° total rotation). These joint rotation values were smaller than those reported in literature for able-bodied people, TF amputees, and HD/HP amputees (Figures 2-21 and 2-22). Different people require different lengths and types of gait training to achieve a certain gait performance level. Higher levels of gait performance are indicated by gait that maintains constant support times, cadence, step length and joint angles between steps, and is symmetric or almost symmetric between sound and prosthetic limbs. Large swing phase hip and knee flexion-extension standard deviations were observed due to various levels of gait performance participants.

Of the three participants, participant 2 showed the best gait performance due to the smallest standard deviations in support times, cadence and step length, and the smallest difference between sound and prosthetic side single-limb support times and step lengths. Additionally, participant 2 had the fastest average walking speed (tied with participant 1).

Participants showed increased anterior pelvic tilt relative to able-bodied people (Figure 2-21). On average, anterior pelvic tilt varied from 6.7° to 18.0° (11.3° total rotation). Anterior pelvic tilt was a gait compensation mechanism to increase lower-limb stability during early stance (if participants could not fully trust the motor to provide adequate lower-limb stability). Furthermore, it was hypothesized that the control system set the hip extension resistance to be higher than what it should have been for ideal gait performance. Hip extension resistance was increased to give each participant a greater sense of stability during mid to late stance. However, the HKAfp was not moving backward as far as it could have during late stance. Therefore, it was hypothesized that participants tilted their pelvis forward (with the 18.0° peak occurring during late stance) to continue the backward motion of

the prosthetic leg. These outcomes support the need for further development of the control system. For example, a lower hip extension resistance would likely reduce the anterior pelvic tilt magnitude because more of the prosthetic leg's backward motion would be coming from the powered hip.

Nevertheless, the powered hip kinematic profiles throughout gait (Figure 9-7) resembled the HD amputee kinematics profiles seen in literature (Figures 2-21 and 2-22). On average, at the beginning and end of each stride, the anterior pelvic tilt was at its minimum, the hip was fully flexed, and the knee was fully extended. In between late stance and early swing, the anterior pelvic tilt was at its maximum, the hip was fully extended, and the knee was fully flexed. Thus, walking trials demonstrated that a successful gait pattern can be achieved with the powered four-bar hip.

Furthermore, a wedge was inserted between the aluminum and carbon fiber components of orthosis-prosthesis adapter (Figure 9-6). This wedge tilted the superior link anteriorly causing neutral position (i.e., standing) to be further into hip flexion. The wedge was advantageous because it brought the hip further away from its extension singularity point, thereby increasing the average mechanical advantage during gait. Another advantage from the wedge was that it increased the maximum allowable torque since the neutral position was, on average, pushed to 11.8° hip flexion relative to the original neutral position, thereby increasing the maximum allowable torque from 70 N-m to 90 N-m during push-off (Figure 7-2). The disadvantage of this shift in neutral position was a decrease in mechanical advantage for higher hip flexion angles and a 11.8° in the overall hip flexion range, but these decreases were not problematic for the level-walking trials conducted.

Able-bodied walking with the HD prosthesis simulator poses one major difference compared to HD amputee walking. When a person uses the HD prosthesis simulator, their prosthetic leg is further away from the body's natural COM location than their sound leg. Consequently, the moment arm between the prosthetic leg and the COM is larger in able-bodied walking than HD amputee walking. This increased moment arm causes a medial-lateral asymmetry between prosthetic and sound legs that increases the difficulty of maintaining medial-lateral balance during prosthetic side single-limb support. Furthermore, the increased moment arm increases frontal plane bending moments between components and, in turn, increases the pin medial-lateral forces. The lateral placement of the HKAFP on the HD simulator was hypothesized to cause the 1 mm medial-lateral translation of anterosuperior pins (Figure 9-8). Tighter press-fits (e.g., hot press-fits), circlips, or male-female threaded pin connectors would likely reduce or eliminate the medial-lateral pin translation. Nevertheless, the powered four-bar hip would likely perform better when tested with HD/HP amputees due to medial-lateral symmetry between prosthetic and sound legs.

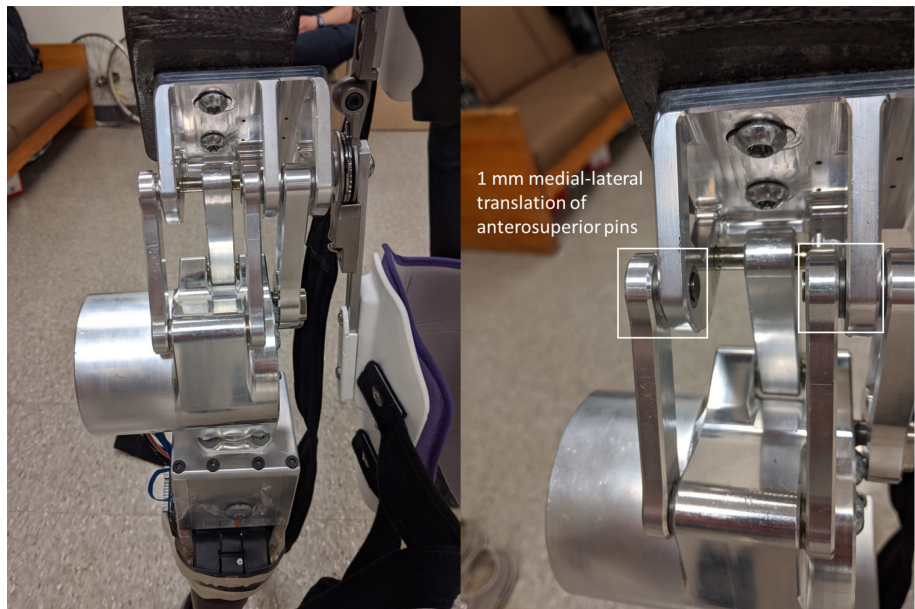


Figure 9-8: Medial-laterally translated anterosuperior pins observed after the completion of level-walking trials with three able-bodied participants.

After level-walking trials were completed, the powered hip was inspected for signs of failure (i.e., cracks and geometric distortion). None were found. All participants successfully produced a level-walking gait pattern for at least 10 strides (without touching the ground on the prosthetic side during prosthetic single-limb support). The powered hip successfully supported a 98 kg person (the heaviest participant) during level-walking. Furthermore, participants expressed that due to augmenting moments coming from the actuator, the powered hip did not feel heavy during gait.

Chapter 10: Summary and Conclusions

This thesis narrates the development of the first powered four-bar hip joint to assist people with HD or HP amputations. The powered hip passed ISO 15032:2000 static compression tests and successfully provided level-ground walking with a HKAFP simulator. Research has demonstrated that the powered four-bar hip is safe for use and viable for further testing.

Hip joints on the market are passive. Most users of passive hip joints have a slow, inefficient gait due to the need for pelvic tilt and rotation to propel their prosthetic limb forward. HD and HP amputees with passive hip joints often face challenges when maintaining lower limb stability due to the lack of musculature and actuator power.

To address these challenges, a powered four-bar hip joint was successfully designed, prototyped, and tested. Össur's Power Knee 2 harmonic drive DC motor was integrated into the hip joint body. The powered hip provides augmenting torques to increase prosthetic limb propulsion and enhance stance-phase limb stability. This should lead to faster, more efficient, and more stable gait than currently available passive hip joints.

The powered hip consists of two linkages: a four-bar linkage that guides hip flexion and extension, and a torque transmission linkage that pushes against the superior link to initiate hip flexion or extension. The motor is screwed to a cylindrical housing that interfaces to an electronics chassis with the use of pyramid adapters. The powered hip and electronics chassis form the prosthetic thigh which interfaces to a knee-ankle-foot prosthesis.

Link lengths were optimized through an iterative process of solving geometric relationships at linkage singularity points and determining the mechanical advantage and link forces at different inputted hip joint and actuator ranges of motion. The optimized linkage configuration achieved large mechanical advantages (up to 164%) within the walking hip flexion-extension range while avoiding overly large link forces (9599 N maximum) and providing an adequate overall hip flexion-extension range and an acceptable cosmesis (fits under clothing with slight anterior bulge). Furthermore, the optimized linkage configuration places the hip ICR anterior to the socket for most of stance phase, thereby enhancing stance-phase limb stability.

Powered hip force analysis was based on three loading scenarios: the 360 N ultimate static compression load recommended by ISO 15032:2000 applied in two different orientations and the 96 N-m maximum motor torque. Link forces were determined by applying static equilibrium equations to each powered hip component. The link forces were inputs to SolidWorks FEA models. FEA provided the stress and displacement distributions on the upper and motor units. The governing yielding safety for structural powered hip parts is 1.09. Fatigue is governed by the output bearing within

the drive flange. Under the maximum allowable torques at different hip ROM regions (Figure 7-2), the governing fatigue life is 82382 strides which is sufficient for early prototype testing. Furthermore, the motor unit displacement distribution shows that under the maximum motor torque of 96 N-m, the drive flange does not displace far enough to touch the motor housing interior surface, thereby confirming that part contact will not inhibit hip function.

The powered hip prototype is made mainly of Al 2024-T351 and 17-4 PH SS H-900. With enough motor torque, it is possible for the powered hip to pass its extension singularity point due to tolerances between parts, so a software extension stop was implemented. Prototype tolerances have been chosen such that cold pressing was possible and the minimum expected friction force between parts exceeded the maximum expected medial-lateral force during static compression testing. ISO 15032:2000 static compression tests showed linearity of force versus displacement. Additionally, no cracks or warped geometry (i.e., fracture or yielding) were observed on the prototype following structural testing. Conclusively, the prototype passed all static compression tests.

Functional walking tests were carried out by three able-bodied people wearing a HD prosthesis simulator placing the HKAFP lateral to the person's right leg. All participants achieved a successful cadence with 10 or more strides using the HD prosthesis simulator. Resulting anterior-posterior pelvic tilt, hip flexion-extension, and knee-flexion gait cycle curves resembled those seen in literature for HD amputees. It is reasonable to conclude that a HD amputee would be able to walk with the powered hip.

10.1 Design Performance

The powered hip was required to provide up to 20° extension and up to 130° flexion. The prototype provides up to 20° extension and up to 100° flexion; therefore, the hip flexion range is 30° short of meeting the criteria. However, for early prototype, users were not required to flex their hip beyond what is required for sit-to-stand or stand-to-sit (approximately 90° hip flexion). Thus, the four-bar hip ROM is acceptable at its current stage of development.

Additionally, the powered hip was required to support a body weight of at least 100 kg. The heaviest participant who walked with the powered hip weighed 98 kg. Therefore, the powered hip can support at least a 98 kg body weight.

The powered hip and chassis were required to have a combined weight of at most, 3.2 kg. The prosthetic thigh prototype weighs 4.337 kg, exceeding the device weight requirement by 1.137 kg. However, walking test participants mentioned that the powered hip did not feel heavy during gait due to the hip flexion-extension assistance the actuator provided. Although, a lighter prosthetic mass would be ideal, the extra prototype mass did not greatly affect participants' gait due to the powerful actuator implemented in the powered hip.

The actuator needed to have a torque capacity of at least 80 N-m, provide an angular velocity of at least 143 °/s and power of at least 99 W. The Össur Power Knee 2 DC motor provides a torque of up to 96 N-m, an angular velocity of up to 300 °/s, and a power of up to 503 W, easily meeting the actuator criteria.

The powered hip was required to withstand ISO 15032:2000 A100 static compression (3360 N), the maximum motor torque (96 N-m) with no body weight, and a combined body weight and torque load for a 100 kg user with a safety factor of 2. The powered hip prototype passed the A-P extension and M-L 3360 N static compression tests. The prototype also sustained walking trials of participants weighing 96 kg on average with no signs of failure. Powered hip FEA with the 96 N-m maximum motor torque showed no signs of yielding. However, it is uncertain whether the output bearing in the drive flange would fail when supporting 100 kg person because allowable motor torque decreases linearly from 96 N-m to 32.7 N-m from 14° hip flexion to 20° hip extension. The allowable motor torque is 96 N-m above 14° hip flexion. Further testing is required to better understand powered hip capabilities.

The powered hip, from the posterosuperior pin and below but not including the chassis, needed to have a length, width, and height of less than 17 cm in neutral position. The respective powered hip neutral position dimensions were 11.61 cm, 13.48 cm and 15.51 cm which meet size criteria.

Cosmetic criteria include the anterior mounting of the hip onto the socket with the motor placed within the prosthetic thigh, a maximum anterior protrusion of 2 cm in the standing position, and a maximum superior protrusion of 17 cm in the sitting position with no protrusion below the bottom surface of the socket. The powered hip superior link is configured such that it screws onto a lamination plate on the same front socket surface as would the Helix3D, thereby fulfilling the anterior mounting criterion. However, the powered hip has an anterior protrusion of 6.68 cm which does not meet the criterion. Users may see a slight bulge through the anterior side of their pants when they are near neutral position with the powered hip. Nevertheless, the powered hip also meets the superior protrusion criteria with a superior protrusion of 11.51 cm and no protrusion below the socket bottom surface, thereby not interfering with sitting.

During mid-swing, the powered hip is required to shorten to enhance toe clearance and reduce the risk of tripping. The powered hip shortens by 23.8 mm during mid-swing and thus, meets the prosthetic shortening criteria.

The powered hip ideally should have a fatigue life of 2 million load cycles. The prototype has a calculated fatigue life of 82382 load cycles (strides). This number of strides is adequate for the bench testing stage of powered hip development.

Table 10-1 summarizes powered hip performance in relation to the design criteria.

Table 10-1: Powered four-bar hip requirements, criteria, and performance.

Requirements	Criteria	Performance
Range of motion	20° extension to 130° flexion	20° extension to 100° flexion
Supported body weight	Minimum of 100 kg	Minimum of 98 kg
Device weight	Maximum of 3.2 kg	4.337 kg
Motor torque capacity	At least 80 N-m	96 N-m
Motor angular velocity	At least 143 °/s	Up to 300 °/s
Maximum motor power	At least 99 W	Up to 503 W
Strength	Withstand three kinds of loads: <ul style="list-style-type: none"> ISO 15032:2000 A100 static compression (3360 N) Combined body weight and torque loading (100 kg user and required torque for hip stability) with a safety factor of 2 Maximum motor torque (96 N-m) with no body weight 	<ul style="list-style-type: none"> Passed ISO 15032:2000 A100 structural tests Walking trials with participants weighing an average of 96 kg were successfully completed with no signs of failure (safety factor of 2.50) Allowable motor torque is 96 N-m above 14° hip flexion and decreases linearly to 32.7 N-m from 14° hip flexion to 20° hip extension
Size	Length, width, and height less than 17 cm at neutral position (i.e., standing)	<ul style="list-style-type: none"> Length = 11.61 cm Width = 13.48 cm Height = 15.51 cm
Cosmesis	<ul style="list-style-type: none"> Hip joint anteriorly mounted onto the socket with the motor placed within the thigh Maximum anterior protrusion of 2 cm in the standing position Maximum superior protrusion of 17 cm in the sitting position No protrusion below the bottom surface of the socket in the sitting position 	<ul style="list-style-type: none"> Anterior socket mounting with a lamination plate Anterior protrusion of 6.68 cm in the standing position Superior protrusion of 15.51 cm in the sitting position No protrusion below the bottom surface of the socket in the sitting position
Prosthetic shortening	Prosthesis length shortens at mid-swing	Mid-swing shortening of 23.8 mm
Fatigue life	2 million load cycles	82382 load cycles

10.2 Future Work

Following walking tests, it was observed that the anterosuperior pins had medial-laterally translated by 1 mm. The prototype could be modified with circlips, threaded pin connections, and/or tighter press fits (e.g., hot press fits) to eliminate this medial-lateral pin translation.

The powered hip control system is still under development. When the control system has been updated, further walking tests will be done with the powered hip. These tests should measure additional

quantities such as sound leg kinematics, and both prosthetic and sound leg kinetics (hip motor torque, and lower-limb forces). The additional measurements would better assess gait symmetry and structural integrity during gait. Future walking tests should include at least one participant weighing 100 kg or more to verify if the powered hip meets the 100 kg body weight requirement.

Prototype strength was governed by the drive flange output bearing load capacity. Under the full 96 N-m motor torque, the output bearing would likely be overloaded due to a large bending moment created by the medial-lateral offset between the drive arm and the bearing. Figure 10-1 presents a design concept that can be implemented in the second powered four-bar hip prototype to potentially solve the output bearing overload problem.

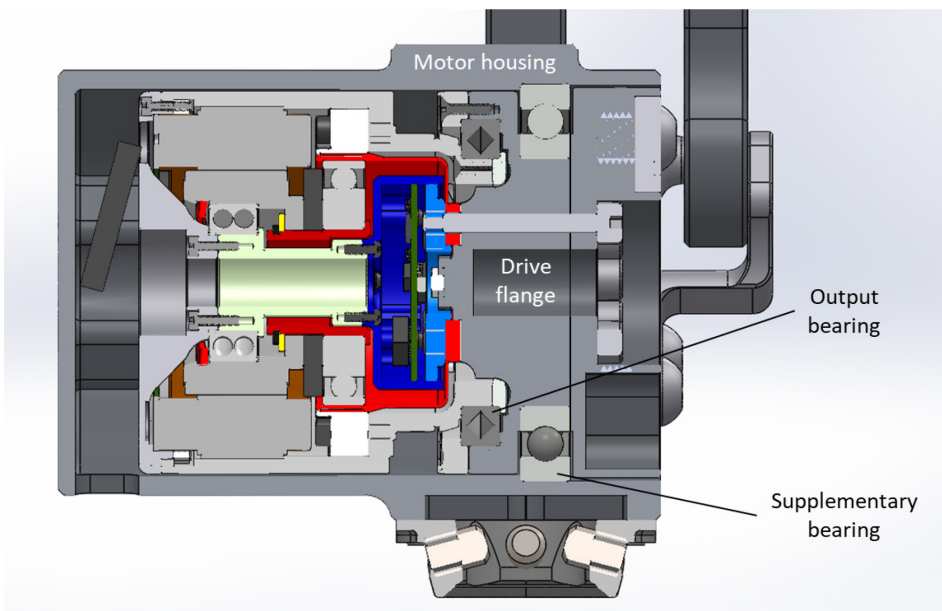


Figure 10-1: Medial-lateral cross-section of powered four-bar hip design concept containing a supplementary bearing that will potentially reduce output bearing loading.

This concept adds a supplementary bearing medial to the output bearing. The supplementary bearing is the SKF 16010 deep groove ball bearing (bore diameter = 50 mm, outside diameter = 80 mm, width = 10 mm, radial static load capacity = 11.4 kN, and radial dynamic load capacity = 16.8 kN) [233]. The supplementary bearing would be pressed in between the drive flange and the motor housing so that its inner race is fixed relative to the drive flange, thus moving with the rotor, and its outer race is fixed relative to the motor housing, keeping the bearing in place. One advantage of this design concept is that it eliminates the possibility of the drive flange contacting the motor housing during operation due to contact occurring between the supplementary bearing and the motor housing. Another advantage is that when the motor operates, loading would be distributed between the output and supplementary bearings, thereby drastically reducing the load on the output bearing, and potentially removing the restriction of allowable motor torque. Furthermore, the fatigue life would

potentially no longer be governed by output bearing, but by the motor shell, thereby potentially increasing the governing fatigue life from 82382 load cycles to 364863 load cycles. The load distribution between the output and supplementary bearings is yet to be determined. It may be possible to remove the output bearing if the supplementary bearing can, by itself, withstand the 96 N·m torque load. Additionally, the strengths of the thinner medial portion of the motor housing and the motor cover (at a further offset than before due to the added bearing) would need to be analyzed before this concept is implemented in the next prototype.

Powered hip performance would benefit from the addition of a hard stop on motor rotation to ensure the motor rotates in the correct direction but does not cross the hip extension singularity point. While a software stop has been implemented, a hard stop would guarantee that the motor does not get jammed during gait if there were to be an operational error in the control algorithm.

Powered hip mechanical advantage is maximal at 10° hip flexion and decreases near ROM extremities (more so near full hip flexion than full hip extension). To better understand the augmentation capability of the powered hip, it would be useful to measure the motor torque output in these ROM regions. A potential setup for measuring motor torque is a fixture keeping the proximal end of the hip in place and a weight tied to the distal end of the hip. The powered hip would then be turned on to determine if the weight can be lifted. This process can be repeated with different weights representing different torque requirements.

The powered hip design focused on level-walking. Therefore, the powered hip was mechanically optimized to provide the largest mechanical advantages within the walking ROM (20° extension and 40° flexion). However, due to the low mechanical advantages near full hip flexion, the powered hip would not perform as well in high hip flexion activities. Stair ascent and descent, and 10° ramp ascent and descent require similar hip moment magnitudes as do sit-to-stand and stand-to-sit [154], [185], [192], [193]. Stair ascent and descent hip moment magnitudes do not vary greatly for stair heights ranging from 102 mm to 178 mm [154]. However, ramp ascent and descent hip moment magnitudes vary considerably for ramp angles ranging from 5.2° to 18° [154]. An 18° ramp ascent requires, on average, 50% more hip moment than do stair ascent and descent and 10° ramp ascent and descent [154], [192], [193]. Maximum hip moment magnitudes occur at approximately 40° hip flexion for stair ascent and descent, and 10° ramp ascent and descent [154], [192], [193]. For an 18° ramp ascent, the maximum hip moment magnitude occurs at approximately 60° hip flexion [154]. For sit-to-stand and stand-to-sit, the maximum hip moment magnitude occurs at approximately 80° hip flexion [185]. Therefore, as shown in Figure 10-2, it would be ideal for the mechanical advantage peak to be centered at 60° hip flexion to best assist ramp ascent and provide balance assistance to other high hip flexion activities. This improved mechanical advantage profile has the same average mechanical

advantage as before. However, reoptimizing link lengths to produce the improved mechanical advantage profile but a larger average mechanical advantage (if possible) would be ideal.

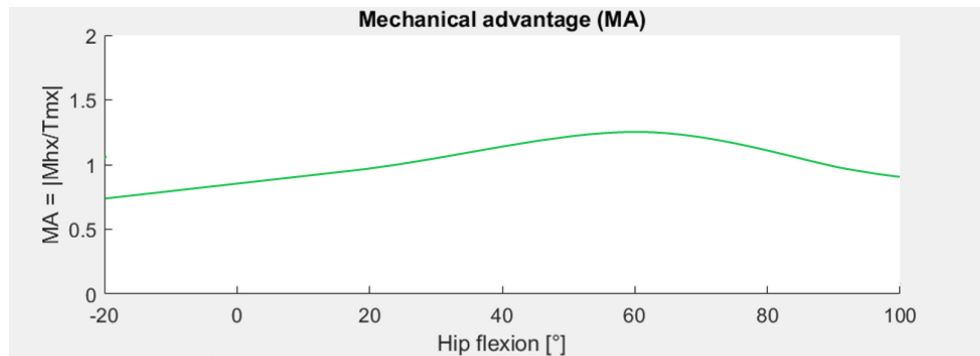


Figure 10-2: Hypothetical mechanical advantage profile centering the peak at 60° hip flexion to optimize stair ascent and descent, ramp ascent and descent, sit-to-stand, and stand-to-sit.

Part of the powered hip re-optimization process should also involve redesigning parts to be better in fatigue so that the 2 million life cycle span could be achieved. A more rigorous weight reduction analysis should be carried out to bring the powered hip mass closer to the 3.2 kg criterion.

Future evaluation of powered hip performance should be completed with hip-level amputees. Hip-level amputee gait data would better represent powered hip performance than gait data from able-bodied participants using a HKAFF simulator and would inform further improvements to the powered four-bar hip prototype.

References

- [1] H. Gholizadeh, N. Baddour, M. Botros, K. Brannen, F. Golshan, and E. D. Lemaire, “Hip disarticulation and hemipelvectomy prostheses: A review of the literature,” *Prosthet. Orthot. Int.*, vol. 45, no. 5, pp. 434–439, Oct. 2021, doi: 10.1097/PXR.0000000000000029.
- [2] F. R. T. Nelson and C. T. Blauvelt, “8 - Anatomy and Orthopaedic Surgery,” in *A Manual of Orthopaedic Terminology (Eighth Edition)*, F. R. T. Nelson and C. T. Blauvelt, Eds., Philadelphia: W.B. Saunders, 2015, pp. 209–282. doi: 10.1016/B978-0-323-22158-0.00008-1.
- [3] P. Yari, P. U. Dijkstra, and J. H. Geertzen, “Functional outcome of hip disarticulation and hemipelvectomy: a cross-sectional national descriptive study in the Netherlands,” *Clin. Rehabil.*, vol. 22, no. 12, pp. 1127–1133, Dec. 2008, doi: 10.1177/0269215508095088.
- [4] Tarina van der Stockt, Martina Lukin, Wanda van Niekerk, Kim Jackson, and Simisola Ajeyalemi, “Prosthetics for Individuals with Hip Disarticulation and Hemipelvectomy Amputations,” Physiopedia. Accessed: Jan. 24, 2023. [Online]. Available: https://www.physio-pedia.com/Prosthetics_for_Individuals_with_Hip_Disarticulation_and_Hemipelvectomy_Amputations
- [5] K. B. Fite, “Overview of the Components Used in Active and Passive Lower-Limb Prosthetic Devices,” in *Full Stride: Advancing the State of the Art in Lower Extremity Gait Systems*, V. Tepe and C. M. Peterson, Eds., New York, NY: Springer, 2017, pp. 55–74. doi: 10.1007/978-1-4939-7247-0_4.
- [6] “Helix3D Hip Joint, right | Hips | Lower Limb Prosthetics | Prosthetics | Ottobock CA Shop,” ottobock. Accessed: Dec. 07, 2022. [Online]. Available: <https://shop.ottobock.ca/en/Prosthetics/Lower-Limb-Prosthetics/Hips/Helix3D-Hip-Joint%2C-right/p/7E10~5R#product-specification-section>
- [7] “C-Leg 4,” Ottobock. Accessed: Dec. 07, 2022. [Online]. Available: <https://www.ottobock.com/en-us/product/3C88-3~23C98-3>
- [8] “Rheo Knee®,” Össur. Accessed: Dec. 07, 2022. [Online]. Available: <https://www.ossur.com/en-ca/prosthetics/knees/rheo-knee>
- [9] “Proprio Foot®,” Össur. Accessed: Dec. 07, 2022. [Online]. Available: <https://www.ossur.com/en-ca/prosthetics/feet/proprio-foot>
- [10] “Power Knee™,” Össur. Accessed: Dec. 07, 2022. [Online]. Available: <https://www.ossur.com/en-ca/prosthetics/knees/power-knee>

- [11] “Empower,” Ottobock. Accessed: Dec. 07, 2022. [Online]. Available: <https://shop.ottobock.us/Prosthetics/Lower-Limb-Prosthetics/Feet---Microprocessor/Empower/p/1A1-2#product-documents-section>
- [12] “BionX emPOWER Ankle - Powered Prosthetic Ankle,” MCOP Prosthetics. Accessed: Dec. 07, 2022. [Online]. Available: <https://mcopro.com/prosthetics/technology/bionx-empower-ankle/>
- [13] E. Ludwigs, M. Bellmann, T. Schmalz, and S. Blumentritt, “Biomechanical Differences between Two Exoprosthetic Hip Joint Systems during Level Walking,” *Prosthet. Orthot. Int.*, vol. 34, no. 4, pp. 449–460, Dec. 2010, doi: 10.3109/03093646.2010.499551.
- [14] Y. Ueyama, T. Kubo, and M. Shibata, “Robotic hip-disarticulation prosthesis: evaluation of prosthetic gaits in a non-amputee individual,” *Adv. Robot.*, vol. 34, no. 1, pp. 37–44, 2020, doi: 10.1080/01691864.2019.1705908.
- [15] M. Song, S. Guo, X. Wang, and H. Qu, “Dynamic Analysis and Performance Verification of a Novel Hip Prosthetic Mechanism,” *Chin. J. Mech. Eng. Engl. Ed.*, vol. 33, no. 1, 2020, doi: 10.1186/s10033-020-0436-5.
- [16] D. Langlois, A. V. Clausen, and A. Einarsson, “Powered prosthetic hip joint,” CA2868528C, Jul. 28, 2020 Accessed: Apr. 05, 2023. [Online]. Available: [https://patents.google.com/patent/CA2868528C/en?q=\(power+hip\)&assignee=ossur&oq=ossur+power+hip](https://patents.google.com/patent/CA2868528C/en?q=(power+hip)&assignee=ossur&oq=ossur+power+hip)
- [17] “Helix3D Hip Joint System - Information for Practitioners.” Ottobock. [Online]. Available: <https://shop.ottobock.ca/en/Prosthetics/Lower-Limb-Prosthetics/Hips/Helix3D-Hip-Joint%2C-right/p/7E10~5R#product-documents-section>
- [18] L. M. Nelson and N. T. Carbone, “Functional Outcome Measurements of a Veteran With a Hip Disarticulation Using a Helix 3D Hip Joint: A Case Report,” *JPO J. Prosthet. Orthot.*, vol. 23, no. 1, pp. 21–26, Jan. 2011, doi: 10.1097/JPO.0b013e318209777c.
- [19] H. Bowker and J. Michael, Eds., *Atlas of Limb Prosthetics: Surgical, Prosthetic, and Rehabilitation Principles*, 2nd ed. Rosemont, IL: American Academy of Orthopedic Surgeons, 1992. [Online]. Available: <https://www.oandplibrary.org/alp/>
- [20] T. Chin, S. Sawamura, R. Shiba, H. Oyabu, Y. Nagakura, and A. Nakagawa, “Energy expenditure during walking in amputees after disarticulation of the hip: a microprocessor-controlled swing-phase control knee versus a mechanical-controlled stance-phase control knee,” *J. Bone Joint Surg. Br.*, vol. 87-B, no. 1, pp. 117–119, Jan. 2005, doi: 10.1302/0301-620X.87B1.14617.

- [21] T. Chin, H. Oyabu, Y. Maeda, I. Takase, and K. Machida, “Energy Consumption During Prosthetic Walking and Wheelchair Locomotion by Elderly Hip Disarticulation Amputees,” *Am. J. Phys. Med. Rehabil.*, vol. 88, no. 5, pp. 399–403, May 2009, doi: 10.1097/PHM.0b013e3181a0dbe2.
- [22] K. A. Jeans, R. H. Browne, and L. A. Karol, “Effect of Amputation Level on Energy Expenditure During Overground Walking by Children with an Amputation,” *J. Bone Jt. Surg.-Am. Vol.*, vol. 93, no. 1, pp. 49–56, Jan. 2011, doi: 10.2106/JBJS.I.01557.
- [23] D. Langlois, “Powered Hip Joint Unexplored Clinical Opportunities of Powered Prosthetics.” Ossur, Oct. 09, 2015.
- [24] F. Nowroozi, M. L. Salvanelli, and L. H. Gerber, “Energy expenditure in hip disarticulation and hemipelvectomy amputees,” *Arch. Phys. Med. Rehabil.*, vol. 64, no. 7, pp. 300–303, Jul. 1983.
- [25] M. T. Houdek, M. E. Kralovec, and K. L. Andrews, “Hemipelvectomy: High-Level Amputation Surgery and Prosthetic Rehabilitation,” *Am. J. Phys. Med. Rehabil.*, vol. 93, no. 7, pp. 600–608, Jul. 2014, doi: 10.1097/PHM.0000000000000068.
- [26] A. Brandt and H. (Helen) Huang, “Effects of extended stance time on a powered knee prosthesis and gait symmetry on the lateral control of balance during walking in individuals with unilateral amputation,” *J. NeuroEngineering Rehabil.*, vol. 16, no. 1, Nov. 2019, doi: 10.1186/s12984-019-0625-6.
- [27] A. M. Karmarkar *et al.*, “Prostheses and wheelchair use in veterans with lower-limb amputation,” *J. Rehabil. Res. Dev.*, vol. 46, no. 5, pp. 567–576, 2009, doi: 10.1682/JRRD.2008.08.0102.
- [28] Isabelle Hoffman, Stacey Cameron, Gabrielle Broome, Kim Jackson, and Evan Thomas, “Lower Limb Amputees and Low Back Pain,” Physiopedia. Accessed: Jan. 18, 2023. [Online]. Available: https://www.physio-pedia.com/Lower_Limb_Amputees_and_Low_Back_Pain
- [29] A. Kušljugić, S. Kapidžić-Duraković, Z. Kudumović, and A. Čičkušić, “Chronic Low Back Pain in Individuals with Lower-limb Amputation,” *Biomol. Biomed.*, vol. 6, no. 2, pp. 67–70, May 2006, doi: 10.17305/bjbms.2006.3177.
- [30] K. Friel, E. Domholdt, and D. G. Smith, “Physical and functional measures related to low back pain in individuals with lower-limb amputation: An exploratory pilot study,” *J. Rehabil. Res. Dev.*, vol. 42, no. 2, pp. 155–166, 2005, doi: 10.1682/JRRD.2004.08.0090.
- [31] D. C. Morgenroth, M. S. Orendurff, A. Shakir, A. Segal, J. Shofer, and J. M. Czerniecki, “The Relationship Between Lumbar Spine Kinematics during Gait and Low-Back Pain in Transfemoral Amputees,” *Am. J. Phys. Med. Rehabil.*, vol. 89, no. 8, pp. 635–643, Aug. 2010, doi: 10.1097/PHM.0b013e3181e71d90.

- [32] H. Devan, P. Hendrick, D. C. Ribeiro, L. A Hale, and A. Carman, “Asymmetrical movements of the lumbopelvic region: Is this a potential mechanism for low back pain in people with lower limb amputation?,” *Med. Hypotheses*, vol. 82, no. 1, pp. 77–85, Jan. 2014, doi: 10.1016/j.mehy.2013.11.012.
- [33] J. Hayden, M. W. van Tulder, A. Malmivaara, and B. W. Koes, “Exercise therapy for treatment of non-specific low back pain,” *Cochrane Database Syst. Rev.*, no. 3, pp. 1–82, 2005, doi: 10.1002/14651858.CD000335.pub2.
- [34] D. G. Smith, D. M. Ehde, M. W. Legro, G. E. Reiber, M. del Aguila, and D. A. Boone, “Phantom Limb, Residual Limb, and Back Pain After Lower Extremity Amputations,” *Clin. Orthop. Relat. Res.*, pp. 29–38, Apr. 1999.
- [35] B. Davies and D. Datta, “Mobility outcome following unilateral lower limb amputation,” *Prosthet. Orthot. Int.*, vol. 27, no. 3, pp. 186–190, Dec. 2003, doi: 10.1080/03093640308726681.
- [36] A. Fernández and J. Formigo, “Are Canadian Prostheses Used? A Long-Term Experience,” *Prosthet. Orthot. Int.*, vol. 29, no. 2, pp. 177–181, Aug. 2005, doi: 10.1080/03093640500217208.
- [37] Z. Dénes and A. Till, “Rehabilitation of patients after hip disarticulation,” *Arch. Orthop. Trauma Surg.*, vol. 116, no. 8, pp. 498–499, Oct. 1997, doi: 10.1007/BF00387586.
- [38] “Falls in the Amputee Population,” Physiopedia. Accessed: Dec. 08, 2022. [Online]. Available: https://www.physio-pedia.com/Falls_in_the_Amputee_Population
- [39] C. Wong, S. Chihuri, and G. Li, “Risk of fall-related injury in people with lower limb amputations: A prospective cohort study,” *J. Rehabil. Med.*, vol. 48, no. 1, pp. 80–85, 2016, doi: 10.2340/16501977-2042.
- [40] B. Engstrom and C. Van de Ven, Eds., *Therapy for Amputees*, 3rd ed. London, United Kingdom: Churchill Livingstone, 1999.
- [41] C. McLaurin, “The canadian hip disarticulation prosthesis,” Prosthetic Services Centre, Department of Veterans Affairs, Toronto, Canada, 15, 1954.
- [42] C. Buesing *et al.*, “Effects of a wearable exoskeleton stride management assist system (SMA®) on spatiotemporal gait characteristics in individuals after stroke: a randomized controlled trial,” *J. NeuroEngineering Rehabil.*, vol. 12, no. 1, Aug. 2015, doi: 10.1186/s12984-015-0062-0.
- [43] Y. Ding *et al.*, “Effect of timing of hip extension assistance during loaded walking with a soft exosuit,” *J. NeuroEngineering Rehabil.*, vol. 13, no. 1, p. 87, Oct. 2016, doi: 10.1186/s12984-016-0196-8.

- [44] “Modular Hip Joint Free Mot. Titan | Hips | Lower Limb Prosthetics | Prosthetics | Ottobock CA Shop.” Accessed: Jan. 18, 2023. [Online]. Available: <https://shop.ottobock.ca/en/Prosthetics/Lower-Limb-Prosthetics/Hips/Modular-Hip-Joint-Free-Mot-Titan/p/7E7>
- [45] M. Karimi, M. Kamali, A. H. Hj. Omar, and J. Mostamand, “Evaluation of Gait Performance of a Hemipelvectomy Amputation Walking with a Canadian Prosthesis,” *Case Rep. Orthop.*, vol. 2014, Apr. 2014, doi: 10.1155/2014/962980.
- [46] K. Schmid-Zalaudek *et al.*, “Kinetic Gait Parameters in Unilateral Lower Limb Amputations and Normal Gait in Able-Bodied: Reference Values for Clinical Application,” *J. Clin. Med.*, vol. 11, no. 10, May 2022, doi: 10.3390/jcm11102683.
- [47] D. Wezenberg, A. G. Cutti, A. Bruno, and H. Houdijk, “Differentiation between solid-ankle cushioned heel and energy storage and return prosthetic foot based on step-to-step transition cost,” *J. Rehabil. Res. Dev.*, vol. 51, no. 10, pp. 1579–1590, 2014, doi: 10.1682/JRRD.2014.03.0081.
- [48] P. G. Adamczyk and A. D. Kuo, “Mechanisms of Gait Asymmetry Due to Push-Off Deficiency in Unilateral Amputees,” *IEEE Trans. Neural Syst. Rehabil. Eng.*, vol. 23, no. 5, pp. 776–785, Sep. 2015, doi: 10.1109/TNSRE.2014.2356722.
- [49] A. G. Cutti, G. Verni, G. L. Migliore, A. Amoresano, and M. Raggi, “Reference values for gait temporal and loading symmetry of lower-limb amputees can help in refocusing rehabilitation targets,” *J. NeuroEngineering Rehabil.*, vol. 15, no. 1, pp. 29–40, Sep. 2018, doi: 10.1186/s12984-018-0403-x.
- [50] A. Rutkowska-Kucharska, M. Kowal, and S. Winiarski, “Relationship between Asymmetry of Gait and Muscle Torque in Patients after Unilateral Transfemoral Amputation,” *Appl. Bionics Biomech.*, vol. 2018, Mar. 2018, doi: 10.1155/2018/5190816.
- [51] I. Loiret *et al.*, “Are wearable insoles a validated tool for quantifying transfemoral amputee gait asymmetry?,” *Prosthet. Orthot. Int.*, vol. 43, no. 5, pp. 492–499, Oct. 2019, doi: 10.1177/0309364619865814.
- [52] T. Varrecchia *et al.*, “Common and specific gait patterns in people with varying anatomical levels of lower limb amputation and different prosthetic components,” *Hum. Mov. Sci.*, vol. 66, pp. 9–21, Aug. 2019, doi: 10.1016/j.humov.2019.03.008.
- [53] L. Nolan, A. Wit, K. Dudziński, A. Lees, M. Lake, and M. Wychowański, “Adjustments in gait symmetry with walking speed in trans-femoral and trans-tibial amputees,” *Gait Posture*, vol. 17, no. 2, pp. 142–151, Apr. 2003, doi: 10.1016/S0966-6362(02)00066-8.

- [54] J. C. Bell, E. J. Wolf, B. L. Schnall, J. E. Tis, L. L. Tis, and M. a. J. Benjamin K. Potter, “Transfemoral Amputations: The Effect of Residual Limb Length and Orientation on Gait Analysis Outcome Measures,” *JBJS*, vol. 95, no. 5, pp. 408–414, Mar. 2013, doi: 10.2106/JBJS.K.01446.
- [55] H. Goujon *et al.*, “A Functional Evaluation of Prosthetic Foot Kinematics During Lower-Limb Amputee Gait,” *Prosthet. Orthot. Int.*, vol. 30, no. 2, pp. 213–223, Aug. 2006, doi: 10.1080/03093640600805134.
- [56] B. S. Baum, B. L. Schnall, J. E. Tis, and J. S. Lipton, “Correlation of residual limb length and gait parameters in amputees,” *Injury*, vol. 39, no. 7, pp. 728–733, Jul. 2008, doi: 10.1016/j.injury.2007.11.021.
- [57] D. A. Winter, Ed., *Biomechanics and Motor Control of Human Movement*, 4th ed. John Wiley & Sons, Inc., 2009.
- [58] V. J. Harandi *et al.*, “Gait compensatory mechanisms in unilateral transfemoral amputees,” *Med. Eng. Phys.*, vol. 77, pp. 95–106, Mar. 2020, doi: 10.1016/j.medengphy.2019.11.006.
- [59] T. Kobayashi, G. Hisano, Y. Namiki, S. Hashizume, and H. Hobara, “Walking characteristics of runners with a transfemoral or knee-disarticulation prosthesis,” *Clin. Biomech.*, vol. 80, Dec. 2020, doi: 10.1016/j.clinbiomech.2020.105132.
- [60] “7E10 Helix3D Instructions for Use.” Ottobock, Apr. 02, 2022. [Online]. Available: <https://shop.ottobock.ca/en/Prosthetics/Lower-Limb-Prosthetics/Hips/Helix3D-Hip-Joint%2C-right/p/7E10~5R#product-documents-section>
- [61] P. L. Ephraim, T. R. Dillingham, M. Sector, L. E. Pezzin, and E. J. MacKenzie, “Epidemiology of limb loss and congenital limb deficiency: A review of the literature,” *Arch. Phys. Med. Rehabil.*, vol. 84, no. 5, pp. 747–761, May 2003, doi: 10.1016/S0003-9993(03)04932-8.
- [62] G. Stark, “Overview of Hip Disarticulation Prostheses;,” *JPO J. Prosthet. Orthot.*, vol. 13, no. 2, pp. 50–53, Jun. 2001, doi: 10.1097/00008526-200106000-00014.
- [63] A. Huffman *et al.*, “Evaluating hip disarticulation outcomes in a 51-patient series,” *J. Orthop.*, vol. 31, pp. 117–120, May 2022, doi: 10.1016/j.jor.2022.04.008.
- [64] S. Hussain, S. Shams, and S. Khan, “Impact of Medical Advancement: Prostheses,” 2019. doi: 10.5772/intechopen.86602.
- [65] H. Ansaripour and S. Chemello, “Finite element analysis of socket optimization in accordance with the deformation of external surface of the stump (transtibial amputation),” 2018.
- [66] D. G. Shurr, R. R. Cooper, J. A. Buckwalter, and T. M. Cook, “Hemipelvectomy and Hip Disarticulation: A Prosthetic Follow-Up,” *Iowa Orthop. J.*, vol. 3, pp. 71–75, 1983.

- [67] “Osteomyelitis,” Johns Hopkins Medicine. Accessed: Jan. 24, 2023. [Online]. Available: <https://www.hopkinsmedicine.org/health/conditions-and-diseases/osteomyelitis>
- [68] S. Bhutani, J. Bhutani, A. Chhabra, and R. Uppal, “Living with Amputation: Anxiety and Depression Correlates,” *J. Clin. Diagn. Res. JCDR*, vol. 10, no. 9, pp. 9–12, Sep. 2016, doi: 10.7860/JCDR/2016/20316.8417.
- [69] R. Singh *et al.*, “Depression and anxiety symptoms after lower limb amputation: the rise and fall,” *Clin. Rehabil.*, vol. 23, no. 3, pp. 281–286, Mar. 2009, doi: 10.1177/0269215508094710.
- [70] C. A. Bell, “Canadian Hip Disarticulation Prosthesis,” *Orthop. Prosthet. Appl. J.*, vol. 10, no. 1, pp. 35–39, Mar. 1956.
- [71] J. Foort, “Construction and Fitting of the Canadian- Type Hip-Disarticulation Prosthesis,” *Artif. Limbs*, vol. 4, no. 2, pp. 39–51, 1957.
- [72] C. A. McLaurin, “The Evolution of the Canadian-Type Hip-Disarticulation Prosthesis,” vol. 4, no. 2, pp. 22–28, 1957.
- [73] R. L. Raiford, “Experiences with the Canadian Hip Disarticulation Prosthesis in the Juvenile,” *Columbia Gen. Hosp.*, vol. 66, no. 1, pp. 71–75.
- [74] S. E. Solomonidis, A. J. Loughran, J. Taylor, and J. P. Paul, “Biomechanics of the hip disarticulation prosthesis,” *Prosthet. Orthot. Int.*, vol. 1, no. 1, pp. 13–18, Apr. 1977, doi: 10.3109/03093647709164599.
- [75] C. W. Radcliffe, “The Biomechanics of the Canadian-Type Hip-Disarticulation Prosthesis,” *Artif. Limbs*, vol. 4, no. 2, pp. 29–38, 1957.
- [76] S. Blumentritt, E. Ludwigs, M. Bellmann, and H. Boiten, “The New Helix3D Hip Joint,” *Orthop.-Tech.*, pp. 1–6, May 2008.
- [77] J. Michael, “Component Selection Criteria: Lower Limb Disarticulations,” *Clin. Prosthet. Orthot.*, vol. 12, no. 3, pp. 99–108, 1988.
- [78] “Modular Hip Joint -Free Motion- | Hips | Lower Limb Prosthetics,” Ottobock. Accessed: Feb. 20, 2023. [Online]. Available: <https://shop.ottobock.us/Prosthetics/Lower-Limb-Prosthetics/Hips/Modular-Hip-Joint--Free-Motion-/p/7E4>
- [79] “Modular Single Axis Hip Joint,” Ottobock. Accessed: Feb. 20, 2023. [Online]. Available: <https://shop.ottobock.us/Prosthetics/Lower-Limb-Prosthetics/Hips/Modular-Single-Axis-Hip-Joint/p/7E5~5R>
- [80] “7E4, 7E5 Modudular Hip Joints - Instructions for Use.” Ottobock, Oct. 14, 2021. [Online]. Available: <https://shop.ottobock.us/Prosthetics/Lower-Limb-Prosthetics/Hips/Modular-Hip-Joint--Free-Motion-/p/7E4>

- [81] “Modular Hip Joint-Child,” Ottobock. Accessed: Feb. 20, 2023. [Online]. Available: <https://shop.ottobock.us/Prosthetics/Lower-Limb-Prosthetics/Pediatric-Prosthetics/Pediatric-Hip-Joints/Modular-Hip-Joint-Child/p/7E8#product-documents-section>
- [82] “Hydraulic Hip Joint,” Ottobock. Accessed: Feb. 20, 2023. [Online]. Available: <https://shop.ottobock.us/Prosthetics/Lower-Limb-Prosthetics/Hips/Hydraulic-Hip-Joint/p/7E9>
- [83] “7E7 Hip - Instructions for Use.” Ottobock, Feb. 17, 2021. [Online]. Available: <https://shop.ottobock.us/Prosthetics/Lower-Limb-Prosthetics/Hips/Modular-Hip-Joint-Free-Mot-Titan/p/7E7#product-documents-section>
- [84] “7E8 Pediatric Modular Hip Joint - Instructions for Use.” Ottobock, Oct. 21, 2021. [Online]. Available: <https://shop.ottobock.us/Prosthetics/Lower-Limb-Prosthetics/Pediatric-Prosthetics/Pediatric-Hip-Joints/Modular-Hip-Joint-Child/p/7E8#product-documents-section>
- [85] “7E9 Hip Joint - Instructions for Use.” Ottobock, Mar. 28, 2022. [Online]. Available: <https://shop.ottobock.us/Prosthetics/Lower-Limb-Prosthetics/Hips/Hydraulic-Hip-Joint/p/7E9#product-documents-section>
- [86] “7E9 Monocentric Hip Joint with Hydraulic Control - Product Information.” Ottobock, Feb. 01, 2014. [Online]. Available: <https://shop.ottobock.us/Prosthetics/Lower-Limb-Prosthetics/Hips/Hydraulic-Hip-Joint/p/7E9#product-documents-section>
- [87] R. Hartenberg and J. Danavit, *Kinematic Synthesis of Linkages*. New York: McGraw-Hill, 1964. Accessed: Mar. 09, 2023. [Online]. Available: <https://ecommons.cornell.edu/handle/1813/58640>
- [88] Matthew West, “Four-Bar Linkages,” Dynamics. Accessed: Mar. 09, 2023. [Online]. Available: <https://dynref.engr.illinois.edu/aml.html>
- [89] C. W. Radcliffe, “Above-knee prosthetics,” *Prosthet. Orthot. Int.*, vol. 1, no. 3, pp. 146–160, Dec. 1977, doi: 10.3109/03093647709164629.
- [90] Shailendra Singh Chauhan and Avadhesh Kumar Khare, “Analysis of Four-bar Linkages Suitable for Above-knee Prosthesis,” *Evergreen*, vol. 9, no. 3, pp. 737–744, Sep. 2022, doi: 10.5109/4843107.
- [91] C. W. Radcliffe, “Four-bar linkage prosthetic knee mechanisms: kinematics, alignment and prescription criteria,” vol. 18, no. 3, pp. 159–173, 1994.
- [92] M. Y. Zarrugh and C. W. Radcliffe, “Simulation of swing phase dynamics in above-knee prostheses,” *J. Biomech.*, vol. 9, no. 5, pp. 283–292, Jan. 1976, doi: 10.1016/0021-9290(76)90050-6.

- [93] C. W. Radcliffe, “Biomechanics of Knee Stability Control with Four-Bar Prosthetic Knees,” presented at the ISPO Australia Annual Meeting, Melbourne, Australia, Nov. 2003. Accessed: Mar. 08, 2023. [Online]. Available: <http://rehabtech.com.au/techguide/pdf/>
- [94] P. Marisami and R. Venkatachalam, “Towards optimal toe-clearance in synthesizing polycentric prosthetic knee mechanism,” *Comput. Methods Biomed. Engin.*, vol. 25, no. 6, pp. 656–667, Apr. 2022, doi: 10.1080/10255842.2021.1972291.
- [95] R. K. Mohanty, R. C. Mohanty, and S. K. Sabut, “A systematic review on design technology and application of polycentric prosthetic knee in amputee rehabilitation,” *Phys. Eng. Sci. Med.*, vol. 43, no. 3, pp. 781–798, Sep. 2020, doi: 10.1007/s13246-020-00882-3.
- [96] “7E10 Helix3D Hip Joint Coding Justification.” Ottobock, Jan. 01, 2015. [Online]. Available: <https://shop.ottobock.ca/en/Prosthetics/Lower-Limb-Prosthetics/Hips/Helix3D-Hip-Joint%2C-right/p/7E10~5R#product-documents-section>
- [97] Purdue University, “Instantaneous Centers of Rotation (Instant Centers).” Accessed: Mar. 13, 2023. [Online]. Available: <https://www.purdue.edu/freeform/me274/>
- [98] Thomas Peacock, “Lecture 8 - Kinematics of Rigid Bodies - Instant Centers of Instantaneous Centers.” Massachusetts Institute of Technology, Mar. 05, 2007. Accessed: Mar. 13, 2023. [Online]. Available: <https://ocw.mit.edu/courses/2-003j-dynamics-and-control-i-spring-2007/>
- [99] T. M. Köhler, M. Bellmann, and S. Blumentritt, “Polycentric Exoprosthetic Knee Joints - Extent of Shortening During Swing Phase,” *Can. Prosthet. Orthot. J.*, vol. 3, no. 1, 2020.
- [100] J. de Vries, “Conventional 4-bar linkage knee mechanisms: A strength-weakness analysis,” *J. Rehabil. Res. Dev.*, vol. 32, no. 1, pp. 36–42, Feb. 1995.
- [101] X. Bonnet, H. Pillet, P. Fodé, F. Lavaste, and W. Skalli, “Gait analysis of a transfemoral amputee with a hydraulic polycentric knee prosthesis,” *Comput. Methods Biomed. Engin.*, vol. 12, no. sup1, pp. 59–60, Aug. 2009, doi: 10.1080/10255840903065530.
- [102] J. Andrysek, S. Klejman, R. Torres-Moreno, W. Heim, B. Steinnagel, and S. Glasford, “Mobility function of a prosthetic knee joint with an automatic stance phase lock,” *Prosthet. Orthot. Int.*, vol. 35, no. 2, pp. 163–170, Jun. 2011, doi: 10.1177/0309364611408495.
- [103] S. A. Gard, D. S. Childress, and J. E. Uellendahl, “The Influence of Four-Bar Linkage Knees on Prosthetic Swing-Phase Floor Clearance,” *JPO J. Prosthet. Orthot.*, vol. 8, no. 2, pp. 34–40, Spring 1996.
- [104] D. S. Chauhan, “Evaluation of the Polycentric Above Knee Prosthesis,” presented at the 15th National Conference on Machines and Mechanisms, Chennai, India: Indian Institute of Technology Madras, 2011. Accessed: Mar. 14, 2023. [Online]. Available: http://www.nacomm2011.ammindia.org/conf_proceedings.html

- [105] J. W. Sensinger, N. Intawachirarat, and S. A. Gard, “Contribution of prosthetic knee and ankle mechanisms to swing-phase foot clearance,” *IEEE Trans. Neural Syst. Rehabil. Eng. Publ. IEEE Eng. Med. Biol. Soc.*, vol. 21, no. 1, pp. 74–80, Jan. 2013, doi: 10.1109/TNSRE.2012.2224885.
- [106] C. Villa *et al.*, “Cross-Slope and Level Walking Strategies During Swing in Individuals With Lower Limb Amputation,” *Arch. Phys. Med. Rehabil.*, vol. 98, no. 6, pp. 1149–1157, Jun. 2017, doi: 10.1016/j.apmr.2016.10.007.
- [107] X. Drevelle, C. Villa, X. Bonnet, I. Loiret, P. Fodé, and H. Pillet, “Vaulting quantification during level walking of transfemoral amputees,” *Clin. Biomech. Bristol Avon*, vol. 29, no. 6, pp. 679–683, Jun. 2014, doi: 10.1016/j.clinbiomech.2014.04.006.
- [108] S. B. Michaud, S. A. Gard, and D. S. Childress, “A preliminary investigation of pelvic obliquity patterns during gait in persons with transtibial and transfemoral amputation,” *J. Rehabil. Res. Dev.*, vol. 37, no. 1, pp. 1–10, 2000.
- [109] D. A. Winter, “Foot Trajectory in Human Gait: A Precise and Multifactorial Motor Control Task,” *Phys. Ther.*, vol. 72, no. 1, pp. 45–53, Jan. 1992, doi: 10.1093/ptj/72.1.45.
- [110] I. Lončarić *et al.*, “The impact of the application of polycentric knee modules on balance control and the level of mobility in trans-femoral amputation,” *Rehabil. Ljubl.*, vol. 15, no. 3, pp. 39–44, Dec. 2016.
- [111] A. Taheri and M. T. Karimi, “Evaluation of the gait performance of above-knee amputees while walking with 3R20 and 3R15 knee joints,” *J. Res. Med. Sci. Off. J. Isfahan Univ. Med. Sci.*, vol. 17, no. 3, pp. 258–263, Mar. 2012.
- [112] K. Yokogushi, H. Narita, E. Uchiyama, S. Chiba, T. Nosaka, and K. Yamakoshi, “Biomechanical and clinical evaluation of a newly designed polycentric knee of transfemoral prosthesis,” *J. Rehabil. Res. Dev.*, vol. 41, no. 5, pp. 675–682, Sep. 2004, doi: 10.1682/jrrd.2003.05.0076.
- [113] S. Pfeifer, R. Riener, and H. Vallery, “An actuated transfemoral prosthesis with optimized polycentric knee joint,” *2012 4th IEEE RAS EMBS Int. Conf. Biomed. Robot. Biomechatronics BioRob*, pp. 1807–1812, Jun. 2012, doi: 10.1109/BioRob.2012.6290745.
- [114] J. F. Soriano, J. E. Rodríguez, and L. A. Valencia, “Performance comparison and design of an optimal polycentric knee mechanism,” *J. Braz. Soc. Mech. Sci. Eng.*, vol. 42, no. 5, Apr. 2020, doi: 10.1007/s40430-020-02313-6.

- [115] E. J. Wolf, V. Q. Everding, A. L. Linberg, B. L. Schnall, J. M. Czerniecki, and J. M. Gambel, “Assessment of transfemoral amputees using C-Leg and Power Knee for ascending and descending inclines and steps,” *J. Rehabil. Res. Dev.*, vol. 49, no. 6, pp. 831–842, 2012, doi: 10.1682/jrrd.2010.12.0234.
- [116] F. A. de Laat, M. J. van der Pluijm, A. A. van Kuijk, J. H. Geertzen, and L. D. Roorda, “Cosmetic effect of knee joint in a knee disarticulation prosthesis,” *J. Rehabil. Res. Dev.*, vol. 51, no. 10, pp. 1545–1554, 2014, doi: 10.1682/JRRD.2014.03.0068.
- [117] “OH5 Knee,” Össur. Accessed: Mar. 17, 2023. [Online]. Available: <https://www.ossur.com/en-us/prosthetics/knees/oh5-knee>
- [118] Nabtesco Corporation, “The 4-Bar Hydraulic Microprocessor Knee,” ALLUX. Accessed: Mar. 17, 2023. [Online]. Available: <https://www.allux.info/contents/spec.html>
- [119] “Total Knee® 2000,” Össur. Accessed: Mar. 17, 2023. [Online]. Available: <https://www.ossur.com/en-ca/prosthetics/knees/total-knee-2000>
- [120] “OHP3 Knee,” Össur. Accessed: Mar. 17, 2023. [Online]. Available: <https://www.ossur.com/en-ca/prosthetics/knees/ohp3-knee>
- [121] “Modular Knee Joint, servo-pneumatic | Knees - Mechanical | Lower Limb Prosthetics | Prosthetics | Ottobock CA Shop.” Accessed: Mar. 17, 2023. [Online]. Available: <https://shop.ottobock.ca/en/Prosthetics/Lower-Limb-Prosthetics/Knees---Mechanical/Modular-Knee-Joint%2C-servo-pneumatic/p/3R106-PRO>
- [122] “Knee Joints,” Tehlin Prosthetic & Orthopaedic. Accessed: Mar. 17, 2023. [Online]. Available: <https://www.tehlin.com/page-41580.html>
- [123] “Graph-Lite™ 4-Bar Pneumatic Knee,” OrtoPed. Accessed: Mar. 17, 2023. [Online]. Available: <https://www.ortoped.ca/en/graph-lite-sup-tm-sup-4-bar-pneumatic-knee.html>
- [124] A. M. El-Sayed, N. A. Hamzaid, and N. A. Abu Osman, “Technology Efficacy in Active Prosthetic Knees for Transfemoral Amputees: A Quantitative Evaluation,” *Sci. World J.*, vol. 2014, 2014, doi: 10.1155/2014/297431.
- [125] K. De Pauw *et al.*, “Prosthetic gait of unilateral lower-limb amputees with current and novel prostheses: A pilot study,” *Clin. Biomech.*, vol. 71, pp. 59–67, Jan. 2020, doi: 10.1016/j.clinbiomech.2019.10.028.
- [126] P. J. Theeven, B. Hemmen, P. R. Brink, R. J. Smeets, and H. A. Seelen, “Measures and procedures utilized to determine the added value of microprocessor-controlled prosthetic knee joints: a systematic review,” *BMC Musculoskelet. Disord.*, vol. 14, no. 1, Nov. 2013, doi: 10.1186/1471-2474-14-333.

- [127] M. Bellmann, T. M. Köhler, and T. Schmalz, “Comparative biomechanical evaluation of two technologically different microprocessor-controlled prosthetic knee joints in safety-relevant daily-life situations,” *Biomed. Eng. Biomed. Tech.*, vol. 64, no. 4, pp. 407–420, Aug. 2019, doi: 10.1515/bmt-2018-0026.
- [128] J. Thiele, C. Schöllig, M. Bellmann, and M. Kraft, “Designs and performance of three new microprocessor-controlled knee joints,” *Biomed. Eng. Biomed. Tech.*, vol. 64, no. 1, pp. 119–126, Feb. 2019, doi: 10.1515/bmt-2017-0053.
- [129] H. Herr and A. Wilkenfeld, “User-adaptive control of a magnetorheological prosthetic knee,” *Ind. Robot Int. J.*, vol. 30, no. 1, pp. 42–55, Jan. 2003, doi: 10.1108/01439910310457706.
- [130] “Ottobock 3R21 Polycentric Modular Knee Joints Instructions,” Manuals+. Accessed: Feb. 20, 2023. [Online]. Available: <https://lb.manuals.plus/ottobock/3r21-polycentric-modular-knee-joints-manual>
- [131] “EBS Knee Joint for Hip Disarticulation,” Ottobock. Accessed: Mar. 18, 2023. [Online]. Available: <https://shop.ottobock.ca/en/Prosthetics/Lower-Limb-Prosthetics/Knees---Mechanical/EBS-Knee-Joint-for-Hip-Disarticulation/p/3R60~5HD#product-documents-section>
- [132] Ottobock, “3R60 Family of Products - Hydraulic Controlled Polycentric Knee Joints - Information for Practitioners.” Aug. 01, 2014. Accessed: Mar. 18, 2023. [Online]. Available: <https://shop.ottobock.ca/en/Prosthetics/Lower-Limb-Prosthetics/Knees---Mechanical/EBS-Knee-Joint-for-Hip-Disarticulation/p/3R60~5HD#product-documents-section>
- [133] Ottobock, “Instructions for Use - 3R60, 3R60=ST, 3R60=KD, 3R60=HD.” Aug. 31, 2020. Accessed: Mar. 18, 2023. [Online]. Available: <https://shop.ottobock.ca/en/Prosthetics/Lower-Limb-Prosthetics/Knees---Mechanical/EBS-Knee-Joint-for-Hip-Disarticulation/p/3R60~5HD#product-documents-section>
- [134] E. Gailledrat *et al.*, “Does the new Helix 3D hip joint improve walking of hip disarticulated amputees?,” *Ann. Phys. Rehabil. Med.*, vol. 56, no. 5, pp. 411–418, Jul. 2013, doi: 10.1016/j.rehab.2013.05.001.
- [135] E. Ludwigs, A. Kannenberg, and D. Wüstefeld, “Evaluation of the Benefits of a New Prosthetic Hip Joint System in Activities of Daily Function in Patients after Hip Disarticulation or Hemipelvectomy,” *JPO J. Prosthet. Orthot.*, vol. 25, no. 3, pp. 118–126, Jul. 2013, doi: 10.1097/JPO.0b013e31829afc1c.
- [136] Jacqueline Perry and Judith M. Burnfield, “Gait Analysis: Normal and Pathological Function,” *J. Sports Sci. Med.*, vol. 9, no. 2, Jun. 2010, Accessed: Mar. 27, 2023. [Online]. Available: <https://www.ncbi.nlm.nih.gov/pmc/articles/PMC3761742/>

- [137] J. Rose, J. G. Gamble, and J. M. Adams, *Human Walking*, 3rd ed. Philadelphia: Lippincott Williams and Wilkins, 2006.
- [138] D. A. Winter, *The biomechanics and motor control of human gait: normal, elderly and pathological*, 2nd ed. Waterloo, Ont.: University of Waterloo Press, 1991. Accessed: Mar. 27, 2023. [Online]. Available: <http://catalog.hathitrust.org/api/volumes/oclc/24741459.html>
- [139] D. S. Pieringer, M. Grimmer, M. F. Russold, and R. Riener, “Review of the actuators of active knee prostheses and their target design outputs for activities of daily living,” in *2017 International Conference on Rehabilitation Robotics (ICORR)*, Jul. 2017, pp. 1246–1253. doi: 10.1109/ICORR.2017.8009420.
- [140] Abby Cain *et al.*, “Gait in prosthetic rehabilitation,” Physiopedia. Accessed: May 15, 2020. [Online]. Available: https://www.physio-pedia.com/Gait_in_prosthetic_rehabilitation
- [141] A. D. Segal *et al.*, “The effects of a controlled energy storage and return prototype prosthetic foot on transtibial amputee ambulation,” *Hum. Mov. Sci.*, vol. 31, no. 4, pp. 918–931, Aug. 2012, doi: 10.1016/j.humov.2011.08.005.
- [142] Stephen Kishner and James Monroe Laborde, “Gait Analysis After Amputation: Overview, Gait Cycle, Adaptive Strategies of Those Who Have Undergone Amputations,” *Medscape*, Dec. 2018, Accessed: Apr. 11, 2023. [Online]. Available: <https://emedicine.medscape.com/article/1237638-overview>
- [143] A. Esquenazi, “Gait Analysis in Lower-Limb Amputation and Prosthetic Rehabilitation,” *Phys. Med. Rehabil. Clin. N. Am.*, vol. 25, no. 1, pp. 153–167, Feb. 2014, doi: 10.1016/j.pmr.2013.09.006.
- [144] C. S. Mary, B. M. Kelly, and A. J. Davis, Eds., “Transfemoral Gait Deviations,” in *Prosthetic Restoration and Rehabilitation of the Upper and Lower Extremity*, New York, NY: Springer Publishing Company, 2013. doi: 10.1891/9781617051142.ap13.
- [145] E. L. Bukowski, “Atlas of Amputations and Limb Deficiencies: Surgical, Prosthetic, and Rehabilitation Principles, ed 3,” *Phys. Ther.*, vol. 86, no. 4, pp. 595–596, Apr. 2006, doi: 10.1093/ptj/86.4.595.
- [146] Abby Cain, “Gait deviations in amputees,” Physiopedia. Accessed: Jan. 18, 2023. [Online]. Available: https://www.physio-pedia.com/Gait_deviations_in_amputees
- [147] D. M. Collins, A. Karmarkar, R. Relich, P. F. Pasquina, and R. A. Cooper, “Review of research on prosthetic devices for lower extremity amputation,” *Crit. Rev. Biomed. Eng.*, vol. 34, no. 5, pp. 379–438, 2006, doi: 10.1615/CritRevBiomedEng.v34.i5.20.

- [148] M. Schaarschmidt, S. W. Lipfert, C. Meier-Gratz, H.-C. Scholle, and A. Seyfarth, “Functional gait asymmetry of unilateral transfemoral amputees,” *Hum. Mov. Sci.*, vol. 31, no. 4, pp. 907–917, Aug. 2012, doi: 10.1016/j.humov.2011.09.004.
- [149] A. D. Segal *et al.*, “Kinematic and kinetic comparisons of transfemoral amputee gait using C-Leg and Mauch SNS prosthetic knees,” *J. Rehabil. Res. Dev.*, vol. 43, no. 7, pp. 857–870, 2006, doi: 10.1682/JRRD.2005.09.0147.
- [150] H. Goujon-Pillet, E. Sapin, P. Fodé, and F. Lavaste, “Three-Dimensional Motions of Trunk and Pelvis During Transfemoral Amputee Gait,” *Arch. Phys. Med. Rehabil.*, vol. 89, no. 1, pp. 87–94, Jan. 2008, doi: 10.1016/j.apmr.2007.08.136.
- [151] S. M. H. J. Jaegers, J. H. Arendzen, and H. J. de Jongh, “Prosthetic gait of unilateral transfemoral amputees: A kinematic study,” *Arch. Phys. Med. Rehabil.*, vol. 76, no. 8, pp. 736–743, Aug. 1995, doi: 10.1016/S0003-9993(95)80528-1.
- [152] A. M. Boonstra, J. M. Schrama, W. H. Eisma, A. L. Hof, and V. Fidler, “Gait analysis of transfemoral amputee patients using prostheses with two different knee joints,” *Arch. Phys. Med. Rehabil.*, vol. 77, no. 5, pp. 515–520, May 1996, doi: 10.1016/S0003-9993(96)90044-1.
- [153] J. J. Genin, G. J. Bastien, B. Franck, C. Detrembleur, and P. A. Willems, “Effect of speed on the energy cost of walking in unilateral traumatic lower limb amputees,” *Eur. J. Appl. Physiol.*, vol. 103, no. 6, pp. 655–663, Aug. 2008, doi: 10.1007/s00421-008-0764-0.
- [154] J. Camargo, A. Ramanathan, W. Flanagan, and A. Young, “A comprehensive, open-source dataset of lower limb biomechanics in multiple conditions of stairs, ramps, and level-ground ambulation and transitions,” *J. Biomech.*, vol. 119, Apr. 2021, doi: 10.1016/j.jbiomech.2021.110320.
- [155] T. Kawaguchi, T. Yamada, and K. Iwashita, “Biomechanical gait analysis for a hip disarticulation prosthesis: power source for the swing phase of a hip disarticulation prosthetic limb,” *J. Phys. Ther. Sci.*, vol. 35, no. 5, pp. 361–365, 2023, doi: 10.1589/jpts.35.361.
- [156] Erik. J. Wolf, V. Q. Everding, A. A. Linberg, J. M. Czerniecki, and C. J. M. Gambel, “Comparison of the Power Knee and C-Leg during step-up and sit-to-stand tasks,” *Gait Posture*, vol. 38, no. 3, pp. 397–402, Jul. 2013, doi: 10.1016/j.gaitpost.2013.01.007.
- [157] M. J. Highsmith, J. T. Kahle, S. L. Carey, D. J. Lura, R. V. Dubey, and W. S. Quillen, “Kinetic Differences Using a Power Knee and C-Leg While Sitting Down and Standing Up: A Case Report,” *JPO J. Prosthet. Orthot.*, vol. 22, no. 4, pp. 237–243, Oct. 2010, doi: 10.1097/JPO.0b013e3181f46b65.
- [158] J. Laferrier and R. Gailey, “Advances in Lower-limb Prosthetic Technology,” *Phys. Med. Rehabil. Clin. N. Am.*, vol. 21, pp. 87–110, Feb. 2010, doi: 10.1016/j.pmr.2009.08.003.

- [159] O. A. Chiriac and D. Bucur, “From Conventional Prosthetic Feet to Bionic Feet. A Review,” in *Proceedings of the International Conference of Mechatronics and Cyber- MixMechatronics - 2020*, G. I. Gheorghe, Ed., in Lecture Notes in Networks and Systems. Cham: Springer International Publishing, 2020, pp. 130–138. doi: 10.1007/978-3-030-53973-3_14.
- [160] J. K. Hitt, R. Bellman, M. Holgate, T. G. Sugar, and K. W. Hollander, “The sparky (spring ankle with regenerative kinetics) project: Design and analysis of a robotic transtibial prosthesis with regenerative kinetics,” presented at the 2007 Proceedings of the ASME International Design Engineering Technical Conferences and Computers and Information in Engineering Conference, DETC2007, 2008, pp. 1587–1596. doi: 10.1115/DETC2007-34512.
- [161] S. K. Au, H. Herr, J. Weber, and E. C. Martinez-Villalpando, “Powered Ankle-Foot Prosthesis for the Improvement of Amputee Ambulation,” in *2007 29th Annual International Conference of the IEEE Engineering in Medicine and Biology Society*, Aug. 2007, pp. 3020–3026. doi: 10.1109/IEMBS.2007.4352965.
- [162] G. L. Novelli and R. M. Andrade, “Towards an Active Ankle-Foot Prosthesis Powered by Dielectric Elastomer Actuators in Antagonistic Pairs,” in *2021 International Symposium on Medical Robotics (ISMR)*, Nov. 2021, pp. 1–6. doi: 10.1109/ISMR48346.2021.9661530.
- [163] Q. Huang, B. Li, F. Jia, and P. Wang, “A Novel Design of Electro-hydraulic Driven Active Powered Ankle-Foot Prosthesis,” *Lect. Notes Comput. Sci. Subser. Lect. Notes Artif. Intell. Lect. Notes Bioinforma.*, vol. 13013 LNAI, pp. 622–630, 2021, doi: 10.1007/978-3-030-89095-7_59.
- [164] A. Poliakov, A. Ryzhkov, M. Kolesova, P. Shtanko, P. Sopin, and P. Bugayov, “Novel Design of an Active Transfemoral Prosthesis with Intellectual-Synergetic Control System,” in *2020 International Conference on Electrical, Communication, and Computer Engineering (ICECCE)*, Jun. 2020, pp. 1–6. doi: 10.1109/ICECCE49384.2020.9179189.
- [165] Y. Jiang, H. An, Y. Liu, Y. Huang, H. Ma, and Q. Wei, “An Active-passive Lightweight Prosthesis Simulating Normal Human Walking Gait,” in *2022 6th International Conference on Robotics and Automation Sciences (ICRAS)*, Jun. 2022, pp. 157–161. doi: 10.1109/ICRAS55217.2022.9842140.
- [166] B. J. Hafner and R. L. Askew, “Physical performance and self-report outcomes associated with use of passive, adaptive, and active prosthetic knees in persons with unilateral, transfemoral amputation: Randomized crossover trial,” *J. Rehabil. Res. Dev.*, vol. 52, no. 6, pp. 677–700, 2015, doi: 10.1682/JRRD.2014.09.0210.
- [167] M. Fan, Y. Chen, B. He, Q. Meng, and H. Yu, “Study on Adaptive Adjustment of Variable Joint Stiffness for a Semi-active Hip Prosthesis,” in *Intelligent Robotics and Applications*, H. Liu, Z.

- Yin, L. Liu, L. Jiang, G. Gu, X. Wu, and W. Ren, Eds., in Lecture Notes in Computer Science. Cham: Springer International Publishing, 2022, pp. 13–23. doi: 10.1007/978-3-031-13822-5_2.
- [168] B. Laschowski and J. Andrysek, “Electromechanical Design of Robotic Transfemoral Prostheses,” presented at the ASME 2018 International Design Engineering Technical Conferences and Computers and Information in Engineering Conference, American Society of Mechanical Engineers Digital Collection, Nov. 2018. doi: 10.1115/DETC2018-85234.
- [169] *Harmonic Drive® Strain Wave Gear Principle | Harmonic Drive SE*, (Apr. 04, 2014). Accessed: Mar. 28, 2023. [Online Video]. Available: <https://www.youtube.com/watch?v=nj1vO3cP7ug>
- [170] “Strain Wave Gear Principle,” Harmonic Drive LLC. Accessed: Mar. 28, 2023. [Online]. Available: <https://www.harmonicdrive.net/technology/harmonicdrive>
- [171] “Harmonic Drive® Gears.” Harmonic Drive SE, Jun. 2022. Accessed: Mar. 28, 2023. [Online]. Available: https://harmonicdrive.de/fileadmin/user_upload/Harmonic_Drive_Gears_EN_1050860_06_2022.pdf
- [172] “High-ratio speed reducer based on elastic deformation of an elliptical gear - MATLAB,” MathWorks. Accessed: Mar. 28, 2023. [Online]. Available: <https://www.mathworks.com/help/sdl/ref/harmonicdrive.html>
- [173] “Instructions for Use - Power Knee™ PKA01.” Össur, Oct. 12, 2022. Accessed: Mar. 29, 2023. [Online]. Available: <https://www.ossur.com/en-ca/prosthetics/knees/power-knee>
- [174] “Power Knee Mainstream Catalog.” Össur. Accessed: Mar. 29, 2023. [Online]. Available: <https://www.ossur.com/en-ca/prosthetics/knees/power-knee>
- [175] E. J. Rouse, L. M. Mooney, and H. M. Herr, “Clutchable series-elastic actuator: Implications for prosthetic knee design,” *Int. J. Robot. Res.*, vol. 33, no. 13, pp. 1611–1625, Nov. 2014, doi: 10.1177/0278364914545673.
- [176] M. Goldfarb, “Consideration of Powered Prosthetic Components as They Relate to Microprocessor Knee Systems,” *JPO J. Prosthet. Orthot.*, vol. 25, no. 4S, pp. P65–P75, Oct. 2013, doi: 10.1097/JPO.0b013e3182a8953e.
- [177] S. Pfeifer, A. Pagel, R. Riener, and H. Vallery, “Actuator With Angle-Dependent Elasticity for Biomimetic Transfemoral Prostheses,” *IEEEASME Trans. Mechatron.*, vol. 20, Jun. 2015, doi: 10.1109/TMECH.2014.2337514.

- [178] T. Lenzi, M. Cempini, L. J. Hargrove, and T. A. Kuiken, “Actively variable transmission for robotic knee prostheses: 2017 IEEE International Conference on Robotics and Automation, ICRA 2017,” *ICRA 2017 - IEEE Int. Conf. Robot. Autom.*, pp. 6665–6671, Jul. 2017, doi: 10.1109/ICRA.2017.7989787.
- [179] E. J. Rouse, L. M. Mooney, and L. J. Hargrove, “The design of a lightweight, low cost robotic knee prosthesis with selectable series elasticity,” in *2016 6th IEEE International Conference on Biomedical Robotics and Biomechatronics (BioRob)*, Singapore, Singapore: IEEE Press, Jun. 2016, p. 1055. doi: 10.1109/BIOROB.2016.7523770.
- [180] L. Mooney and H. Herr, “Continuously-Variable Series-Elastic Actuator,” *IEEE Int. Conf. Rehabil. Robot. Proc.*, vol. 2013, pp. 1–6, Jun. 2013, doi: 10.1109/ICORR.2013.6650402.
- [181] M. Wu, T. Driver, S.-K. Wu, and X. Shen, “Design and Preliminary Testing of a Pneumatic Muscle-Actuated Transfemoral Prosthesis,” *J. Med. Devices*, vol. 8, no. 4, Aug. 2014, doi: 10.1115/1.4026830.
- [182] “High Torque Series Brushless DC Motors - Direct Drive Housed and Frameless Brushless DC Motors - Engineering Guide.” Hathaway Emoteq, Inc.
- [183] D. Langlois, “Power Hip Proof-Of-Concept Testing - Technical Brief - Version 1.0.” Ossur, May 08, 2012.
- [184] S. J. Mulholland and U. P. Wyss, “Activities of daily living in non-Western cultures: range of motion requirements for hip and knee joint implants,” *Int. J. Rehabil. Res.*, vol. 24, no. 3, pp. 191–198, Sep. 2001.
- [185] C. Pinheiro *et al.*, “Kinematic and kinetic study of sit-to-stand and stand-to-sit movements towards a human-like skeletal model*,” in *2019 IEEE 6th Portuguese Meeting on Bioengineering (ENBENG)*, Feb. 2019, pp. 1–4. doi: 10.1109/ENBENG.2019.8692569.
- [186] International Organization for Standardization, *Prostheses. Structural testing of hip joints.*, Under Review. 2000.
- [187] C. D. Fryar, Q. Gu, and C. L. Ogden, “Anthropometric reference data for children and adults: United States, 2007-2010,” *Vital Health Stat. 11.*, no. 252, pp. 1–48, Oct. 2012.
- [188] J. P. Vidusic, *Machine design projects*. New York: Ronald Press Co, 1957. Accessed: Oct. 30, 2023. [Online]. Available: <http://books.google.com/books?id=RcA3AAAAMAAJ>
- [189] R. C. Juvinall and K. M. Marshek, *Fundamentals of Machine Component Design*, 5th ed. Wiley, 2012. Accessed: Oct. 28, 2019. [Online]. Available: <https://www.wiley.com/en-us/Fundamentals+of+Machine+Component+Design%2C+6th+Edition-p-9781118987681>

- [190] National Aeronautics and Space Administration (NASA), *Man-Systems Integration Standards - NASA STD 3000 - Anthropometry and Biomechanics*, vol. 1, 2 vols. NASA, 1995. [Online]. Available: <https://msis.jsc.nasa.gov/sections/section03.htm>
- [191] C. Tudor-Locke *et al.*, “How Many Steps/day Are Enough? For Adults,” *Int. J. Behav. Nutr. Phys. Act.*, vol. 8, no. 1, Jul. 2011, doi: 10.1186/1479-5868-8-79.
- [192] E. Reznick, K. R. Embry, R. Neuman, E. Bolívar-Nieto, N. P. Fey, and R. D. Gregg, “Lower-limb kinematics and kinetics during continuously varying human locomotion,” *Sci. Data*, vol. 8, no. 1, Oct. 2021, doi: 10.1038/s41597-021-01057-9.
- [193] A. Protopapadaki, W. I. Drechsler, M. C. Cramp, F. J. Coutts, and O. M. Scott, “Hip, knee, ankle kinematics and kinetics during stair ascent and descent in healthy young individuals,” *Clin. Biomech.*, vol. 22, no. 2, pp. 203–210, Feb. 2007, doi: 10.1016/j.clinbiomech.2006.09.010.
- [194] “Isotropic,” Instron. Accessed: Sep. 03, 2023. [Online]. Available: <https://www.instron.com/en-us/resources/glossary/isotropic>
- [195] R. C. Hibbeler, *Mechanics of materials*, Tenth edition. Boston: Pearson, 2017.
- [196] “Yield criteria for metals,” University of Cambridge. Accessed: Sep. 03, 2023. [Online]. Available: https://www.doitpoms.ac.uk/tplib/metal-forming-1/yield_criteria.php
- [197] K. Kersch, “3D-Vibration Testing for Automotive Components,” 2020. doi: 10.25673/35154.
- [198] “ARMCO 17-4 PH Stainless Steel Product Data Bulletin.” AK Steel, 2018.
- [199] “Aluminum 2024-T4; 2024-T351,” MatWeb Material Property Data. Accessed: Sep. 04, 2023. [Online]. Available: <https://www.matweb.com/search/datasheet.aspx?matguid=67d8cd7c00a04ba29b618484f7ff7524&n=1>
- [200] “17-4 PH Stainless Steel Bar - 17-4 ASTM A564 Supplier | Best Stainless,” Best Stainless & Alloys. [Online]. Available: <https://www.beststainless.com/17-4-ph-stainless-steel.html>
- [201] J.-H. Wu and C.-K. Lin, “Tensile and fatigue properties of 17-4 PH stainless steel at high temperatures,” *Metall. Mater. Trans. A*, vol. 33, no. 6, pp. 1715–1724, Jun. 2002, doi: 10.1007/s11661-002-0180-8.
- [202] “M2 Molybdenum High Speed Tool Steel (UNS T11302),” AZoM. Accessed: Nov. 15, 2022. [Online]. Available: <https://www.azom.com/article.aspx?ArticleID=6174>
- [203] Ch. R. Sohar, A. Betzwar Kotas, C. Gierl, B. Weiss, and H. Danninger, “Fatigue behaviour of M2 and M42 high speed steel up to the gigacycle regime,” *Kov. Mater.*, vol. 47, pp. 147–158, Jan. 2009.

- [204] “INA HN0808 full complement needle bearings,” Nodes. Accessed: Jan. 11, 2022. [Online]. Available: <https://www.nodeshk.com/ina/needle-bearings/hn0808.html>
- [205] “JTEKT Koyo (NRB) B-68,” MiMotion. Accessed: Sep. 12, 2023. [Online]. Available: <https://www.motioncanada.ca/products/sku/00090438?fromSisterSite=true>
- [206] M. Labrosse, “MCG 4102/5108 Finite Element Analysis.” University of Ottawa, Sep. 2019.
- [207] Q. Grimal and P. Laugier, “Quantitative Ultrasound Assessment of Cortical Bone Properties Beyond Bone Mineral Density,” *IRBM*, vol. 40, no. 1, pp. 16–24, Feb. 2019, doi: 10.1016/j.irbm.2018.10.006.
- [208] J. Currey, “The structure and mechanical properties of bone,” in *Bioceramics and their Clinical Applications*, Elsevier, 2008, pp. 3–27. doi: 10.1533/9781845694227.1.3.
- [209] L.-C. Gerhardt and A. Boccaccini, “Review – Bioactive Glass and Glass-Ceramic Scaffolds for Bone Tissue Engineering,” *Materials*, vol. 3, Jul. 2010, doi: 10.3390/ma3073867.
- [210] G. A. Daysal *et al.*, “The relationship between hip joint space width, center edge angle and acetabular depth,” *Osteoarthritis Cartilage*, vol. 15, no. 12, pp. 1446–1451, Dec. 2007, doi: 10.1016/j.joca.2007.05.016.
- [211] “Mesh Quality Checks SOLIDWORKS Help,” Dassault Systèmes. Accessed: Sep. 06, 2023. [Online]. Available: https://help.solidworks.com/2024/English/SolidWorks/cworks/c_Mesh_Quality_Checks.htm?verRedirect=1
- [212] Dassault Systèmes, “Pin Connectors SOLIDWORKS Help.” Accessed: Sep. 11, 2023. [Online]. Available: https://help.solidworks.com/2024/english/SolidWorks/cworks/c_Pin_Connectors.htm?verRedirect=1
- [213] H. Mayer, R. Schuller, and M. Fitzka, “Fatigue of 2024-T351 aluminium alloy at different load ratios up to 1010 cycles,” *Int. J. Fatigue*, vol. 57, pp. 113–119, Dec. 2013, doi: 10.1016/j.ijfatigue.2012.07.013.
- [214] “Strength Specifications of Metric Threaded Fasteners,” Westfield Fasteners. Accessed: Nov. 13, 2023. [Online]. Available: https://www.westfieldfasteners.co.uk/Ref_Strength_Spec.html
- [215] A. Marcelo, A. Uehara, R. M. Utiyama, and I. Ferreira, “Fatigue Properties of High Strength Bolts,” *Procedia Eng.*, vol. 10, pp. 1298–1303, Dec. 2011, doi: 10.1016/j.proeng.2011.04.216.
- [216] “THK Cross-Roller Ring Series Compact, Highly Rigid Swivel Ring Achieving a Superb Rotation Accuracy.” THK Co., Ltd. [Online]. Available: <https://www.thkstore.com/mwdownloads/download/link/id/301/>

- [217] C. H. Simmons, D. E. Maguire, and N. Phelps, “21 - Limits and fits,” in *Manual of Engineering Drawing (Fifth Edition)*, Oxford: Butterworth-Heinemann, 2020, pp. 279–291. doi: 10.1016/B978-0-12-818482-0.00021-9.
- [218] “Linear Dimensions Tolerance Chart (ISO 2768-1),” AmesWeb. Accessed: Sep. 13, 2022. [Online]. Available: <https://amesweb.info/fits-tolerances/iso-2768-linear-dimensions-tolerances.aspx>
- [219] “Angular Dimensions Tolerances (ISO 2768-1),” AmesWeb. Accessed: Sep. 13, 2022. [Online]. Available: <https://amesweb.info/fits-tolerances/iso-2768-angular-dimensions-tolerances.aspx>
- [220] “International Standard ISO 286-1, Geometrical product specifications (GPS) — ISO code system for tolerances on linear sizes — Part 1: Basis of tolerances, deviations and fits (Second Edition).” International Organization for Standardization (ISO), Apr. 15, 2010.
- [221] “International Standard ISO 286-2, Geometrical product specifications (GPS) — ISO code system for tolerances on linear sizes — Part 2: Tables of standard tolerance classes and limit deviations for holes and shafts (Second Edition).” International Organization for Standardization (ISO), Jun. 15, 2010.
- [222] “Fit tolerances and applications,” mec Engineering Spreadsheets. Accessed: Sep. 05, 2022. [Online]. Available: <http://www.mec-engineering-spreadsheets.com/documentation-area/fit-tolerances-and-applications/>
- [223] International Organization for Standardization ISO, “Surface Roughness in Manufacturing,” ISO Finishing. Accessed: Sep. 14, 2022. [Online]. Available: <https://isofinishing.com/surface-roughness-in-manufacturing/>
- [224] “Formulas for Interference (Press & Shrink) Fit Calculations,” AmesWeb. Accessed: Sep. 21, 2023. [Online]. Available: <https://amesweb.info/press-fit/interference-fit-formulas.aspx>
- [225] Alexander H. Slocum, *Precision Machine Design*. Dearborn, MI: Society of Manufacturing Engineers, 1995.
- [226] “Static Friction Coefficients,” StructX. Accessed: Jun. 10, 2022. [Online]. Available: https://structx.com/Material_Properties_005a.html
- [227] A. Fanous, “Hip Disarticulation Prosthesis Simulator,” University of Ottawa, Ottawa, Ontario, Canada, 2021.
- [228] “Newport 3 – Unique Patented Disk Technology Adjusts Easily for Hip Development,” Orthomerica. Accessed: Oct. 23, 2023. [Online]. Available: <https://www.orthomerica.com/products/newport/newport-3/>

- [229] “Pro-Flex® ST Waterproof Prosthetic Foot,” Össur. Accessed: Oct. 23, 2023. [Online]. Available: <https://www.ossur.com/en-ca/prosthetics/feet/pro-flex-st>
- [230] M. Vezočnik and M. B. Juric, “Average Step Length Estimation Models’ Evaluation Using Inertial Sensors: A Review,” *IEEE Sens. J.*, vol. 19, no. 2, pp. 396–403, Jan. 2019, doi: 10.1109/JSEN.2018.2878646.
- [231] C. Tudor-Locke *et al.*, “Walking cadence (steps/min) and intensity in 21–40 year olds: CADENCE-adults,” *Int. J. Behav. Nutr. Phys. Act.*, vol. 16, no. 1, Jan. 2019, doi: 10.1186/s12966-019-0769-6.
- [232] M. J. Highsmith *et al.*, “Gait Training Interventions for Lower Extremity Amputees: A Systematic Literature Review,” *Technol. Innov.*, vol. 18, no. 2–3, pp. 99–113, Sep. 2016, doi: 10.21300/18.2-3.2016.99.
- [233] “16010 - Deep groove ball bearing,” SKF. Accessed: Nov. 30, 2022. [Online]. Available: <https://www.skf.com/ca/en/products/rolling-bearings/ball-bearings/deep-groove-ball-bearings/productid-16010>
- [234] L. Li, D. H. Myszka, A. P. Murray, and C. W. Wampler, “Using the Singularity Trace to Understand Linkage Motion Characteristics,” in *Volume 6A: 37th Mechanisms and Robotics Conference*, Portland, Oregon, USA: American Society of Mechanical Engineers, Aug. 2013, pp. 6–13. doi: 10.1115/DETC2013-13244.
- [235] S. Zlatanov, “Generalized singularity analysis of mechanisms,” Doctoral, University of Toronto, Toronto, Canada, 1998.
- [236] D. Croccolo, M. De Agostinis, and N. Vincenzi, “Experimental study of friction in aluminium bolted joints,” *EPJ Web Conf.*, vol. 6, 2010, doi: 10.1051/epjconf/20100608003.
- [237] “Fastener Torque,” Engineering Library. Accessed: Nov. 12, 2022. [Online]. Available: <https://engineeringlibrary.org/reference/fastener-torque-nasa-design-manual>
- [238] “Metric Bolts - Tightening Torques,” The Engineering Toolbox. Accessed: Jul. 01, 2022. [Online]. Available: https://www.engineeringtoolbox.com/metric-bolts-maximum-torque-d_2054.html
- [239] “Overview of materials for Polylactic Acid (PLA) Biopolymer,” MatWeb Material Property Data. Accessed: Sep. 18, 2023. [Online]. Available: <https://www.matweb.com/search/DataSheet.aspx?MatGUID=ab96a4c0655c4018a8785ac4031b9278&ckck=1>
- [240] Z. Oksiuta, M. Jalbrzykowski, J. Mystkowska, E. Romanczuk, and T. Osiecki, “Mechanical and Thermal Properties of Polylactide (PLA) Composites Modified with Mg, Fe, and Polyethylene (PE) Additives,” *Polymers*, vol. 12, no. 12, Dec. 2020, doi: 10.3390/polym12122939.

Appendix A: Candidate Designs

This appendix describes previously considered powered four-bar hip designs and reasons why they were eliminated from the selection process. Brief engineering analyses are outlined for designs that were likely to fulfill the design criteria.

A.1 Single-Axis Powered Four-Bar Hip

The most basic approach of powering a prosthetic hip is to fix the motor to the socket and have the prosthetic hip center be coaxial with the motor center (Figure A-1). The motor would rotate in either direction to provide hip flexion or extension. This design would require fewer components than other approaches and be lighter since most of the prosthetic hip mass would be the motor mass. The disadvantage of this design, however, is that the motor would protrude to an extent where an individual would not be able to fit the prosthetic hip under their clothing, and/or they would have difficulty with sitting and bending over. For optimal cosmesis, the motor would be placed within the prosthetic thigh.

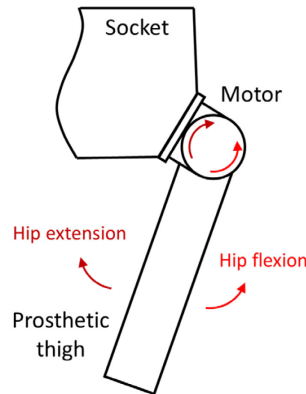


Figure A-1: Single-axis powered hip with the motor attached to the anterior face of the socket.

For the motor to be within the prosthetic thigh, torque must be transmitted from the motor to the hip center of rotation. A four-bar linkage would guide the pendulum motion of the prosthetic thigh and transmit simultaneously power from the thigh to the hip.

A.2 Direct Drive Four-Bar Hip with Posterior Motor

When the motor is centered at one of the four-bar pin linkage pins, motor torque is transferred to one of the links and directly drives linkage motion. One candidate design centered the motor at the posteroinferior pin (Figure A-2). The motor is housed inside two inferior link halves screwed together and is interfaced with the posterior link via shaft-pin connections. Motor torque is applied on one side of the powered hip (either the medial or lateral side), and rotation is transmitted to the other side through the H-shaped posterior link. Throughout hip motion, the motor remains fixed relative to the

inferior link and applies torque to the posterior link. Since a four-bar linkage is a closed kinematic chain, posterior link rotation is transferred to the inferior and anterior links resulting in the overall pendulum motion of the thigh.

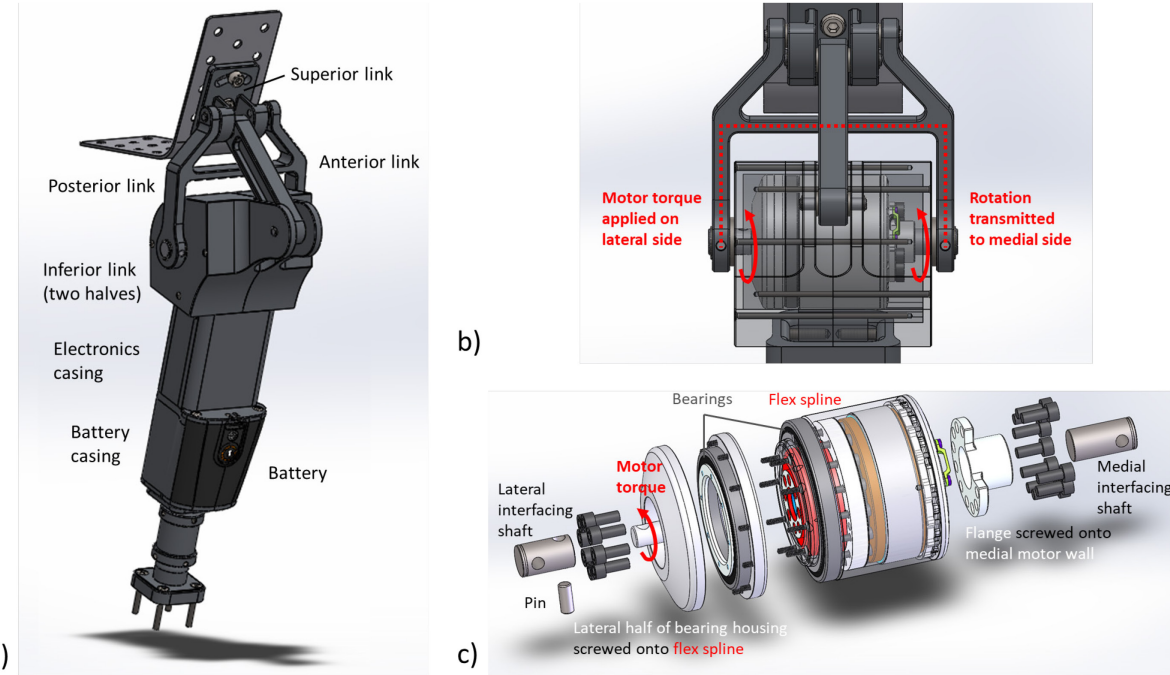


Figure A-2: Direct-drive posterior motor hip for a right-leg prosthesis: a) hip joint integrated within prosthetic thigh, b) motor torque transmission to the linkage, c) motor-linkage interfacing.

Figure A-3 shows four frames of this design's ROM from 37° hip extension to 127° hip flexion. Hip flexion and extension are limited by contact with the prosthetic socket. Neutral position occurs when the prosthetic thigh is tilted backward slightly, placing the knee behind the hip, and promoting stance phase stability. Changes in motor angle are indicated by changes in the angle between the posterior link and the inferior link's upper edge. The motor inputs torque at posteroinferior pin. Output torque occurs at the hip joint's ICR. Viewing the hip laterally, CW torque generates hip flexion, and CCW torque generates hip extension.

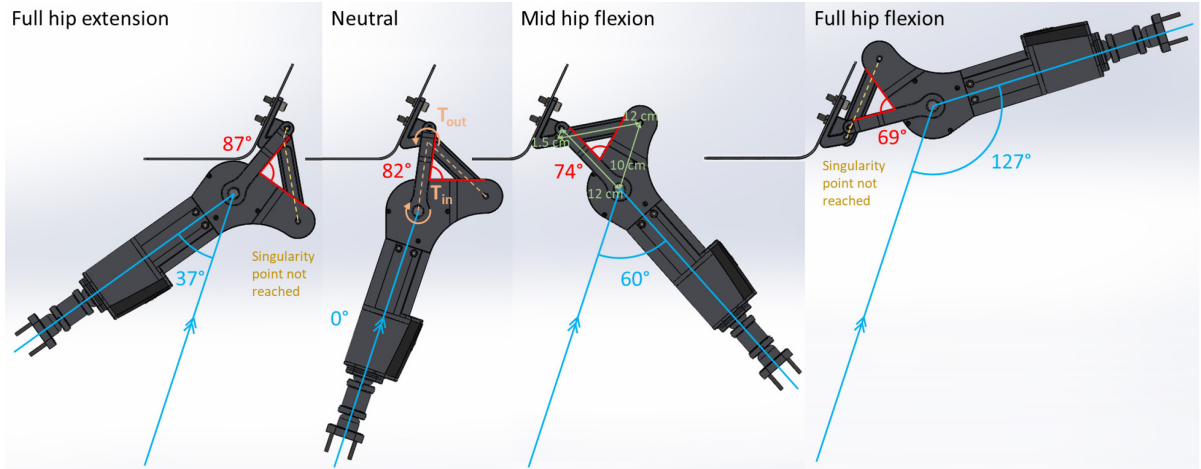


Figure A-3: Direct-drive posterior motor hip range of motion. Hip flexion-extension angle is in blue, motor angle is in red, and link dimensions are in green.

Posterior link length is 12 cm, inferior link length is 10 cm, anterior link length is 12 cm, and superior link length is 1.5 cm. Link lengths were selected through a trial-and-error process with a four-bar linkage model in the SolidWorks (CAD) software. Helix3D link lengths were initially selected and were adjusted until the lengths shown in Figure A-3 were obtained. These lengths correlate to an optimal combination of hip ROM and mechanical advantage for the directly driven four-bar hip with a posterior motor. The 3D model confirmed that the device moves through its expected ROM without structural interference, and that the device does not protrude too much in the standing (neutral) and sitting positions.

The powered hip's ROM depends on singularity point location within four-bar linkage ROM. A four-bar linkage has two singularity points, instances in linkage motion at which the driving link can no longer move the mechanism [234], [235]. The linkage becomes locked, and the mechanical advantage goes to zero [234], [235]. At a singularity point in a four-revolute linkage occurs when the driven pivots are collinear [234], [235]. Ideally, hip flexion and extension should be physically limited before the joint can reach its two singularity points. Otherwise, hip ROM will be limited to one or both singularity points, and the mechanism can become jammed if the joint is forced beyond a singularity point.

In the case of this candidate design, a singularity point results when the anterior and superior links are collinear. As demonstrated in Figure A-3, the extension singularity point occurs far beyond the physical hip extension limit, and the flexion singularity point occurs slightly beyond the physical hip flexion limit. Therefore, the design has an unrestricted hip flexion-extension ROM of 164°. The angle between the posterior link and the inferior link's upper edge changes from 87° to 69° (i.e., the motor rotates 18° CW when the hip rotates from full extension to full flexion).

Substituting $\Delta\theta_{motor} = 18^\circ$ and $\Delta\theta_{hip} = 164^\circ$ in Eq. (4-5) yields $(MA)_{average} = 0.11$ for this candidate design. Figure A-3 shows that the design's mechanical advantage remains approximately constant from full hip extension to mid hip flexion, and gradually decreases as the linkage approaches full hip flexion. Ideally, mechanical advantage should be 1 or greater throughout hip ROM because the Össur actuator torque capacity falls within hip flexion-extension moment requirements. Although this design has a large ROM, it was rejected due to its low average mechanical advantage.

A.3 Direct Drive Four-Bar Hip with Anterior Motor

The motor can also be centered at the anteroinferior pin (Figure A-4). Like the posterior motor design, the motor is housed inside two inferior link halves screwed together but is instead interfaced with the anterior link via the same shaft-pin connections shown in Figure A-2. Like the previous design, the motor remains fixed relative to the inferior link throughout hip motion. In this case, the motor applies torque to the H-shaped anterior link to drive the motion of the inferior and posterior links, resulting in the overall pendulum motion of the thigh.

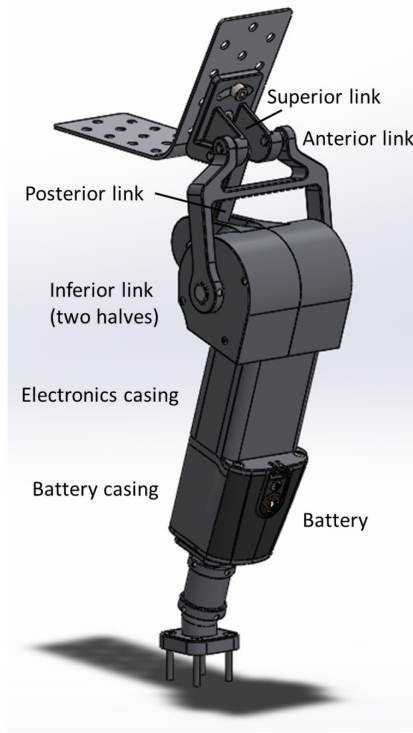


Figure A-4: Direct-drive anterior motor hip for a right-leg prosthesis.

In the previous candidate design, the posterior link connected to the superior link anterior pin and the anterior link connected to the superior posterior pin (i.e., the anterior and posterior links crossed each other). Unlike the previous design, this design's posterior link connects to the superior link

posterior pin, and the anterior link connects to the superior link anterior pin (i.e., the anterior and posterior links do not cross each other).

Figure A-5 shows four frames of this design's ROM from 23° hip extension to 122° hip flexion. Hip extension is limited by a stop in the superior link, and hip flexion is limited by contact with the prosthetic socket. Like in the previous design, the knee joint is placed slightly behind the hip joint in neutral position to enhance stance phase stability. Changes in motor angle are indicated by changes in the angle between the anterior link and the inferior link's upper edge. The motor inputs torque at the anteroinferior pin, and as before, output torque occurs at the hip joint's ICR. Viewing the hip laterally, CCW torque generates hip flexion, and CW torque generates hip extension.

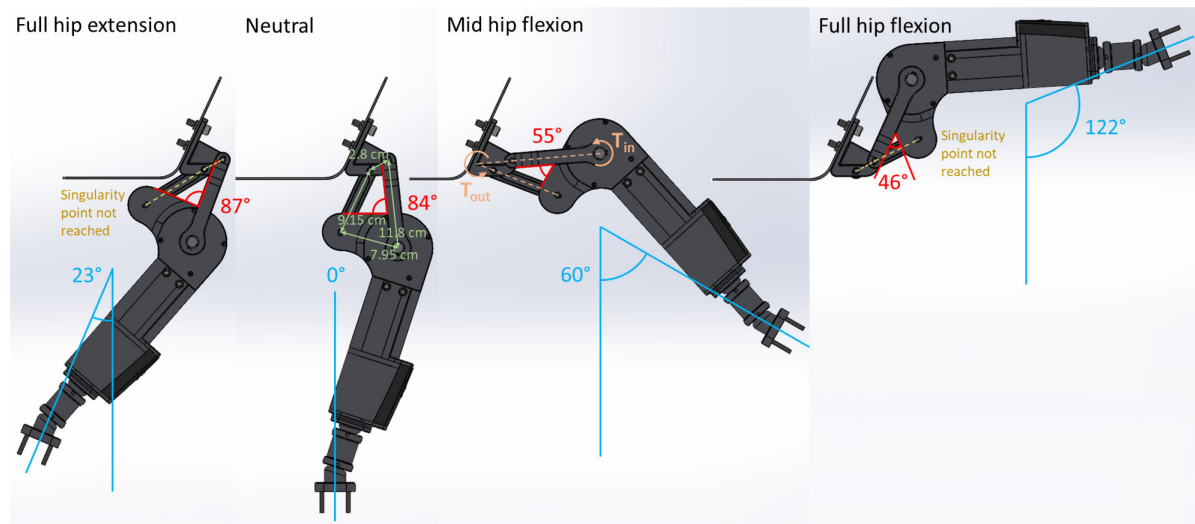


Figure A-5: Direct-drive anterior motor hip range of motion. Hip flexion-extension angle is in blue, motor angle is in red, and link dimensions are in green.

Posterior link length is 9.15 cm, inferior link length is 7.95 cm, anterior link length is 11.8 cm, and superior link length is 2.8 cm. Like for the previous design, link lengths were selected through a SolidWorks modelling trial-and-error process. The selected lengths result in an optimal combination of hip ROM and mechanical advantage for the directly driven four-bar hip with an anterior motor. The 3D model confirmed that the design has no structural interference and does not overly protrude in the standing or sitting positions.

Figure A-5 demonstrates that hip flexion and extension singularity points occur slightly beyond their respective physical limits. Thus, the design has an unrestricted hip flexion-extension ROM of 145°. The angle between the anterior link and the inferior link's upper edge changes from 87° to 46° (i.e., the motor rotates 41° CCW) when the hip moves from full extension to full flexion.

Substituting $\Delta\theta_{motor} = 41^\circ$ and $\Delta\theta_{hip} = 145^\circ$ in Eq. (4-5) yields $(MA)_{average} = 0.28$ for this candidate design. A greater change in motor angle for a given change in hip flexion-extension

results in a larger mechanical advantage. Figure A-5 shows that the design's mechanical advantage peaks in between neutral and mid flexion positions and tapers off near hip ROM extremities. Calculations presented in Sections 5.4 and 5.5 demonstrated that for best performance, mechanical advantage should be maximal near neutral position. Like the previous design, this design was rejected due to its low mechanical advantage.

A.4 Summary

Table A-1 compares the posterior motor direct-drive four-bar hip to the anterior motor direct-drive four-bar hip. Compared to the posterior motor design, the anterior motor design has a shorter average link length, a smaller ROM, and a larger mechanical advantage. The four-bar linkage design process presents a trade-off between ROM and mechanical advantage.

Table A-1: Design specifications for the posterior motor direct-drive four-bar hip and the anterior motor direct-drive four-bar hip.

Design Specifications	Posterior Motor Design	Anterior Motor Design
Posterior link length	12 cm	9.15 cm
Inferior link length	10 cm	7.95 cm
Anterior link length	12 cm	11.8 cm
Superior link length	1.5 cm	2.8 cm
Maximum hip extension	37°	23°
Maximum hip flexion	127°	122°
Average mechanical advantage	0.11	0.28

Both posterior motor and anterior motor designs satisfy the 20° hip extension criterion but fall slightly short of the 130° hip flexion criterion. Nevertheless, both designs have been eliminated due to their average MAs being substantially below 1.

Appendix B: MATLAB Code

This appendix contains the 36 MATLAB scripts used for the powered hip working analysis. These scripts are listed as subsection titles. Appendix B.1 contains the main program with seven analysis options whose scripts are contained in Appendices B.2 to B.8. ‘Main.m’ can be run indefinitely with any analysis option from 1 to 7. Appendices B.9 to B.36 are the remaining subprogram scripts listed in alphabetical order.

To run the MATLAB code, the user is required to save the ‘m’ files listed from Appendices B.1 to B.36 in the same folder. Additionally, the user is required to save the ‘RAW_data.mat’ file and the following Excel files in the same folder containing the MATLAB code:

- Healthy hip flexion-extension - Camargo et al. – 2021.csv
- Healthy knee flexion-extension - Camargo et al. 2021.csv
- Healthy sagittal hip moment - Camargo et al. 2021.csv
- Healthy sagittal hip power - Camargo et al. 2021.csv
- Healthy sagittal knee moment - Camargo et al. 2021.csv
- Healthy sagittal knee power - Camargo et al. 2021.csv
- Healthy sagittal pelvic tilt - Ludwigs et al. 2010.csv
- Helix3D hip flexion-extension - Ludwigs et al. 2010.csv
- Helix3D knee flexion-extension - Ludwigs et al. 2010.csv
- Helix3D sagittal hip moment - Ludwigs et al. 2010.csv
- Helix3D sagittal knee moment - Ludwigs et al. 2010.csv
- Helix3D sagittal pelvic tilt - Ludwigs et al. 2010.csv
- HKAFP kinematic data of individual strides.xlsx
- ISO 15032 AP extension 03-31-2023.xls
- ISO 15032 ML 04-19-2023.xls
- TF amputee C-leg hip flexion-extension - Segal et al. 2006.csv
- TF amputee C-leg knee flexion-extension - Segal et al. 2006.csv
- TF amputee C-leg sagittal hip moment - Segal et al. 2006.csv
- TF amputee C-leg sagittal hip power - Segal et al. 2006.csv
- TF Amputee C-leg sagittal knee moment - Segal et al. 2006.csv
- TF amputee C-leg sagittal knee power - Segal et al. 2006.csv
- TF level walking kinematics and kinetics mean and SD.xlsx

The listed ‘mat’, ‘csv’, ‘xlsx’, and ‘xls’ files are not included in the thesis due to the nature of the files and the large amount of information they contain. Please contact thesis co-supervisors Dr. Edward Lemaire and/or Dr. Natalie Baddour to obtain these supplementary files.

B.1 Main.m

```
%% Powered four-bar hip working analysis
flag = 0; % Flag becomes true when valid input is entered
prompt = "\nEnter '1' for TF gait data plots, '2' for literature plots, "
+ ...
    "'3' for linkage optimization, '4' for ICR plots, \n" + ...
    "'5' for force analysis, '6' for stress analysis, " + ...
    "or '7' for structural and functional test results: ";
AnalysisOption = input(prompt);

while flag == 0
    if sigdigits(AnalysisOption) == 1 && AnalysisOption >= 1 &&
AnalysisOption <= 7
        flag = 1; % Input is valid
    else
        fprintf("\nInvalid input. Please try again.\n")
        AnalysisOption = input(prompt);
    end
end

switch AnalysisOption
    case 1
        run('TFdata6.m') % Plot TF amputee gait data collected from TOHRC
CAREN
    case 2
        run('LiteraturePlot.m') % Plot gait data from literature
    case 3
        run('OptimizeLinkage8.m') % Find optimal link lengths and
corresponding linkage mechanical advantage
    case 4
        run('ICRLinkages.m') % Find hip instantaneous center of rotation
throughout walking range of motion
    case 5
        run('Forces.m') % Find maximum forces and moments expected on each
mechanical part during device operation
    case 6
        run('Stresses.m') % Find maximum vonMises stresses for weight
bearing loads and press-fit loads
    case 7
        run('Evaluation.m') % Plot structural and functional test results
end
```

B.2 TFdata6.m

```
%% Transfemoral amputee (TF) level walking data (prosthetic leg) from
TOHRC CAREN
% Note: SI units with angles in degrees
close all
```

```

% Extracting data from 'TF level walking kinematics and kinetics mean and SD.xlsx'
ThetaFlexHipMean = readxlsxTF('Hip flexion angle (°) mean, SD','A2:A102');
ThetaFlexHipSD = readxlsxTF('Hip flexion angle (°) mean, SD','B2:B102');

ThetaTiltMean = -readxlsxTF('Posterior pelvic tilt(°)mean,SD','A2:A102');
% Anterior pelvic tilt is positive
ThetaTiltSD = readxlsxTF('Posterior pelvic tilt(°)mean,SD','B2:B102');

GRFyMean = readxlsxTF('GRFy (BW) mean, SD','A2:A68');
GRFySD = readxlsxTF('GRFy (BW) mean, SD','B2:B68');

GRFzMean = readxlsxTF('GRFz (BW) mean, SD','A2:A68');
GRFzSD = readxlsxTF('GRFz (BW) mean, SD','B2:B68');

MhxMean = readxlsxTF('Mhx flexion (N-m-kg-1) mean, SD','A2:A102');
MhxSD = readxlsxTF('Mhx flexion (N-m-kg-1) mean, SD','B2:B102');

% Filling in missing zero GRF values for swing phase
for i = (length(GRFyMean)+1):length(ThetaFlexHipMean)
    GRFyMean(i) = 0;
    GRFySD(i) = 0;

    GRFzMean(i) = 0;
    GRFzSD(i) = 0;
end

% Defining gait cycle percent data
GCPPercent_xlsx = transpose(linspace(0,100,length(ThetaFlexHipMean)));

% Plots of TF amputee gait data extracted from Excel
GaitPlot4(1,'kmat',GCPPercent_xlsx,[ThetaTiltMean-ThetaTiltSD, ...
    ThetaTiltMean,ThetaTiltMean+ThetaTiltSD],...
    'Anterior (+) and posterior (-) pelvic tilt','\theta_t_i_l_t
    [°]',1,61+17/30,'top')

GaitPlot4(2,'kmat',GCPPercent_xlsx,[ThetaFlexHipMean-ThetaFlexHipSD, ...
    ThetaFlexHipMean,ThetaFlexHipMean+ThetaFlexHipSD],...
    'Hip flexion (+) and extension (-)','\theta_f_l_e_x
    [°]',1,61+17/30,'top')

GaitPlot4(3,'kin',GCPPercent_xlsx,[GRFyMean-
    GRFySD,GRFyMean,GRFyMean+GRFySD],...
    'Forward (+) and backward (-) ground reaction force','GRFy
    [BW]',1,61+17/30,'top')

GaitPlot4(4,'kin',GCPPercent_xlsx,[GRFzMean-
    GRFzSD,GRFzMean,GRFzMean+GRFzSD],...
    'Upward ground reaction force','GRFz [BW]',1,61+17/30,'top')

GaitPlot4(5,'kin',GCPPercent_xlsx,[MhxMean-MhxSD,MhxMean,MhxMean+MhxSD],...
    'Hip flexion (+) and extension (-) moment','Mhx [N-
    m/kg]',1,61+17/30,'top')

% Extracting data from 'RAW_data.mat'
SpatioTemp = open('RAW_data.mat');

```

```

S2L = SpatioTemp.S2.Left;
S2R = SpatioTemp.S2.Right;
S3L = SpatioTemp.S3.Left;
S3R = SpatioTemp.S3.Right;
S4L = SpatioTemp.S4.Left;
S4R = SpatioTemp.S4.Right;
S7L = SpatioTemp.S7.Left;
S7R = SpatioTemp.S7.Right;
S8L = SpatioTemp.S8.Left;
S8R = SpatioTemp.S8.Right;

Subjects = [S2L,S2R,S3R,S3L,S4L,S4R,S7R,S7L,S8L,S8R];

GaitSpeed = double.empty; % [m/s]
GaitTime = double.empty; % [s]

for i = 1:length(Subjects)
    if rem(i,2) ~= 0 % Odd elements of 'Subjects' correspond to prosthetic
leg
        GaitTime = cat(2,GaitTime,Subjects(i).GaitTime);
    end
    GaitSpeed = cat(2,GaitSpeed,Subjects(i).GaitSpeed);
end

GaitTimeMean = mean(GaitTime); % Don't need gait time standard deviation
GaitSpeedMean = mean(GaitSpeed);
GaitSpeedSD = std(GaitSpeed);

% Hip flexion velocity and acceleration
diff_GaitTimeMean = GaitTimeMean/(length(ThetaFlexHipMean)-1);

OmegaFlexHipMean = diff(ThetaFlexHipMean)./diff_GaitTimeMean;
OmegaFlexHipMean = cat(1,OmegaFlexHipMean,OmegaFlexHipMean(end)); % Concatenation to equalize vector lengths

AlphaFlexHipMean = diff(OmegaFlexHipMean)./diff_GaitTimeMean;
AlphaFlexHipMean = cat(1,AlphaFlexHipMean,AlphaFlexHipMean(end));

% Anterior pelvic tilt velocity and acceleration
OmegaTiltMean = diff(ThetaTiltMean)./diff_GaitTimeMean;
OmegaTiltMean = cat(1,OmegaTiltMean,OmegaTiltMean(end));

AlphaTiltMean = diff(OmegaTiltMean)./diff_GaitTimeMean;
AlphaTiltMean = cat(1,AlphaTiltMean,AlphaTiltMean(end));

% Walking speed
fprintf('\nTF amputee level-walking speed at TOHRC CAREN was %f ± %f
m/s.\n\n',...
        GaitSpeedMean,GaitSpeedSD)

% Flag indicating that TF amputee gait data has been imported into MATLAB
TFdata = 1;

```

B.3 LiteraturePlot.m

```

%% Obtaining TF amputee gait cycle data
if not(exist('TFdata','var'))

```

```

run('TFdata6.m')
else
    fprintf('\n') % Spacing to enhance command window display
end
close all

%% Parameters for data processing

% Hip flexion-extension
filename1 = "Helix3D hip flexion-extension - Ludwigs et al. 2010.csv";
filename2 = "TF amputee C-leg hip flexion-extension - Segal et al.
2006.csv";
filename3 = "Healthy hip flexion-extension - Camargo et al. - 2021.csv";

% Pelvic tilt
filename4 = "Helix3D sagittal pelvic tilt - Ludwigs et al. 2010.csv";
filename5 = "Healthy sagittal pelvic tilt - Ludwigs et al. 2010.csv";

% Hip moment (sagittal plane)
filename6 = "Helix3D sagittal hip moment - Ludwigs et al. 2010.csv";
filename7 = "TF amputee C-leg sagittal hip moment - Segal et al.
2006.csv";
filename8 = "Healthy sagittal hip moment - Camargo et al. 2021.csv";

% Hip power (sagittal plane)
filename9 = "TF amputee C-leg sagittal hip power - Segal et al. 2006.csv";
filename10 = "Healthy sagittal hip power - Camargo et al. 2021.csv";

% Knee flexion-extension
filename11 = "Helix3D knee flexion-extension - Ludwigs et al. 2010.csv";
filename12 = "TF amputee C-leg knee flexion-extension - Segal et al.
2006.csv";
filename13 = "Healthy knee flexion-extension - Camargo et al. 2021.csv";

% Knee moment (sagittal plane)
filename14 = "Helix3D sagittal knee moment - Ludwigs et al. 2010.csv";
filename15 = "TF amputee C-leg sagittal knee moment - Segal et al.
2006.csv";
filename16 = "Healthy sagittal knee moment - Camargo et al. 2021.csv";

% Knee power (sagittal plane)
filename17 = "TF amputee C-leg sagittal knee power - Segal et al.
2006.csv";
filename18 = "Healthy sagittal knee power - Camargo et al. 2021.csv";

% Curve fitting variables
NumPoints = 101;
PercentGC = linspace(0,100,NumPoints);
PolyDeg = 20;

%% Converting raw digitized data to plottable/processable data

% Zero hip angle occurs at vertical line
% Zero knee angle occurs at line collinear to thigh
% Sign convention: flexion (+), extension (-)

% Hip flexion-extension

```

```

HipAmputeeHipFlexion = readmatrix(filename1);
    HipAmputeeHipFlexion(:,2) = -(HipAmputeeHipFlexion(:,2) - 90);
KneeAmputeeHipFlexion = readmatrix(filename2);
HealthyHipFlexion = readmatrix(filename3);

% Pelvic tilt
HipAmputeePelvicTilt = readmatrix(filename4);
KneeAmputeePelvicTilt = [transpose(PercentGC), ThetaTiltMean]; % TOHRC data
used since none exists in literature
HealthyPelvicTilt = readmatrix(filename5);

% Hip moment (sagittal plane)
HipAmputeeHipMoment = readmatrix(filename6);
KneeAmputeeHipMoment = readmatrix(filename7);
    KneeAmputeeHipMoment(:,2) = -KneeAmputeeHipMoment(:,2);
HealthyHipMoment = readmatrix(filename8);
    HealthyHipMoment(:,2) = -HealthyHipMoment(:,2);

% Hip power (sagittal plane)
KneeAmputeeHipPower = readmatrix(filename9);
HealthyHipPower = readmatrix(filename10);

% Knee flexion-extension
HipAmputeeKneeFlexion = readmatrix(filename11);
    HipAmputeeKneeFlexion(:,2) = -(HipAmputeeKneeFlexion(:,2) - 180);
KneeAmputeeKneeFlexion = readmatrix(filename12);
HealthyKneeFlexion = readmatrix(filename13);

% Knee moment (sagittal plane)
HipAmputeeKneeMoment = readmatrix(filename14);
    HipAmputeeKneeMoment(:,2) = -HipAmputeeKneeMoment(:,2);
KneeAmputeeKneeMoment = readmatrix(filename15);
    KneeAmputeeKneeMoment(:,2) = -KneeAmputeeKneeMoment(:,2);
HealthyKneeMoment = readmatrix(filename16);
    HealthyKneeMoment(:,2) = -HealthyKneeMoment(:,2);

% Knee power (sagittal plane)
KneeAmputeeKneePower = readmatrix(filename17);
HealthyKneePower = readmatrix(filename18);

%% Plotting data

% Hip flexion-extension
GaitPlot5(1,HipAmputeeHipFlexion(1:end-1,:),KneeAmputeeHipFlexion(1:end-1,:),
HealthyHipFlexion,...,
'Hip flexion and extension','Gait cycle [%]', 'Joint angle [°]')

% Pelvic tilt
GaitPlot5(2,HipAmputeePelvicTilt(1:end-1,:),
KneeAmputeePelvicTilt,HealthyPelvicTilt,...,
'Pelvic tilt (sagittal plane)', 'Gait cycle [%]', 'Horizontal angle [°]')

% Hip moment (sagittal plane)
GaitPlot5(3,HipAmputeeHipMoment,KneeAmputeeHipMoment,HealthyHipMoment,...,
'Hip moment (sagittal plane)', 'Gait cycle [%]', 'Joint moment [N-m/kg]')

```

```

% Hip power (sagittal plane)
GaitPlot5(4,0,KneeAmputeeHipPower(1:end-1,:),HealthyHipPower, ...
    'Hip power (sagittal plane)', 'Gait cycle [%]', 'Joint power [W/kg]')

% Knee flexion-extension
GaitPlot5(5,HipAmputeeKneeFlexion(1:end-
1,:),KneeAmputeeKneeFlexion,HealthyKneeFlexion, ...
    'Knee flexion and extension', 'Gait cycle [%]', 'Joint angle [°]')

% Knee moment (sagittal plane)
GaitPlot5(6,HipAmputeeKneeMoment(1:end-
1,:),KneeAmputeeKneeMoment,HealthyKneeMoment, ...
    'Knee moment (sagittal plane)', 'Gait cycle [%]', 'Joint moment [N-
m/kg]')

% Knee power (sagittal plane)
GaitPlot5(7,0,KneeAmputeeKneePower,HealthyKneePower, ...
    'Knee power (sagittal plane)', 'Gait cycle [%]', 'Joint power [W/kg]')

```

B.4 OptimizeLinkage8.m

```

%% Kinematics portion of link length optimization loop
% SW file: 'Hip-knee-ankle prosthesis 19.sldasm'
% Note: units of cm, deg, N, and N-cm are used
close all

% Model dimensions that have been chosen
rc = 5.35;
Alpha = 35;
Beta = 65;
r2 = sqrt(2*rc^2*(1-cosd(180-Alpha-Beta)));
Theta_h = (Beta-Alpha)/2;
r4 = 3.3;
Theta4 = 207;
Theta1Ext = Theta4;
Theta1Flex = Theta4-180;
ThetaTilt = 0;

% Chosen maximum hip extension and hip flexion angles which occur at
% singularities of the four-bar mechanism
ThetaExtMax = 36.5;
ThetaFlexMax = 109.5;

% Chosen angles of motor relative to housing at extreme hip joint
% positions
ThetaM_Ext = 89.1;
ThetaM_Flex = -39;
DeltaThetaM = ThetaM_Ext - ThetaM_Flex;

% Iteration parameters
NumPoints = 61; % For hip flexion-extension range
NumFrames = 7; % For frame-by-frame linkage motion plot
NumCheckpts = 100000; % For FindICR function

% Initializing vectors containing all values of ThetaFlex and Theta2
% corresponding to the chosen range of hip flexion

```

```

ThetaFlex = transpose(linspace(-ThetaExtMax,ThetaFlexMax,NumPoints));
Theta2 = zeros(length(ThetaFlex),1);
for i = 1:length(ThetaFlex)
    if ThetaFlex(i) < 0
        Theta2(i) = ThetaFlex(i) + Theta_h + 360;
    else
        Theta2(i) = ThetaFlex(i) + Theta_h;
    end
end

% Defining intermediate angles
Theta2Ext = 360 - ThetaExtMax + Theta_h;
Theta2Flex = ThetaFlexMax + Theta_h;
ThetaB_Ext = Theta1Ext - Theta2Ext + 180;
ThetaB_Flex = Theta1Flex - Theta2Flex + 180;
ThetaB_Extp = ThetaB_Ext + Theta_h + Alpha;
ThetaB_Flexp = ThetaB_Flex + Theta_h + Alpha;

% Solving for r1 and r3 by trigonometry
r1 = (r2*r4*(cosd(ThetaB_Flex)+cosd(ThetaB_Ext))) / ...
       (2*r4+r2*(cosd(ThetaB_Flex)-cosd(ThetaB_Ext)));
r3 = sqrt((r1+r4)^2 + r2^2 - 2*(r1+r4)*r2*cosd(ThetaB_Ext));

% Solving for Theta3 during max hip extension and max hip flexion
% by loop closure
Theta3Ext = loopclosure(r1,r2,r3,r4,Theta1Ext,Theta2Ext,Theta4);
Theta3Flex = loopclosure(r1,r2,r3,r4,Theta1Flex,Theta2Flex,Theta4);

% Finding hip joint co-ordinates throughout joint range of motion by
% solving for intersection points of two circles
[yA,zA,yB,zB,yC,zC,yD,zD] = LinkagePoints(r1,r2,r3,r4, ...
                                               Theta2,Theta4,ThetaTilt);

% Defining lamination plate co-ordinates
y1 = -14.66160949;
z1 = -0.98974039;
y2 = -2.75352961;
z2 = -0.98974039;
y3 = 2.65262553;
z3 = 9.62043647;

% Calculating other intermediate dimensions
rDF_Ext = sqrt((r1+r4)^2 + rc^2 - 2*rc*(r1+r4)*cosd(ThetaB_Extp));
ThetaF_Ext = asind((r1+r4)*sind(ThetaB_Extp)/rDF_Ext);
rDF_Flex = sqrt((r1-r4)^2 + rc^2 - 2*rc*(r1-r4)*cosd(ThetaB_Flexp));
ThetaF_Flex = asind((r1-r4)*sind(ThetaB_Flexp)/rDF_Flex);

% Solving for rm and ra by trigonometry
rm = (rDF_Flex^2 - rDF_Ext^2)/...
      (2*(rDF_Flex*cosd(ThetaF_Flex-ThetaM_Flex+Alpha) -
          rDF_Ext*cosd(ThetaF_Ext-ThetaM_Ext+Alpha)));
ra = sqrt(rm^2 + rDF_Ext^2 - 2*rm*rDF_Ext*cosd(ThetaF_Ext-
          ThetaM_Ext+Alpha));

% Checking for the singularity caused by the drive-arm being parallel with
% the motor
Theta1 = zeros(length(Theta2),1);

```

```

Theta3 = zeros(length(Theta2),1);
ThetaE = zeros(length(Theta2),1);
for i = 1:length(Theta2)
    [Theta1(i),Theta3(i)] =
trigsolve9(yB(i),zB(i),yC(i),zC(i),yD,zD,r1,r2,r3,r4,Theta2(i),Theta4,Thet
aTilt,1);
    if i >= 2 && Theta3(i) < Theta3(i-1)
        [Theta1(i),Theta3(i)] =
trigsolve9(yB(i),zB(i),yC(i),zC(i),yD,zD,r1,r2,r3,r4,Theta2(i),Theta4,Thet
aTilt,-1);
    end
    if Theta1(i) > 360
        Theta1(i) = Theta1(i) - 360;
    end
    ThetaE(i) = acosd((rc^2+r3^2-ra^2-rm^2-2*rc*r3*cosd(180-
Theta3(i)+ThetaFlex(i)+Beta))/(-2*ra*rm));
end
SingE = 0;
for i = 1:(length(ThetaE)-1)
    if ThetaE(i+1) > ThetaE(i)
        SingE = 1;
    end
end

% Finding additional hip joint co-ordinates throughout joint range of
% motion by trigonometry
rDF = sqrt(rc^2 + r3^2 - 2*rc*r3*cosd(180-Theta3+ThetaFlex+Beta));
ThetaFp = asind((ra./rDF).*sind(ThetaE));
ThetaFpp = asind((r3./rDF).*sind(180-Theta3+ThetaFlex+Beta));
yF = r1*cosd(Theta1) + rc*cosd(360-Alpha+ThetaFlex);
zF = r1*sind(Theta1) + rc*sind(360-Alpha+ThetaFlex);
yE = yF + rm*cosd(ThetaFlex + ThetaFp + ThetaFpp + Beta);
zE = zF + rm*sind(ThetaFlex + ThetaFp + ThetaFpp + Beta);

% Calculating motor angle relative to housing
Theta_m = 180 - ThetaFp - ThetaFpp - Beta;

% Checking for the singularity caused by the drive-arm being parallel
with
% the superior link
rAE = sqrt(yE.^2 + zE.^2);
ThetaDp = acosd((rAE.^2 - r4.^2 - ra.^2)/(-2*r4*ra));
SingDp = 0;
ThetaFlexMaxTrue = ThetaFlexMax;
for i = 1:(length(ThetaDp)-1)
    if ThetaDp(i+1) < ThetaDp(i)
        SingDp = 1;
        ThetaFlexMaxTrue = ThetaFlex(i);
        break
    end
end

% Solving for Theta1 and Theta 3 during standing by trigonometry
ThetaStand = 0; % Hip flexion angle when standing
[Theta1Stand,Theta3Stand] =
trigsolve8(r1,r2,r3,r4,ThetaStand+Theta_h,Theta4);

```

```

% Calculating the length from the anterior edge of the lamination plate to
% the joint's frontmost point during standing
% (i.e. finding how much the device protudes forward when a person stands)
r_curve = 1; % Curvature radius at ends of motor housing
y_plate = 2.78627650; % y-coordinate of the anterior edge of the plate
r_motor = 3.85; % Radius of the motor without the housing
tH = 0.3; % Thickness of motor housing
l1 = r1*cosd(Theta1Stand) + r2*cosd(ThetaStand+Theta_h) + r_curve -
y_plate;
l2 = r1*cosd(Theta1Stand) + rc*cosd(Alpha) + r_motor + tH - y_plate;
l = max(l1,l2);

% Solving for Theta1 and Theta3 during sitting by trigonometry
ThetaSit = 90; % Hip flexion angle at sitting position
[Theta1Sit,Theta3Sit] = trigsolve5(r1,r2,r3,r4,ThetaSit+Theta_h,Theta4);

% Calculating the height from bottom surface of lamination plate to the
% joint's uppermost point during sitting
% (i.e. finding how much the device sticks up when a person sits)
zBottom = -1.13974039; % z-coordinate of bottom surface of lamination
plate
h1 = r1*sind(Theta1Sit) + r2*sind(ThetaSit+Theta_h) + r_curve - zBottom;
h2 = r1*sind(Theta1Sit) + rc*cosd(Alpha) + r_motor + tH - zBottom;
h = max(h1,h2);

% Calculating how much the device sticks above or below the lamination
% plate in the sitting position
DeltaZ = r1*sind(Theta1Sit) - r_curve - zBottom; % Positive means above
and negative means below

% Plotting prosthetic hip joint motion in the sagittal plane
Diff = (NumPoints-1)/(NumFrames-1); % Difference in indices of plotted
items (selected evenly spaced values in arrays are plotted)
ColorAxis = [170/255 170/255 170/255];
ColorLamPlate = [255/255 100/255 100/255];
ColorLink = [0/255 108/255 206/255];
ColorArm = [161/255 0/255 206/255];
ColorMotor = [255/255 116/255 0/255];
Y12_lam = [y1 y2]; % Lamination plate lines
Z12_lam = [z1 z2];
Y23_lam = [y2 y3];
Z23_lam = [z2 z3];
figure(1)
plot([-23 23],[0 0],'Color',ColorAxis) % x-axis
axis equal
hold on
plot([0 0],[-18 18],'Color',ColorAxis) % y-axis
title('Powered four-bar hip motion range in the sagittal plane')
xlabel('y[cm]')
ylabel('z[cm]')
plot(Y12_lam,Z12_lam,'Color',ColorLamPlate) % Plotting lamination plate
lines
plot(Y23_lam,Z23_lam,'Color',ColorLamPlate)
for i = 1:NumFrames
    j = 1+(i-1)*Diff;
    Y_post = [yA yB(j)]; % Lines for links
    Z_post = [zA zB(j)];

```

```

Y_inf = [yB(j) yC(j)];
Z_inf = [zB(j) zC(j)];
Y_ant = [yC(j) yD];
Z_ant = [zC(j) zD];
Y_sup = [yD yA];
Z_sup = [zD zA];
Y_arm = [yD yE(j)];
Z_arm = [zD zE(j)];
Y_mot = [yE(j) yF(j)];
Z_mot = [zE(j) zF(j)];
plot(Y_post,Z_post,'Color',ColorLink,'LineWidth',1) % Plotting 4-bar
linkage lines
plot(Y_inf, Z_inf, 'Color',ColorLink,'LineWidth',1)
plot(Y_ant, Z_ant, 'Color',ColorLink,'LineWidth',1)
plot(Y_sup, Z_sup, 'Color',ColorLink,'LineWidth',1)
plot(Y_arm, Z_arm, 'Color',ColorArm, 'LineWidth',1) % Plotting drive
arm line
plot(Y_mot, Z_mot, 'Color',ColorArm, 'LineWidth',1) % Plotting motor
arm line
theta = 0:1:360;
Y_motor = yF(j) + r_motor*cosd(theta);
Z_motor = zF(j) + r_motor*sind(theta);
plot(Y_motor,Z_motor,'Color',ColorMotor); % Plotting motor cicle
pause(0.1);
LamPlate = plot([NaN,NaN], 'Color',ColorLamPlate); % Plotting dummies
for color-based legend
    Link      = plot([NaN,NaN], 'Color',ColorLink);
    Arm       = plot([NaN,NaN], 'Color',ColorArm);
    Motor     = plot([NaN,NaN], 'Color',ColorMotor);
end
legend([LamPlate Link Arm Motor], 'Lamination Plate', 'Link', 'Drive Arm and
Motor Arm', 'Motor', 'Location', 'Northwest');
hold off

% Plotting hip flexion angle vs. relative motor angle
figure(2)
plot(Theta_m,ThetaFlex, 'LineWidth',1)
title('Hip rotation vs. motor rotation')
xlabel('Relative motor angle [°]')
ylabel('Hip flexion [°]')

% Displaying optimized four-bar linkage inputs and outputs
fprintf('\nOptimized four-bar linkage parameters:\n')
fprintf('\nThetaExtMax\tThetaFlexMax\tThetaM_Ext\tThetaM_Flex\tDeltaThetaM
\n')
inputs =
double([ThetaExtMax,ThetaFlexMax,ThetaM_Ext,ThetaM_Flex,DeltaThetaM])
fprintf('r1\tr3\trA\trM\ tl\th\ tDeltaZ\ tThetaFlexMaxTrue\ tSingE\ tSingDp\n')
outputs = double([r1,r3,ra,rm,l,h,DeltaZ,ThetaFlexMaxTrue,SingE,SingDp])

%% Kinetics portion of link length optimization loop

% Hip joint physical range of motion
ThetaExtHipMaxDev = 20;
ThetaFlexHipMaxDev = 100;

% Hip joint angles

```

```

ThetaFlex = transpose(linspace(-
ThetaExtHipMaxDev,ThetaFlexHipMaxDev,NumPoints));
ThetaTilt = 0;
Theta2 = ThetaFlex + Theta_h;
[Theta1,Theta3,Theta_a,Theta_m] = Kinematics1(ThetaFlex,ThetaTilt, ...
    Theta_h,Theta4,Beta,r1,r2,r3,r4,rc,ra,rm);
ThetaB = Theta1 - Theta2 - 180;

% Hip joint co-ordinates A,B,C,D
[yA,zA,yB,zB,yC,zC,yD,zD] =
LinkagePoints(r1,r2,r3,r4,Theta2,Theta4,ThetaTilt);

% Location of ICR relative to origin (point A)
[y_ICR_optloop,z_ICR_optloop] =
FindICR(NumCheckpts,yA,zA,yB,zB,yC,zC,yD,zD);

% Max motor torque
Tmx = 9600;

% Drive-arm force
F7_optloop = Tmx./ (rm.* (cosd(Theta_a).*sind(Theta_m-ThetaFlex) +
sind(Theta_a).*cosd(Theta_m-ThetaFlex)));

% Solving simplified static equilibrium of device parts
[~,~,~,~,~,Mhx] = SimpStaticEquil4(NumPoints,F7_optloop,Tmx,Alpha,Beta, ...
    ThetaFlex,ThetaTilt,Theta1,Theta3,Theta4,Theta_a,rc,r4, ...
    y_ICR_optloop,z_ICR_optloop);

% Mechanical advantage for the entire hip flexion-extension range
MA_optloop = Mhx/Tmx;

% Plot of mechanical advantage (MA) vs. hip flexion angle
HipFlexPlot(3,'MA',ThetaFlex,MA_optloop,'Mechanical advantage (MA)', 'MA = Mhx/Tmx')

% Plot of drive arm force vs. hip flexion angle
HipFlexPlot(4,'kin',ThetaFlex,F7_optloop,'Drive arm force', 'F7 [N]')

%% Flag indicating that link length optimization loop has been completed
Optimized = 1;

```

B.5 ICRLinkages.m

```

%% Finding and plotting instantaneous center of rotation (ICR) of four-bar
linkages
% Note: units of cm and deg are used
close all

% Data processing parameters
NumPoints = 101;
NumFrames = 11;
NumCheckpts = 100000; % For FindICR function
PercentGC = transpose(linspace(0,100,NumPoints));

% Transfemoral amputee (TF) gait data from TOHRC CAREN gait trials
if not(exist('TFdata','var'))
    run('TFdata6.m')

```

```

end
close all

% Extracting data from Ludwigs 2010
filename1 = "Helix3D hip flexion-extension - Ludwigs et al. 2010.csv";
filename2 = "Helix3D sagittal pelvic tilt - Ludwigs et al. 2010.csv";
PercentGC_FlexHelix_xlsx = readmatrix(filename1,'Range','A1:A130');
ThetaFlexHelix_xlsx = 90 - readmatrix(filename1,'Range','B1:B130');
PercentGC_TiltHelix_xlsx = readmatrix(filename2,'Range','A1:A133');
ThetaTiltHelix_xlsx = readmatrix(filename2,'Range','B1:B133');

% Reducing data to 'NumPoints' points by linear interpolation
ThetaFlexHelix = zeros(NumPoints,1);
ThetaTiltHelix = zeros(NumPoints,1);
ThetaFlexHelix(1) = ThetaFlexHelix_xlsx(1);
ThetaTiltHelix(1) = ThetaTiltHelix_xlsx(1);
for n = 2:NumPoints
    for i = 1:numel(ThetaFlexHelix_xlsx)-1
        if PercentGC_FlexHelix_xlsx(i) <= PercentGC(n) &&
PercentGC_FlexHelix_xlsx(i+1) >= PercentGC(n)
            ThetaFlexHelix(n) = (ThetaFlexHelix_xlsx(i+1)-
ThetaFlexHelix_xlsx(i))/...
                (PercentGC_FlexHelix_xlsx(i+1)-
PercentGC_FlexHelix_xlsx(i))*...
                    (PercentGC(n)-PercentGC_FlexHelix_xlsx(i)) +
ThetaFlexHelix_xlsx(i);
        end
    end

    for i = 1:numel(ThetaTiltHelix_xlsx)-1
        if PercentGC_TiltHelix_xlsx(i) <= PercentGC(n) &&
PercentGC_TiltHelix_xlsx(i+1) >= PercentGC(n)
            ThetaTiltHelix(n) = (ThetaTiltHelix_xlsx(i+1)-
ThetaTiltHelix_xlsx(i))/...
                (PercentGC_TiltHelix_xlsx(i+1)-
PercentGC_TiltHelix_xlsx(i))*...
                    (PercentGC(n)-PercentGC_TiltHelix_xlsx(i)) +
ThetaTiltHelix_xlsx(i);
        end
    end
end

% Helix3D link lengths
r1_Helix = 10.8;
r2_Helix = 5.6;
r3_Helix = 6.7;
r4_Helix = 2.7;

% Designed hip joint parameters
if not(exist('Optimized','var'))
    run('LinkageParam.m')
    r1 = r1*100; % Multiplication by 100 is to convert m to cm
    r2 = r2*100;
    r3 = r3*100;
    r4 = r4*100;
end
Theta4 = 207;

```

```

% Finding co-ordinates of Helix3D linkage joints throughout the gait cycle
[yA_Helix1,zA_Helix1,yB_Helix1,zB_Helix1,yC_Helix1,zC_Helix1,yD_Helix1,zD_Helix1] = ...

HelixPoints(r1_Helix,r2_Helix,r3_Helix,r4_Helix,ThetaFlexHelix,ThetaTiltHelix); % Based off Ludwigs 2010 data
[yA_Helix2,zA_Helix2,yB_Helix2,zB_Helix2,yC_Helix2,zC_Helix2,yD_Helix2,zD_Helix2] = ...

HelixPoints(r1_Helix,r2_Helix,r3_Helix,r4_Helix,ThetaFlexHipMean,ThetaTiltMean); % Based off TOHRC CAREN TF amputee data

% Finding co-ordinates of designed linkage joints throughout the gait cycle
[yA1,zA1,yB1,zB1,yC1,zC1,yD1,zD1] =
LinkagePoints(r1,r2,r3,r4,ThetaFlexHelix,Theta4,ThetaTiltHelix); % Based off Ludwigs 2010 data
[yA2,zA2,yB2,zB2,yC2,zC2,yD2,zD2] =
LinkagePoints(r1,r2,r3,r4,ThetaFlexHipMean,Theta4,ThetaTiltMean); % Based off TOHRC CAREN TF amputee data

% Computing ICR of Helix3D throughout gait cycle
[y_ICR_Helix1,z_ICR_Helix1] = FindICR(NumCheckpts,yA_Helix1,zA_Helix1,...  

yB_Helix1,zB_Helix1,yC_Helix1,zC_Helix1,yD_Helix1,zD_Helix1);
[y_ICR_Helix2,z_ICR_Helix2] = FindICR(NumCheckpts,yA_Helix2,zA_Helix2,...  

yB_Helix2,zB_Helix2,yC_Helix2,zC_Helix2,yD_Helix2,zD_Helix2);

% Computing ICR of designed hip joint throughout gait cycle
[y_ICR1,z_ICR1] = FindICR(NumCheckpts,yA1,zA1,yB1,zB1,yC1,zC1,yD1,zD1);
[y_ICR2,z_ICR2] = FindICR(NumCheckpts,yA2,zA2,yB2,zB2,yC2,zC2,yD2,zD2);

% Plotting lines representing orientation of links and ICR throughout gait cycle
PlotICR(1,'Helix3D ICR throughout GC based off Ludwigs 2010 data',...
yA_Helix1,zA_Helix1,yB_Helix1,zB_Helix1,yC_Helix1,zC_Helix1,...  

yD_Helix1,zD_Helix1,y_ICR_Helix1,z_ICR_Helix1,NumFrames)
PlotICR(2,'Helix3D ICR throughout GC based off TOHRC CAREN TF amputee data',...
yA_Helix2,zA_Helix2,yB_Helix2,zB_Helix2,yC_Helix2,zC_Helix2,...  

yD_Helix2,zD_Helix2,y_ICR_Helix2,z_ICR_Helix2,NumFrames)
PlotICR(3,'Powered hip ICR throughout GC based off Ludwigs 2010 data',...
yA1,zA1,yB1,zB1,yC1,zC1,yD1,zD1,y_ICR1,z_ICR1,NumFrames)
PlotICR(4,'Powered hip ICR throughout GC based off TOHRC CAREN TF amputee data',...
yA2,zA2,yB2,zB2,yC2,zC2,yD2,zD2,y_ICR2,z_ICR2,NumFrames)

% Spacing to enhance command window display
fprintf('\n')

```

B.6 Forces.m

```

%% Obtaining TF amputee gait cycle data
if not(exist('TFdata','var'))
    run('TFdata6.m')
end
close all

```

```

% Note: SI units with angles in degrees

% Parameters for iterative calculations
NumPointsROMDev = 61; % For motor only analysis
NumPointsGC = 51; % For static analysis throughout gait cycle
Width = 3;
ZeroArray = zeros(NumPointsGC,1);
ZeroMatrix = zeros(NumPointsGC,Width);
Delta = (length(ThetaFlexHipMean)-1)/(NumPointsGC-1);
GCPPercent = transpose(linspace(0,100,NumPointsGC));

% Selecting specific datapoints to reduce dataset size and program run
% time
ThetaFlexHipData = ZeroArray;
OmegaFlexHip = ZeroArray;
AlphaFlexHip = ZeroArray;
ThetaTiltData = ZeroArray;
OmegaTilt = ZeroArray;
AlphaTilt = ZeroArray;
GRFyData = ZeroMatrix;
GRFzData = ZeroMatrix;
MhxData = ZeroMatrix;
for i = 1:NumPointsGC
    Index = round((i-1)*Delta + 1);
    ThetaFlexHipData(i) = ThetaFlexHipMean(Index);
    OmegaFlexHip(i) = OmegaFlexHipMean(Index);
    AlphaFlexHip(i) = AlphaFlexHipMean(Index);
    ThetaTiltData(i) = ThetaTiltMean(Index);
    OmegaTilt(i) = OmegaTiltMean(Index);
    AlphaTilt(i) = AlphaTiltMean(Index);
    GRFyData(i,:) = [GRFyMean(Index)-
    GRFySD(Index),GRFyMean(Index),GRFyMean(Index)+GRFySD(Index)];
    GRFzData(i,:) = [GRFzMean(Index)-
    GRFzSD(Index),GRFzMean(Index),GRFzMean(Index)+GRFzSD(Index)];
    MhxData(i,:) = [MhxMean(Index)-
    MhxSD(Index),MhxMean(Index),MhxMean(Index)+MhxSD(Index)];
end

%% Converting normalized kinetic data into data for a 100 kg person
m_design = 100;
g = 9.81;
GRFy_100kg = GRFyData*m_design*g;
GRFz_100kg = GRFzData*m_design*g;
Mhx_100kg = MhxData*m_design;

%% Obtaining linkage dimensions
if ~exist('Optimized','var')
    run('LinkageParam.m')
else
    dh = 4.65/100;
end

%% Performing conversions for unit consistency
if exist('Optimized','var')
    rC = rc/100; % Division by 100 to convert cm to m
    rM = rm/100;

```

```

    r_4 = r4/100;
else
    rC = rc;
    rM = rm;
    r_4 = r4;
end

%% General info
% SW file: 'Hip-knee-ankle prosthesis 19.sldasm'
% SI units are used
% Angular quantities are in rees

% Excel sheet where results are written
FileName = 'Forces.xlsx';

% Safety factor for gait cycle analysis
SF = 1;

% Symbolic variables
syms Theta_FlexHip(t) Theta_Tilt(t)

% Names of force and moment variables to be calculated
VarNamesAP = {'Fhy'; 'Fhz'; 'F2y'; 'F2z'; 'F5iy'; 'F5iz'; 'F5sy'; ...
    'F5sz'; 'F6'; 'F7'; 'Fes'; 'Ffs'; 'Mhx'; 'M2x'; 'Tmx'};
VarNamesML = {'Fhx'; 'Fhz'; 'Mhy'; 'F5x'; 'F5iy'; 'F5iz'; 'F6x'; ...
    'F6l1'; 'F6m1'; 'F7x'; 'F7yz'; 'M10x'; 'Tmx'};
VarNamesGC = {'Fhy'; 'Fhz'; 'F2y'; 'F2z'; 'F5'; 'F6'; 'F7'; 'Mhx'; ...
    'M2x'; 'Tmx'};
VarNamesMotor = {'Fhy'; 'Fhz'; 'F5'; 'F6'; 'F7'; 'FR'; 'Mhx'; 'Tmx'};

% Allocating memory for results to be saved in
SolValuesAP = zeros(length(VarNamesAP),2);
SolValuesGC_MeanMinus1SD = zeros(length(VarNamesGC),NumPointsGC);
SolValuesGC_Mean = zeros(length(VarNamesGC),NumPointsGC);
SolValuesGC_MeanPlus1SD = zeros(length(VarNamesGC),NumPointsGC);
SolValuesMotor = zeros(length(VarNamesMotor),NumPointsROMDev);

% Model dimensions

%%% Hip-knee-ankle-foot prosthesis
l_COM_D = 38/100; % Average length taken because polycentric joint changes
height
m_leg = 8.43886;

%%% Power Hip Prosthesis
l_APOffset = 1/100; % Max allowable AP offset as per ISO 15032
d2l = (1.84165398 + 0.8/2 + 1.6/2)/100; % Division by 100 is to convert cm
to m
d2m = (0.11834602 + 0.8/2 + 1.6/2)/100;

%%% Posterior Link
Theta_es = 35.58281581;

%%% Superior Link
dfs = 6.46445617/100;
ds1l = 1.56125457/100;
ysl = -0.12042843/100;

```

```

zsl = 2.44311320/100;
Theta_lp = 117;
Theta_s11 = 14.58728473;

%% ISO 15032-2000 static force equilibrium: anterior-posterior (A-P)
Sheet = 1; % Specifying Excel sheet in 'Forces.xlsx'

% Assumptions (both due to motor being off)
F7 = 0;
Tmx = 0;

for condition = 1:2
    if condition == 1
        fprintf("\nCondition 1: ISO 15032-2000 A100 A-P compression at
full hip extension with extension stop\n");
        APext = 1; % Hip joint is fully extended
        Range = 'B2'; % Place results in Excel column B

        % Hip joint angles
        ThetaFlexHip = -ThetaExtHipMaxDev;
        ThetaTilt = 0;
        [~,Theta3,~,~] = Kinematics1(ThetaFlexHip,ThetaTilt,Theta_h, ...
            Theta4,Beta,r1,r2,r3,r4,rc,ra,rm);

        % Defining ISO 15032-2000 coordinate system rotation matrix for AP
        ext.
        Theta_fpup_APext = -19.12473863;
        RotMatrix1 = rotation(Theta_fpup_APext);

        % Distance variables from ISO 15032-2000 for AP extension
        fprimeTH = -159/1000; % Division by 1000 is to convert mm to m
        fprimeH = -83/1000;
        delta_uprimeTHH = 200/1000;

        % Solving for hip and knee joint reactions for ISO 15032-2000 AP
        extension
        Fprime = 3360; % Newtons
        SqrtHip = sqrt((fprimeTH-fprimeH)^2 + delta_uprimeTHH^2);

        Fh_fprime = Fprime*abs(fprimeTH-fprimeH)/SqrtHip; % Signs are wrt
        ISO 15032-2000 AP ext. free-body diagram (FBD)
        Fh_uprime = Fprime*(delta_uprimeTHH)/SqrtHip;
        Fh = RotMatrix1*[-Fh_fprime;Fh_uprime]; % Signs are wrt
        biomechanics coordinate system
        Fhy = -Fh(1); % Signs are wrt simplified equilibrium FBDs
        Fhz = Fh(2);
        Mhx = Fprime*delta_uprimeTHH*abs(fprimeH)/SqrtHip;

        elseif condition == 2
            fprintf("\nCondition 2: ISO 15032-2000 A100 A-P compression at
full hip flexion with flexion stop\n");
            APext = 0; % Hip joint is fully flexed
            Range = 'C2'; % Place results in Excel column C

            % Hip joint angles
            ThetaFlexHip = ThetaFlexHipMaxDev;
            ThetaTilt = 0;

```

```

[~,Theta3,~,~] = Kinematics1(ThetaFlexHip,ThetaTilt,Theta_h, ...
    Theta4,Beta,r1,r2,r3,r4,rc,ra,rm);

% Defining ISO 15032-2000 coordinate system rotation matrix for AP
flex.
Theta_fpup_APflex = 180-73.9080519;
RotMatrix2 = rotation(Theta_fpup_APflex);

% Distance variables from ISO 15032-2000 for AP flexion
fprimeTH = 43/1000; % Division by 1000 is to convert mm to m
fprimeH = 29/1000;

% Solving for hip and knee joint reactions for ISO 15032-2000 AP
flexion
SqrtHip = sqrt((fprimeTH-fprimeH)^2 + delta_uprimeTHH^2);
Fh_fprime = Fprime*(fprimeTH-fprimeH)/SqrtHip; % Signs are wrt ISO
15032-2000 AP flex. FBD
Fh_uprime = Fprime*(delta_uprimeTHH)/SqrtHip;
Fh = RotMatrix2*[Fh_fprime;Fh_uprime]; % Signs are wrt
biomechanics coordinate system
Fhy = -Fh(1); % Signs are wrt simplified equilibrium FBDs
Fhz = Fh(2);
Mhx = -Fprime*delta_uprimeTHH*abs(fprimeH)/SqrtHip;
end

% Simplified static equilibrium
[F2y,F2z,F5iy,F5iz,F5sy,F5sz,F6,Fes,Ffs,M2x] = ...
    SimpStaticEquil5(APext,Fhy,Fhz,Mhx,Alpha,Beta,ThetaFlexHip, ...
    Theta3,Theta_es,Theta_lp,Theta_s11,dfs,dh,ds11,rc);

% Exporting results to Excel File
Sol4Excel = double([Fhy; Fhz; F2y; F2z; F5iy; F5iz; F5sy; F5sz; F6;
F7; ...;
    Fes; Ffs; Mhx; M2x; Tmx]);
writecell(VarNamesAP,FileName,'Sheet',Sheet,'Range','A2');
writematrix(Sol4Excel,FileName,'Sheet',Sheet,'Range',Range);

% Saving results for further analysis
SolValuesAP(:,condition) = Sol4Excel;
end

% Writing Excel column titles
Col1Label = 'Load';
Col2Label = 'AP Extension (N or N-m)';
Col3Label = 'AP Flexion (N or N-m)';
writematrix(Col1Label,FileName,'Sheet',Sheet,'Range','A1');
writematrix(Col2Label,FileName,'Sheet',Sheet,'Range','B1');
writematrix(Col3Label,FileName,'Sheet',Sheet,'Range','C1');

%% ISO 15032-2000 static force equilibrium: medial-lateral (M-L)
Sheet = 2; % Specifying Excel sheet in 'Forces.xlsx'
fprintf("\nCondition 3: ISO 15032-2000 A100 M-L compression at full hip
extension with extension stop\n")
syms F5x F5iz F6x F6l1 F6ml

% Hip joint angles
ThetaFlexHip = -ThetaExtHipMaxDev;

```

```

ThetaTilt = 0;
[Theta1,Theta3,~,~] = Kinematics1(ThetaFlexHip,ThetaTilt,Theta_h, ...
Theta4,Beta,r1,r2,r3,r4,rc,ra,rm);

% Distance variables from ISO 15032-2000 for ML
oprimeTH = -106/1000;
oprimeH = -86/1000;

% Solving for hip and knee joint reactions for ISO 15032-2000 ML
DenomH = sqrt((oprimeTH-oprimeH)^2 + delta_uprimeTHH^2);
Fhx = Fprime*abs(oprimeTH-oprimeH)/DenomH;
Fhz = Fprime*delta_uprimeTHH/DenomH;
Mhy = Fhz*abs(oprimeTH) - Fhx*delta_uprimeTHH;

% Assumption that AP offset doesn't exceed 10 mm as per ISO 15032-2000
M10x = Fhz*l_APoffset;

% Solving for the rest of the reactions

%%% Power Hip Prosthesis (Upper Portion) - finding unknowns simultaneously
SumFx_PHP = F5x + F6x - Fhx == 0;
SumFy_PHP = -F5iy + (F6l1+F6m1)*cosd(Theta3) == 0;
SumFz_PHP = F5iz + (F6l1+F6m1)*sind(Theta3) - Fhz == 0;
SumMx_PHP = M10x - F5iy*(r1*sind(Theta1-180)+r4*sind(Theta4-180)) - ...
F5iz*(r1*cosd(Theta1-180)+r4*cosd(Theta4-180)) - Fhz*ySL == 0;
SumMy_PHP = Mhy - F5x*(r1*sind(Theta1-180)+r4*sind(Theta4-180)) - ...
F6x*r3*sind(Theta3) - ...
F6l1*sind(Theta3)*d2l + F6m1*sind(Theta3)*d2m - Fhx*zSL == 0;
SumMz_PHP = F5x*(r1*cosd(Theta1-180)+r4*cosd(Theta4-180)) + ...
F6x*r3*cosd(Theta3) + F6l1*cosd(Theta3)*d2l - ...
F6m1*cosd(Theta3)*d2m - Fhx*ySL == 0;
Sol_PHP =
solve([SumFx_PHP,SumFy_PHP,SumFz_PHP,SumMx_PHP,SumMy_PHP,SumMz_PHP],...
[F5x,F5iy,F5iz,F6x,F6l1,F6m1]);

% Convert solution values into a usable form
F5x = Sol_PHP.F5x;
F5iy = Sol_PHP.F5iy;
F5iz = Sol_PHP.F5iz;
F6x = Sol_PHP.F6x;
F6l1 = Sol_PHP.F6l1;
F6m1 = Sol_PHP.F6m1;

% Assumptions
F7yz = 0; % Torque loads and structural loads are separate due to
tolerancing
F7x = 0; % Same reasoning as directly above
Tmx = 0; % Motor is off

% Exporting results to Excel file
Sol4Excel = double([Fhx; Fhz; Mhy; F5x; F5iy; F5iz; F6x; F6l1; F6m1; ...
F7x; F7yz; M10x; Tmx]);
writecell(VarNamesML,FileName,'Sheet',Sheet,'Range','A2');
writematrix(Sol4Excel,FileName,'Sheet',Sheet,'Range','B2');

% Saving results for further analysis
SolValuesML = Sol4Excel;

```

```

% Writing Excel column titles
Col1Label = 'Load';
Col2Label = 'ML (N or N-m)';
writematrix(Col1Label,FileName,'Sheet',Sheet,'Range','A1');
writematrix(Col2Label,FileName,'Sheet',Sheet,'Range','B1');

%% Static force equilibrium (sagittal plane) throughout the gait cycle
Sheet = 3; % Specifying first out of three sheets (mean-1SD, mean, mean+1SD) in Excel
fprintf("\nStatic force equilibrium (sagittal plane) throughout the gait cycle\n")

% Hip joint angles
ThetaFlexHip = ThetaFlexHipData;
ThetaTilt = ThetaTiltData;
[Theta1,Theta3,Theta_a,Theta_m] = Kinematics1(ThetaFlexHip,ThetaTilt,...  

Theta_h,Theta4,Beta,r1,r2,r3,r4,rc,ra,rm);

% Instantaneous center of rotation (ICR) throughout gait cycle
NumCheckpts = 100000;
Theta2 = ThetaFlexHip + Theta_h;
if exist('Optimized','var')
    [yA,zA,yB,zB,yC,zC,yD,zD] = LinkagePoints(r1,r2,r3,r4,...  

Theta2,Theta4,ThetaTilt); % Calculation done in cm for accuracy
else
    [yA,zA,yB,zB,yC,zC,yD,zD] =  

LinkagePoints(r1*100,r2*100,r3*100,r4*100,...  

Theta2,Theta4,ThetaTilt); % Calculation done in cm (m x 100) for accuracy
end
[y_ICR,z_ICR] = FindICR(NumCheckpts,yA,zA,yB,zB,yC,zC,yD,zD);
y_ICR = y_ICR/100; % Division by 100 to convert cm to m
z_ICR = z_ICR/100;

% Mechanical advantage throughout gait cycle
syms Tmx
F7 = Tmx./(rM.*cosd(Theta_a).*sind(Theta_m-ThetaFlexHip) + ...  

sind(Theta_a).*cosd(Theta_m-ThetaFlexHip));
Mhx = F7.* (cosd(Theta_a).* (z_ICR-r_4.*sind(Theta4-ThetaTilt-180)) + ...  

sind(Theta_a).* (r_4.*cosd(Theta4-ThetaTilt-180)-y_ICR));
MA = double(Mhx/Tmx);

% Acceleration of the hip-knee-ankle-foot prosthesis center of mass
y_COM = r_4*cosd(Theta4-Theta_Tilt-180) - l_COM_D*sind(-Theta_FlexHip);
z_COM = r_4*sind(Theta4-Theta_Tilt-180) - l_COM_D*cosd(-Theta_FlexHip);
[a_COMy,a_COMz] = Kinematics4(ThetaFlexHip,OmegaFlexHip,AlphaFlexHip,...  

ThetaTilt,OmegaTilt,AlphaTilt,y_COM,z_COM);

% Hip joint reactions
Fhy = SF*(GRFy_100kg - m_leg*a_COMy);
Fhz = SF*(GRFz_100kg - m_leg*(a_COMz+g));
Mhx = SF*(-Mhx_100kg); % Mhx points towards hip extension in FBD

% Required motor torque and resulting drive arm force throughout gait cycle
Tmx = Mhx./MA;

```

```

F7 = Tmx./(rM.*cosd(Theta_a).*sind(Theta_m-ThetaFlexHip) + ...
           sind(Theta_a).*cosd(Theta_m-ThetaFlexHip)));;

% Simplified static equilibrium
[F5,F6,F2y,F2z,M2x] = SimpStaticEquil3(NumPointsGC,Width,Fhy,Fhz, ...
                                         F7,Tmx,Alpha,Beta,ThetaFlexHip,Theta1,Theta3,Theta_a,dh,rC);

for j = 1:Width

    % Exporting results to Excel File
    for i = 1:NumPointsGC
        ThetaFlexHipExcel = round(ThetaFlexHip(i),2); % Mean hip flexion
        angle corresponds to j=2
        Sol4Excel = [Fhy(i,j); Fhz(i,j); F2y(i,j); F2z(i,j); F5(i,j); ...
                     F6(i,j); F7(i,j); Mhx(i,j); M2x(i,j); Tmx(i,j)];
        if i < 26
            StrCatArg = char('A'+i);
        elseif i < 52
            StrCatArg = strcat('A',char('A'+i-26));
        elseif i < 78
            StrCatArg = strcat('B',char('A'+i-52));
        elseif i < 106
            StrCatArg = strcat('C',char('A'+i-78));
        end
        writematrix(strcat('ThetaFlexHip =
',num2str(ThetaFlexHipExcel),'.'),FileName, ...
                    'Sheet',Sheet+j-1,'Range',strcat(StrCatArg,'1'));
        writematrix(Sol4Excel,FileName,'Sheet',Sheet+j-
1,'Range',strcat(StrCatArg,'2'));

        % Saving results for further analysis
        if j == 1
            SolValuesGC_MeanMinus1SD(:,i) = Sol4Excel;
        elseif j == 2
            SolValuesGC_Mean(:,i) = Sol4Excel;
        elseif j == 3
            SolValuesGC_MeanPlus1SD(:,i) = Sol4Excel;
        end
    end

    % Inserting more info into the Excel file
    ColALabel = 'Load (N or N-m)';
    writematrix(ColALabel,FileName,'Sheet',Sheet+j-1,'Range','A1');
    writecell(VarNamesGC,FileName,'Sheet',Sheet+j-1,'Range','A2');

end

% Graphing results as function of percent gait cycle
FigNumber = 1;
Title = 'Hip flexion (+) and extension (-) moment';
yLabel = 'Mhx [N-m]';
GaitPlot4(FigNumber,'kin',GCPPercent,-Mhx,Title,yLabel,1,61+17/30,'top') % Negative sign to make hip flexion positive

FigNumber = 2;
Title = 'Motor torque required for hip joint stability: lateral view CW
(+), lateral view CCW (-)';

```

```

yLabel = 'Tmx [N-m]';
GaitPlot4(FigNumber,'Tmx',GCPPercent,Tmx,Title,yLabel,1,61+17/30,'bottom')

FigNumber = 3;
Title = 'Mechanical advantage (MA)';
yLabel = 'MA = |Tmx/Mhx|';
GaitPlot4(FigNumber,'MA',GCPPercent,MA,Title,yLabel,0,61+17/30,'bottom')

FigNumber = 4;
Title = 'Posterior tensile (+) and compressive (-) link force';
yLabel = 'F5 [N]';
GaitPlot4(FigNumber,'kin',GCPPercent,F5,Title,yLabel,1,61+17/30,'bottom')

FigNumber = 5;
Title = 'Anterior tensile (+) and compressive (-) link force';
yLabel = 'F6 [N]';
GaitPlot4(FigNumber,'kin',GCPPercent,F6,Title,yLabel,1,61+17/30,'bottom')

FigNumber = 6;
Title = 'Drive arm compressive (+) and tensile (-) force';
yLabel = 'F7 [N]';
GaitPlot4(FigNumber,'kin',GCPPercent,F7,Title,yLabel,1,61+17/30,'bottom')

%% Effect of motor torque only
Sheet = 6; % Specifying Excel sheet in 'Forces.xlsx'
fprintf("\nEffect of motor torque only throughout device range of motion\n\n")

% Max motor torque assumed
Tmx = 96;

% Hip joint angles
ThetaFlexHip = transpose(linspace(
    ThetaExtHipMaxDev,ThetaFlexHipMaxDev,NumPointsROMDev));
ThetaTilt = 0;
[Theta1,Theta3,Theta_a,Theta_m] = Kinematics1(ThetaFlexHip,ThetaTilt, ...
    Theta_h,Theta4,Beta,r1,r2,r3,r4,rc,ra,rm);
Theta2 = ThetaFlexHip + Theta_h;

if exist('Optimized','var')
    % Obtaining previously calculated linkage optimization results if they exist
    Y_ICR = y_ICR_optloop;
    z_ICR = z_ICR_optloop;
    F7 = F7_optloop;
    MA = MA_optloop;

    % Simplified static equilibrium
    [F5,F6,FR,Fhy,Fhz,Mhx] = SimpStaticEquil4(NumPointsROMDev,F7,Tmx, ...

Alpha,Beta,ThetaFlexHip,ThetaTilt,Theta1,Theta3,Theta4,Theta_a,rc,r_4, ...
    y_ICR/100,z_ICR/100);
    % Division by 100 to convert cm to m
else
    % ICR throughout range of hip motion
    [yA,zA,yB,zB,yC,zC,yD,zD] =
    LinkagePoints(r1*100,r2*100,r3*100,r4*100, ...

```

```

    Theta2,Theta4,ThetaTilt); % Calculation done in cm (m x 100) for
accuracy
[y_ICR,z_ICR] = FindICR(NumCheckpts,yA,zA,yB,zB,yC,zC,yD,zD);
y_ICR = y_ICR/100; % Division by 100 to convert cm to m
z_ICR = z_ICR/100;

% Drive arm force
F7 = Tmx./ (rM.* (cosd(Theta_a).*sind(Theta_m-ThetaFlexHip) + ...
sind(Theta_a).*cosd(Theta_m-ThetaFlexHip)));
% Simplified static equilibrium
[F5,F6,FR,Fhy,Fhz,Mhx] = SimpStaticEquil4(NumPointsROMDev,F7,Tmx,...);

Alpha,Beta,ThetaFlexHip,ThetaTilt,Theta1,Theta3,Theta4,Theta_a,rC,r_4, ...
y_ICR,z_ICR);

% Mechanical advantage
MA = Mhx./Tmx;
end

% Maximum allowable motor torque throughout hip joint range of motion
Tmx_allow = zeros(NumPointsROMDev,1);
for i = 1:length(F7)
    if F7(i) > 3271 % The equivalent static radial load equals the basic
static load rating when F7 = 3271 N
        Tmx_allow(i) = (3271/F7(i))*96;
    else
        Tmx_allow(i) = 96;
    end
end

% Exporting results to Excel File
for i = 1:NumPointsROMDev
    ThetaFlexHipExcel = round(ThetaFlexHip(i),2);
    Sol4Excel = [Fhy(i); Fhz(i); F5(i); F6(i); F7(i); FR(i); Mhx(i); Tmx];

    if i < 26
        StrCatArg = char('A'+i);
    elseif i < 52
        StrCatArg = strcat('A',char('A'+i-26));
    elseif i < 78
        StrCatArg = strcat('B',char('A'+i-52));
    elseif i < 106
        StrCatArg = strcat('C',char('A'+i-78));
    elseif i < 132
        StrCatArg = strcat('D',char('A'+i-106));
    end
    writematrix(strcat('ThetaFlexHip =
',num2str(ThetaFlexHipExcel),'.'),FileName, ...
'Sheet',Sheet,'Range',strcat(StrCatArg,'1'));

    writematrix(Sol4Excel,FileName,'Sheet',Sheet,'Range',strcat(StrCatArg,'2'));
);

    % Saving results for further analysis
    SolValuesMotor(:,i) = Sol4Excel;
end

```

```

% Inserting more info into the Excel file
ColALabel = 'Load (N or N-m)';
writematrix(ColALabel,FileName,'Sheet',Sheet,'Range','A1');
writecell(VarNamesMotor,FileName,'Sheet',Sheet,'Range','A2');

% Graphing results
FigNumber = 7;
Title = 'Mechanical advantage (MA)';
yLabel = 'MA = |Mhx/Tmx|';
HipFlexPlot(FigNumber,'MA',ThetaFlexHip,MA,Title,yLabel)

FigNumber = 8;
Title = 'Posterior link force magnitude';
yLabel = 'F5 [N]';
HipFlexPlot(FigNumber,'kin',ThetaFlexHip,F5,Title,yLabel)

FigNumber = 9;
Title = 'Anterior link force magnitude';
yLabel = 'F6 [N]';
HipFlexPlot(FigNumber,'kin',ThetaFlexHip,F6,Title,yLabel)

FigNumber = 10;
Title = 'Drive arm force magnitude';
yLabel = 'F7 [N]';
HipFlexPlot(FigNumber,'kin',ThetaFlexHip,F7,Title,yLabel)

FigNumber = 11;
Title = 'Maximum allowable motor torque';
yLabel = '(Tmx)_a_l_l_o_w [N-m]';
HipFlexPlot(FigNumber,'Tmx',ThetaFlexHip,Tmx_allow,Title,yLabel)

%% Flag indicating that forces calculations are complete
ForceCalcs = 1;

```

B.7 Stresses.m

```

%% General info
% SW file: 'Hip-knee-ankle Prosthesis 19.sldasm'
% Units of mm, °, N, and MPa are used

%% Prerequisite force analysis
if not(exist('ForceCalcs','var'))
    run('Forces.m')
end

%% Posterior link (PL) vonMises stress
des = 5 + 13.20100533/2;

%%% External loads (N) from 'Forces.m': ISO 15032 AP extension
F5sy =
SolValuesAP(table(cell2ind('B8')).Var1(1),table(cell2ind('B8')).Var1(2));
F5sz =
SolValuesAP(table(cell2ind('B9')).Var1(1),table(cell2ind('B9')).Var1(2));

%%% Internal loads (N or N-mm)
Vy_p_PL = F5sy*cosd(Theta_es) + F5sz*cosd(90-Theta_es);

```

```

Pz_p_PL = -F5sy*sind(Theta_es) + F5sz*sind(90-Theta_es);
Mx_p_PL = F5sy*des*cosd(Theta_es) + F5sz*des*cosd(90-Theta_es);

%%% Section properties
b_PL = 20;
h_PL = 16;
yA_p_PL = -b_PL/2;
yB_p_PL = 0;
yB_bar_p_PL = -b_PL/4;
yC_p_PL = b_PL/2;
tx_p_PL = h_PL;
A_PL = b_PL*h_PL;
A_p_PL = (b_PL/2)*h_PL;
Ix_p_PL = (h_PL*b_PL^3)/12;
Qx_p_PL = yB_bar_p_PL*A_p_PL;

%%% vonMises stress (MPa) at critical cross-sectional points
Sigma_vA_PL = vonMises(0,0,Pz_p_PL,-Mx_p_PL,0,0,0,Vy_p_PL,0,0,0,0,...  

    A_PL,Ix_p_PL,1,1,Qx_p_PL,1,1,1,1,1,0,yA_p_PL,0,tx_p_PL,1,1,0,0,0,...  

    1,1,1); % 0s and 1s placed for inputs that don't influence stress  

values

Sigma_vB_PL = vonMises(0,0,Pz_p_PL,-Mx_p_PL,0,0,0,Vy_p_PL,0,0,0,0,...  

    A_PL,Ix_p_PL,1,1,Qx_p_PL,1,1,1,1,1,0,yB_p_PL,0,tx_p_PL,1,1,0,0,0,...  

    1,1,1);

Sigma_vC_PL = vonMises(0,0,Pz_p_PL,-Mx_p_PL,0,0,0,Vy_p_PL,0,0,0,0,...  

    A_PL,Ix_p_PL,1,1,Qx_p_PL,1,1,1,1,1,0,yC_p_PL,0,tx_p_PL,1,1,0,0,0,...  

    1,1,1);

Sigma_v_PL = [Sigma_vA_PL,Sigma_vB_PL,Sigma_vC_PL];
Point_PL = MaxStressPoint(Sigma_v_PL);
fprintf("\nThe maximum posterior link vonMises stress is %f MPa at point  

%s.\n",...  

    max(Sigma_v_PL),Point_PL)

%% Anterior link (AL) vonMises stress

%%% External load (N) from 'Forces.m': ISO 15032 ML
F6x =
SolValuesML(table(cell2ind('B8')).Var1(1),table(cell2ind('B8')).Var1(2));
F611 =
SolValuesML(table(cell2ind('B9')).Var1(1),table(cell2ind('B9')).Var1(2));

%%% Internal load (N or N-mm)
Pz_p_AL = F611;
My_p_AL = F6x*(1000*r3/2); % Multiplication by 1000 to convert m to mm

%%% Section properties
b_AL = 15;
h_AL = 8;
xA_p_AL = h_AL/2;
xB_p_AL = -h_AL/2;
A_AL = b_AL*h_AL;
Iy_p_AL = (b_AL*h_AL^3)/12;

%%% vonMises stress (MPa) at critical cross-sectional points

```

```

Sigma_vA_AL = vonMises(0,0,Pz_p_AL,0,My_p_AL,0,0,0,0,0,0,0,0,...  

    A_AL,1,Iy_p_AL,1,1,1,1,1,1,xA_p_AL,0,0,1,1,1,0,0,0,...  

    1,1,1);  
  

Sigma_vB_AL = vonMises(0,0,Pz_p_AL,0,My_p_AL,0,0,0,0,0,0,0,0,...  

    A_AL,1,Iy_p_AL,1,1,1,1,1,1,xB_p_AL,0,0,1,1,1,0,0,0,...  

    1,1,1);  
  

Sigma_v_AL = [Sigma_vA_AL,Sigma_vB_AL];  

Point_AL = MaxStressPoint(Sigma_v_AL);  

fprintf("\nThe maximum anterior link vonMises stress is %f MPa at point  

%s.\n",...  

    max(Sigma_v_AL),Point_AL)  
  

%% Drive arm (DA) vonMises stress  
  

%%% External load (N) from 'Forces.m': motor only analysis at 20° hip  

extension  

F7 =  

SolValuesMotor(table(cell2ind('B6')).Var1(1),table(cell2ind('B6')).Var1(2))  

);  
  

%%% Internal load (N)  

Pz_p_DA = F7;  
  

%%% Section properties  

b_DA = 20;  

h_DA = 12.7;  

A_DA = b_DA*h_DA;  
  

%%% vonMises stress (MPa) equal in magnitude to average stress  

Sigma_v_DA = abs(Pz_p_DA/A_DA);  

fprintf("\nDrive arm vonMises stress is uniform at %f MPa.\n",Sigma_v_DA)  
  

%% Posterosuperior shaft (PSS) vonMises stress  

dlat = 19+8/2;  

dmed = 12+17.6/2;  
  

%%% External load (N) from 'Forces.m': ISO 15032 AP extension  

F5s = sqrt(F5sy^2+F5sz^2);  
  

%%% Static equilibrium to determine other external loads (N or N-mm)  

syms Flat Fmed  

SumFz_pp = -Flat + F5s - Fmed == 0;  

SumMy_pp = Flat*dlat - Fmed*dmed == 0;  

Sol = solve([SumFz_pp,SumMy_pp],[Flat Fmed]);  

Flat = double(Sol.Flat);  

Fmed = double(Sol.Fmed);  
  

%%% Internal loads (N or N-mm)  

My_pp = Fmed*dmed;  

Vz_pp = Fmed;  
  

%%% Section properties  

D_PSS = 8;  

zA_pp_PSS = D_PSS/2;  

zB_pp_PSS = 0;

```

```

zB_bar_p_PSS = -(2*D_PSS)/(3*pi);
ty_pp_PSS = D_PSS;
A_PSS = (pi*D_PSS^2)/4;
Ap_PSS = A_PSS/2;
Iy_pp_PSS = (pi*D_PSS^4)/64;
Qy_pp_PSS = zB_bar_p_PSS*Ap_PSS;

%%% vonMises stress (MPa) at critical cross-sectional points
Sigma_vA_PSS = vonMises(0,0,0,0,-My_pp,0,0,0,-Vz_pp,0,0,0,0,
A_PSS,1,Iy_pp_PSS,1,1,Qy_pp_PSS,1,1,1,1,0,0,zA_pp_PSS,1,ty_pp_PSS,1,0,0,0,
...
1,1,1);

Sigma_vB_PSS = vonMises(0,0,0,0,-My_pp,0,0,0,-Vz_pp,0,0,0,0,
A_PSS,1,Iy_pp_PSS,1,1,Qy_pp_PSS,1,1,1,1,0,0,zB_pp_PSS,1,ty_pp_PSS,1,0,0,0,
...
1,1,1);

Sigma_vC_PSS = Sigma_vA_PSS;

Sigma_v_PSS = [Sigma_vA_PSS,Sigma_vB_PSS,Sigma_vC_PSS];
Point_PSS = MaxStressPoint(Sigma_v_PSS);
fprintf("\nThe maximum posterosuperior shaft vonMises stress is %f MPa at
points %s.\n",...
max(Sigma_v_PSS),Point_PSS)

%% Cold pressing forces and respective von Mises stresses at hole
interface

% Quantities pertaining to interference fits
delta_min = 0.004;
delta_max = 0.024;
Do = 20;
Di = 0;
D = 8;
Eo = 73100; % Aluminum 2024-T351
Ei = 200000; % 17-4 PH stainless steel H900
vo = 0.33;
vi = 0.285;
mu_s = 0.45; % Steel shaft moving against an aluminum hole (dry contact)

% Posterosuperior shaft (PSS)
l_PSS = 25.6;
[Fp_PSS_min,sigma_v_PSS_min] =
InterferenceFit(delta_min,Do,Di,D,l_PSS,Eo,Ei,vo,vi,mu_s);
[Fp_PSS_max,sigma_v_PSS_max] =
InterferenceFit(delta_max,Do,Di,D,l_PSS,Eo,Ei,vo,vi,mu_s);
fprintf("\nThe cold press force required to insert the posterosuperior
shaft into the superior link ranges from %f N to %f N.\n",...
Fp_PSS_min,Fp_PSS_max)

% Posteroinferior shaft (PIS)
l_PIS = 34.2;
[Fp_PIS_min,sigma_v_PIS_min] =
InterferenceFit(delta_min,Do,Di,D,l_PIS,Eo,Ei,vo,vi,mu_s);

```

```

[Fp_PIS_max,sigma_v_PIS_max] =
InterferenceFit(delta_max,Do,Di,D,l_PIS,Eo,Ei,vo,vi,mu_s);
fprintf("\nThe cold press force required to insert the posteroinferior
shaft into the motor housing ranges from %f N to %f N.\n",...
Fp_PIS_min,Fp_PIS_max)

% Anteroinferior shaft or lateral anterosuperior shaft (AISorLASS)
l_AISorLASS = 8;
[Fp_AISorLASS_min,sigma_v_AISorLASS_min] =
InterferenceFit(delta_min,Do,Di,D,l_AISorLASS,Eo,Ei,vo,vi,mu_s);
[Fp_AISorLASS_max,sigma_v_AISorLASS_max] =
InterferenceFit(delta_max,Do,Di,D,l_AISorLASS,Eo,Ei,vo,vi,mu_s);
fprintf("\nThe cold press force required to insert the anteroinferior
shaft or lateral anterosuperior shaft into an anterior link " + ...
"ranges from %f N to %f N.\n",Fp_AISorLASS_min,Fp_AISorLASS_max)

% Medial anterosuperior shaft (MASS)
l_MASS = 16;
[Fp_MASS_min,sigma_v_min] =
InterferenceFit(delta_min,Do,Di,D,l_MASS,Eo,Ei,vo,vi,mu_s);
[Fp_MASS_max,sigma_v_max] =
InterferenceFit(delta_max,Do,Di,D,l_MASS,Eo,Ei,vo,vi,mu_s);
fprintf("\nThe cold press force required to insert the medial
anterosuperior shaft into the superior link ranges from %f N to %f
N.\n",...
Fp_MASS_min,Fp_MASS_max)
fprintf("\nThe von Mises stress at the hole interface ranges from %f MPa
to %f MPa.\n\n",...
sigma_v_min,sigma_v_max)

```

B.8 Evaluation.m

```

%% Importing test results and plotting the data
% Quantities and units: time(s), force (N), displacement (mm),
% gait cycle (%), and angle (°)
close all

% Extracting data from 'ISO 15032 AP extension 03-31-2023.xls'
Time_AP = readxlxsxSOAP('A-P','A4:A872');
Fprime_AP = readxlxsxSOAP('A-P','B4:B872');
Delta_l_AP = readxlxsxSOAP('A-P','C4:C872');

% Extracting data from 'ISO 15032 ML 04-19-2023.xls'
Time_DL = readxlxsxISOML('ML Test','A4:A880');
Fprime_DL = readxlxsxISOML('ML Test','B4:B880');
Delta_l_DL = readxlxsxISOML('ML Test','C4:C880');

% Extracting data from 'HKAfp kinematic data of individual strides.xlsx'
PercentGC_Tilt_Farshad = [];
ThetaTiltHKAfp_Farshad = [];
PercentGC_HipMotor_Farshad = [];
ThetaHipMotorHKAfp_Farshad = [];
PercentGC_FlexKnee_Farshad = [];
ThetaFlexKneeHKAfp_Farshad = [];

PercentGC_Tilt_Hossein = [];
ThetaTiltHKAfp_Hossein = [];

```

```

PercentGC_HipMotor_Hossein = [];
ThetaHipMotorHKAFP_Hossein = [];
PercentGC_FlexKnee_Hossein = [];
ThetaFlexKneeHKAFP_Hossein = [];

PercentGC_Tilt_Yousef = [];
ThetaTiltHKAFP_Yousef = [];
PercentGC_HipMotor_Yousef = [];
ThetaHipMotorHKAFP_Yousef = [];
PercentGC_FlexKnee_Yousef = [];
ThetaFlexKneeHKAFP_Yousef = [];

i = double('B');
while i >= double('B') && i <= double('Z') + 3
    if i+1 > double('Z')
        Col_Theta = strcat(char('A'),char('A'+i-double('Z')));
        if i > double('Z')
            Col_PercentGC = strcat(char('A'),char('A'+i-double('Z')-1));
        else
            Col_PercentGC = char(i);
        end
    else
        Col_PercentGC = char(i);
        Col_Theta = char(i+1);
    end

PercentGC_Tilt_Farshad = cat(1,PercentGC_Tilt_Farshad, ...
    readxlsxHKAFP('Farshad pelvic tilt',...
        strcat(Col_PercentGC,'2',':',Col_PercentGC,'90')));
ThetaTiltHKAFP_Farshad = cat(1,ThetaTiltHKAFP_Farshad, ...
    readxlsxHKAFP('Farshad pelvic tilt',...
        strcat(Col_Theta,'2',':',Col_Theta,'90')));
PercentGC_HipMotor_Farshad = cat(1,PercentGC_HipMotor_Farshad, ...
    readxlsxHKAFP('Farshad hip motor angle',...
        strcat(Col_PercentGC,'2',':',Col_PercentGC,'355')));
ThetaHipMotorHKAFP_Farshad = cat(1,ThetaHipMotorHKAFP_Farshad, ...
    readxlsxHKAFP('Farshad hip motor angle',...
        strcat(Col_Theta,'2',':',Col_Theta,'355')));

PercentGC_Tilt_Hossein = cat(1,PercentGC_Tilt_Hossein, ...
    readxlsxHKAFP('Hossein pelvic tilt',...
        strcat(Col_PercentGC,'2',':',Col_PercentGC,'91')));
ThetaTiltHKAFP_Hossein = cat(1,ThetaTiltHKAFP_Hossein, ...
    readxlsxHKAFP('Hossein pelvic tilt',...
        strcat(Col_Theta,'2',':',Col_Theta,'91')));
PercentGC_HipMotor_Hossein = cat(1,PercentGC_HipMotor_Hossein, ...
    readxlsxHKAFP('Hossein hip motor angle',...
        strcat(Col_PercentGC,'2',':',Col_PercentGC,'357')));
ThetaHipMotorHKAFP_Hossein = cat(1,ThetaHipMotorHKAFP_Hossein, ...
    readxlsxHKAFP('Hossein hip motor angle',...
        strcat(Col_Theta,'2',':',Col_Theta,'357')));

PercentGC_Tilt_Yousef = cat(1,PercentGC_Tilt_Yousef, ...
    readxlsxHKAFP('Yousef pelvic tilt',...
        strcat(Col_PercentGC,'2',':',Col_PercentGC,'124')));
ThetaTiltHKAFP_Yousef = cat(1,ThetaTiltHKAFP_Yousef, ...
    readxlsxHKAFP('Yousef pelvic tilt',...

```

```

        strcat(Col_Theta,'2',':',Col_Theta,'124'))));
PercentGC_HipMotor_Yousef = cat(1,PercentGC_HipMotor_Yousef, ...
    readxlxsHKAfp('Yousef hip motor angle',...
        strcat(Col_PercentGC,'2',':',Col_PercentGC,'489')));
ThetaHipMotorHKAfp_Yousef = cat(1,ThetaHipMotorHKAfp_Yousef, ...
    readxlxsHKAfp('Yousef hip motor angle',...
        strcat(Col_Theta,'2',':',Col_Theta,'489')));

i = i + 3;
end

i = double('A');
while i >= double('A') && i <= double('T') - 1
    Col_PercentGC = char(i);
    Col_Theta = char(i+1);

    PercentGC_FlexKnee_Farshad = cat(1,PercentGC_FlexKnee_Farshad, ...
        readxlxsHKAfp('Farshad knee flexion',...
            strcat(Col_PercentGC,'2',':',Col_PercentGC,'319')));
    ThetaFlexKneeHKAfp_Farshad = cat(1,ThetaFlexKneeHKAfp_Farshad, ...
        readxlxsHKAfp('Farshad knee flexion',...
            strcat(Col_Theta,'2',':',Col_Theta,'319')));

    PercentGC_FlexKnee_Hossein = cat(1,PercentGC_FlexKnee_Hossein, ...
        readxlxsHKAfp('Hossein knee flexion',...
            strcat(Col_PercentGC,'2',':',Col_PercentGC,'364')));
    ThetaFlexKneeHKAfp_Hossein = cat(1,ThetaFlexKneeHKAfp_Hossein, ...
        readxlxsHKAfp('Hossein knee flexion',...
            strcat(Col_Theta,'2',':',Col_Theta,'364')));

    PercentGC_FlexKnee_Yousef = cat(1,PercentGC_FlexKnee_Yousef, ...
        readxlxsHKAfp('Yousef knee flexion',...
            strcat(Col_PercentGC,'2',':',Col_PercentGC,'429')));
    ThetaFlexKneeHKAfp_Yousef = cat(1,ThetaFlexKneeHKAfp_Yousef, ...
        readxlxsHKAfp('Yousef knee flexion',...
            strcat(Col_Theta,'2',':',Col_Theta,'429')));

    i = i + 2;
end

% Concatenating data from the 3 participants
PercentGC_Tilt =
cat(1,PercentGC_Tilt_Farshad,PercentGC_Tilt_Hossein,PercentGC_Tilt_Yousef)
;
ThetaTiltHKAfp =
cat(1,ThetaTiltHKAfp_Farshad,ThetaTiltHKAfp_Hossein,ThetaTiltHKAfp_Yousef)
;
PercentGC_HipMotor =
cat(1,PercentGC_HipMotor_Farshad,PercentGC_HipMotor_Hossein,PercentGC_HipM
otor_Yousef);
ThetaHipMotorHKAfp =
cat(1,ThetaHipMotorHKAfp_Farshad,ThetaHipMotorHKAfp_Hossein,ThetaHipMotorH
KAfp_Yousef);
PercentGC_FlexKnee =
cat(1,PercentGC_FlexKnee_Farshad,PercentGC_FlexKnee_Hossein,PercentGC_Flex
Knee_Yousef);

```

```

ThetaFlexKneeHKAFF =
cat(1,ThetaFlexKneeHKAFF_Farshad,ThetaFlexKneeHKAFF_Hossein,ThetaFlexKneeHKAFF_Yousef);

% Aligning number of datapoints by linear interpolation
NumPointsTilt = 76;
NumPointsHipKnee = 101;
DeltaTilt = 100/(NumPointsTilt-1);
DeltaHipKnee = 100/(NumPointsHipKnee-1);
PercentGC_Tilt_Mean = zeros(NumPointsTilt,1);
ThetaTiltHKAFF_30Strides = zeros(NumPointsTilt,30);
PercentGC_HipKnee_Mean = zeros(NumPointsHipKnee,1);
ThetaHipMotorHKAFF_30Strides = zeros(NumPointsHipKnee,30);
ThetaFlexKneeHKAFF_30Strides = zeros(NumPointsHipKnee,30);

for n = 1:NumPointsTilt
    PercentGC_Tilt_Mean(n) = (n-1)*DeltaTilt;
end

for n = 1:NumPointsHipKnee
    PercentGC_HipKnee_Mean(n) = (n-1)*DeltaHipKnee;
end

n = 1;
j = 1;
for i = 1:numel(PercentGC_Tilt)-1
    if PercentGC_Tilt(i) == 0
        ThetaTiltHKAFF_30Strides(n,j) = ThetaTiltHKAFF(i);
    end

    if PercentGC_Tilt(i) <= n*DeltaTilt && PercentGC_Tilt(i+1) >=
n*DeltaTilt
        ThetaTiltHKAFF_30Strides(n+1,j) = ...
            (ThetaTiltHKAFF(i+1)-ThetaTiltHKAFF(i))/(PercentGC_Tilt(i+1)-
PercentGC_Tilt(i))*...
            (PercentGC_Tilt_Mean(n+1)-PercentGC_Tilt(i)) +
ThetaTiltHKAFF(i);
        n = n + 1;
    end

    if PercentGC_Tilt(i) == 100
        n = 1;
        j = j + 1;
    end
end

n = 1;
j = 1;
for i = 1:numel(PercentGC_HipMotor)-1
    if PercentGC_HipMotor(i) == 0
        ThetaHipMotorHKAFF_30Strides(n,j) = ThetaHipMotorHKAFF(i);
    end

    if PercentGC_HipMotor(i) <= n*DeltaHipKnee && PercentGC_HipMotor(i+1)
>= n*DeltaHipKnee
        ThetaHipMotorHKAFF_30Strides(n+1,j) = ...

```

```

        (ThetaHipMotorHKAfp(i+1)-
ThetaHipMotorHKAfp(i))/(PercentGC_HipMotor(i+1)-PercentGC_HipMotor(i))*...
        (PercentGC_HipKnee_Mean(n+1)-PercentGC_HipMotor(i)) +
ThetaHipMotorHKAfp(i);
        n = n + 1;
    end

    if PercentGC_HipMotor(i) == 100
        n = 1;
        j = j + 1;
    end
end

n = 1;
j = 1;
for i = 1:numel(PercentGC_FlexKnee)-1
    if PercentGC_FlexKnee(i) == 0
        ThetaFlexKneeHKAfp_30Strides(n,j) = ThetaFlexKneeHKAfp(i);
    end

    if PercentGC_FlexKnee(i) <= n*DeltaHipKnee && PercentGC_FlexKnee(i+1)
    >= n*DeltaHipKnee
        ThetaFlexKneeHKAfp_30Strides(n+1,j) = ...
        (ThetaFlexKneeHKAfp(i+1)-
ThetaFlexKneeHKAfp(i))/(PercentGC_FlexKnee(i+1)-PercentGC_FlexKnee(i))*...
        (PercentGC_HipKnee_Mean(n+1)-PercentGC_FlexKnee(i)) +
ThetaFlexKneeHKAfp(i);
        n = n + 1;
    end

    if PercentGC_FlexKnee(i) == 100
        n = 1;
        j = j + 1;
    end
end

% Calculating mean and standard deviation at each percent GC datapoint
ThetaTiltHKAfp_Mean = zeros(NumPointsTilt,1);
ThetaTiltHKAfp_SD = zeros(NumPointsTilt,1);
ThetaHipMotorHKAfp_Mean = zeros(NumPointsHipKnee,1);
ThetaHipMotorHKAfp_SD = zeros(NumPointsHipKnee,1);
ThetaFlexKneeHKAfp_Mean = zeros(NumPointsHipKnee,1);
ThetaFlexKneeHKAfp_SD = zeros(NumPointsHipKnee,1);

for n = 1:NumPointsTilt
    ThetaTiltHKAfp_Mean(n) = mean(ThetaTiltHKAfp_30Strides(n,:));
    ThetaTiltHKAfp_SD(n) = std(ThetaTiltHKAfp_30Strides(n,:));
end

for n = 1:NumPointsHipKnee
    ThetaHipMotorHKAfp_Mean(n) = mean(ThetaHipMotorHKAfp_30Strides(n,:));
    ThetaHipMotorHKAfp_SD(n) = std(ThetaHipMotorHKAfp_30Strides(n,:));
    ThetaFlexKneeHKAfp_Mean(n) = mean(ThetaFlexKneeHKAfp_30Strides(n,:));
    ThetaFlexKneeHKAfp_SD(n) = std(ThetaFlexKneeHKAfp_30Strides(n,:));
end

```

```

ThetaHipMotorHKAFP_MeanMinus1SD = ThetaHipMotorHKAFP_Mean -
ThetaHipMotorHKAFP_SD;
ThetaHipMotorHKAFP_MeanPlus1SD = ThetaHipMotorHKAFP_Mean +
ThetaHipMotorHKAFP_SD;

% Converting hip motor angle to hip flexion angle with lookup table and
linear interpolation
if not(exist('Alpha','var'))
    run('LinkageParam.m')
end

NumPointsHipMotor = 12001;
ThetaFlexHip = transpose(linspace(
ThetaExtHipMaxDev,ThetaFlexHipMaxDev,NumPointsHipMotor));
ThetaTilt = 0;
[~,~,~,Theta_m] = Kinematics1(ThetaFlexHip,ThetaTilt, ...
Theta_h,Theta4,Beta,r1,r2,r3,r4,rc,ra,rm);

ThetaFlexHipHKAFP_MeanMinus1SD = zeros(NumPointsHipKnee,1);
ThetaFlexHipHKAFP_Mean = zeros(NumPointsHipKnee,1);
ThetaFlexHipHKAFP_MeanPlus1SD = zeros(NumPointsHipKnee,1);

for n = 1:NumPointsHipKnee
    for i = 1:NumPointsHipMotor-1
        if Theta_m(i+1) <= ThetaHipMotorHKAFP_MeanPlus1SD(n) && ...
            Theta_m(i) >= ThetaHipMotorHKAFP_MeanPlus1SD(n)
            ThetaFlexHipHKAFP_MeanMinus1SD(n) = (ThetaFlexHip(i+1)-
ThetaFlexHip(i))/(Theta_m(i+1)-Theta_m(i))*...
                (ThetaHipMotorHKAFP_MeanPlus1SD(n)-Theta_m(i)) +
ThetaFlexHip(i);
            % The lower the hip flexion angle is, the higher is the motor
angle
        end

        if Theta_m(i+1) <= ThetaHipMotorHKAFP_Mean(n) && ...
            Theta_m(i) >= ThetaHipMotorHKAFP_Mean(n)
            ThetaFlexHipHKAFP_Mean(n) = (ThetaFlexHip(i+1)-
ThetaFlexHip(i))/(Theta_m(i+1)-Theta_m(i))*...
                (ThetaHipMotorHKAFP_Mean(n)-Theta_m(i)) + ThetaFlexHip(i);
        end

        if Theta_m(i+1) <= ThetaHipMotorHKAFP_MeanMinus1SD(n) && ...
            Theta_m(i) >= ThetaHipMotorHKAFP_MeanMinus1SD(n)
            ThetaFlexHipHKAFP_MeanPlus1SD(n) = (ThetaFlexHip(i+1)-
ThetaFlexHip(i))/(Theta_m(i+1)-Theta_m(i))*...
                (ThetaHipMotorHKAFP_MeanMinus1SD(n)-Theta_m(i)) +
ThetaFlexHip(i);
            % The higher the hip flexion angle is, the lower is the motor
angle
        end
    end
end

% Aligning hip flexion angle data with hip joint configuration during
standing
ThetaFlexHipHKAFP_MeanMinus1SD = ThetaFlexHipHKAFP_MeanMinus1SD - 11.8;
ThetaFlexHipHKAFP_Mean = ThetaFlexHipHKAFP_Mean - 11.8;

```

```

ThetaFlexHipHKAFP_MeanPlus1SD = ThetaFlexHipHKAFP_MeanPlus1SD - 11.8;

% Plotting force vs. time from static compression tests
figure(1)
hold on
title('ISO 15032-2000 Compression Tests')
xlabel('Time (s)')
ylabel('Force [N]')
plot(Time_AP,Fprime_AP,'Color',[0.98 0 0],'LineWidth',1) % ML force vs.
time plot is almost identical
hold off

% Plotting force vs. displacement from static compression tests
figure(2)
hold on
title('ISO 15032-2000 A-P Extension Compression Test')
xlabel('Downward displacement of upper attachment [mm]')
ylabel('Force [N]')
plot(Delta_l_AP(468:638)-Delta_l_AP(468),Fprime_AP(468:638),...
      'Color',[0.98 0 0],'LineWidth',1)
hold off

figure(3)
hold on
title('ISO 15032-2000 M-L Compression Test')
xlabel('Downward displacement of upper attachment [mm]')
ylabel('Force [N]')
plot(Delta_l_ML(470:642)-Delta_l_ML(470),Fprime_ML(470:642),...
      'Color',[0.98 0 0],'LineWidth',1)
hold off

% Plotting anterior-posterior pelvic tilt angle vs. % gait cycle from
% walking tests
GaitPlot4(4,'kmat',PercentGC_Tilt_Mean,[ThetaTiltHKAFP_Mean-
ThetaTiltHKAFP_SD,...%
      ThetaTiltHKAFP_Mean,ThetaTiltHKAFP_Mean+ThetaTiltHKAFP_SD],...
      'Anterior pelvic tilt','\theta_t_i_l_t [°]',1,65.54548234,'top')

% Plotting hip flexion-extension angle vs. % gait cycle from walking tests
GaitPlot4(5,'kmat',PercentGC_HipKnee_Mean,[ThetaFlexHipHKAFP_MeanMinus1SD,
...
      ThetaFlexHipHKAFP_Mean,ThetaFlexHipHKAFP_MeanPlus1SD],...
      'Hip flexion (+) and extension (-)','\theta_f_l_e_x_ _h_i_p
[°]',1,65.54548234,'top')

% Plotting hip flexion-extension angle vs. % gait cycle from walking tests
GaitPlot4(6,'kmat',PercentGC_HipKnee_Mean,[ThetaFlexKneeHKAFP_Mean-
ThetaFlexKneeHKAFP_SD,...%
      ThetaFlexKneeHKAFP_Mean,ThetaFlexKneeHKAFP_Mean+ThetaFlexKneeHKAFP_SD],...
      'Knee flexion (+) and extension (-)','\theta_f_l_e_x_ _k_n_e_e
[°]',1,65.54548234,'bottom')

```

B.9 cell2ind.m

```

%% Converting Excel cell reference to a row-column index pair
function indices = cell2ind(cell) % (e.g., 'B2' -> row 1, column 1)

```

```

if length(cell) == 2
    row = uint8(cell(2)-49); % MATLAB sees '1' as 49
    col = uint8(cell(1)-65); % MATLAB sees 'A' as 65
    indices = [row,col];
elseif cell(1) == 'A'
    row = uint8(cell(3)-49);
    col = uint8(cell(2)-65+26); % 'A' + 26
    indices = [row,col];
elseif cell(1) == 'B'
    row = uint8(cell(3)-49);
    col = uint8(cell(2)-65+2*26); % 'AA' + 2*26
    indices = [row,col];
elseif cell(1) == 'C'
    row = uint8(cell(3)-49);
    col = uint8(cell(2)-65+3*26); % 'BA' + 3*26
    indices = [row,col];
end
end

```

B.10 circintersec.m

```

%% Finding the points of intersection of two circles with centers (y1,z1),
(y2,z2), and respective radii of r1 and r2
% Code obtained from Roger Stafford @
https://www.mathworks.com/matlabcentral/answers/196755-fsolve-to-find-circle-intersections
function [y,z] = circintersec(y1,z1,r1,y2,z2,r2)
P1 = transpose([y1 z1]);
P2 = transpose ([y2 z2]);
d2 = sum((P2-P1).^2);
P0 = (P1+P2)/2+(r1^2-r2^2)/d2/2*(P2-P1);
t = ((r1+r2)^2-d2)*(d2-(r2-r1)^2);

if t <= 0
    fprintf('The two circles do not intersect.\n')
else
    T = sqrt(t)/d2/2*[0 -1;1 0]*(P2-P1);
    Pa = transpose(P0 + T); % Pa and Pb are circles' intersection
points
    Pb = transpose(P0 - T);
end

y = [Pa(1) Pb(1)];
z = [Pa(2) Pb(2)];
end

```

B.11 FindICR.m

```

%% Finding co-ordinates of instantaneous center of rotation (ICR)
function [y_ICR,z_ICR] = FindICR(NumCheckpts,yA,zA,yB,zB,yC,zC,yD,zD)

% Number of points per dataset
NumPoints = length(yB);

% z = my + b
m_post = zeros(NumPoints,1); % m represents slope
b_post = zeros(NumPoints,1); % b represents z-intercept

```

```

m_ant = zeros(NumPoints,1);
b_ant = zeros(NumPoints,1);

y_lower = -50; % cm
y_upper = 50;
y = transpose(linspace(y_lower,y_upper,NumCheckpts));

y_ICR = zeros(NumPoints,1);
z_ICR = zeros(NumPoints,1);

warning('off','MATLAB:polyfit:RepeatedPointsOrRescale')

for i = 1:NumPoints
    PostLineCoeff = polyfit([yA,yB(i)],[zA,zB(i)],1);
    m_post(i) = PostLineCoeff(1);
    b_post(i) = PostLineCoeff(2);

    if length(yD)>1
        AntLineCoeff = polyfit([yC(i),yD(i)],[zC(i),zD(i)],1);
    else
        AntLineCoeff = polyfit([yC(i),yD],[zC(i),zD],1);
    end
    m_ant(i) = AntLineCoeff(1);
    b_ant(i) = AntLineCoeff(2);

    z_post = m_post(i)*y + b_post(i)*ones(size(y));
    z_ant = m_ant(i)*y + b_ant(i)*ones(size(y));

    z_diff = abs(z_post(1)-z_ant(1)); % Absolute difference between
    the first elements of the z-coordinate arrays
    Index = 1; % Initially, first element array is assumed to have the
    minimum absolute difference

    % Finding point of intersection for the line passing through the
    % posterior link (length r1) and the line passing through the
    anterior link (length r3)
    for j = 1:NumCheckpts
        if abs(z_post(j)-z_ant(j)) < z_diff
            z_diff = abs(z_post(j)-z_ant(j));
            Index = j;
        end
    end
    y_ICR(i) = y(Index);
    z_ICR(i) = 0.5*(z_post(Index)+z_ant(Index));
end

end

```

B.12 GaitPlo4.m

```

%% Plotting a parameter (mean +/- 1 SD) as a function of gait cycle
percent
function GaitPlot4(FigNumber, DataType, GCPercent, Parameter, Title, yLabel, ...
MeanSD, TOPPercent, LabelVertAlign)
switch DataType
case 'kmat'
    Color = [0 0.439 0.753]; % Blue

```

```

        case 'kin'
            Color = [0.98 0 0]; % Red
        case 'MA'
            Color = [0.075 0.761 0.286]; % Green
        case 'Tmx'
            Color = [0.965 0.4 0.016]; % Orange
    end
    GCPPercent = transpose(GCPPercent);
    Parameter = transpose(Parameter);
    figure(FigNumber)
    hold on
    title>Title)
    xlabel('Gait cycle [%]')
    ylabel(yLabel)
    if MeanSD == 1

        fill([GCPPercent,fliplr(GCPPercent)], [Parameter(1,:),fliplr(Parameter(3,:))])
        ...
        Color,'LineStyle','none','FaceAlpha',0.1);
        plot(GCPPercent,Parameter(2,:),'Color',Color,'LineWidth',1);
    else
        plot(GCPPercent,Parameter,'Color',Color,'LineWidth',1);
    end
    xline(0,'--',{'Foot strike'},'LabelOrientation','horizontal',...
        'LabelVerticalAlignment',LabelVertAlign,'Color',[0.047 0.482
0.18],... % Green
        'LineWidth',1);
    xline(TOPPercent,'--',{'Toe off'},'LabelOrientation','horizontal',...
        'LabelVerticalAlignment',LabelVertAlign,'Color',[0.047 0.482
0.18],... % Green
        'LineWidth',1);
    hold off
end

```

B.13 GaitPlot5.m

```

%% Plotting a gait parameter as a function of % gait cycle for HD/HP and
TF amputees, and healthy individuals
function
GaitPlot5(FigNumber,DataHDHP,DataTF,DataHealthy,Title,xLabel,yLabel)
    figure(FigNumber)
    hold on
    title>Title)
    xlabel(xLabel)
    ylabel(yLabel)
    if DataHDHP ~= 0
        plot(DataHDHP(:,1),DataHDHP(:,2),':','Color',[0 0.4470
0.7410],'Linewidth',2)
    end
    plot(DataTF(:,1),DataTF(:,2),'--','Color',[0.8500 0.3250
0.0980],'Linewidth',2)
    plot(DataHealthy(:,1),DataHealthy(:,2),'-','Color',[0.9290 0.6940
0.1250],'Linewidth',1)
    if DataHDHP ~= 0
        legend('HD/HP amputees','TF amputees','Able-bodied
individuals','Location','best')
    else

```

```

        legend('TF amputees','Able-bodied individuals','Location','best')
    end
    hold off
end

```

B.14 HelixPoints.m

```

%% Finding co-ordinates of Helix3D linkage joints throughout the gait
cycle
%%% Note: units are cm and deg
function
[yA_Helix,zA_Helix,yB_Helix,zB_Helix,yC_Helix,zC_Helix,yD_Helix,zD_Helix]
= ...

```

HelixPoints(r1_Helix,r2_Helix,r3_Helix,r4_Helix,ThetaFlexHelix,ThetaTiltHelix)

```

% Number of points per dataset
NumPoints = length(ThetaFlexHelix);

% Point A set to be the origin (0,0) and fixed relative to the socket
yA_Helix = 0;
zA_Helix = 0;

% Point B
yB_Helix = r1_Helix*cosd(ThetaFlexHelix+270);
zB_Helix = r1_Helix*sind(ThetaFlexHelix+270);

% Point D
yD_Helix = r4_Helix*cosd(360-ThetaTiltHelix);
zD_Helix = r4_Helix*sind(360-ThetaTiltHelix);

% Point C
yCsolns_Helix = zeros(NumPoints,2);
zCsolns_Helix = zeros(NumPoints,2);
for i = 1:NumPoints
    [yCsolns_Helix(i,:),zCsolns_Helix(i,:)] =
circintersec(yB_Helix(i),zB_Helix(i),r2_Helix,yD_Helix(i),zD_Helix(i),r3_Helix);
end
yC_Helix = yCsolns_Helix(:,2); % All positive yC (corresponding to the
second column)
zC_Helix = zCsolns_Helix(:,2); % Each zC corresponding with each
positive yC

end

```

B.15 HipFlexPlot.m

```

%% Plotting a parameter as a function of hip flexion angle (°)
function HipFlexPlot(FigNumber, DataType, ThetaFlexHip, FM, Title, yLabel)
switch DataType
    case 'MA'
        Color = [0.075 0.761 0.286]; % Light green
    case 'kin'
        Color = [0.98 0 0]; % Red
    case 'Tmx'

```

```

        Color = [0.965 0.4 0.016]; % Orange
    end
    figure(FigNumber)
    title>Title)
    xlabel('Hip flexion [°]')
    ylabel(yLabel)
    hold on
    plot(ThetaFlexHip,FM,'Color',Color,'LineWidth',1)
    hold off
end

```

B.16 InterferenceFit.m

```

%% Calculate interference fit cold pressing force and von Mises stress on
hole interface
function [Fp,sigma_v] = InterferenceFit(delta,Do,Di,D,l,Eo,Ei,vo,vi,mu_s)
    % Interference pressure due to diametrical interference delta
    p = delta/((D/Eo)*((Do^2+D^2)/(Do^2-D^2)+vo)+(D/Ei)*((D^2+Di^2)/(D^2-
Di^2)-vi));

    % Contact area
    A = pi*D*l;

    % Require cold pressing force to insert shaft into hole
    Fp = mu_s*p*A;

    % Radial stress on hole
    sigma_r = -p;

    % Circumferential stress on hole
    sigma_theta = p*(Do^2+D^2)/(Do^2-D^2);

    % von Mises stress on hole interface
    sigma_v = sqrt(sigma_r^2 - sigma_r*sigma_theta + sigma_theta^2);
end

```

B.17 Kinematics1.m

```

%% Finding link angles based off hip flexion/extension angle
function [Theta1,Theta3,Theta_a,Theta_m] =
Kinematics1(ThetaFlexHip,ThetaTilt,...,
ThetaH,Theta4,Beta,r1,r2,r3,r4,rc,ra,rm)

    % Number of points per dataset
    NumPoints = length(ThetaFlexHip);

    % Angle of motor housing (inferior link)
    Theta2 = ThetaFlexHip + ThetaH;

    % Co-ordinates of pin joint pivots
    [~,~,yB,zB,yC,zC,yD,zD] =
LinkagePoints(r1,r2,r3,r4,Theta2,Theta4,ThetaTilt);

    % Angles of the posterior link, anterior link, motor and drive arm
    Theta1 = zeros(NumPoints,1);
    Theta3 = zeros(NumPoints,1);
    ThetaE = zeros(NumPoints,1);

```

```

for i = 1:NumPoints
    if length(ThetaTilt)>1
        [Theta1(i),Theta3(i)] = trigsolve9(yB(i),zB(i),yC(i),zC(i),...
            yD(i),zD(i),r1,r2,r3,r4,Theta2(i),Theta4,ThetaTilt(i),1);
    else
        [Theta1(i),Theta3(i)] = trigsolve9(yB(i),zB(i),yC(i),zC(i),...
            yD,zD,r1,r2,r3,r4,Theta2(i),Theta4,ThetaTilt,1);
    end
    if i >= 2
        if ((ThetaFlexHip(i) > ThetaFlexHip(i-1)) && (Theta3(i) <
Theta3(i-1))) ...
            || ((ThetaFlexHip(i) < ThetaFlexHip(i-1)) &&
(Theta3(i) > Theta3(i-1)))
            if length(ThetaTilt)>1
                [Theta1(i),Theta3(i)] =
trigsolve9(yB(i),zB(i),yC(i),zC(i),...

```

yD(i),zD(i),r1,r2,r3,r4,Theta2(i),Theta4,ThetaTilt(i),-1);
 else
 [Theta1(i),Theta3(i)] =
trigsolve9(yB(i),zB(i),yC(i),zC(i),...

```

                    yD,zD,r1,r2,r3,r4,Theta2(i),Theta4,ThetaTilt,-1);
            end
        end
    end
    if Theta1(i) > 360
        Theta1(i) = Theta1(i) - 360;
    end
    ThetaE(i) = acosd((rc^2+r3^2-ra^2-rm^2-2*rc*r3*cosd(180-
Theta3(i)+ThetaFlexHip(i)+Beta))/(-2*ra*rm));
    end
%     rDF = sqrt(rc^2 + r3^2 - 2*rc*r3*cosd(180-Theta3+ThetaFlexHip+Beta))
%     rDF = sqrt(ra^2 + rm^2 - 2*ra*rm*cosd(ThetaE));
    ThetaFp = asind((ra./rDF).*sind(ThetaE));
    ThetaFpp = asind((r3./rDF).*sind(180-Theta3+ThetaFlexHip+Beta));
    Theta_m = 180 - ThetaFp - ThetaFpp - Beta;
    Theta_a = ThetaE - Theta_m + ThetaFlexHip;
end

```

B.18 Kinematics4.m

```

%% Hip-knee-ankle-foot prosthesis center of mass (COM) acceleration
function [a_COMy,a_COMz] =
Kinematics4(ThetaFlexHip,OmegaFlexHip,AlphaFlexHip, ...
    ThetaTilt,OmegaTilt,AlphaTilt,y_COM,z_COM)

% Symbolic variables
syms Theta_FlexHip(t) Theta_Tilt(t)

% Number of points per dataset
NumPoints = length(ThetaFlexHip);

% y and z acceleration components
a_COMy = zeros(NumPoints,1);
a_COMz = zeros(NumPoints,1);
for i = 1:NumPoints
    aCOMy = diff(y_COM,t,t);

```

```

aCOMy =
subs(aCOMy,{Theta_FlexHip,diff(Theta_FlexHip,t),diff(Theta_FlexHip,t,t),...
.
.
.
Theta_Tilt,diff(Theta_Tilt,t),diff(Theta_Tilt,t,t)},...
{ThetaFlexHip(i),OmegaFlexHip(i),AlphaFlexHip(i),...
ThetaTilt(i),OmegaTilt(i),AlphaTilt(i)});

aCOMz = diff(z_COM,t,t);
aCOMz =
subs(aCOMz,{Theta_FlexHip,diff(Theta_FlexHip,t),diff(Theta_FlexHip,t,t),...
.
.
.
Theta_Tilt,diff(Theta_Tilt,t),diff(Theta_Tilt,t,t)},...
{ThetaFlexHip(i),OmegaFlexHip(i),AlphaFlexHip(i),...
ThetaTilt(i),OmegaTilt(i),AlphaTilt(i)});

a_COMy(i) = aCOMy;
a_COMz(i) = aCOMz;
end

end

```

B.19 LinkageParam.m

```

%% Initializing linkage parameters (optimized link lengths used)

% Angles in deg.
Alpha = 35;
Beta = 65;
Theta_h = (Beta-Alpha)/2;
Theta4 = 207;
ThetaExtHipMaxDev = 20;
ThetaFlexHipMaxDev = 100;

% Lengths in m
dh = 4.65/100; % Division by 100 is to convert cm to m
rc = 5.35/100;
r1 = 6.1224/100;
r2 = sqrt(2*rc^2*(1-cosd(180-Alpha-Beta)));
r3 = 7.0854/100;
r4 = 3.3/100;
ra = 8.2285/100;
rm = 3.2739/100;

```

B.20 LinkagePoints.m

```

%% Computing linkage points A,B,C,D for a given hip joint range of motion
%%% Note: units are cm and deg
function [yA,zA,yB,zB,yC,zC,yD,zD] = LinkagePoints(r1,r2,r3,r4,Theta2, ...
Theta4,ThetaTilt)

% Number of points per dataset
NumPoints = length(Theta2);

% Calculation of pin joint coordinates
yA = 0; % Point A set to be the origin, fixed relative to the socket
zA = 0;
yC = zeros(NumPoints,1);
zC = zeros(NumPoints,1);

```

```

yD = r4*cosd(Theta4-ThetaTilt-180);
zD = r4*sind(Theta4-ThetaTilt-180);
yDprime = yD + r2*cosd(Theta2) + r4*cosd(Theta4-ThetaTilt);
zDprime = zD + r2*sind(Theta2) + r4*sind(Theta4-ThetaTilt);
for i = 1:NumPoints
    if length(ThetaTilt)>1
        [yCtemp,zCtemp] =
circintersec(yD(i),zD(i),r3,yDprime(i),zDprime(i),r1);
    else
        [yCtemp,zCtemp] =
circintersec(yD,zD,r3,yDprime(i),zDprime(i),r1);
    end
    yC(i) = yCtemp(2); % Second intersection point is the one that
makes physical sense
    zC(i) = zCtemp(2);
end
yB = yC - yD - r2*cosd(Theta2) - r4*cosd(Theta4-ThetaTilt);
zB = zC - zD - r2*sind(Theta2) - r4*sind(Theta4-ThetaTilt);

end

```

B.21 loopclosure.m

```

%% Solving loop closure equation for link angle
function Theta3 = loopclosure(r1,r2,r3,r4,Theta1,Theta2,Theta4)
    Theta3 = acosd(-(r1*cosd(Theta1)+r2*cosd(Theta2)+r4*cosd(Theta4))/r3);
end

```

B.22 MaxStressPoint.m

```

%% Finding the point(s) on a cross-section at which stress is maximal
function Point = MaxStressPoint(Sigma_v)
    MaxIndex = find(Sigma_v == max(Sigma_v));
    if numel(MaxIndex) == 1
        switch MaxIndex
            case 1
                Point = 'A';
            case 2
                Point = 'B';
            case 3
                Point = 'C';
        end
    elseif numel(MaxIndex) == 2
        if all(MaxIndex == [1,2])
            Point = 'A and B';
        elseif all(MaxIndex == [1,3])
            Point = 'A and C';
        elseif all(MaxIndex == [2,3])
            Point = 'B and C';
        end
    elseif numel(MaxIndex) == 3
        Point = 'A, B and C';
    end
end

```

B.23 PlotICR.m

```
%% Plotting lines representing orientation of links throughout gait cycle
function PlotICR(Fig,Title,yA,zA,yB,zB,yC,zC,yD,zD,y_ICR,z_ICR,NumFrames)

    % Number of points per dataset
    NumPoints = length(yB);

    figure(Fig)

    for i = 1:NumFrames

        Delta = (NumPoints-1)/(NumFrames-1);
        Index = (i-1)*Delta + 1;

        Y_post = [yA yB(Index)];
        Z_post = [zA zB(Index)];

        Y_inf = [yB(Index) yC(Index)];
        Z_inf = [zB(Index) zC(Index)];

        Y_ant = [yC(Index) yD(Index)];
        Z_ant = [zC(Index) zD(Index)];

        Y_sup = [yA yD(Index)];
        Z_sup = [zA zD(Index)];

        Y_post_ICR = [yA y_ICR(Index)];
        Z_post_ICR = [zA z_ICR(Index)];

        Y_ant_ICR = [y_ICR(Index) yD(Index)];
        Z_ant_ICR = [z_ICR(Index) zD(Index)];

        if i < 0.6*NumFrames           % If in the stance phase
            ColorCodeLink = '#0072BD'; % Dark blue
            ColorCodeICR = '#A2142F'; % Mahogany
        else                           % If in the swing phase
            ColorCodeLink = '#C5DBF5'; % Light blue
            ColorCodeICR = '#FFCECE'; % Pink
        end

        % Mechanism range
        axis([-15 45 -15 45])
        plot([0 0], [-15 45], 'Color', '#AAAAAA') % x-axis
        plot([-15 45], [0 0], 'Color', '#AAAAAA') % y-axis

        hold on

        title>Title)
        xlabel('y [cm]')
        ylabel('z [cm]')

        % Plotting dummies for color-based legend
        LinkageStance = plot([NaN,NaN], 'color', '#0072BD');
        LinkageSwing = plot([NaN,NaN], 'color', '#C5DBF5');
```

```

InterLineStance = plot([NaN,NaN],      'color','#A2142F');
InterLineSwing  = plot([NaN,NaN],      'color','#FFCECE');
ICR            = plot([NaN,NaN],'o','color','#A2142F');

plot(Y_post,Z_post,'Color',ColorCodeLink)
plot(Y_inf, Z_inf, 'Color',ColorCodeLink)
plot(Y_ant, Z_ant, 'Color',ColorCodeLink)
plot(Y_sup, Z_sup, 'Color',ColorCodeLink)

plot(Y_post_ICR,Z_post_ICR,'Color',ColorCodeICR)
plot(Y_ant_ICR, Z_ant_ICR, 'Color',ColorCodeICR)

plot(y_ICR(Index),z_ICR(Index),'o','Color',ColorCodeICR);

legend([LinkageStance,LinkageSwing,InterLineStance,InterLineSwing,
ICR],...
        {'4-bar linkage during stance phase (StP)', '4-bar linkage
during swing phase (SwP)',...
         'ICR intersection lines during StP', 'ICR intersection lines
during SwP',...
         'ICR at one frame during the gait cycle'}));

pause(0.25);
end

hold off

end

```

B.24 readxlsxHKAFP.m

```

function Data = readxlsxHKAFP(Sheet,Range)
Data = readcell('HKAFP kinematic data of individual strides.xlsx',...
'Sheet',Sheet,'Range',Range);
Data = cell2mat(Data);
end

```

B.25 readxlsxISOAP.m

```

function Data = readxlsxISOAP(Sheet,Range)
Data = readcell('ISO 15032 AP extension 03-31-2023.xls',...
'Sheet',Sheet,'Range',Range);
Data = cell2mat(Data);
end

```

B.26 readxlsxISOML.m

```

function Data = readxlsxISOML(Sheet,Range)
Data = readcell('ISO 15032 ML 04-19-2023.xls',...
'Sheet',Sheet,'Range',Range);
Data = cell2mat(Data);
end

```

B.27 readxlsxTF.m

```

function Data = readxlsxTF(Sheet,Range)

```

```

Data = readcell('TF level walking kinematics and kinetics mean and
SD.xlsx',...
    'Sheet',Sheet,'Range',Range);
Data = cell2mat(Data);
end

```

B.28 Rotation.m

```

%% Calculate the 2D rotation matrix given an angle of rotation (in
degrees)
function RotMatrix = rotation(Theta)
    RotMatrix = [cosd(Theta), -sind(Theta); sind(Theta), cosd(Theta)];
end

```

B.29 sigdigits.m

```

% SIGDIGITS returns significant digits in a numeric non-uint64 number.
% Returns "significant" digits in a number, in the sense that if you
% printed any fewer digits the reverse conversion would not equal the
% original number. I.e., the value returned from this function is the
% minimum number of digits you must print in order to recover the original
% number with a reverse conversion.
% Programmer: James Tursa
% Code obtained from
https://www.mathworks.com/matlabcentral/answers/142819-how-to-find-number-of-significant-figures-in-a-decimal-number
function n = sigdigits(x)
if( ~isnumeric(x) || ~isfinite(x) || isa(x,'uint64') )
    error('Need any finite numeric type except uint64');
end
if( x == 0 )
    n = 0;
    return;
end
x = abs(x);
y = num2str(x,'%25.20e'); % Print out enough digits for any double
z = [' ' y]; % Pad beginning to allow rounding spillover
n = find(z=='e') - 1; % Find the exponent start
e = n;
while( str2double(y) == str2double(z) ) % While our number is still equal
to our rounded number
    zlast = z;
    c = z(e); % Least significant printed digit
    if( c == '.' )
        e = e - 1;
        c = z(e);
    end
    z(e) = '0'; % 0 the least significant printed digit
    e = e - 1;
    if( c >= '5' ) % Round up if necessary
        c = z(e);
        if( c == '.' )
            e = e - 1;
            c = z(e);
        end
    end
    while( true ) % The actual rounding loop
        if( c == ' ' )

```

```

        z(e) = '1';
        break;
    elseif( c < '9' )
        z(e) = z(e) + 1;
        break;
    else
        z(e) = '0';
        e = e - 1;
        c = z(e);
        if( c == '.' )
            e = e - 1;
            c = z(e);
        end
    end
end
n = n - 1;
z = zlast(1:n); % Get rid of exponent
while( z(n) == '0' ) % Don't count trailing 0's
    n = n - 1;
end
n = n - 2; % Don't count initial blank and the decimal point.
end

```

B.30 SimpStaticEquil3.m

```

%% Simplified static equilibrium for AP TF amputee gait cycle analysis
function [F5,F6,F2y,F2z,M2x] =
SimpStaticEquil3(NumPoints,Width,Fhy,Fhz, ...
F7,Tmx,Alpha,Beta,ThetaFlex,Theta1,Theta3,Theta_a,dh,rc)

syms F5 F6

% Superior Link loads
F5Sol = zeros(NumPoints,Width);
F6Sol = zeros(NumPoints,Width);
for j = 1:Width
    for i = 1:NumPoints
        SumFy_SL = -F5*cosd(Theta1(i)-180) + 2*F6*cosd(180-Theta3(i))
+ ...
        F7(i,j)*cosd(Theta_a(i)) + Fhy(i,j) == 0;
        SumFz_SL = -F5*sind(Theta1(i)-180) - 2*F6*sind(180-Theta3(i))
+ ...
        F7(i,j)*sind(Theta_a(i)) - Fhz(i,j) == 0;
        Sol = solve([SumFy_SL,SumFz_SL],[F5,F6]);
        F5Sol(i,j) = Sol.F5;
        F6Sol(i,j) = Sol.F6;
    end
end
F5 = F5Sol;
F6 = F6Sol;

% Motor Housing loads
F2y = Fhy;
F2z = Fhz;
M2x = -Tmx + F5.*cosd(Theta1-180).*rc.*sind(Alpha-ThetaFlex) + ...

```

```

F5.*sind(Theta1-180)*rc.*cosd(Alpha-ThetaFlex) - ...
2*F6.*cosd(180-Theta3)*rc.*sind(Beta+ThetaFlex) - ...
2*F6.*sind(180-Theta3)*rc.*cosd(Beta+ThetaFlex) + ...
F2y*dh.*cosd(ThetaFlex) - F2z*dh.*sind(ThetaFlex);

end

```

B.31 SimpStaticEquil4.m

```

%% Simplified static equilibrium for motor only analysis
function [F5,F6,FR,Fhy,Fhz,Mhx] = SimpStaticEquil4(NumPoints,F7,Tmx, ...
    Alpha,Beta,ThetaFlex,ThetaTilt,Theta1,Theta3,Theta4,Theta_a,rc,r4, ...
    Y_ICR,z_ICR)

syms F5 F6 FR

% Motor Housing loads
F5Sol = zeros(NumPoints,1);
F6Sol = zeros(NumPoints,1);
FRSol = zeros(NumPoints,1);
for i = 1:NumPoints
    SumFy = F5*cosd(Theta1(i)-180) - 2*F6*cosd(180-Theta3(i)) - ...
        F7(i)*cosd(Theta_a(i)) + FR*cosd(ThetaFlex(i)) == 0;
    SumFz = F5*sind(Theta1(i)-180) + 2*F6*sind(180-Theta3(i)) - ...
        F7(i)*sind(Theta_a(i)) + FR*sind(ThetaFlex(i)) == 0;
    SumMx = Tmx - F5*cosd(Theta1(i)-180)*rc*sind(Alpha-ThetaFlex(i)) - ...
        ...
        F5*sind(Theta1(i)-180)*rc*cosd(Alpha-ThetaFlex(i)) + ...
        2*F6*cosd(180-Theta3(i))*rc*sind(Beta+ThetaFlex(i)) + ...
        2*F6*sind(180-Theta3(i))*rc*cosd(Beta+ThetaFlex(i)) == 0;
    Sol = solve([SumFy,SumFz,SumMx],[F5,F6,FR]);
    F5Sol(i) = Sol.F5;
    F6Sol(i) = Sol.F6;
    FRSol(i) = Sol.FR;
end
F5 = F5Sol;
F6 = F6Sol;
FR = FRSol;

% Superior Link loads
Fhy = F5.*cosd(Theta1-180) - 2*F6.*cosd(180-Theta3) -
F7.*cosd(Theta_a);
Fhz = -F5.*sind(Theta1-180) - 2*F6.*sind(180-Theta3) +
F7.*sind(Theta_a);
Mhx = F7.* (cosd(Theta_a).* (z_ICR-r4.*sind(Theta4-ThetaTilt-180)) + ...
sind(Theta_a).* (r4.*cosd(Theta4-ThetaTilt-180)-y_ICR));

```

```
end

```

B.32 SimpStaticEquil5.m

```

%% Simplified static equilibrium for AP conditions in ISO 15032-2000
function [F2y,F2z,F5iy,F5iz,F5sy,F5sz,F6,Fes,Ffs,M2x] = ...
SimpStaticEquil5(APext,Fhy,Fhz,Mhx,Alpha,Beta,ThetaFlex,Theta3, ...
Theta_es,Theta_lp,Theta_s11,dfs,dh,ds11,rc)

syms F5iy F5iz F5sy F5sz F6 Fes Ffs

```

```

% Mechanical stop forces
if APext == 1 % AP extension case with extension stop
    Fstop = Fes;
    Ffs = 0;
else % AP flexion case with flexion stop
    Fstop = Ffs;
    Fes = 0;
end

% Overall hip joint equilibrium
F2y = Phy;
F2z = Phz;
if APext == 1
    y_ICR = 2.81989310/100; % Division by 100 is to convert cm to m
    z_ICR = 3.94128185/100;
    y_ICR_p = -4.93576958/100;
    z_ICR_p = 17.66087402/100;
else
    y_ICR = 2.94778043/100;
    z_ICR = 1.22380965/100;
    y_ICR_p = 9.57780595/100;
    z_ICR_p = -6.58016489/100;
end
M2x = -F2y*z_ICR_p + F2z*y_ICR_p + Mhx;

% Motor Housing (MH) equilibrium
SumFy_MH = -F2y + F5iy - 2*F6*cosd(180-Theta3) + ...
    Ffs*cosd(Theta_lp-90) == 0;
SumFz_MH = F2z - F5iz + 2*F6*sind(180-Theta3) - ...
    Ffs*sind(Theta_lp-90) == 0;
SumMx_MH = -M2x - F5iy*rc*sind(Alpha-ThetaFlex) + ...
    F5iz*rc*cosd(Alpha-ThetaFlex) + ...
    2*F6*cosd(180-Theta3)*rc*sind(Beta+ThetaFlex) + ...
    2*F6*sind(180-Theta3)*rc*cosd(Beta+ThetaFlex) - ...
    F2y*dh*cosd(ThetaFlex) + F2z*dh*sind(ThetaFlex) - ...
    Ffs*cosd(Theta_lp-90)*rc*sind(180-Beta-ThetaFlex) + ...
    Ffs*sind(Theta_lp-90)*rc*cosd(180-Beta-ThetaFlex) == 0;

% Superior Link (SL) equilibrium
SumFy_SL = F5sy + 2*F6*cosd(180-Theta3) + Phy - ...
    Fes*cosd(Theta_es) - Ffs*cosd(Theta_lp-90) == 0;
SumFz_SL = -F5sz - 2*F6*sind(180-Theta3) - Phz + ...
    Fes*sind(Theta_es) + Ffs*sind(Theta_lp-90) == 0;
SumMx_SL = Mhx + F5sy*z_ICR + F5sz*y_ICR - ...
    Fes*cosd(Theta_es)*(dsll*sind(Theta_sll)+z_ICR) - ...
    Fes*sind(Theta_es)*(dsll*cosd(Theta_sll)+y_ICR) + Ffs*dfs == 0;

% Solving for unknowns
Sol =
solve([SumFy_MH, SumFz_MH, SumMx_MH, SumFy_SL, SumFz_SL, SumMx_SL], ...
    [F5iy, F5iz, F5sy, F5sz, F6, Fstop]);
F5iy = Sol.F5iy;
F5iz = Sol.F5iz;
F5sy = Sol.F5sy;
F5sz = Sol.F5sz;
F6 = Sol.F6;

```

```

if APext == 1
    Fes = Sol.Fes;
else
    Ffs = Sol.Ffs;
end

end

```

B.33 trigsolve5.m

```

%% Solving trigometric equation for link angles
function [Theta1,Theta3] = trigsolve5(r1,r2,r3,r4,Theta2,Theta4)

syms x real

Theta3 = 360 - acosd(-(r1*cosd(x)+r2*cosd(Theta2)+r4*cosd(Theta4))/r3);
% Theta3 = acosd(-(r1*cosd(x)+r2*cosd(Theta2)+r4*cosd(Theta4))/r3);
LHS = r1*sind(x) + r2*sind(Theta2) + r3*sind(Theta3) + r4*sind(Theta4);

Theta1 = vpa(vpasolve(LHS == 0,x) + 360,10);
Theta3 = 360 - acosd(
(r1*cosd(Theta1)+r2*cosd(Theta2)+r4*cosd(Theta4))/r3);
% Theta3 = acosd(-(r1*cosd(Theta1)+r2*cosd(Theta2)+r4*cosd(Theta4))/r3);

Theta3 = vpa(Theta3,10);

end

```

B.34 trigsolve8.m

```

%% Solving trigometric equation for link angles
function [Theta1,Theta3] = trigsolve8(r1,r2,r3,r4,Theta2,Theta4)

syms x real

% Theta3 = 360 - acosd(-(r1*cosd(x)+r2*cosd(Theta2)+r4*cosd(Theta4))/r3);
Theta3 = acosd(-(r1*cosd(x)+r2*cosd(Theta2)+r4*cosd(Theta4))/r3);
LHS = r1*sind(x) + r2*sind(Theta2) + r3*sind(Theta3) + r4*sind(Theta4);

Theta1 = vpa(vpasolve(LHS == 0,x) + 360,10);
% Theta3 = 360 - acosd(
(r1*cosd(Theta1)+r2*cosd(Theta2)+r4*cosd(Theta4))/r3);
Theta3 = acosd(-(r1*cosd(Theta1)+r2*cosd(Theta2)+r4*cosd(Theta4))/r3);

Theta3 = vpa(Theta3,10);

end

```

B.35 trigsolve9.m

```

%% Solving trigometric equation for link angles
function [Theta1,Theta3] = trigsolve9(yB,zB,yC,zC,yD,zD,r1,r2,r3,r4, ...
Theta2,Theta4,ThetaTilt,sign)
Theta1 = Theta2 + 360 - acosd((yB.* (yC-yB)+zB.* (zC-zB))./(r1*r2));
Theta3 = Theta4 - ThetaTilt - sign*acosd((yD.* (yC-yD)+zD.* (zC-
zD))./(r3*r4));
end

```

B.36 vonMises

```
%% Calculate von Mises stress at a point on a part cross-section
function Sigma_v = vonMises(Px,Py,Pz,Mx,My,Mz,Vxy,Vyz,Vzx,Tx,Ty,Tz, ...
A,Ix,Iy,Iz,Qx,Qy,Qz,Jxy,Jyz,Jzx,x,y,z,tx,ty,tz,cxy,cyz,czx, ...
sign_xy,sign_yz,sign_zx)

% Normal stresses
Sigma_x = Px/A - My*z/Iy - Mz*y/Iz;
Sigma_y = Py/A - Mx*z/Ix - Mz*x/Iz;
Sigma_z = Pz/A - Mx*y/Ix - My*x/Iy;

% Shear stresses
Tau_xy = (Vxy*Qz)/(Iz*tz) + sign_xy*Ty*cxy/Jxy;
Tau_yz = (Vyz*Qx)/(Ix*tx) + sign_yz*Tz*cyz/Jyz;
Tau_zx = (Vzx*Qy)/(Iy*ty) + sign_zx*Tx*czx/Jzx ;
%%% Note: Tau_xy = Tau_yx, Tau_yz = Tau_zy, Tau_zx = Tau_xz

% von Mises stress
Sigma_v = sqrt((1/2)*(((Sigma_x - Sigma_y)^2 + (Sigma_y - Sigma_z)^2 ...
+ ...
(Sigma_z - Sigma_x)^2)+3*(Tau_xy^2 + Tau_yz^2 + Tau_zx^2)));
end
```

Appendix C: Linkage Geometry

Link lengths were calculated from geometric relationships. Link length calculations, as well as force calculations (Chapter 5) and stress calculations (Chapter 6) were carried out with respect to the coordinate system illustrated in Figure C-1, the standard coordinate system used for biomechanics.

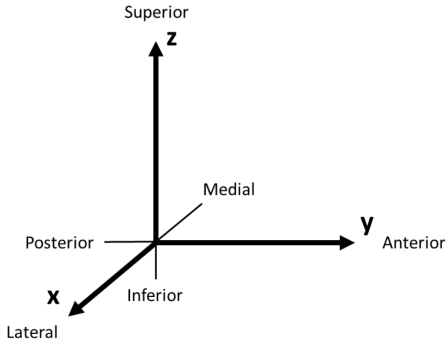


Figure C-1: Engineering analysis coordinate system.

Figure C-2 illustrates the dimensions that define powertrain linkages. Hip ROM was assumed to be governed by four-bar linkage singularity points. This assumption was then checked by determining the location of motor singularity points within hip ROM.

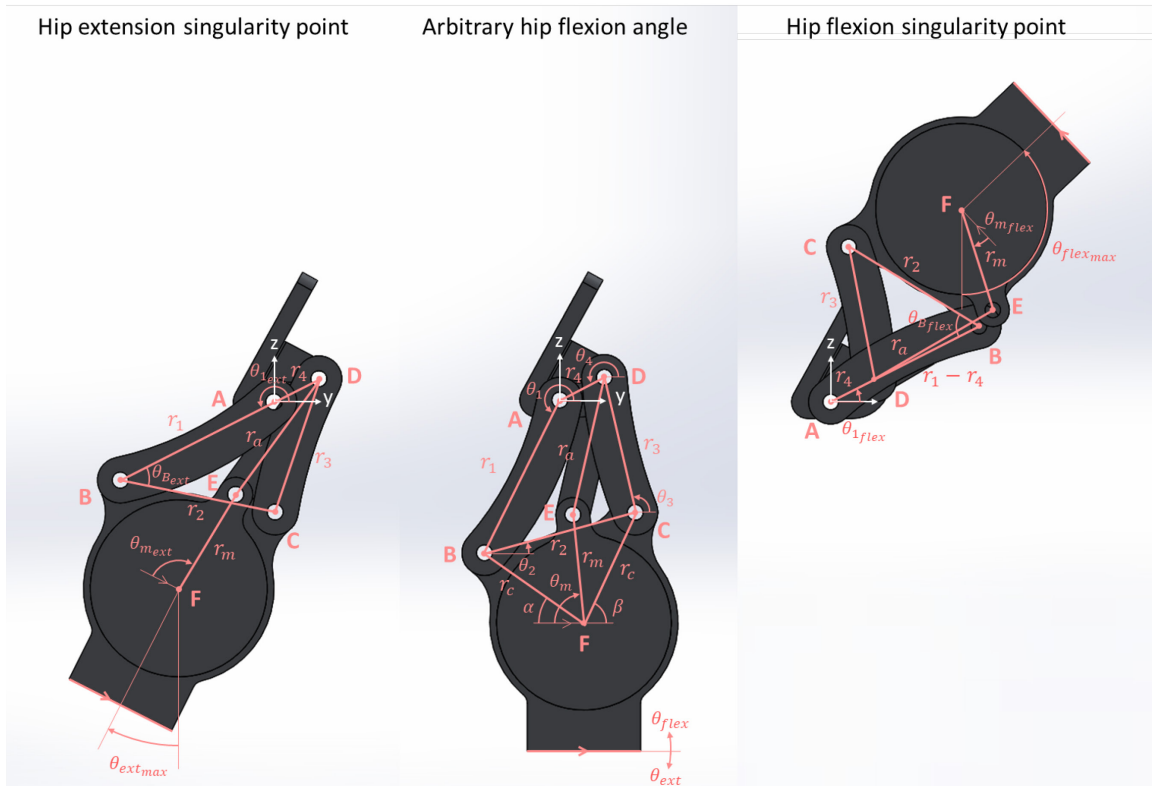


Figure C-2: Powered hip sagittal plane dimensions at arbitrary and singularity hip flexion-extension positions. Lateral view shown. Dimensions shown on an earlier powered hip model with the motor protruding medially. Origin at point A. Positive y is anterior and positive z is superior.

Motor housing geometry is defined by triangle BCF (Figure C-3).

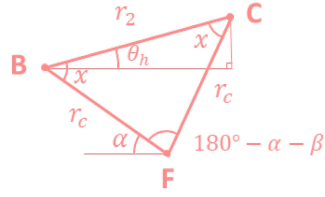


Figure C-3: Triangle BCF defining motor housing geometry.

Summation of angles to 180° and alternate angle properties provide Eq. (C-1) a relationship between motor housing angles,

$$\theta_h = \frac{\beta - \alpha}{2} \quad (\text{C-1})$$

where θ_h is the angle between edge of the motor housing and inferior link line r_2 , and α and β are each an angle between the bottom edge of the motor housing and line r_c connecting the motor center to inferior pivot B or C. Eq. (C-2) applies the cosine law to triangle BCF and can be used to calculate r_2 with known geometric parameters.

$$r_2 = \sqrt{2r_c^2(1 - \cos(180^\circ - \alpha - \beta))} \quad (\text{C-2})$$

Inferior link angle θ_2 (i.e., the angle from the horizontal to line r_2) is defined by Eq. (C-3),

$$\theta_2 = \theta_{flex} + \theta_h = 360^\circ - \theta_{ext} + \theta_h \quad (\text{C-3})$$

where θ_{flex} and θ_{ext} are hip flexion and extension angles.

Figure C-4 shows triangle BCD at the hip extension and flexion singularity positions.

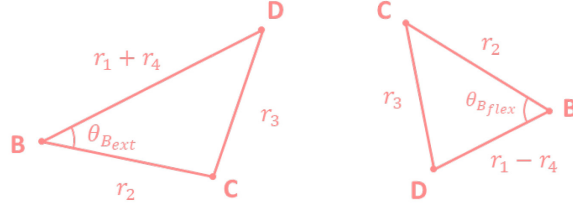


Figure C-4: Triangle BCD at hip extension (left) and hip flexion (right) singularity positions.

Applying the cosine law to triangle BCD at both singularity positions gives Eq. (C-4) and (C-5) which relate four-bar linkage link lengths to each other.

$$r_3^2 = (r_1 + r_4)^2 + r_2^2 - 2(r_1 + r_4)r_2 \cos \theta_{B_{ext}} \quad (\text{C-4})$$

$$r_3^2 = (r_1 - r_4)^2 + r_2^2 - 2(r_1 - r_4)r_2 \cos \theta_{B_{flex}} \quad (\text{C-5})$$

r_1 is posterior link (AB) length, r_2 is inferior link (BC) length, r_3 is anterior link (CD) length, and r_4 is superior link (DA) length. $\theta_{B_{ext}}$ is the angle at point B when the hip is at its extension singularity

point, and $\theta_{B\text{flex}}$ is the angle at point B when the hip at its flexion singularity point. Eq. (C-6) and (C-7) define $\theta_{B\text{ext}}$ and $\theta_{B\text{flex}}$ in terms of known angular quantities. $\theta_{ext_{max}}$ is maximum allowable hip extension (i.e., the hip extension angle at the hip extension singularity position). $\theta_{flex_{max}}$ is maximum allowable hip flexion (i.e., the hip flexion angle at the hip flexion singularity position). $\theta_{1\text{ext}}$ is the posterior link angle at maximum allowable hip extension. $\theta_{1\text{flex}}$ is the posterior link angle at maximum allowable hip flexion.

$$\theta_{B\text{ext}} = \theta_{1\text{ext}} + \theta_{ext_{max}} - \theta_h - 180^\circ \quad (\text{C-6})$$

$$\theta_{B\text{flex}} = \theta_{1\text{flex}} - \theta_{flex_{max}} - \theta_h + 180^\circ \quad (\text{C-7})$$

Equating Eq. (C-4) to Eq. (C-5) and isolating for r_1 yields Eq. (C-8) for calculating posterior link length (r_1) with only two other link lengths (r_2 and r_4):

$$r_1 = \frac{r_2 r_4 (\cos \theta_{B\text{flex}} + \cos \theta_{B\text{ext}})}{2r_4 + r_2 (\cos \theta_{B\text{flex}} - \cos \theta_{B\text{ext}})} \quad (\text{C-8})$$

r_3 can then be determined by substituting r_1 , r_2 , and r_3 in Eq. (C-4) or (C-5).

Figure C-5 shows triangles BDF and DEF at the hip extension singularity position.

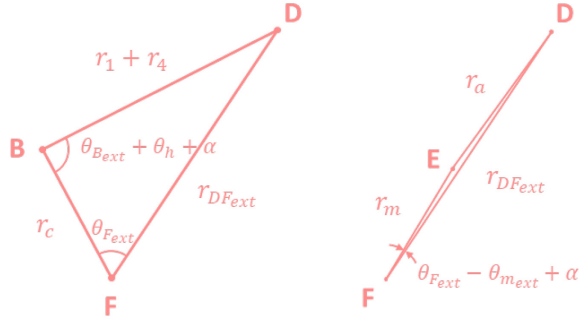


Figure C-5: Triangle BDF (left) and triangle DEF (right) at the hip extension singularity position.

Applying the cosine law to these triangles at the hip extension singularity position yields Eq. (C-9) and (C-10) which relate drive arm length r_a to motor arm length r_m .

$$r_{DFext}^2 = (r_1 + r_4)^2 + r_c^2 - 2r_c(r_1 + r_4) \cos(\theta_{B\text{ext}} + \theta_h + \alpha) \quad (\text{C-9})$$

$$r_a^2 = r_m^2 + r_{DFext}^2 - 2r_m r_{DFext} \cos(\theta_{F\text{ext}} - \theta_{m\text{ext}} + \alpha) \quad (\text{C-10})$$

Figure C-6 shows triangles BDF and DEF at the hip flexion singularity position.

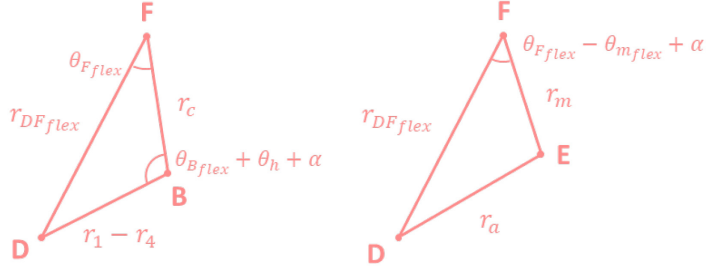


Figure C-6: Triangle BDF (left) and triangle DEF (right) at the hip flexion singularity position.

Applying the cosine law to these triangles at the hip flexion singularity position yields Eq. (C-11) and (C-12) which also relate r_a to r_m .

$$r_{DF_flex}^2 = (r_1 - r_4)^2 + r_c^2 - 2r_c(r_1 - r_4) \cos(\theta_{B_flex} + \theta_h + \alpha) \quad (\text{C-11})$$

$$r_a^2 = r_m^2 + r_{DF_flex}^2 - 2r_m r_{DF_flex} \cos(\theta_{F_flex} - \theta_{m_flex} + \alpha) \quad (\text{C-12})$$

Equating Eq. (C-10) to Eq. (C-12), substituting Eq. (C-9) and (C-11) in the resulting equation, and isolating for r_m yields Eq. (C-13), an expression for motor arm length in terms of motor angle at hip flexion and extension singularity positions (θ_{m_flex} and $\theta_{m_{ext}}$).

$$r_m = \frac{r_{DF_flex}^2 - r_{DF_{ext}}^2}{2[r_{DF_flex} \cos(\theta_{F_flex} - \theta_{m_flex} + \alpha) - r_{DF_{ext}} \cos(\theta_{F_{ext}} - \theta_{m_{ext}} + \alpha)]} \quad (\text{C-13})$$

r_a can be then calculated by substituting r_m in Eq. (C-10) or (C-12).

Figure C-7 shows triangles DEF and DCF at an arbitrary hip flexion-extension position. θ_E , the angle between the motor arm r_m and the drive arm r_a , can be calculated throughout hip ROM. The change in θ_E relative to the change in θ_{flex} indicates whether the singularity point at which the motor and drive arms are collinear has been crossed.

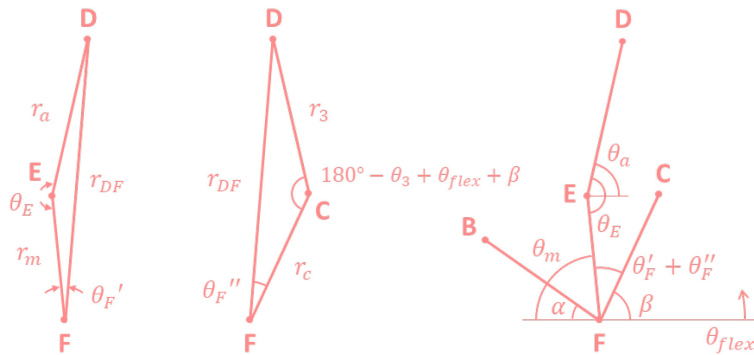


Figure C-7: Triangles DEF and DCF at an arbitrary hip flexion-extension position, and motor-related angular parameters near point F.

Applying cosine law to triangles DEF and DCF yields Eq. (C-14) and (C-15). Equating Eq. (C-14) to (C-15), and isolating for θ_E in terms of r_m and r_a gives an expression, Eq. (C-16), that can be used to determine linkage singularity.

$$r_{DF}^2 = r_c^2 + r_3^2 - 2r_c r_3 \cos(180^\circ - \theta_3 + \theta_{flex} + \beta) \quad (\text{C-14})$$

$$r_{DF}^2 = r_a^2 + r_m^2 - 2r_a r_m \cos \theta_E \quad (\text{C-15})$$

$$\theta_E = \cos^{-1} \left(\frac{r_c^2 + r_3^2 - r_a^2 - r_m^2 - 2r_c r_3 \cos(180^\circ - \theta_3 + \theta_{flex} + \beta)}{-2r_a r_m} \right) \quad (\text{C-16})$$

θ_m , the motor angle at an arbitrary hip flexion-extension position, can be determined by applying sine law triangles DEF and DCF, isolating for θ_F' and θ_F'' (Eq. (C-17) and (C-18)), and applying the summation of angles to 180° near point F (Eq. (C-19)). θ_m can then be used to calculate the corresponding drive arm angle θ_a (Eq. (C-20)).

$$\theta_F' = \sin^{-1} \left(\frac{r_a}{r_{DF}} \sin \theta_E \right) \quad (\text{C-17})$$

$$\theta_F'' = \sin^{-1} \left(\frac{r_3}{r_{DF}} \sin(180^\circ - \theta_3 + \theta_{flex} + \beta) \right) \quad (\text{C-18})$$

$$\theta_m = 180^\circ - \theta_F' - \theta_F'' - \beta \quad (\text{C-19})$$

$$\theta_a = \theta_E - \theta_m + \theta_{flex} \quad (\text{C-20})$$

Point E coordinates (y_E, z_E) are components of the vector sum of \vec{r}_1 , \vec{r}_c , and \vec{r}_m (Figure C-8).

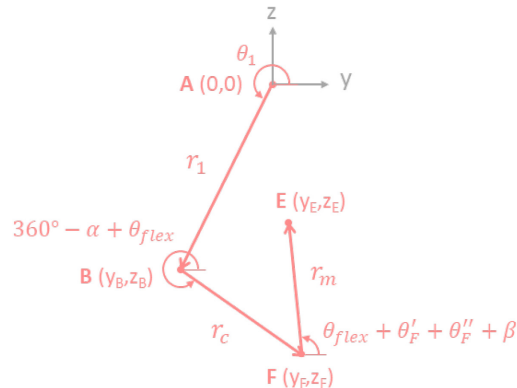


Figure C-8: Linkage vector diagram from point A to point F.

(y_E, z_E) can be calculated as the sum of point F coordinates (y_F, z_F) and \vec{r}_m components (Eq. (C-21) and (C-22)).

$$y_E = y_F + r_{m_y} = [r_1 \cos \theta_1 + r_c \cos(360^\circ - \alpha + \theta_{flex})] + [r_m \cos(\theta_{flex} + \theta_F' + \theta_F'' + \beta)] \quad (\text{C-21})$$

$$z_E = z_F + r_{m_z} = [r_1 \sin \theta_1 + r_c \sin(360^\circ - \alpha + \theta_{flex})] + [r_m \sin(\theta_{flex} + \theta_F' + \theta_F'' + \beta)] \quad (\text{C-22})$$

Figure C-9 shows triangle ADE at an arbitrary hip flexion-extension position.

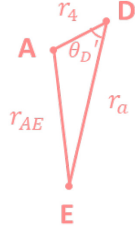


Figure C-9: Triangle ADE at an arbitrary hip flexion-extension position.

θ_D' , the angle between lines AD and DE can be found by calculating r_{AE} , the length of line AE (Eq. (C-23)), applying cosine law to triangle ADE, and isolating for θ_D' (Eq. (C-24)). The change in θ_D' relative to the change in θ_{flex} indicates whether the singularity point at which the drive arm and superior link are collinear has been crossed (more details in Section 4.3).

$$r_{AE} = \sqrt{y_E^2 + z_E^2} \quad (\text{C-23})$$

$$\theta_D' = \cos^{-1} \left(\frac{r_{AE}^2 - r_4^2 - r_a^2}{-2r_4r_a} \right) \quad (\text{C-24})$$

Figure C-10 presents loop closure and dot product diagrams for four-bar linkage ABCD at an arbitrary hip flexion-extension angle.

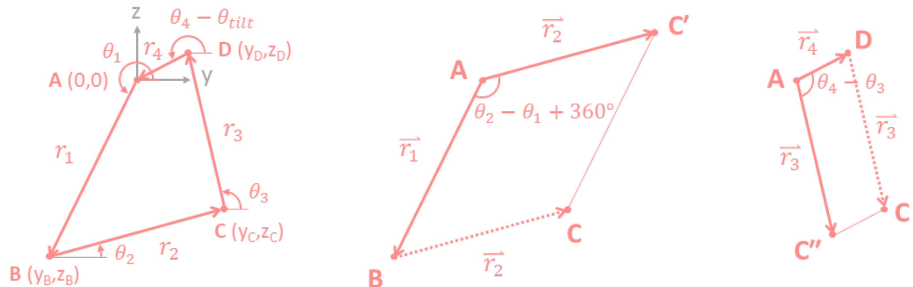


Figure C-10: Linkage ABCD loop closure and dot product diagrams at an arbitrary hip flexion-extension position.

Angles θ_1 and θ_3 can be determined by applying the dot product to vectors \vec{r}_1 and \vec{r}_2 (Eq. (C-25) and (C-26)) and vectors \vec{r}_3 and \vec{r}_4 (Eq. (C-28) and (C-29)), and isolating for θ_1 (Eq. (C-27)) and θ_3 (Eq. (C-30)).

$$\vec{r}_1 \cdot \vec{r}_2 = (y_B \hat{j} + z_B \hat{k}) \cdot ((y_C - y_B) \hat{j} + (z_C - z_B) \hat{k}) = y_B(y_C - y_B) + z_B(z_C - z_B) \quad (\text{C-25})$$

$$\vec{r}_1 \cdot \vec{r}_2 = r_1 r_2 \cos(\theta_2 - \theta_1 + 360^\circ) \quad (\text{C-26})$$

$$\theta_1 = \theta_2 + 360^\circ - \cos^{-1} \left(\frac{y_B(y_C - y_B) + z_B(z_C - z_B)}{r_1 r_2} \right) \quad (\text{C-27})$$

$$\vec{r}_3 \cdot \vec{r}_4 = ((y_C - y_D) \hat{j} + (z_C - z_D) \hat{k}) \cdot (y_D \hat{j} + z_D \hat{k}) = y_D(y_C - y_D) + z_D(z_C - z_D) \quad (\text{C-28})$$

$$\vec{r}_3 \cdot \vec{r}_4 = r_3 r_4 \cos(\theta_4 - \theta_{\text{tilt}} - \theta_3) \quad (\text{C-29})$$

$$\theta_3 = \theta_4 - \theta_{\text{tilt}} - \cos^{-1} \left(\frac{y_D(y_C - y_D) + z_D(z_C - z_D)}{r_3 r_4} \right) \quad (\text{C-30})$$

θ_{tilt} is the pelvic tilt angle which is set to zero for linkage optimization (Section 4.3) and set to gait cycle values for gait cycle force analysis (Section 5.3).

Point B coordinates (y_B, z_B) can be expressed in terms of point C coordinates (y_C, z_C) and point D coordinates (y_D, z_D) from four-bar linkage loop closure (Eq. (C-31) and (C-32)). Point D' $(y_{D'}, z_{D'})$ coordinates can be obtained by summing the terms in brackets.

$$y_B = y_C - (y_D + r_2 \cos \theta_2 + r_4 \cos(\theta_4 - \theta_{\text{tilt}})) = y_C - y_{D'} \quad (\text{C-31})$$

$$z_B = z_C - (z_D + r_2 \sin \theta_2 + r_4 \sin(\theta_4 - \theta_{\text{tilt}})) = z_C - z_{D'} \quad (\text{C-32})$$

Point D coordinates (y_D, z_D) relative to point A $(0,0)$ can be calculated with Eq. (C-33) and (C-34).

$$y_D = r_4 \cos(\theta_4 - \theta_{\text{tilt}} - 180^\circ) \quad (\text{C-33})$$

$$z_D = r_4 \sin(\theta_4 - \theta_{\text{tilt}} - 180^\circ) \quad (\text{C-34})$$

Eq. (C-35) is the equation of a r_1 radius circle centered at point B:

$$y_B^2 + z_B^2 = r_1^2 \quad (\text{C-35})$$

Point C coordinates (y_C, z_C) relative to point A $(0,0)$ can be determined by finding the rightmost intersection point of the radius r_3 circle centered at point D, and the radius r_1 circle centered at point D' (Figure C-11).

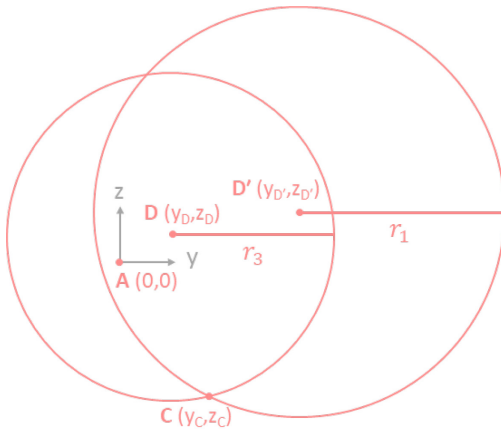


Figure C-11: Point C represented as the rightmost intersection point of two circles.

(C-36) is the r_3 radius circle equation. Substituting Eq. (C-31) and (C-32) into Eq. (C-35) gives the r_1 radius circle equation (Eq. (C-37)).

$$(y_C - y_D)^2 + (z_C - z_D)^2 = r_3^2 \quad (\text{C-36})$$

$$(y_C - y_{D'})^2 + (z_C - z_{D'})^2 = r_1^2 \quad (\text{C-37})$$

Eq. (C-38) is the formula for the rightmost intersection point of the two circles in Figure C-11, i.e., the formula for the coordinates of point C.

$$\begin{aligned} \left[\begin{matrix} y_C \\ z_C \end{matrix} \right] &= \frac{1}{2} \left[\begin{matrix} y_D + y_{D'} \\ z_D + z_{D'} \end{matrix} \right] + \frac{r_3^2 - r_1^2}{2[(y_{D'} - y_D)^2 + (z_{D'} - z_D)^2]} \left[\begin{matrix} y_{D'} - y_D \\ z_{D'} - z_D \end{matrix} \right] \\ &- \frac{\sqrt{[(r_1 + r_3)^2 - (y_{D'} - y_D)^2 - (z_{D'} - z_D)^2][(y_{D'} - y_D)^2 + (z_{D'} - z_D)^2 - (r_1 - r_3)^2]}}{2[(y_{D'} - y_D)^2 + (z_{D'} - z_D)^2]} \left[\begin{matrix} z_D - z_{D'} \\ y_{D'} - y_D \end{matrix} \right] \end{aligned} \quad (\text{C-38})$$

Figure C-12 illustrates dimensions measuring powered hip protrusion in the standing and sitting positions.

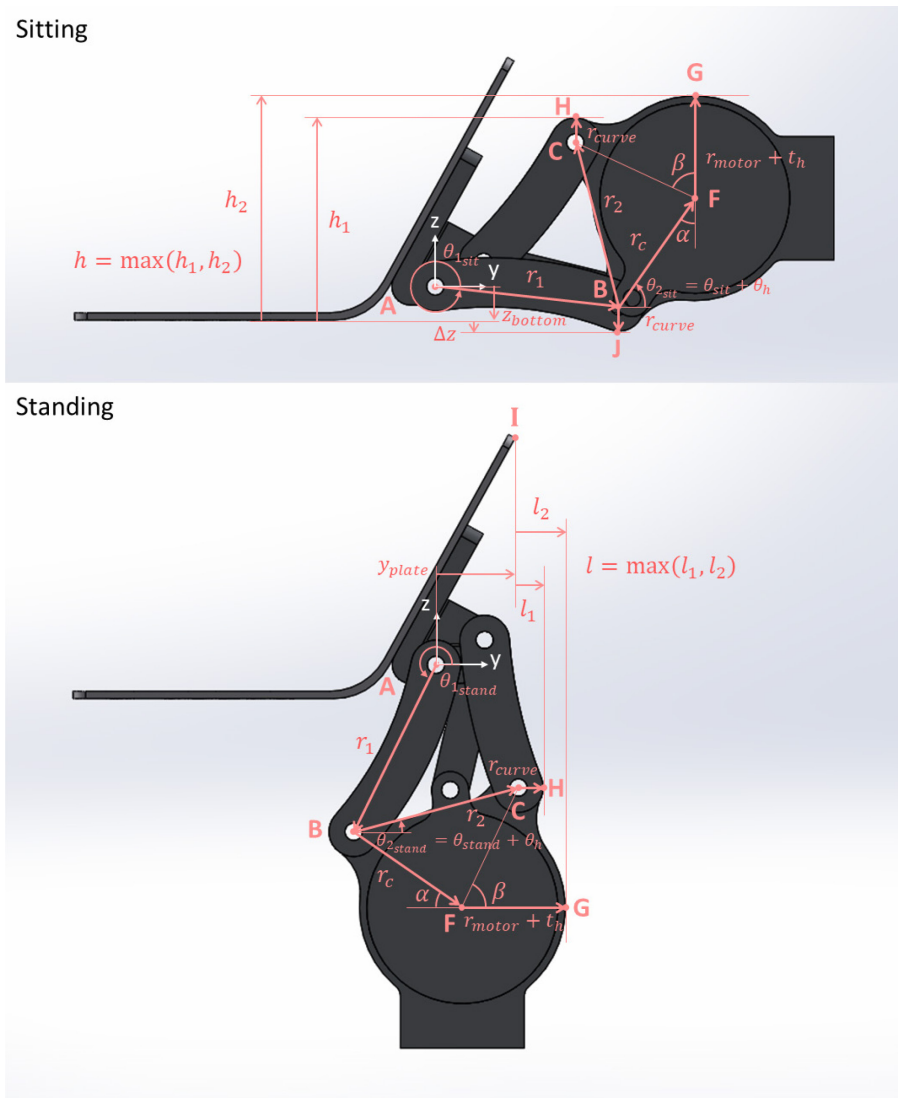


Figure C-12: Powered hip sagittal plane dimensions at sitting and standing. Lateral view shown. Dimensions shown on an earlier powered hip model with the motor protruding medially. Origin at point A. Positive y is anterior and positive z is superior.

These dimensions are used to assess cosmesis and user comfort. l is the horizontal protrusion in front of the lamination plate when the user is standing; l indicates whether the hip would interfere with pants in the standing position. h is the vertical protrusion above the bottom surface of the lamination plate when the user is sitting; h indicates whether the hip would interfere with pants in the sitting position. Δz is the vertical protrusion relative to the lamination plate bottom surface. Negative Δz values indicate that the hip protrudes below the lamination plate bottom surface. Positive Δz values indicate that the hip bottom surface is above the lamination plate bottom surface. Δz indicates whether the hip would cause uncomfortable sitting due to the hip blocking socket contact with the chair.

Motor housing geometry results in anterior link protrusion (horizontal or vertical distance to point H), motor housing protrusion (horizontal or vertical distance to point G), or posterior link protrusion (vertical distance to point J). l and h are the maximum values of anterior link and motor housing protrusions (Eq. (C-39) to (C-44)). Δz is posterior link protrusion (Eq. (C-45)).

$$l_1 = r_1 \cos \theta_{1_{stand}} + r_2 \cos(\theta_{stand} + \theta_h) + r_{curve} - y_{plate} \quad (\text{C-39})$$

$$l_2 = r_1 \cos \theta_{1_{stand}} + r_c \cos \alpha + r_{motor} + t_h - y_{plate} \quad (\text{C-40})$$

$$l = \max(l_1, l_2) \quad (\text{C-41})$$

$$h_1 = r_1 \sin \theta_{1_{sit}} + r_2 \sin(\theta_{stand} + \theta_h) + r_{curve} - z_{bottom} \quad (\text{C-42})$$

$$h_2 = r_1 \sin \theta_{1_{sit}} + r_c \cos \alpha + r_{motor} + t_h - z_{bottom} \quad (\text{C-43})$$

$$h = \max(h_1, h_2) \quad (\text{C-44})$$

$$\Delta z = r_1 \sin \theta_{1_{sit}} - r_{curve} - z_{bottom} \quad (\text{C-45})$$

Angle β determines length l_1 and height h_1 . A slighter smaller β would result in l or h being the horizontal or vertical distance between points A and G, instead of l or h being the horizontal or vertical distance between points A and H. For optimal performance, values of angle α have been chosen to be much smaller than values of angle β (as described in Section 4.3). Therefore, Δz will always be the vertical distance from the lamination plate bottom surface to point J.

Appendix D: Link Length Optimization Iterations

Please refer to Figure 4-5 for optimization variable definitions. $F_{7\max}$ is the maximum drive arm force within the powered hip range of motion, occurring at the 20° full hip extension. The 184 powertrain link length optimization iterations are presented in Table D-1 to Table D-40. Variable values are listed in table pairs with one table listing inputs that remained constant for a group of trials and the other table listing the inputs and outputs for the individual trials of the group. Unlisted values are values that were not determined for a specific trial due to early elimination based on other values. For brevity, mechanical advantages and range of motion singularity points are not presented.

Please run ‘OptimizeLinkage8.m’ (Appendix B.4) for specific trials to learn more about how mechanical advantage varies throughout the hip flexion-extension range of motion and how the hip behaves near its singularity points. Furthermore, the program will output a motion plot, providing information on range of motion restrictions due to structural interference. Some l , h , and Δz values may be slightly different than the values currently outputted by the program. These minor differences in values are due to minor dimensional modifications to the lamination plate and superior link throughout the optimization process.

Table D-1: Fixed inputs for link length optimization iterations 1 to 4.

Fixed Inputs	r_c	r_2	r_4	α	β	θ_4
Values	5.7335 cm	11.4670 cm	2.8000 cm	0.0000°	0.0000°	199.8334°

Table D-2: Link length optimization iterations 1 to 4.

Trial	Inputs (°)				Outputs (cm)							
	$\theta_{ext\max}$	$\theta_{flex\max}$	θ_{mext}	θ_{mflex}	r_1	r_3	r_a	r_m	l	h	Δz	$F_{7\max}$
1	46.8280	114.9334	71.8174	2.0047	7.5000	12.0000	4.5000	5.2179	11.0558	13.8502	-	-
2	45.0000	120.0000	77.0000	2.0000	7.0318	11.5008	3.9894	5.0604	10.8288	13.5020	-	-
3	40.0000	120.0000	80.0000	0.0000	11.7108	13.2220	8.7755	3.8737	7.8268	12.5197	-	-
4	40.0000	120.0000	85.0000	0.0000	11.7108	13.2220	8.7757	3.8700	7.8268	12.5197	-	-

Table D-3: Fixed inputs for link length optimization iterations 5 and 6.

Fixed Inputs	r_c	r_2	r_4	α	β	θ_4
Values	5.7335 cm	11.4670 cm	2.8000 cm	0.0000°	0.0000°	200.9248°

Table D-4: Link length optimization iterations 5 and 6.

Trial	Inputs (°)				Outputs (cm)							
	$\theta_{ext\max}$	$\theta_{flex\max}$	θ_{mext}	θ_{mflex}	r_1	r_3	r_a	r_m	l	h	Δz	$F_{7\max}$
5	35.0000	120.0000	85.0000	5.0000	23.4293	21.9645	20.0876	3.6088	1.0243	10.9008	-	-
6	45.0000	120.0000	77.0000	2.0000	6.6506	11.5061	3.6215	5.2101	11.3700	14.1402	-	-

Table D-5: Fixed inputs for link length optimization iterations 7 to 54.

Fixed Inputs	r_c	r_2	r_4	α	β	θ_4
Values	5.3500 cm	6.8778 cm	2.2000 cm	35.0000°	65.0000°	207.0357°

Table D-6: Link length optimization iterations 7 to 54.

Trial	Inputs (°)				Outputs (cm)							
	θ_{ext_max}	θ_{flex_max}	θ_{m_ext}	θ_{m_flex}	r_1	r_3	r_a	r_m	l	h	Δz	$F_{7\max}$
7	26.6287	133.6203	94.5931	26.2388	7.5000	6.1000	6.2000	4.7762	2.0253	9.0881	-0.4444	-
8	25.0000	125.0000	100.0000	20.0000	11.2873	9.0063	10.9219	3.3517	-0.3840	9.1981	-0.3344	-
9	27.0000	133.0000	100.0000	20.0000	7.5255	6.1624	6.8301	4.2003	2.0748	9.1427	-0.3897	-
10	22.0000	128.0000	95.0000	5.0000	11.1963	8.6057	11.7110	2.2622	-1.0022	8.6633	-0.8692	-
11	27.0000	133.0000	95.0000	25.0000	7.5255	6.1624	6.3518	4.6734	2.0748	9.1427	-0.3897	-
12	25.0000	130.0000	95.0000	25.0000	8.9814	7.0391	7.9445	4.2454	0.9176	8.9990	-0.5334	-
13	25.0000	130.0000	125.0000	5.0000	8.9814	7.0391	9.4128	3.0528	0.9176	8.9990	-0.5334	-
14	25.0000	130.0000	125.0000	25.0000	8.9814	7.0391	7.7277	5.0880	0.9176	8.9990	-0.5334	-
15	20.0000	125.0000	105.0000	5.0000	14.9488	11.8918	15.5742	1.6966	-3.8594	8.4221	-1.1104	-
16	20.0000	125.0000	115.0000	5.0000	14.9488	11.8918	15.5792	1.6627	-3.8594	8.4221	-1.1104	-
17	20.0000	125.0000	115.0000	-35.0000	14.9488	11.8918	16.3265	0.9153	-3.8594	8.4221	-1.1104	-
18	20.0000	125.0000	115.0000	-25.0000	14.9488	11.8918	16.2159	1.0259	-3.8594	8.4221	-1.1104	-
19	20.0000	125.0000	115.0000	-9.4000	14.9488	11.8918	15.9611	1.2808	-3.8594	8.4221	-1.1104	-
20	27.0000	133.0000	115.0000	-9.4000	7.5255	6.1624	8.6167	2.5676	2.0748	9.1427	-0.3897	-
21	27.0000	133.0000	105.0000	15.0000	7.5255	6.1624	7.2381	3.8408	2.0748	9.1427	-0.3897	-
22	27.0000	133.0000	105.0000	20.0000	7.5255	6.1624	4.2734	2.0748	9.1427	-0.3897	-	
23	27.0000	133.0000	100.0000	15.0000	7.5255	6.1624	7.2473	3.7817	2.0748	9.1427	-0.3897	-
24	27.0000	133.0000	95.0000	15.0000	7.5255	6.1624	7.2483	3.7757	2.0748	9.1427	-0.3897	-
25	27.0000	133.0000	95.0000	10.0000	7.5255	6.1624	7.6088	3.4147	2.0748	9.1427	-0.3897	-
26	27.0000	133.0000	95.0000	5.0000	7.5255	6.1624	7.9202	3.1030	2.0748	9.1427	-0.3897	-
27	27.0000	133.0000	95.0000	-5.0000	7.5255	6.1624	8.4217	2.6009	2.0748	9.1427	-0.3897	-
28	27.0000	133.0000	95.0000	-20.0000	7.5255	6.1624	8.9502	2.0720	2.0748	9.1427	-0.3897	-
29	27.0000	133.0000	95.0000	-19.0000	7.5255	6.1624	8.9214	2.1008	2.0748	9.1427	-0.3897	-
30	15.0000	145.0000	95.0000	25.0000	8.0338	5.1619	6.8723	3.7028	-0.1282	7.5729	-1.9596	-
31	15.0000	155.0000	95.0000	25.0000	6.7896	4.2394	5.4046	4.0592	0.7710	7.5690	-1.9635	-
32	10.0000	155.0000	95.0000	25.0000	7.4268	4.1510	6.0407	3.6297	-0.3089	7.0081	-2.5243	-
33	15.0000	135.0000	95.0000	25.0000	10.7688	7.5229	9.9528	3.1446	-2.1052	7.5364	-1.9960	-
34	17.0000	143.0000	95.0000	25.0000	7.9946	5.3503	6.8549	3.8320	0.1882	7.8245	-1.7080	-
35	17.0000	133.0000	95.0000	25.0000	10.9152	7.8472	10.1105	3.2778	-1.8382	7.8374	-1.6951	-
36	22.0000	138.0000	95.0000	25.0000	7.8205	5.7870	6.6960	4.2075	1.0751	8.4791	-1.0534	-
37	22.0000	133.0000	95.0000	25.0000	9.0770	6.7769	8.0778	3.9734	0.3021	8.5519	-0.9805	-
38	22.0000	128.0000	95.0000	25.0000	11.1963	8.6057	10.3736	3.6611	-1.0022	8.6633	-0.8692	-
39	22.0000	130.0000	95.0000	25.0000	10.1966	7.7246	9.2957	3.7978	-0.3869	8.6121	-0.9204	-
40	24.0000	132.0000	95.0000	25.0000	8.7063	6.7034	7.6586	4.2023	0.8886	8.8250	-0.7075	-
41	25.0000	130.0000	95.0000	25.0000	8.9814	7.0391	7.9445	4.2454	0.9176	8.9990	-0.5334	-
42	25.0000	132.0000	95.0000	25.0000	8.3739	6.5578	7.2881	4.3451	1.2603	8.9445	-0.5880	-
43	25.0000	125.0000	95.0000	25.0000	11.2873	9.0063	10.4155	3.9330	-0.3840	9.1981	-0.3344	-
44	25.0000	128.0000	95.0000	25.0000	9.7368	7.6628	8.7576	4.1327	0.4913	9.0654	-0.4670	-
45	27.0000	143.0000	95.0000	25.0000	6.0766	5.2319	4.8104	4.9763	2.8401	8.9671	-0.5653	-
46	27.0000	138.0000	95.0000	25.0000	6.6647	5.5830	5.4332	4.8437	2.5296	9.0401	-0.4923	-
47	30.0000	135.0000	95.0000	25.0000	5.3681	5.7991	4.0820	5.9233	4.3293	9.8171	0.2847	-
48	30.0000	145.0000	95.0000	25.0000	4.6875	5.4929	3.5361	6.0642	4.5832	9.6627	0.1302	-
49	30.0000	160.0000	95.0000	45.0000	4.1746	5.3083	2.3912	7.4899	4.7740	9.5429	0.0104	-
50	26.0000	134.0000	95.0000	25.0000	7.5948	6.0929	6.4366	4.5719	1.8676	9.0110	-0.5214	-
51	28.0000	136.0000	95.0000	25.0000	6.7322	5.7459	5.4988	4.9172	2.6515	9.1794	-0.3531	-
52	28.0000	132.0000	95.0000	25.0000	7.4507	6.2290	6.2589	4.7796	2.2850	9.2732	-0.2592	-
53	28.0000	127.0000	95.0000	25.0000	8.8231	7.2608	7.7182	4.5560	1.5846	9.4467	-0.0857	-
54	28.0000	130.0000	95.0000	25.0000	7.9182	6.5664	6.7555	4.6983	2.0465	9.3330	-0.1994	-

Table D-7: Fixed inputs for link length optimization iterations 55 to 58.

Fixed Inputs	r_c	r_2	r_4	α	β	θ_4
Values	5.3500 cm	6.5137 cm	2.2000 cm	35.0000°	70.0000°	207.0357°

Table D-8: Link length optimization iterations 55 to 58.

Trial	Inputs (°)				Outputs (cm)							
	θ_{ext_max}	θ_{flex_max}	θ_{m_ext}	θ_{m_flex}	r_1	r_3	r_a	r_m	l	h	Δz	$F_{7\max}$
55	28.0000	136.0000	95.0000	25.0000	6.4005	5.2489	5.1585	4.9786	2.8628	9.3210	-0.2115	-
56	28.0000	132.0000	95.0000	25.0000	6.9771	5.6431	5.7688	4.8569	2.5743	9.4344	-0.0981	-
57	27.0000	133.0000	95.0000	25.0000	7.0397	5.5754	5.8504	4.7488	2.3775	9.3181	-0.2144	-
58	27.5000	135.0000	95.0000	25.0000	6.6297	5.3450	5.4058	4.8822	2.6689	9.3041	-0.2283	-

Table D-9: Fixed inputs for link length optimization iterations 59 to 62.

Fixed Inputs	r_c	r_2	r_4	α	β	θ_4
Values	5.3500 cm	7.2288 cm	2.2000 cm	35.0000°	60.0000°	207.0357°

Table D-10: Link length optimization iterations 59 to 62.

Trial	Inputs ($^{\circ}$)				Outputs (cm)							
	θ_{ext_max}	θ_{flex_max}	θ_{m_ext}	θ_{m_flex}	r_1	r_3	r_a	r_m	l	h	Δz	$F_{7\max}$
59	28.0000	136.0000	95.0000	25.0000	7.0328	6.2563	5.8067	4.8670	2.4628	9.0511	-0.4813	-
60	28.0000	132.0000	95.0000	25.0000	7.9147	6.8417	6.7373	4.7135	2.0062	9.1162	-0.4162	-
61	27.0000	133.0000	95.0000	25.0000	8.0041	6.7786	6.8440	4.6088	1.7812	8.9710	-0.5614	-
62	27.5000	135.0000	95.0000	25.0000	7.3721	6.4105	6.1687	4.7609	2.2031	9.0045	-0.5280	-

Table D-11: Fixed inputs for link length optimization iterations 63 to 66.

Fixed Inputs	r_c	r_2	r_4	α	β	θ_4
Values	5.3500 cm	6.5137 cm	2.2000 cm	40.0000 $^{\circ}$	65.0000 $^{\circ}$	207.0357 $^{\circ}$

Table D-12: Link length optimization iterations 63 to 66.

Trial	Inputs ($^{\circ}$)				Outputs (cm)							
	θ_{ext_max}	θ_{flex_max}	θ_{m_ext}	θ_{m_flex}	r_1	r_3	r_a	r_m	l	h	Δz	$F_{7\max}$
63	28.0000	136.0000	95.0000	25.0000	6.0125	5.5713	5.2093	4.9818	2.7787	9.1645	-0.0838	-
64	28.0000	132.0000	95.0000	25.0000	6.5920	5.9439	5.9439	4.8796	2.4833	9.2520	0.0037	-
65	27.0000	133.0000	95.0000	25.0000	6.6789	5.8889	5.9106	4.7745	2.2789	9.1338	-0.1145	-
66	27.5000	135.0000	95.0000	25.0000	6.2519	5.6643	5.4607	4.8939	2.5802	9.1378	-0.1106	-

Table D-13: Fixed inputs for link length optimization iterations 67 to 70.

Fixed Inputs	r_c	r_2	r_4	α	β	θ_4
Values	5.3500 cm	7.2288 cm	2.2000 cm	30.0000 $^{\circ}$	65.0000 $^{\circ}$	207.0357 $^{\circ}$

Table D-14: Link length optimization iterations 67 to 70.

Trial	Inputs ($^{\circ}$)				Outputs (cm)							
	θ_{ext_max}	θ_{flex_max}	θ_{m_ext}	θ_{m_flex}	r_1	r_3	r_a	r_m	l	h	Δz	$F_{7\max}$
67	28.0000	136.0000	95.0000	25.0000	7.4436	5.8903	5.7754	4.8404	2.5000	9.1667	-0.6166	-
68	28.0000	132.0000	95.0000	25.0000	8.2997	6.4904	6.6976	4.6714	2.0635	9.2666	-0.5167	-
69	27.0000	133.0000	95.0000	25.0000	8.3588	6.4099	6.7733	4.5670	1.8495	9.1254	-0.6579	-
70	27.5000	135.0000	95.0000	25.0000	7.7638	6.0449	6.1239	4.7286	2.2499	9.1336	-0.6496	-

Table D-15: Fixed inputs for link length optimization iterations 71 to 78.

Fixed Inputs	r_c	r_2	r_4	α	β	θ_4
Values	5.3500 cm	6.8778 cm	2.2000 cm	35.0000 $^{\circ}$	65.0000 $^{\circ}$	207.0357 $^{\circ}$

Table D-16: Link length optimization iterations 71 to 78.

Trial	Inputs ($^{\circ}$)				Outputs (cm)							
	θ_{ext_max}	θ_{flex_max}	θ_{m_ext}	θ_{m_flex}	r_1	r_3	r_a	r_m	l	h	Δz	$F_{7\max}$
71	26.0000	136.0000	95.0000	25.0000	7.2102	5.8227	6.0221	4.6464	2.0777	8.9702	-0.5623	-
72	26.0000	140.0000	95.0000	25.0000	6.6045	5.4252	5.3703	4.7743	2.4085	8.9040	-0.6285	-
73	26.5000	136.0000	95.0000	25.0000	7.0880	5.7994	5.8878	4.7134	2.2249	9.0239	-0.5085	-
74	26.5000	134.5000	95.0000	25.0000	7.3595	5.9857	6.1791	4.6601	2.0790	9.0545	-0.4779	-
75	26.5000	133.5000	95.0000	25.0000	7.5608	6.1280	6.3952	4.6221	1.9708	9.0770	-0.4555	-
76	26.5000	133.5000	95.0000	-19.0000	7.5608	6.1280	6.9320	2.0805	1.9708	9.0770	-0.4555	-
77	26.5000	133.5000	95.0000	-20.0000	7.5608	6.1280	8.9604	2.0521	1.9708	9.0770	-0.4555	-
78	27.0000	134.0000	95.0000	-19.0000	7.3234	6.0203	8.7373	2.1080	2.1816	9.1190	-0.4135	-

Table D-17: Fixed inputs for link length optimization iterations 79 and 80.

Fixed Inputs	r_c	r_2	r_4	α	β	θ_4
Values	5.1500 cm	6.6207 cm	2.2000 cm	35.0000 $^{\circ}$	65.0000 $^{\circ}$	207.0357 $^{\circ}$

Table D-18: Link length optimization iterations 79 and 80.

Trial	Inputs ($^{\circ}$)				Outputs (cm)							
	θ_{ext_max}	θ_{flex_max}	θ_{m_ext}	θ_{m_flex}	r_1	r_3	r_a	r_m	l	h	Δz	$F_{7\max}$
79	27.0000	133.0000	95.0000	-20.0000	7.0608	5.8605	8.3999	2.1216	2.1860	9.1357	-0.2330	-
80	26.5000	133.5000	95.0000	-20.0000	7.0962	5.8281	8.4119	2.1017	2.0852	9.0745	-0.2941	-

Table D-19: Fixed inputs for link length optimization iterations 81 to 148.

Fixed Inputs	r_c	r_2	r_4	α	β	θ_4
Values	5.3500 cm	6.8778 cm	2.2000 cm	35.0000°	65.0000°	207.0357°

Table D-20: Link length optimization iterations 81 to 148.

Trial	Inputs (°)				Outputs (cm)							
	$\theta_{ext\ max}$	$\theta_{flex\ max}$	$\theta_{m\ ext}$	$\theta_{m\ flex}$	r_1	r_3	r_a	r_m	l	h	Δz	$F_{7\ max}$ (N)
81	27.0000	133.0000	92.0000	-13.0000	7.5255	6.1624	8.7322	2.2992	2.0748	9.1427	-0.3897	-
82	27.0000	133.0000	94.0000	-13.0000	7.5255	6.1624	8.7313	2.2931	2.0748	9.1427	-0.3897	-
83	27.0000	133.0000	90.0000	-20.0000	7.5255	6.1624	8.9535	2.0860	2.0748	9.1427	-0.3897	-
84	27.0000	133.0000	95.0000	-15.0000	7.5255	6.1624	8.7981	2.2242	2.0748	9.1427	-0.3897	-
85	27.0000	133.0000	92.0000	-18.0000	7.5255	6.1624	8.8933	2.1372	2.0748	9.1427	-0.3897	-
86	27.0000	133.0000	100.0000	-10.0000	7.5255	6.1624	8.6235	2.4016	2.0748	9.1427	-0.3897	-
87	27.0000	133.0000	97.0000	-13.0000	7.5255	6.1624	8.7309	2.2898	2.0748	9.1427	-0.3897	-
88	27.0000	133.0000	90.0000	-25.0000	7.5255	6.1624	9.0864	1.9516	2.0748	9.1427	-0.3897	-
89	27.0000	133.0000	98.0000	-12.0000	7.5255	6.1624	8.6960	2.3252	2.0748	9.1427	-0.3897	-
90	27.0000	133.0000	95.0000	-10.0000	7.5255	6.1624	8.6232	2.3992	2.0748	9.1427	-0.3897	-
91	27.0000	133.0000	90.0000	-15.0000	7.5255	6.1624	8.8009	2.2403	2.0748	9.1427	-0.3897	-
92	27.0000	133.0000	90.0000	-10.0000	7.5255	6.1624	8.6253	2.4180	2.0748	9.1427	-0.3897	-
93	27.0000	123.0000	110.0000	-10.0000	11.3059	9.2415	12.5531	1.9009	0.0757	9.5646	0.0322	-
94	27.0000	123.0000	95.0000	-25.0000	11.3059	9.2415	12.9352	1.5299	0.0757	9.5646	0.0322	-
95	27.0000	128.0000	95.0000	-25.0000	8.8833	7.1918	10.4816	1.7518	1.3571	9.2981	-0.2344	-
96	27.0000	138.0000	95.0000	-15.0000	6.6647	5.5830	7.8735	2.4032	2.5296	9.0401	-0.4923	-
97	50.0000	115.0000	60.0000	-60.0000	3.8597	6.7035	7.3902	2.1331	6.7435	10.9547	1.4222	-
98	50.0000	115.0000	60.0000	-35.0000	3.8597	6.7035	6.7011	2.8479	6.7435	10.9547	1.4222	-
99	55.0000	110.0000	60.0000	-45.0000	2.9968	6.8133	6.3156	2.7000	7.3109	10.9975	1.4650	-
100	40.0000	125.0000	70.0000	-32.0000	5.3330	6.3487	7.7066	2.4702	5.0914	10.4030	0.8705	-
101	35.0000	115.0000	96.0000	-21.0000	10.9180	9.8186	12.8067	1.9549	2.2477	11.0110	1.4785	24920
102	34.0000	116.0000	95.5000	-20.5000	11.0154	9.7853	12.8512	1.9201	1.9518	10.8396	1.3071	-
103	35.0000	125.0000	83.0000	-26.0000	6.7683	6.6073	8.7525	2.2546	3.8055	10.1256	0.5931	-
104	32.0000	128.0000	86.0000	-23.0000	7.0956	6.4644	8.8525	2.2098	3.1476	9.7769	0.2444	19450
105	30.0000	140.0000	85.0000	-24.5000	5.8327	5.4554	7.4426	2.3772	3.3987	9.3016	-0.2309	20523
106	32.0000	133.0000	89.0000	-25.0000	6.2332	5.9183	8.0055	2.2948	3.5220	9.6215	0.0890	21819
107	28.0000	142.0000	89.0000	-23.0000	5.9982	5.3077	7.4534	2.3426	3.0256	9.0802	-0.4522	28745
108	30.0000	137.0000	90.9000	-24.0000	6.1581	5.6365	7.7806	2.3018	3.2451	9.3538	-0.1787	26921
109	30.0000	139.0000	90.2000	-24.5000	5.9337	5.5101	7.5511	2.3419	3.3511	9.3179	-0.2146	25480
110	30.0000	140.0000	89.9000	-24.8000	5.8327	5.4554	7.4487	2.3594	3.3987	9.3016	-0.2309	25123
111	33.0000	133.0000	88.0000	-26.0000	6.0025	5.9036	7.8458	2.3331	3.7769	9.7051	0.1727	19453
112	31.0000	140.0000	88.6000	-25.8000	5.6518	5.4781	7.3410	2.3916	3.6282	9.3931	-0.1394	22202
113	30.0000	138.0000	90.5000	-24.3000	6.0419	5.5703	7.6634	2.3208	3.3000	9.3352	-0.1972	25881
114	30.0000	137.0000	86.0000	-24.0000	6.1581	5.6365	7.7832	2.3104	3.2451	9.3538	-0.1787	21501
115	30.0000	137.0000	70.0000	-22.0000	6.1581	5.6365	7.7682	2.5346	3.2451	9.3538	-0.1787	7806
116	30.0000	137.0000	75.0000	-24.0000	6.1581	5.6365	7.8083	2.3940	3.2451	9.3538	-0.1787	10414
117	30.0000	137.0000	-20.0000	80.0000	6.1581	5.6365	7.6676	2.4742	3.2451	9.3538	-0.1787	13287
118	30.0000	137.0000	-24.0000	80.0000	6.1581	5.6365	7.7933	2.3445	3.2451	9.3538	-0.1787	14113
119	30.0000	137.0000	-24.0000	82.0000	6.1581	5.6365	7.7890	2.3302	3.2451	9.3538	-0.1787	16187
120	30.0000	137.0000	-24.0000	83.0000	6.1581	5.6365	7.7872	2.3241	3.2451	9.3538	-0.1787	17380
121	32.0000	138.0000	70.0000	-22.0000	5.6555	5.5973	7.3243	2.6631	3.7726	9.5151	-0.0174	7984
122	30.0000	138.0000	70.0000	-22.0000	6.0419	5.5703	7.6414	2.5594	3.3000	9.3352	-0.1972	7793
123	30.0000	140.0000	70.0000	-22.0000	5.8327	5.4554	7.4104	2.6074	3.3987	9.3016	-0.2309	7764
124	30.0000	139.0000	70.0000	-22.0000	5.9337	5.5101	7.5223	2.5836	3.3511	9.3179	-0.2146	7779
125	30.0000	150.0000	70.0000	-22.0000	5.1084	5.1038	6.5696	2.8252	3.7405	9.1818	-0.3507	7580
126	40.0000	139.0000	70.0000	-22.0000	4.8329	6.1036	6.8180	2.9328	5.2257	10.2586	0.7261	7728
127	30.0000	133.0000	95.0000	-19.0000	6.7213	5.9790	8.2292	2.3377	2.9790	9.4424	-0.0900	25698
128	33.0000	133.0000	95.0000	-19.0000	6.0025	5.9036	7.6182	2.5835	3.7769	9.7051	0.1727	14650
129	30.0000	137.0000	95.0000	-19.0000	6.1581	5.6365	7.6240	2.4667	3.2451	9.3538	-0.1787	21543
130	30.0000	137.0000	74.0000	-23.0000	6.1581	5.6365	7.7817	2.4392	3.2451	9.3538	-0.1787	9704
131	30.0000	137.0000	72.0000	-22.0000	6.1581	5.6365	7.7587	2.5018	3.2451	9.3538	-0.1787	8603
132	30.0000	137.0000	70.0000	-20.0000	6.1581	5.6365	7.7028	2.6085	3.2451	9.3538	-0.1787	7534
133	30.0000	137.0000	65.0000	-27.0000	6.1581	5.6365	7.9481	2.4545	3.2451	9.3538	-0.1787	6839
134	30.0000	137.0000	68.0000	-24.0000	6.1581	5.6365	7.8412	2.4997	3.2451	9.3538	-0.1787	7377
135	30.0000	137.0000	70.0000	-24.0000	6.1581	5.6365	7.8302	2.4647	3.2451	9.3538	-0.1787	8078
136	30.0000	137.0000	90.0000	-24.0000	6.1581	5.6365	7.7807	2.3021	3.2451	9.3538	-0.1787	26060
137	43.0000	117.0000	78.0000	-34.0000	5.6291	6.8471	8.1912	2.3786	5.4970	10.8557	1.3232	10280
138	43.0000	117.0000	80.6000	-34.0000	5.6291	6.8471	8.1904	2.3760	5.4970	10.8557	1.3232	10400
139	43.0000	107.0000	80.6000	-34.0000	9.4717	9.5669	12.0366	2.0298	4.7051	12.0988	2.5663	-
140	42.0000	118.0000	81.7000	-32.9000	5.7928	6.8279	8.2808	2.3611	5.2969	10.7844	1.2519	11040
141	43.0000	112.0000	83.6000	-31.8000	6.8477	7.6054	9.3495	2.2951	5.2472	11.2519	1.7194	11380
142	43.0000	122.0000	78.7000	-35.6000	4.9299	6.4758	7.5251	2.4373	5.6394	10.6267	1.0942	9766
143	43.0000	125.0000	77.8000	-36.4000	4.6387	6.3375	7.2467	2.4679	5.6984	10.5307	0.9983	9485
144	43.0000	128.0000	77.0000	-37.0000	4.4083	6.2355	7.0216	2.4988	5.7449	10.4545	0.9221	9243
145	45.0000	130.0000	74.2000	-39.8000	3.9478	6.2518	7.5415	2.3021	6.0919	10.5010	0.9685	8120
146	45.0000	120.0000	76.5000	-36.5000	4.6420	6.5504	7.3765	2.4665	5.9835	10.7497	1.2172	8696

147	45.0000	122.0000	78.5000	-35.5000	4.4576	6.4651	7.2012	2.4847	6.0125	10.6839	1.1514	8578
148	45.0000	115.0000	77.0000	-36.0000	5.2838	6.8773	7.9838	2.4138	5.8818	10.9778	1.4454	9219

Table D-21: Fixed inputs for link length optimization iterations 149 and 150.

Fixed Inputs	r_c	r_2	r_4	α	β	θ_4
Values	5.3500 cm	6.5137 cm	2.2000 cm	40.0000°	65.0000°	207.0357°

Table D-22: Link length optimization iterations 149 and 150.

Trial	Inputs (°)				Outputs (cm)							
	θ_{ext_max}	θ_{flex_max}	θ_{m_ext}	θ_{m_flex}	r_1	r_3	r_a	r_m	l	h	Δz	$F_{7\max}$ (N)
149	43.0000	122.0000	78.5000	-35.5000	4.1956	6.2136	7.1359	2.5062	5.6160	10.4197	1.1714	6506
150	43.0000	125.0000	77.7000	-36.3000	3.9932	6.1218	6.9493	2.5208	5.6561	10.3478	1.0995	6398

Table D-23: Fixed inputs for link length optimization iterations 151 and 152.

Fixed Inputs	r_c	r_2	r_4	α	β	θ_4
Values	5.3500 cm	6.5137 cm	2.2000 cm	35.0000°	70.0000°	207.0357°

Table D-24: Link length optimization iterations 151 and 152.

Trial	Inputs (°)				Outputs (cm)							
	θ_{ext_max}	θ_{flex_max}	θ_{m_ext}	θ_{m_flex}	r_1	r_3	r_a	r_m	l	h	Δz	$F_{7\max}$ (N)
151	43.0000	122.0000	78.0000	-36.0000	4.8490	6.0216	7.4636	2.4298	5.6990	10.6404	1.1079	33740
152	43.0000	125.0000	77.0000	-36.0000	4.5941	5.8950	7.1947	2.4824	5.7461	10.5437	1.0112	30500

Table D-25: Fixed inputs for link length optimization iterations 153 and 154.

Fixed Inputs	r_c	r_2	r_4	α	β	θ_4
Values	5.3500 cm	6.8778 cm	2.2000 cm	40.0000°	60.0000°	207.0357°

Table D-26: Link length optimization iterations 153 and 154.

Trial	Inputs (°)				Outputs (cm)							
	θ_{ext_max}	θ_{flex_max}	θ_{m_ext}	θ_{m_flex}	r_1	r_3	r_a	r_m	l	h	Δz	$F_{7\max}$ (N)
153	43.0000	122.0000	78.5000	-35.5000	4.1830	6.6478	7.1244	2.5070	5.5900	10.4167	1.1684	5274
154	43.0000	125.0000	77.0000	-36.0000	3.9611	6.5524	6.9113	2.5318	5.6376	10.3480	1.0996	5180

Table D-27: Fixed inputs for link length optimization iterations 155 and 156.

Fixed Inputs	r_c	r_2	r_4	α	β	θ_4
Values	5.3500 cm	6.8778 cm	2.2000 cm	30.0000°	70.0000°	207.0357°

Table D-28: Link length optimization iterations 155 and 156.

Trial	Inputs (°)				Outputs (cm)							
	θ_{ext_max}	θ_{flex_max}	θ_{m_ext}	θ_{m_flex}	r_1	r_3	r_a	r_m	l	h	Δz	$F_{7\max}$ (N)
155	43.0000	122.0000	78.5000	-35.5000	5.5821	6.2536	7.8050	2.3781	5.6989	10.8139	1.0307	56190
156	43.0000	125.0000	77.0000	-36.0000	5.2422	6.0775	7.4626	2.4314	5.7637	10.6927	0.9095	42150

Table D-29: Fixed inputs for link length optimization iterations 157 and 158.

Fixed Inputs	r_c	r_2	r_4	α	β	θ_4
Values	5.3500 cm	7.2288 cm	2.2000 cm	35.0000°	60.0000°	207.0357°

Table D-30: Link length optimization iterations 157 and 158.

Trial	Inputs (°)				Outputs (cm)							
	θ_{ext_max}	θ_{flex_max}	θ_{m_ext}	θ_{m_flex}	r_1	r_3	r_a	r_m	l	h	Δz	$F_{7\max}$ (N)
157	43.0000	122.0000	78.0000	-35.0000	4.9492	6.9199	7.5244	2.4548	5.6059	10.6199	1.0874	6646
158	43.0000	125.0000	77.0000	-36.0000	4.6262	6.7734	7.2235	2.4809	5.6760	10.5274	0.9949	6492

Table D-31: Fixed inputs for link length optimization iterations 159 and 160.

Fixed Inputs	r_c	r_2	r_4	α	β	θ_4
Values	5.3500 cm	7.2288 cm	2.2000 cm	30.0000°	65.0000°	207.0357°

Table D-32: Link length optimization iterations 159 and 160.

Trial	Inputs ($^{\circ}$)				Outputs (cm)							
	θ_{ext_max}	θ_{flex_max}	θ_{m_ext}	θ_{m_flex}	r_1	r_3	r_a	r_m	l	h	Δz	$F_{7\max}$ (N)
159	43.0000	122.0000	78.0000	-35.0000	4.9492	6.9199	7.5244	2.4548	5.6059	10.6199	1.0874	18540
160	43.0000	125.0000	77.0000	-36.0000	4.6262	6.7734	7.2235	2.4809	5.6760	10.5274	0.9949	17470

Table D-33: Fixed inputs for link length optimization iterations 161 to 164.

Fixed Inputs	r_c	r_2	r_4	α	β	θ_4
Values	5.3500 cm	6.8778 cm	2.2000 cm	35.0000 $^{\circ}$	65.0000 $^{\circ}$	207.0357 $^{\circ}$

Table D-34: Link length optimization iterations 161 to 164.

Trial	Inputs ($^{\circ}$)				Outputs (cm)							
	θ_{ext_max}	θ_{flex_max}	θ_{m_ext}	θ_{m_flex}	r_1	r_3	r_a	r_m	l	h	Δz	$F_{7\max}$ (N)
161	40.0000	120.0000	83.5000	-30.5000	6.1020	6.7805	8.4351	2.3385	4.8841	10.6230	1.0905	12520
162	43.0000	114.0000	82.0000	-32.0000	6.2663	7.2280	8.7716	2.3551	5.3666	11.0632	1.5308	10850
163	41.0000	114.0000	85.5000	-29.5000	7.2397	7.6376	9.5962	2.2578	4.7714	11.0899	1.5574	12960
164	44.0000	114.0000	80.5000	-34.5000	5.8439	7.0846	8.4629	2.3585	5.6222	11.0510	1.5185	10120

Table D-35: Fixed inputs for link length optimization iterations 165 to 171.

Fixed Inputs	r_c	r_2	r_4	α	β	θ_4
Values	5.3500 cm	6.8778 cm	2.2000 cm	35.0000 $^{\circ}$	65.0000 $^{\circ}$	207.0357 $^{\circ}$

Table D-36: Link length optimization iterations 165 to 171.

Trial	Inputs ($^{\circ}$)				Outputs (cm)							
	θ_{ext_max}	θ_{flex_max}	θ_{m_ext}	θ_{m_flex}	r_1	r_3	r_a	r_m	l	h	Δz	$F_{7\max}$ (N)
165	42.0000	114.0000	84.0000	-31.0000	6.7297	7.4098	9.1683	2.3006	5.0843	11.0762	1.5437	11860
166	43.0000	113.0000	82.9000	-32.3000	6.5371	7.4005	9.0534	2.3138	5.3110	11.1512	1.6187	11140
167	43.0000	111.0000	84.0000	-31.0000	7.2073	7.8514	9.6849	2.2831	5.1731	11.3684	1.8359	11630
168	42.5000	112.5000	84.1000	-31.3000	6.9496	7.6156	9.4177	2.2832	5.1300	11.2147	1.6822	11760
169	43.0000	111.5000	83.9000	-31.6000	7.0206	7.7227	9.5167	2.2832	5.2116	11.3079	1.7755	11540
170	43.5000	111.5000	83.0000	-32.4000	6.7431	7.5939	9.2817	2.3041	5.3629	11.2868	1.7543	11040
171	43.0000	115.0000	81.7000	-33.2000	6.0282	7.0814	8.5692	2.3471	5.4154	10.9858	1.4533	10730

Table D-37: Fixed inputs for link length optimization iterations 172 to 179.

Fixed Inputs	r_c	r_2	r_4	α	β	θ_4
Values	5.3500 cm	6.8778 cm	3.3000 cm	35.0000 $^{\circ}$	65.0000 $^{\circ}$	207.0000 $^{\circ}$

Table D-38: Link length optimization iterations 172 to 179.

Trial	Inputs ($^{\circ}$)				Outputs (cm)							
	θ_{ext_max}	θ_{flex_max}	θ_{m_ext}	θ_{m_flex}	r_1	r_3	r_a	r_m	l	h	Δz	$F_{7\max}$ (N)
172	36.0000	114.0000	88.0000	-39.0000	5.8072	6.8132	7.8915	3.2949	6.0397	11.2859	1.7534	9647
173	36.0000	108.0000	90.0000	-38.0000	6.4634	7.2638	8.5159	3.2521	5.8594	11.6478	2.1154	10240
174	35.0000	109.0000	91.0000	-37.0000	6.6406	7.2708	8.6228	3.2264	5.5729	11.6125	2.0800	11230
175	35.0000	108.0000	91.0000	-37.0000	6.7922	7.3810	8.7746	3.2105	5.5275	11.6940	2.1615	11380
176	36.0000	109.0000	89.9000	-38.3000	6.3304	7.1699	8.3941	3.2553	5.8960	11.5748	2.0423	10140
177	37.0000	109.0000	88.5000	-39.5000	6.0345	7.0850	8.1760	3.2861	6.2030	11.5384	2.0059	9194
178	37.0000	110.0000	88.3000	-39.6000	5.9276	7.0127	8.0724	3.2950	6.2296	11.4783	1.9459	9100
179	36.5000	109.5000	89.1000	-39.0000	6.1224	7.0854	8.2285	3.2739	6.0667	11.5240	1.9915	9599

Table D-39: Extra inputs for link length optimization iterations 180 to 184.

Trial	r_c	r_2	r_4	α	β	θ_4
180	5.3500 cm	6.8778 cm	3.5000 cm	35.0000 $^{\circ}$	65.0000 $^{\circ}$	207.0000 $^{\circ}$
181	5.3500 cm	6.8778 cm	3.0000 cm	35.0000 $^{\circ}$	65.0000 $^{\circ}$	207.0000 $^{\circ}$
182	5.3500 cm	6.8778 cm	3.3000 cm	40.0000 $^{\circ}$	60.0000 $^{\circ}$	207.0000 $^{\circ}$
183	5.3500 cm	6.8778 cm	3.3000 cm	40.0000 $^{\circ}$	65.0000 $^{\circ}$	207.0000 $^{\circ}$
184	5.5000 cm	6.8778 cm	3.3000 cm	40.0000 $^{\circ}$	60.0000 $^{\circ}$	207.0000 $^{\circ}$

Table D-40: Link length optimization iterations 180 to 184.

Trial	Inputs (°)				Outputs (cm)							
	$\theta_{ext, max}$	$\theta_{flex, max}$	$\theta_{m, ext}$	$\theta_{m, flex}$	r_1	r_3	r_a	r_m	l	h	Δz	$F_{7, max}$ (N)
180	36.5000	109.5000	88.0000	-41.0000	5.7158	6.9452	7.8266	3.4932	6.4937	11.5448	2.0123	8522
181	36.5000	109.5000	90.0000	-34.0000	6.9927	7.4885	9.0286	2.9831	5.3785	11.5201	1.9877	11560
182	36.5000	109.5000	88.3000	-39.4000	5.1588	7.0459	7.6282	3.3855	6.1324	11.1215	1.8731	8541
183	36.0000	109.0000	88.6900	-39.4200	5.1753	6.6354	7.6352	3.3581	6.1408	11.1420	1.8937	9114
184	37.0000	110.0000	87.7600	-38.8800	5.3077	7.2484	7.8752	3.4053	6.2310	11.2365	1.8732	8329

Appendix E: Thread Engagement Lengths

Typically, threaded connections consist of a steel screw and an aluminum threaded hole, or a steel screw and a steel threaded hole. Screw failure is governed by axial yielding of the screw cylindrical cross-section at its minor diameter (estimated to be 90% of its major diameter) and hole failure is governed by thread shear yielding [189]. Since replacing a screw is often more convenient than replacing a threaded hole, the screw preload at which the hole yields in shear ($(P_{hole})_{sy}$) should approximately equal or slightly exceed the screw preload at which the screw yields in tension ($(P_{screw})_y$) [189].

$$(P_{hole})_{sy} \geq (P_{screw})_y \quad (\text{E-1})$$

$$(P_{hole})_{sy} = A_s (S_{hole})_{sy} \quad (\text{E-2})$$

$$(P_{screw})_y = A_t (S_{screw})_y \quad (\text{E-3})$$

$$A_s = \pi D \left(\frac{3}{4} l \right) \quad (\text{E-4})$$

$$A_t = \frac{\pi}{4} \left(\frac{9}{10} D \right)^2 \quad (\text{E-5})$$

A_s is the screw-hole shear area over which screw and hole threads engage. Spacing between threads is a quarter of the thread pitch; therefore, the hole's shear area covers three quarters of the thread engagement length [189]. A_t is the screw tensile area. D is the thread major diameter. l is the thread engagement length. $(S_{hole})_{sy}$ is the hole thread shear strength. $(S_{screw})_y$ is the screw tensile yield strength. The distortion energy theory gives the following relationship between shear yield strength (S_{sy}) and tensile yield strength (S_y) [189].

$$S_{sy} = \frac{S_y}{\sqrt{3}} \quad (\text{E-6})$$

Combining Eq. (E-1), (E-2), (E-3), (E-4), (E-5) and (E-6), and solving for l gives Eq. (E-7), the requirement for thread engagement length.

$$l \geq \frac{27\sqrt{3}(S_{screw})_y}{100(S_{hole})_y} D \quad (\text{E-7})$$

The stronger the screw is relative to the hole, the longer is the thread engagement length needed to fulfill the requirement. Class 12.9 ($S_y = 1100 \text{ MPa}$) screws were used in the powered hip FEA model. In the FEA model, screws were inserted into Al 2024-T351 holes ($S_y = 310 \text{ MPa}$) and 17-4 PH SS H900 holes ($S_y = 1172 \text{ MPa}$). Superior link screws were inserted into steel inserts with a yield strength assumed to be the same as that of the screw. The drive flange helicoils (optional but included in the FEA model) were assumed to also have the same yield strength as that of the screw.

For a class 12.9 screw inserted into an Al 2024-T351 hole, the thread engagement length requirement is given by Eq. (E-8).

$$l \geq 1.66D \quad (\text{E-8})$$

For a class 12.9 screw inserted into a 17-4 PH SS H900 hole, the thread engagement length requirement is given by Eq. (E-9).

$$l \geq 0.44D \quad (\text{E-9})$$

If the screw and hole are of equal yield strength, the thread engagement length requirement is given by Eq. (E-10).

$$l \geq 0.47D \quad (\text{E-10})$$

Table E-1 lists the minimum required and implemented thread engagement lengths for all screw-hole combinations.

Table E-1: FEA model specifications for powered hip screw sets including thread engagement lengths.

Screw set	Superior link	Drive arm screw-on	Motor housing	Output bearing cover	Motor cover
Hole tensile yield strength (MPa)	1100	1100	1172	310	1172
Screw tensile yield strength (MPa)	1100	1100	1100	1100	1100
Thread major diameter (mm)	8.00	8.00	6.00	2.50	2.00
Minimum required thread engagement length (mm)	3.76	3.76	2.64	4.15	0.88
Implemented thread engagement length (mm)	10.00	8.00	3.25	4.30	3.10

All implemented thread engagement lengths were selected based on readily available screw length and wherever possible, thread engagement lengths originally implemented in the Power Knee 2 motor. Class 12.9 screws were not readily available for all required thread major diameters. In the metal prototype, class 10.9 screws ($S_y = 940 \text{ MPa}$) were used for the superior link, drive arm screw-on, and output bearing cover screw sets. From Eq. (E-7), the use of class 10.9 screws instead of class 12.9 screws decreases the required thread engagement length. Furthermore, all implemented thread engagement lengths exceed the minimum required lengths for class 12.9 screws, conveniently allowing for screw axial yielding to be the governing mode of failure for all threaded connections.

For the drive arm screw-on screws, the minimum required thread engagement length was calculated assuming helicoils would be used. However, helicoils were not used in the metal prototype because the fabrication process was facilitated when the helicoils were not included. Without the helicoils, class 10.9 screws were inserted into the Al 2024-T351 drive flange which increased the minimum required thread engagement length to 11.36 mm from the initial 8.00 mm. Consequently, drive flange thread stripping would occur at a lower screw preload than that for screw yielding. However, the minimum screw yielding safety factor for the drive screw-on is 1.22 at the full 96 N·m motor torque, meaning that the failure of this threaded connection is not a concern (even though it would occur by drive flange thread stripping).

Appendix F: Screw Preload Torques

Screw preload torques serve as boundary conditions between FEA components. Screws create a friction joint between parts being fastened together. In the powered hip FEA, screw preloads were set equal to the normal forces required to produce enough static friction to prevent relative motion between components.

Figure F-1 represents the worst-case loading between the socket and superior link friction surfaces. The worst-case scenario occurred ISO 15032:2000 M-L static compression. The load was assumed to act at the centroid of the superior link posterior face and be equally distributed between both superior link screws.

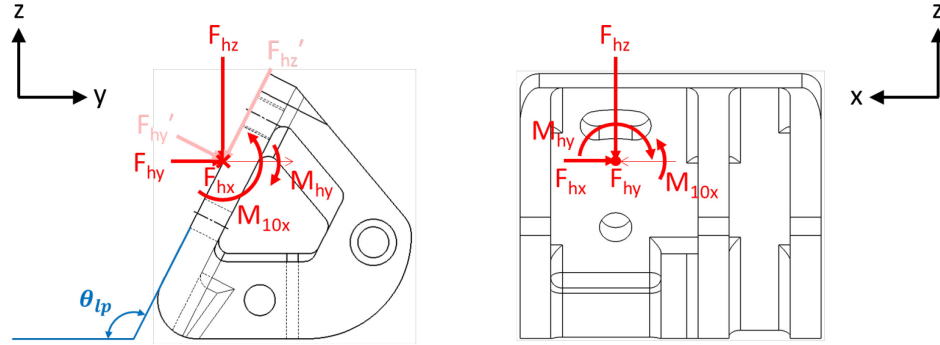


Figure F-1: Superior link screw loads acting at the screw pair centroid. $F_{hx} = 334.3 \text{ N}$, $F_{hy} = 0 \text{ N}$, $F_{hz} = 3343 \text{ N}$, $M_{10x} = 33.43 \text{ Nm}$, and $M_{hy} = 287.5 \text{ Nm}$ are static compression loads in the ISO 15032:2000 ML condition. $\theta_{lp} = 117^\circ$ is the lamination plate obtuse angle. Older model shown.

The friction force keeping the superior link from sliding relative to the socket depends on F_{hy}' and F_{hz}' , force components perpendicular and parallel to the friction surface. F_{hy}' and F_{hz}' were obtained by rotating F_{hy} and F_{hz} .

$$\begin{bmatrix} F_{hy}' \\ -F_{hz}' \end{bmatrix} = \begin{bmatrix} \cos(90^\circ - \theta_{lp}) & \sin(90^\circ - \theta_{lp}) \\ -\sin(90^\circ - \theta_{lp}) & \cos(90^\circ - \theta_{lp}) \end{bmatrix} \begin{bmatrix} F_{hy} \\ -F_{hz} \end{bmatrix} \quad (\text{F-1})$$

Screw preload torque (T) is expressed as follows:

$$T = KDP \quad (\text{F-2})$$

K is the nut factor, D is the screw major diameter, and P is the screw axial preload. K varies depending on screw coating and lubrication, but K is commonly assumed to be 0.2 [236], [237]. D is 8 mm for the superior link screws.

For the superior link, P was set equal to the normal force (F_n) required for sufficient static friction (F_s) minus the compressive force component perpendicular to the friction surface (F_{hy}')

divided by the number of screws ($N = 2$). F_s was set equal to vector sum of the compressive force component parallel to the friction surface (F_{hz}') and the force from the couple created by M_{hy} acting on the screws separated by a distance ($d = 3\text{ cm}$) along the superior link posterior face. During the ISO 15032:2000 M-L static compression test, the aluminum superior link is in contact with a steel end attachment. As a conservative approach, the minimum value of $\mu_s = 0.45$ was taken for aluminum-steel dry surface contact [226].

$$P = \frac{F_n - F_{hy}'}{N} \quad (\text{F-3})$$

$$F_n = \frac{F_s}{\mu_s} \quad (\text{F-4})$$

$$F_s = \sqrt{\left(\frac{M_{hy}}{d} + F_{hx}\right)^2 + (F_{hz}' \cos(90^\circ - \theta_{lp}))^2} \quad (\text{F-5})$$

M_{10x} is a CCW sagittal plane moment as a result of the 10 mm A-P offset causing the bottom portion of the superior link posterior face to push into the end attachment. M_{10x} shifts the force equivalent location downward and increases the amount compression between the superior link and end attachment. ISO 15032:2000 recommends that this offset is a maximum of 10 mm. As this offset approaches zero, M_{10x} approaches zero, thereby providing less compression (i.e., less normal force to aid with static friction). As a conservative approach, the effects of M_{10x} on static friction were not included in the calculation of F_s for the superior link. Superior link screw preload torque T was calculated to be 17.2 N-m.

Motor torque is transferred to the drive arm screw-on causing the drive arm screw-on to slide relative to the drive flange. Figure F-2 represents the worst-case loading on the drive arm screw-on.

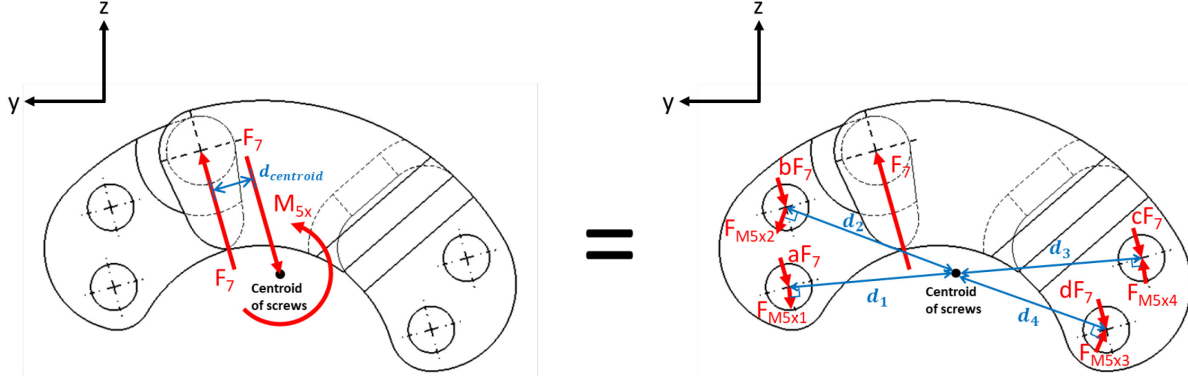


Figure F-2: Drive arm screw-on free-body diagram and equivalent free-body diagram with loads distributed among the component's four screws. $F_7 = 9599 \text{ N}$ under maximum motor torque. Older model shown.

M_{5x} is the reaction moment counteracting the rotational effect of F_7 offset to the centroid of screws. Both M_{5x} and F_7 are transferred to the friction surface between the drive arm screw-on and drive flange. M_{5x} is distributed among the four screws as distinct forces acting at different perpendicular distances. F_7 is unequally distributed among the four screws (a, b, c, and d are different fractions of F_7). Anterior force pairs contain forces that are both pointing down. Posterior force pairs contain forces that are both pointing up. Thus, the anterior drive-arm screws take more load than the posterior ones. It was assumed that 75% of F_7 is absorbed by the anterior screws and 25% by the posterior screws. Therefore, the anterior screw loads are the governing loads for deciding screw preload torques. Conservatively, the larger preload torque was used for both anterior and posterior screws.

For the drive arm screw-on, screw preload torque was calculated using Eq. (F-2) with $D = 8 \text{ mm}$. Axial preload P , on each screw, is given by Eq. (F-6), the normal force acting F_n on the friction surface divided by number of anterior screws ($N = 2$). F_n was calculated using Eq. (F-4).

$$P = \frac{F_n}{N} \quad (\text{F-6})$$

The static friction F_s resisted by the anterior screws was assumed to be 75% of drive arm force F_7 (Eq. (F-7)). For the drive arm screw-on, screw preload torque was calculated to be 12.8 N-m.

$$F_s = 0.75F_7 \quad (\text{F-7})$$

Both motor torque T_{mx} and drive arm force F_7 are transferred to the friction surface between the motor housing and motor cover. Figure F-3 shows the worst-case loading on this friction surface.

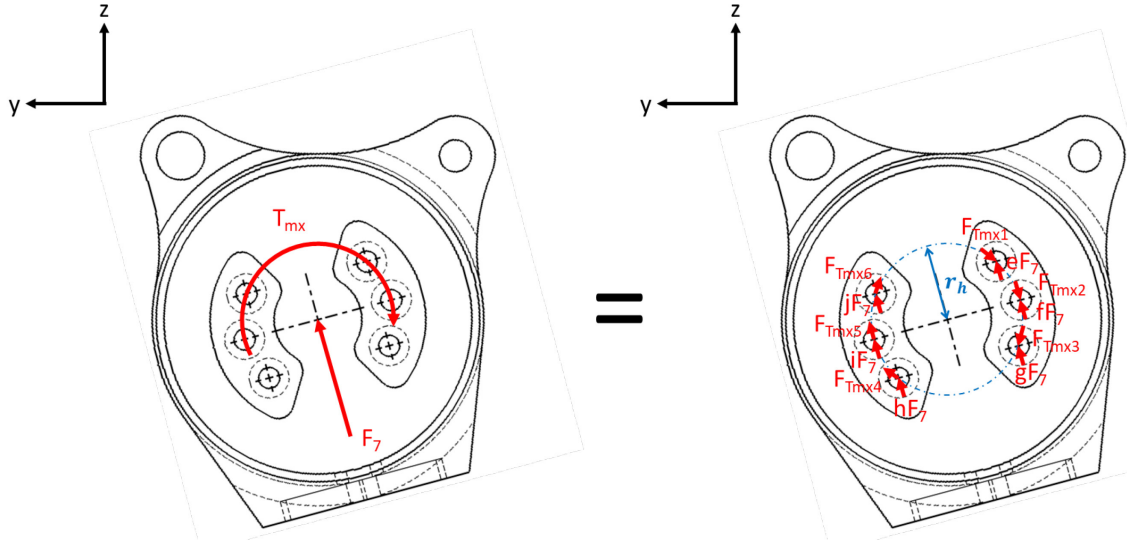


Figure F-3: Motor housing screw loads acting at the screw pattern centroid and equivalent screw loading distributed among the component's six screws. $F_7 = 9599 \text{ N}$ under maximum motor torque ($T_{mx} = 96 \text{ Nm}$). Older model shown.

Following a similar rationale, 75% of F_7 was again assumed to be absorbed by the anterior screws. Motor housing screw preload torque was calculated to be 6.4 N-m using Eq. (F-2), (F-4), (F-6), and (F-7) with $D = 6 \text{ mm}$.

The output bearing cover screws ($D = 2.5 \text{ mm}$), and the motor cover screws ($D = 2 \text{ mm}$) are arranged in a circular pattern around the motor housing axis. Assuming that F_7 is equally distributed among each set of screws, the static friction F_s supported by a set of screws is simply F_7 .

$$F_s = F_7 \quad (\text{F-8})$$

Eq. (F-2), (F-4), (F-6), and (F-8) were used to calculate screw preload torque values. A preload torque of 0.89 N-m was found for the output bearing cover screws and a preload torque of 0.80 N-m was found for the motor cover screws.

Due to variations in the nut tightening factor (K), superior link, drive arm screw-on and motor housing screw preload torques were increased by 10% as a conservative approach.

In case F_7 was not distributed equally among the output bearing cover or motor cover screw sets, their preload torques were increased by 25-30% as a conservative approach. For the output bearing cover and motor cover screw sets, the 75-25 screw load distribution was not assumed due to a potential overestimation of the required preload torque. The Power Knee 2 motor originally had the output bearing cover and motor cover screws torqued to 0.65 N-m. It was not advisable to overly exceed this torque due to potential screw stripping.

Table F-1 lists the calculated and corrected (increased) screw preload torques.

Table F-1: Calculated and corrected screw preload torques used for powered hip FEA.

Screw set	Superior link	Drive arm screw-on	Motor housing	Output bearing cover	Motor cover
Calculated preload torque (N·m)	17.2	12.8	6.4	0.89	0.80
Corrected preload torque (N·m)	19.0	14.1	7.1	1.15	1.00

The corrected preload torques for the superior link, drive arm screw-on, and motor housing screws were well below the recommended maximum tightening torques for class 10.9 screws [238]. None of the screws yielded during structural and functional tests.

Appendix G: 3D Printed Prototype

During the link length optimization process, a 3D printed prototype was constructed (Figure G-1) to assess hip joint motion and how this motion was affected by ROM singularity points. The prototype was made of polylactide (PLA: mass density = 1300 kg/m³ [239], elastic modulus = 3466 MPa [240], yield strength = 49.2 MPa [240]) and was powered by a FITEC FS5106B servomotor (mass = 41 g, max torque at 6V = 0.59 N-m, max speed at 6V = 375 °/s). The prototype had overall dimensions of 9.5 cm x 7.4 cm x 20.1 cm and a 194 g mass. Servomotor torque was powered by a battery providing a constant electrical current. Torque was varied by a potentiometer providing variable electrical resistance. A larger potentiometer resistance resulted in a larger voltage drop across the servomotor and a larger servomotor torque.

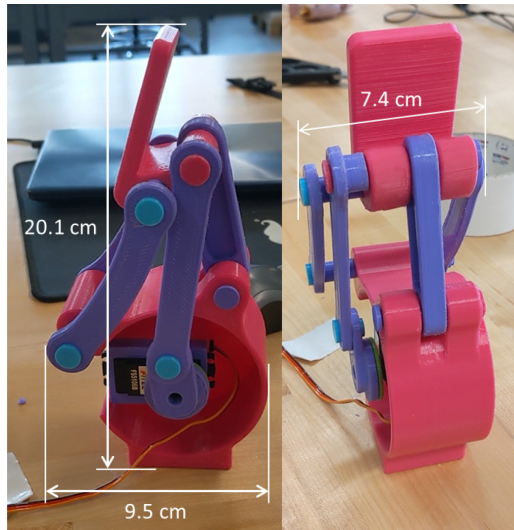


Figure G-1: 3D printed powered hip joint. Design based on link length optimization iteration 29.

Optimization iteration 29 link lengths (Table G-1 and G-2) were selected for the prototype because iteration 29 provided adequate ROM (20° hip extension to 111.5° hip flexion), and sufficient mechanical advantage for stance phase stability (ranging from 0.67 to 1.13 in the walking ROM).

Table G-1: Linkage optimization iteration 29. Variables defined in Figure 4-5.

Trial	Inputs (°)				Outputs (cm)							
	θ_{ext_max}	θ_{flex_max}	θ_{m_ext}	θ_{m_flex}	r_1	r_3	r_a	r_m	l	h	Δz	Sing.
29	27	133	95	-19	7.5255	6.1624	8.9214	2.1008	2.0748	9.1427	-0.3897	Yes

Table G-2: Fixed inputs for linkage optimization iteration 29. Variables defined in Figure 4-5.

Fixed Inputs	r_c	r_2	r_4	α	β	θ_4
Values	5.35 cm	6.88 cm	2.20 cm	35.0°	65.0°	207.0357°

Iteration 29 had a maximum drive arm force of 42400 N for a 96 N-m motor torque. Since drive arm force is directly proportional to motor torque, scaling this force to the 3D printed prototype maximum servomotor torque of 0.59 N-m gives a drive arm force of 261 N. Applying Eq. (6-16) to the drive arm cross-sectional area of 75 mm² gave a tensile stress of 3.48 MPa, well below the 49.2 MPa PLA yield strength, which indicated that the prototype was easily able to support maximum servomotor torque.

Despite not being used for walking tests, the 3D printed prototype provided information for how the joint behaves as it approaches and crosses singularity points (Figure G-2). Four-bar linkage ROM singularity points occur when posterior and superior link pivots are collinear. Motor-linkage ROM singularity points occur when drive arm and motor arm pivots are collinear ($\theta_{D'} = 180^\circ$). Prototype hip extension was physically limited by posterior link rear face contact with the superior link angled surface. Prototype hip flexion was physically limited by posterior link front face contact with the superior link anterosuperior edge. Governing ROM singularity points were from the motor linkage because they occurred at lower hip flexion-extension angles than the corresponding four-bar linkage ROM singularity points. This observation reinforced the fact that ROM singularity points can occur at multiple instances during hip ROM and that design performance was dependant on where the usable hip ROM was relative to these singularity points. Prototype hip flexion and extension stops were implemented to prevent hip motion prior to reaching motor linkage ROM singularity points.

Loose tolerancing between 3D printed parts introduced functional challenges. In a small region of motor rotation ($\Delta\theta_{m_1} \cong 20^\circ$) located near full hip extension, motor rotation resulted in little to no overall hip flexion or extension. This stall near full hip extension was due to increased space (and therefore, poor contact) between the middle motor linkage pivot and the motor and drive arms. Furthermore, increased space between the anterosuperior pivot and the drive arm and superior link allowed the drive arm to push upward more than intended. This extra upward motion resulted in $\Delta\theta_{m_2} \cong 20^\circ$ CW drive arm rotation beyond the hip extension singularity point, even though the singularity point was theoretically supposed to prevent further motor rotation. Hip flexion from full hip extension was stalled until the motor rotated CCW through $\Delta\theta_{m_1} + \Delta\theta_{m_2}$. Hip motion near full hip extension or full hip flexion required larger servomotor torques than motion in the middle of the ROM due to the decreased mechanical advantage near ROM extremities. This observation informed the trade-off between having a larger ROM but lower average mechanical advantage or having a smaller ROM but larger average mechanical advantage.

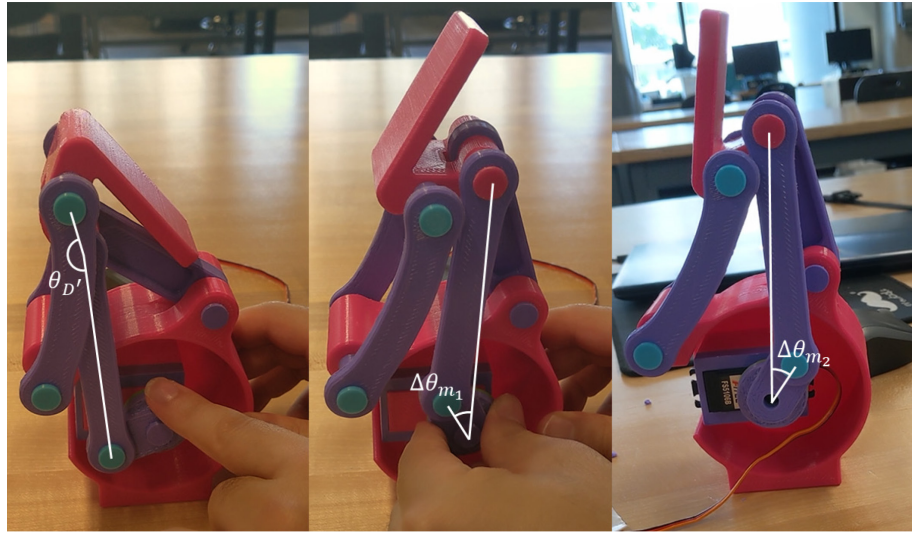


Figure G-2: 3D printed powered hip prototype behavior as it nears or crosses ROM singularity points. $\theta_{D'}$ is the angle used to determine the motor linkage singularity point near full hip flexion. $\Delta\theta_{m_1}$ and $\Delta\theta_{m_2}$ are angles measuring the range of servomotor rotation in which hip motion stalled.

Unlike the design presented in Chapter 4, the 3D printed prototype's drive arm was connected to a shaft cantilevered from the superior link. As a result, the drive arm's push or pull on the superior link caused noticeable frontal plane hip motion while the servomotor was operating. This frontal plane hip motion was compounded by loose tolerancing. This observation informed that the drive arm needs to be supported by the superior link on both sides rather than one side only.

Tolerancing in the 3D printed prototype ranged from ± 0.1 mm to ± 0.2 mm, which posed problems for shaft and press fit connections. Metal prototype tolerancing for shafts and press fits needs to be tighter to ensure smooth sagittal motion without unnecessary movement in other planes.

Appendix H: Screw Safety Factors

Table H-1 lists the safety factors for the screws implemented in the powered hip FEA model.

Table H-1: Yielding and one million load cycle fatigue safety factors for powered hip FEA model screws. Screw nomenclature defined by Figure 6-22.

Screw	Safety factor (yielding)	Safety factor (fatigue)
S1	4.04	3.03
S2	4.06	3.05
M1	2.38	1.79
M2	3.19	2.39
M3	1.76	1.32
M4	1.22	0.92
MI1	1.31	0.98
MI2	1.38	1.04
MI3	1.36	1.02
MI4	2.42	1.82
MI5	2.52	1.89
MI6	1.46	1.10
MI7	1.41	1.06
MI8	1.45	1.09
MI9	1.41	1.06
MI10	1.39	1.04
MI11	1.40	1.05
MI12	1.34	1.01
LI1	1.40	1.05
LI2	1.44	1.08
LI3	1.43	1.07
LI4	1.41	1.06
LI5	1.37	1.03
LI6	1.31	0.98
LI7	1.24	0.93
LI8	1.20	0.90
LI9	1.17	0.88
LI10	1.17	0.88
LI11	1.19	0.89
LI12	1.23	0.92
LI13	1.27	0.95
LI14	1.32	0.99
LI15	1.37	1.03
L1	2.59	1.94
L2	4.07	3.05
L3	2.60	1.95
L4	1.54	1.16
L5	1.51	1.13
L6	1.45	1.09

Appendix I: Engineering Drawings

Powered four-bar hip assembly drawings are presented in Figures I-1 to I-3. Individual part drawings are presented in Figures I-4 to I-20. Drawings are shown for parts that required machining out of Al 2024-T351 or 17-4 PH SS H900.

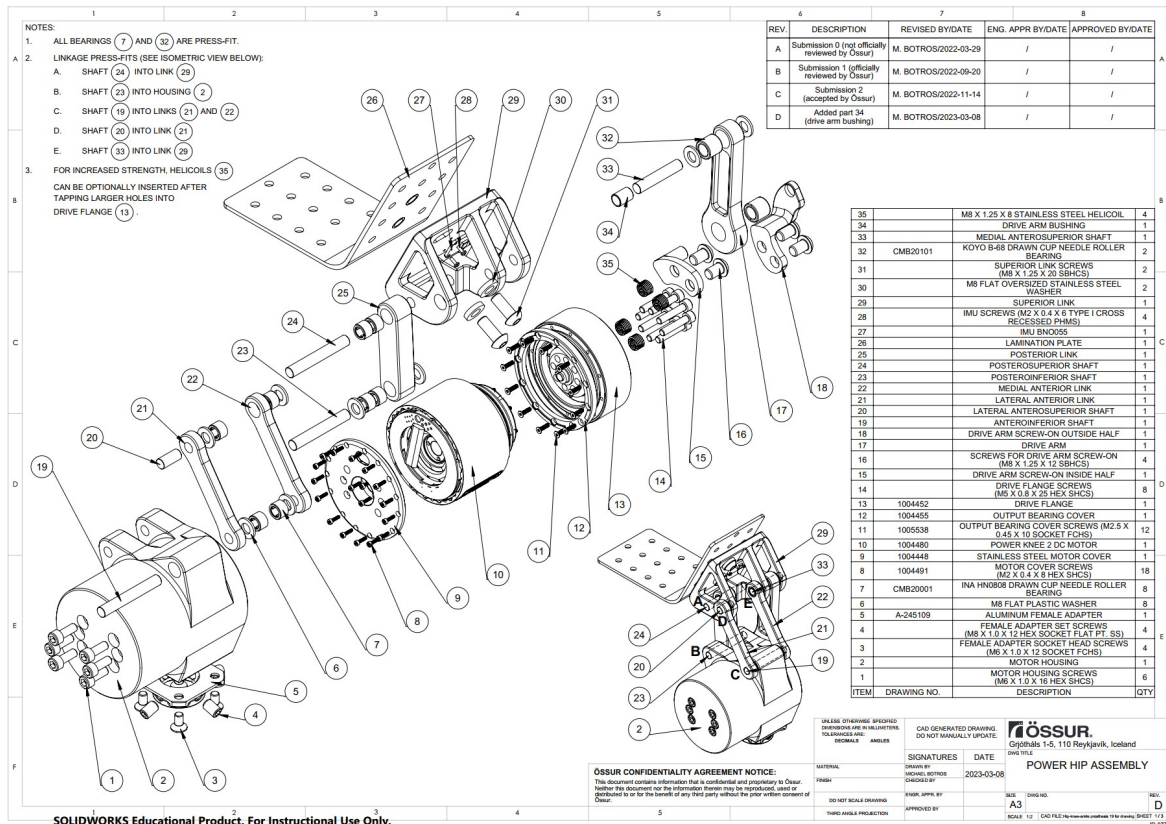


Figure I-1: Powered four-bar hip assembly. Lateral isometric view.

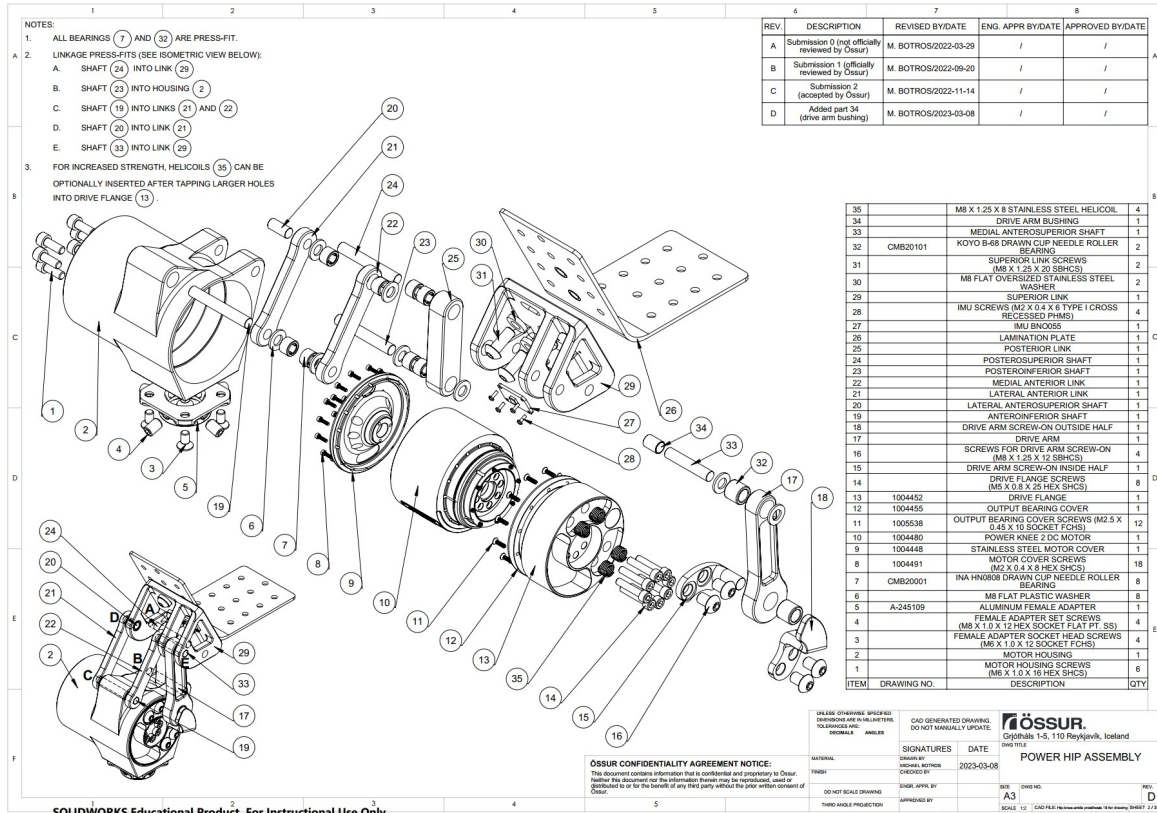


Figure I-2: Powered four-bar hip assembly. Medial isometric view.

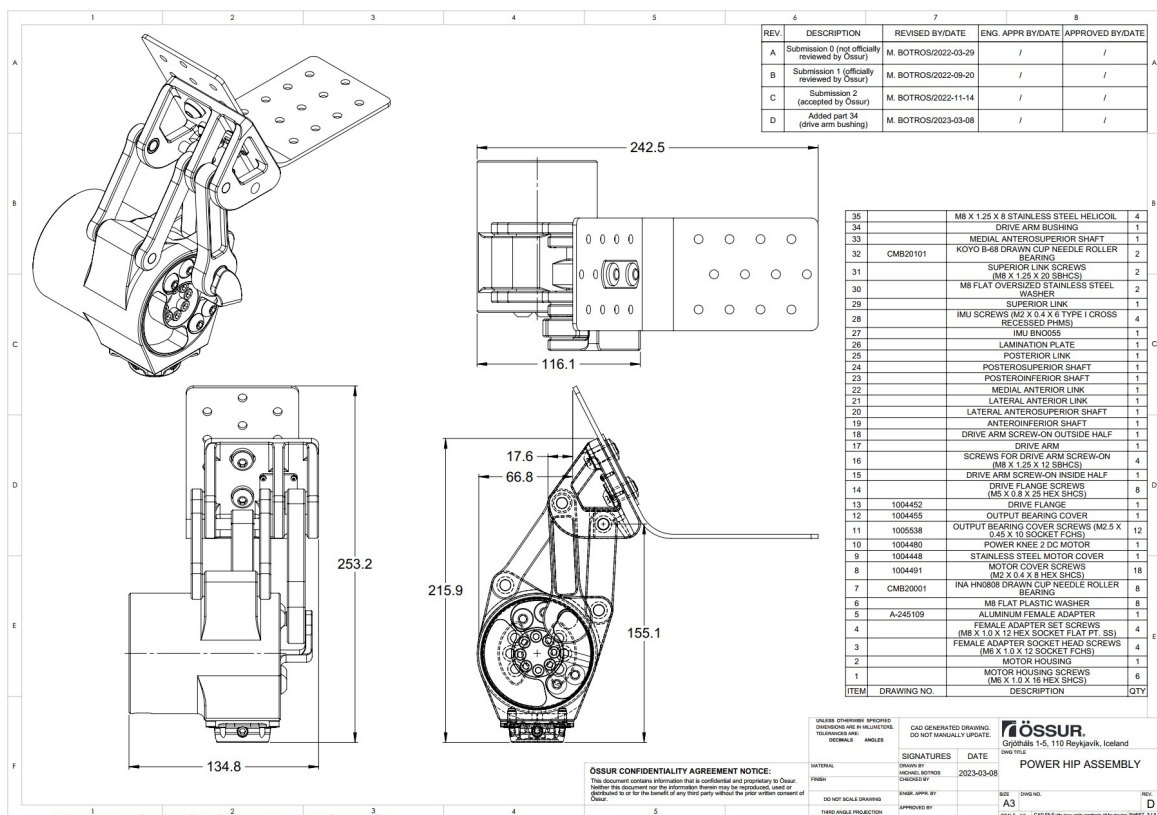


Figure I-3: Powered four-bar hip assembly. Orthogonal views.

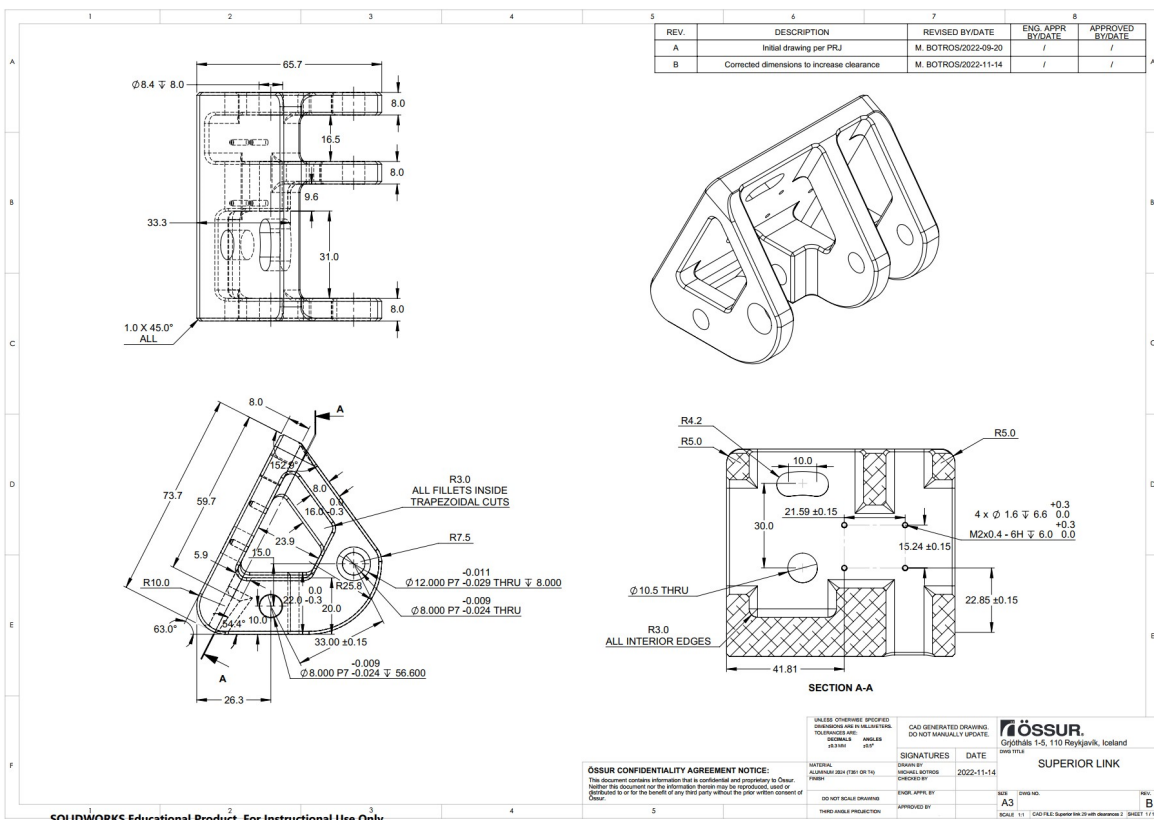


Figure I-4: Superior link.

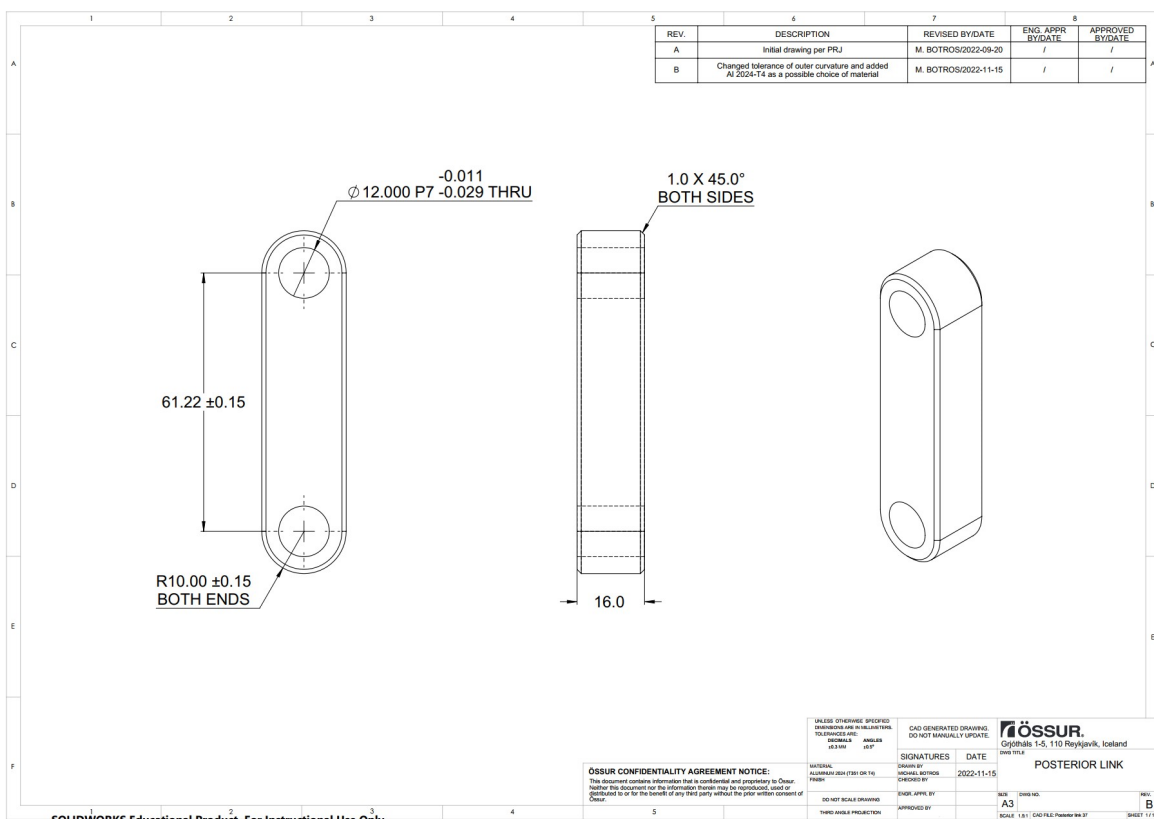


Figure I-5: Posterior link.

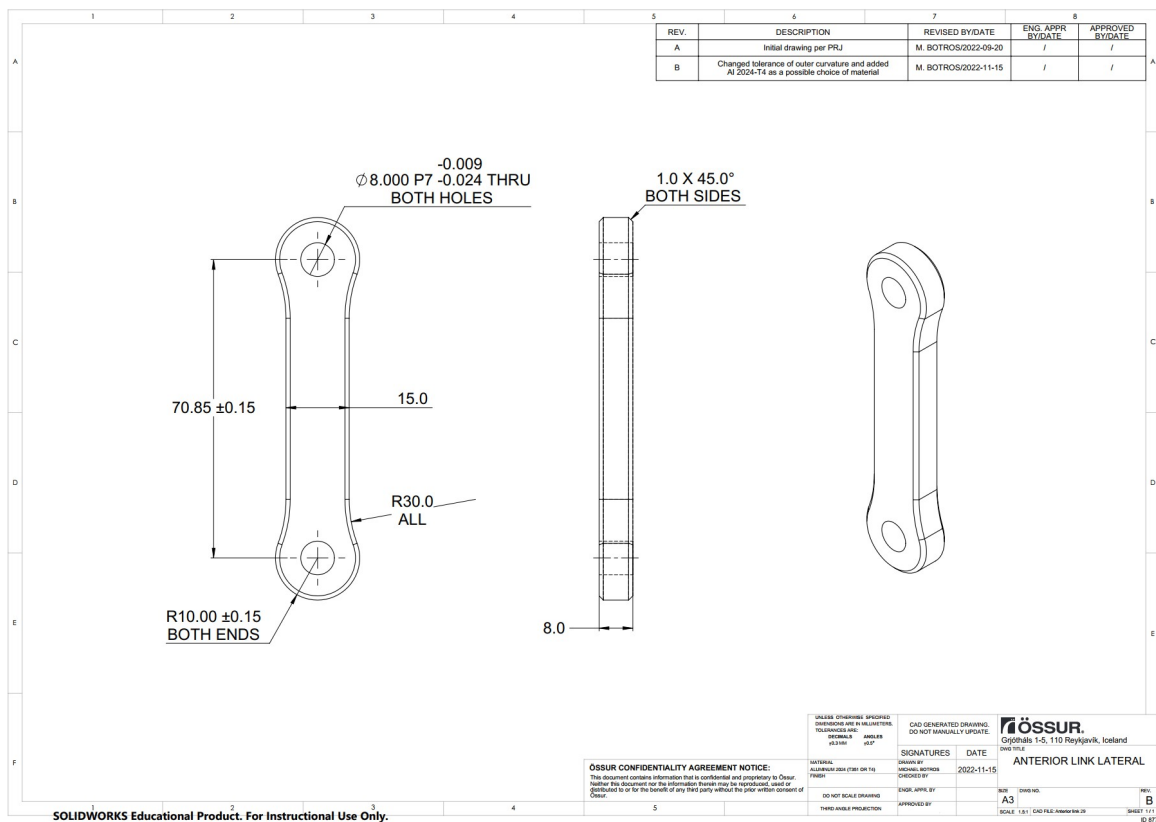


Figure I-6: Lateral anterior link.

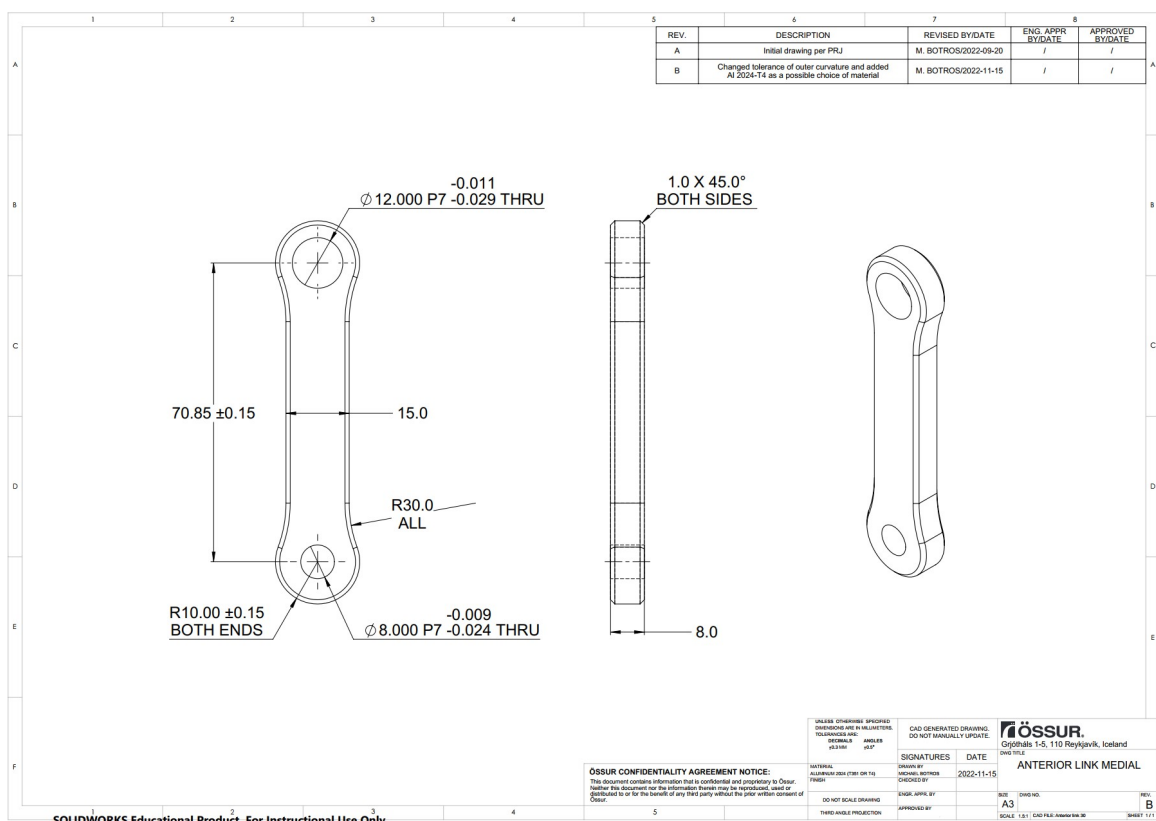


Figure I-7: Medial anterior link.

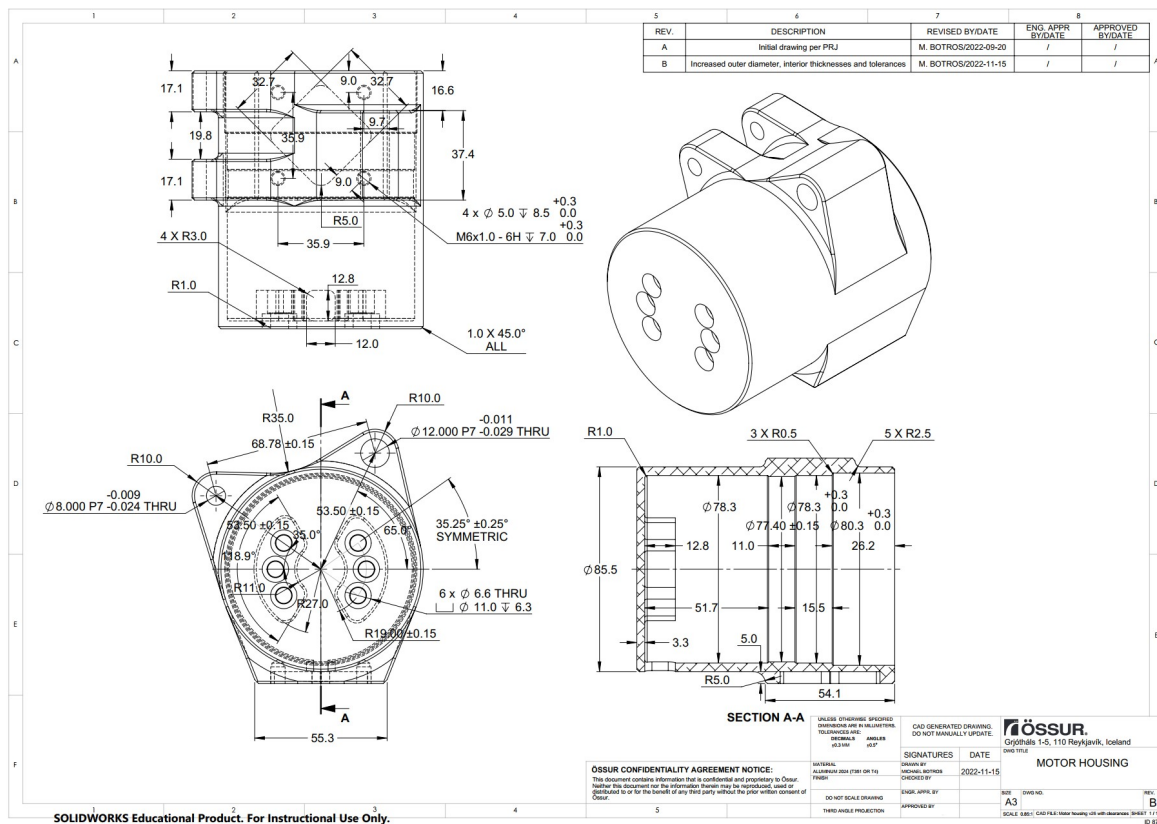


Figure I-8: Motor housing.

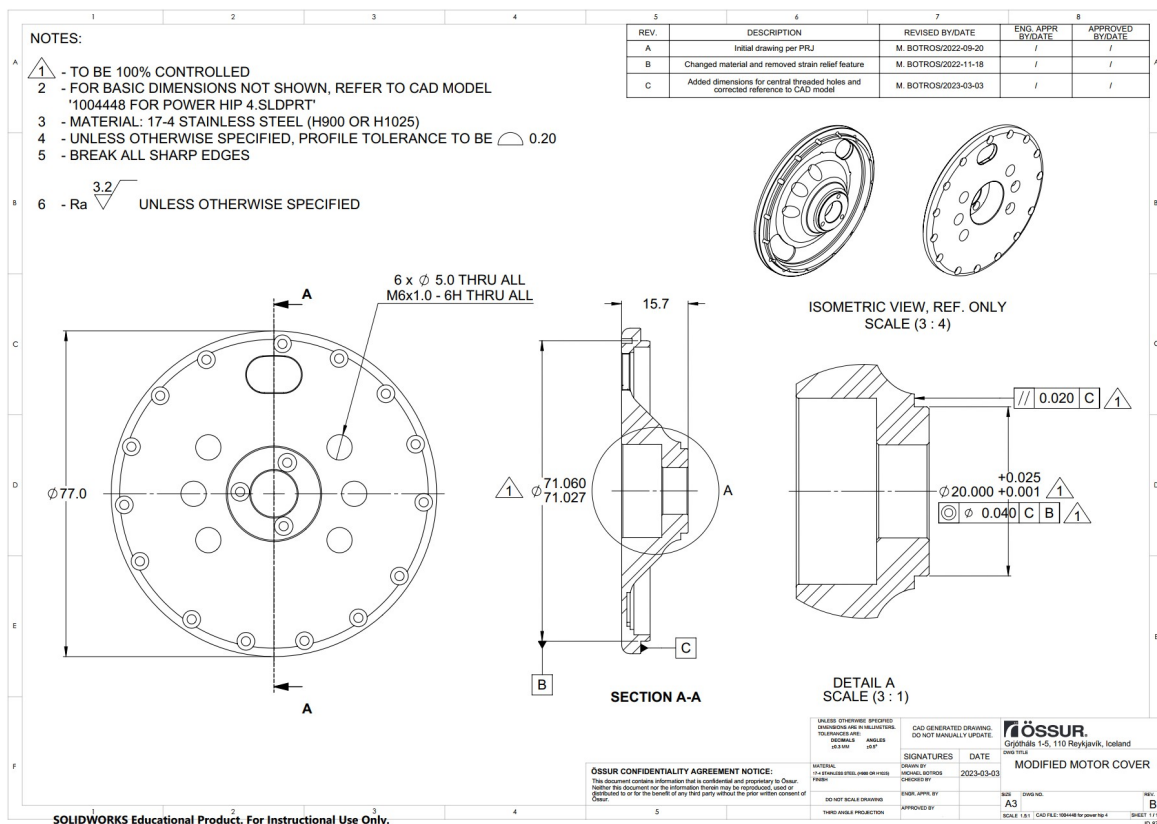


Figure I-9: Motor cover.

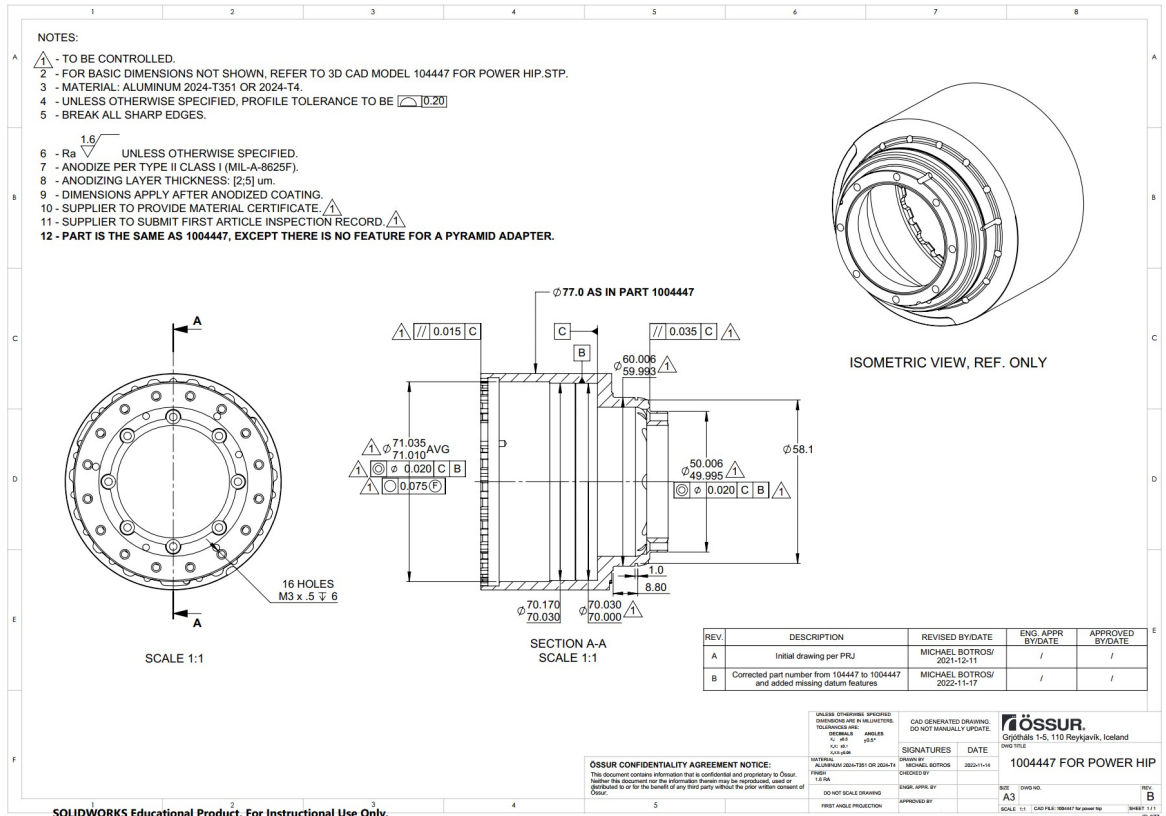


Figure I-10: Motor shell.

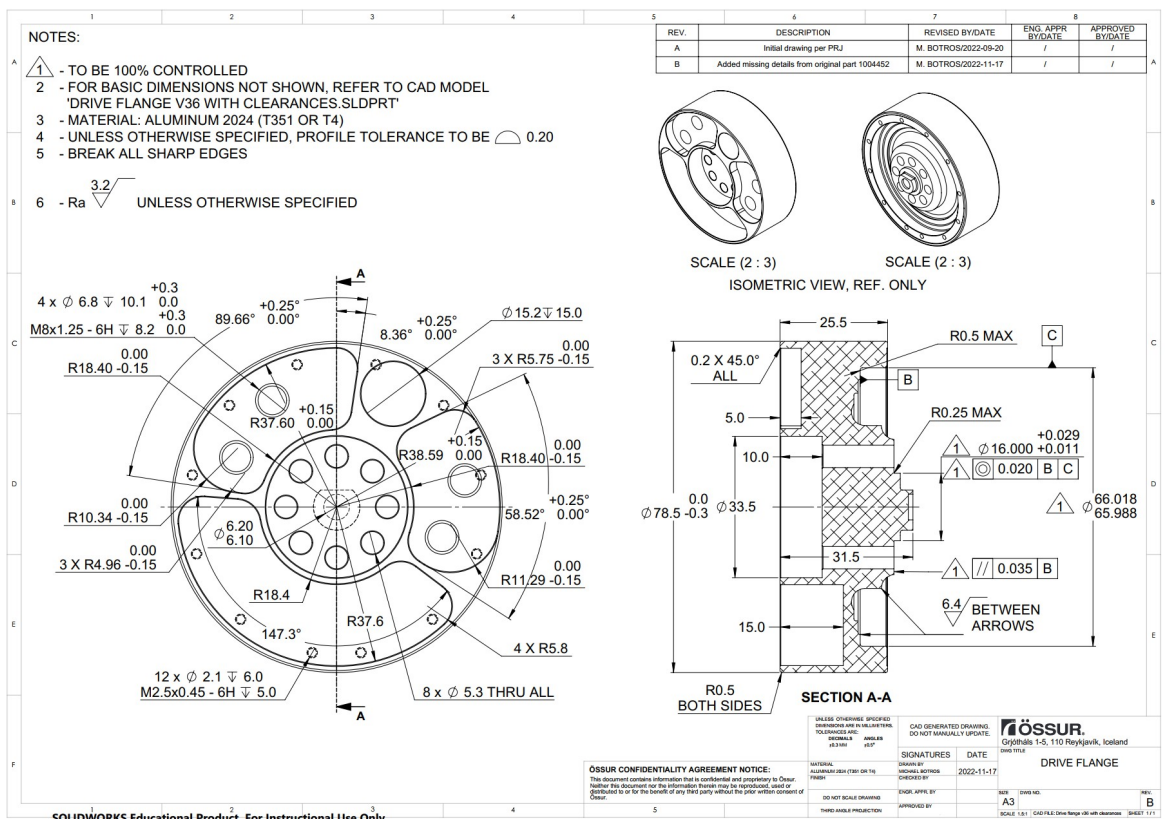


Figure I-11: Drive flange.

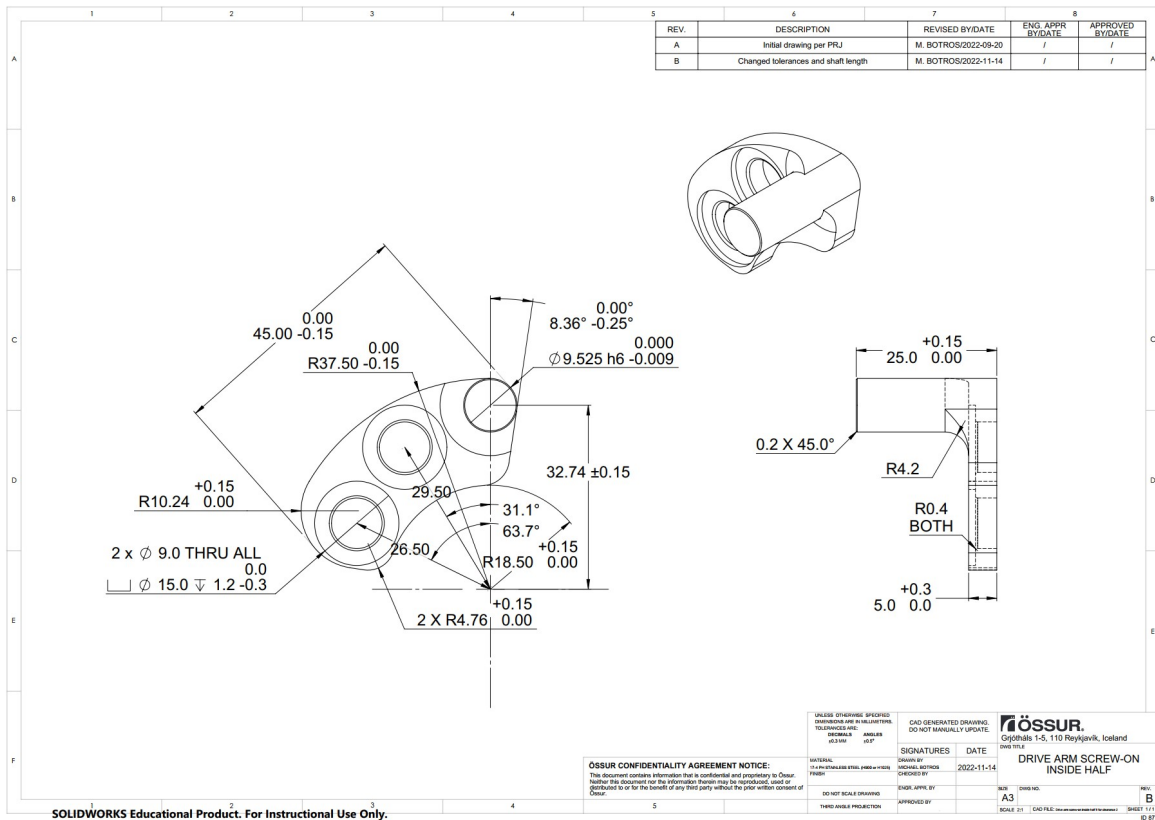


Figure I-12: Drive arm screw-on inside half.

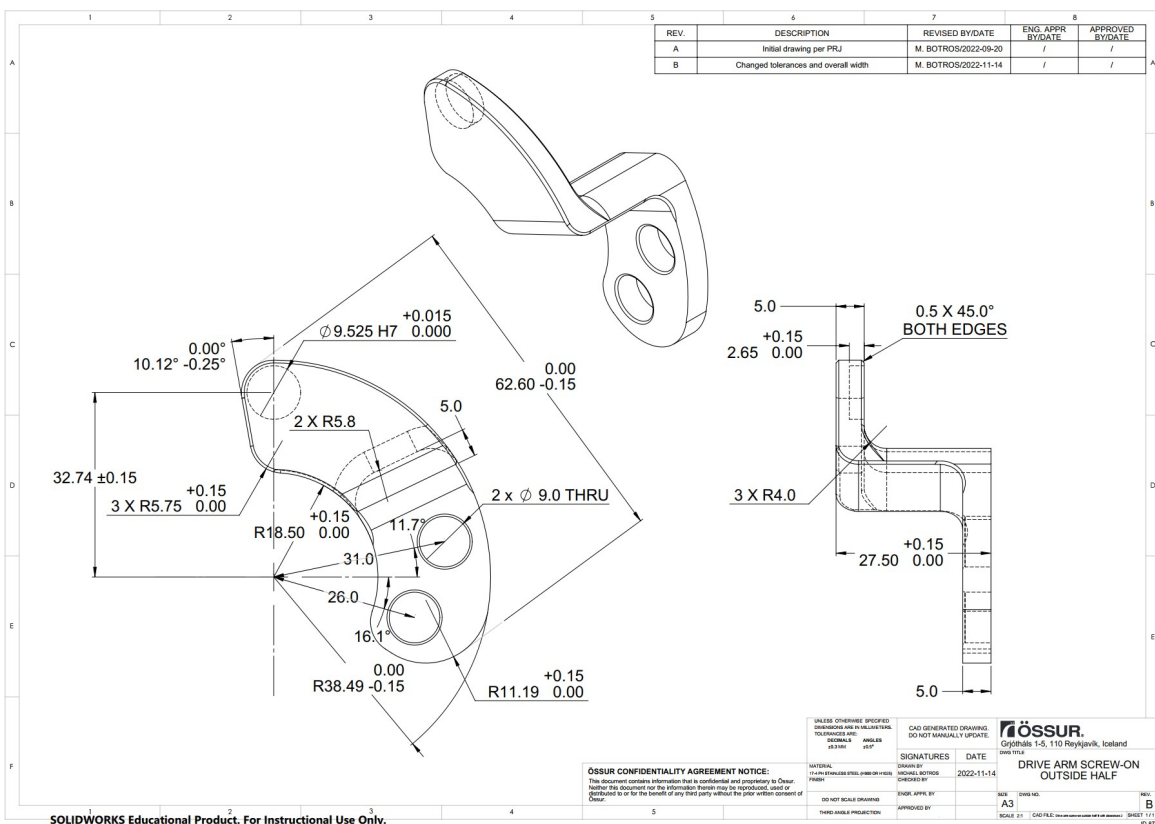


Figure I-13: Drive arm screw-on outside half.

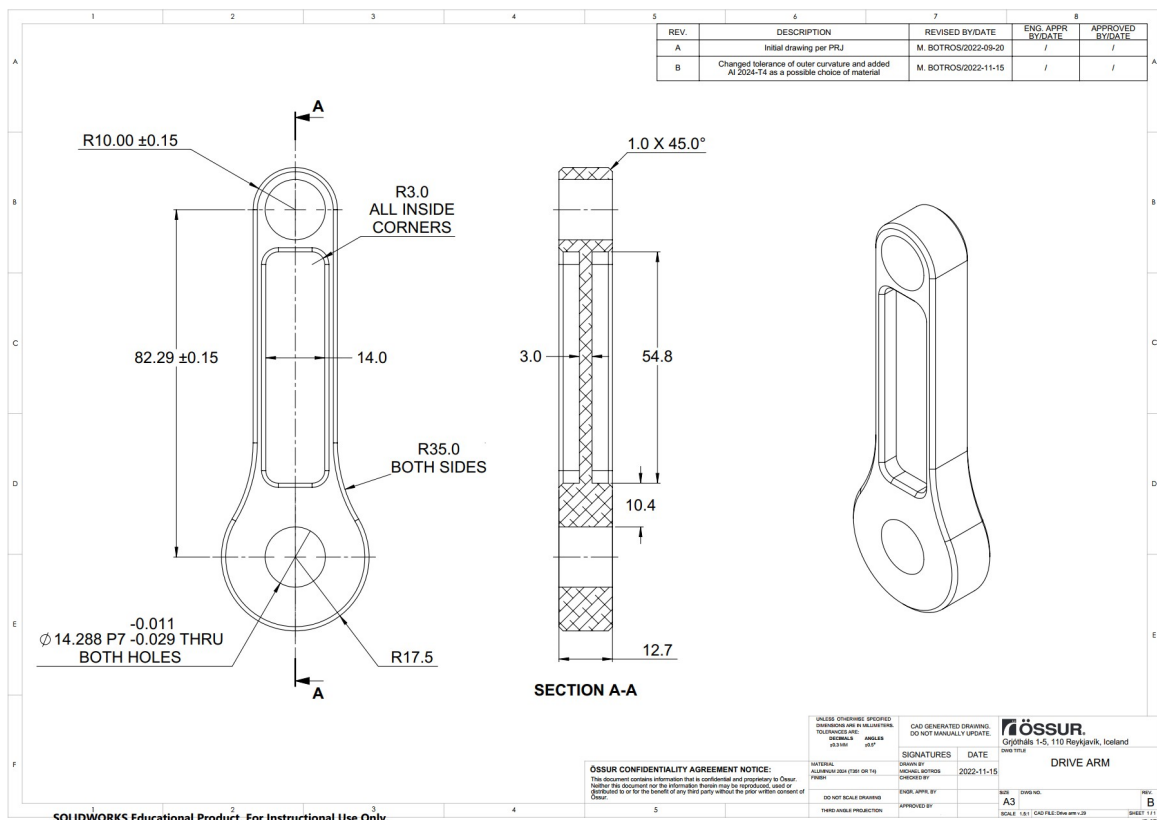


Figure I-14: Drive arm.

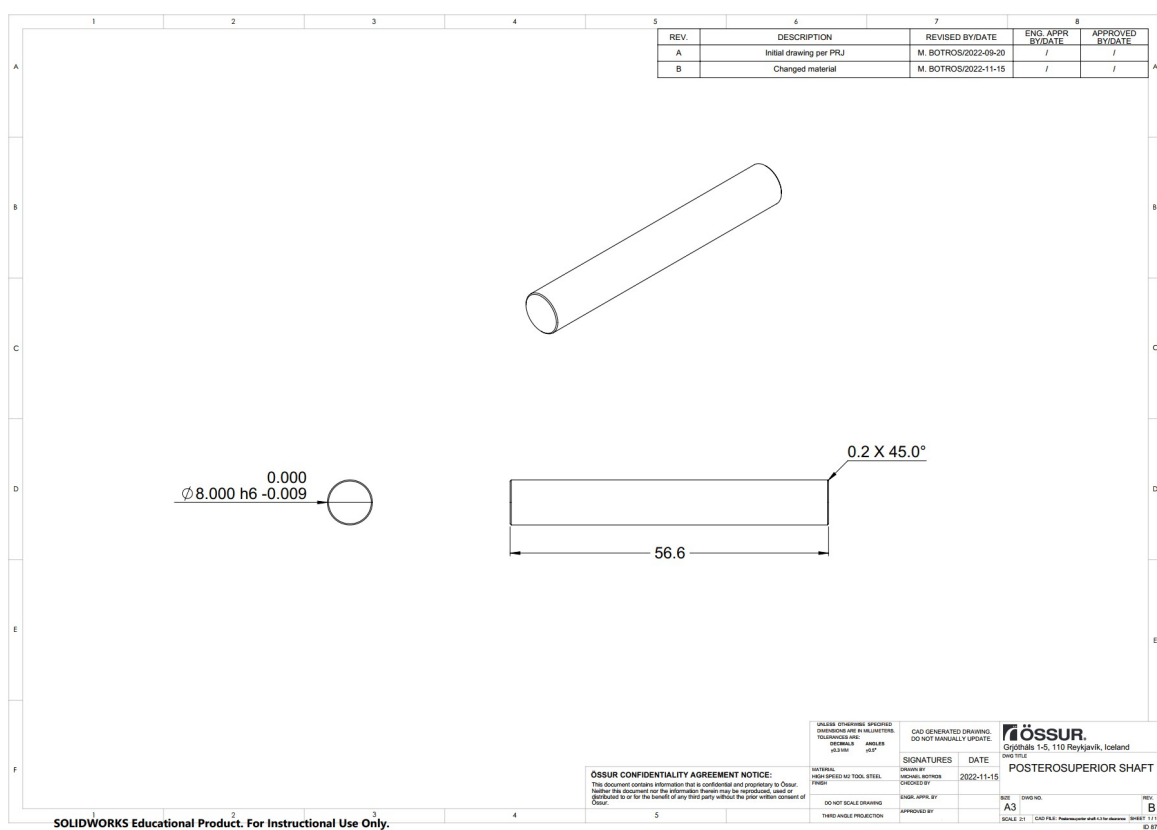


Figure I-15: Posterosuperior shaft.

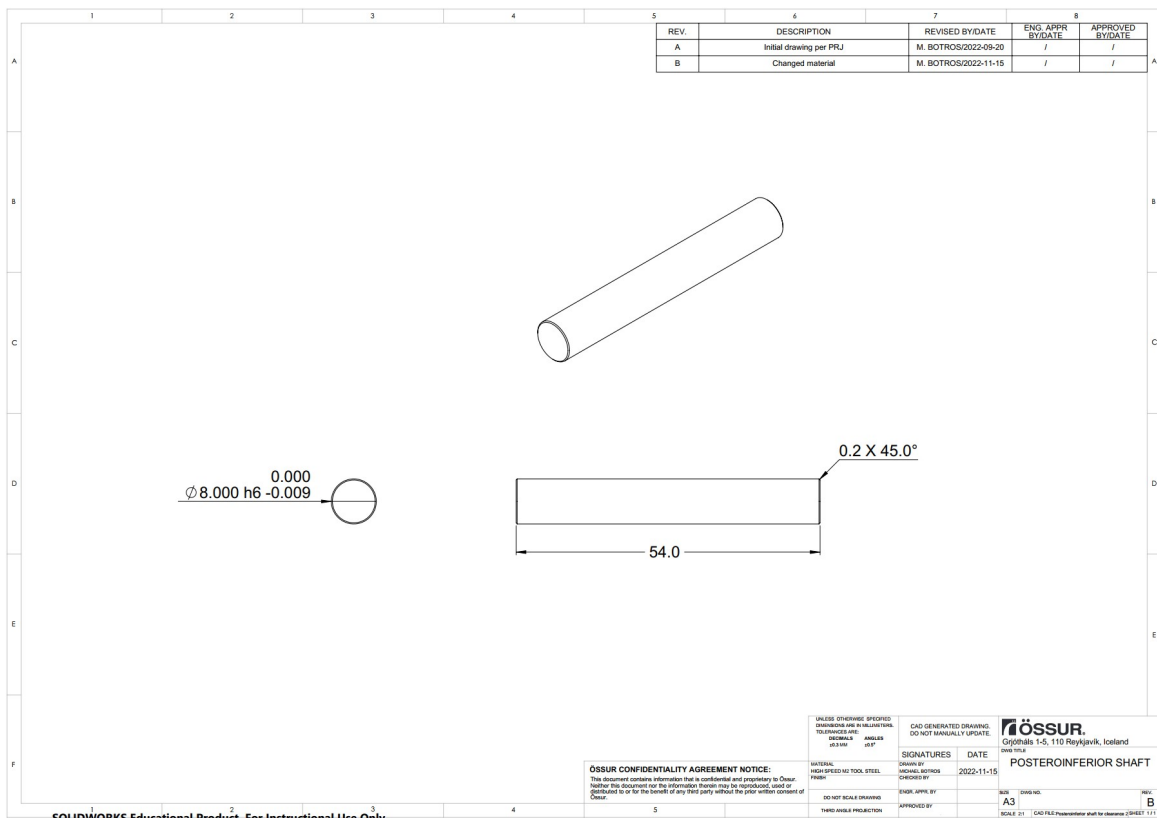


Figure I-16: Posteroinferior shaft.

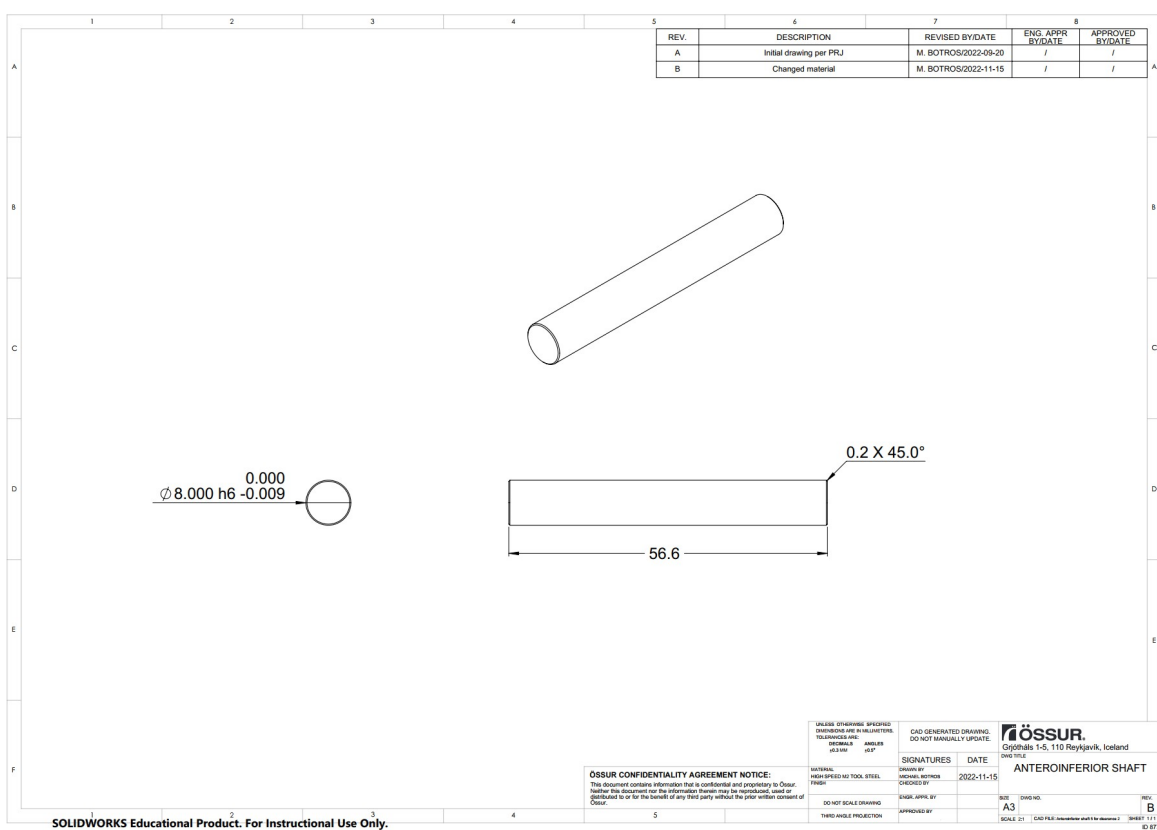


Figure I-17: Anteroinferior shaft.

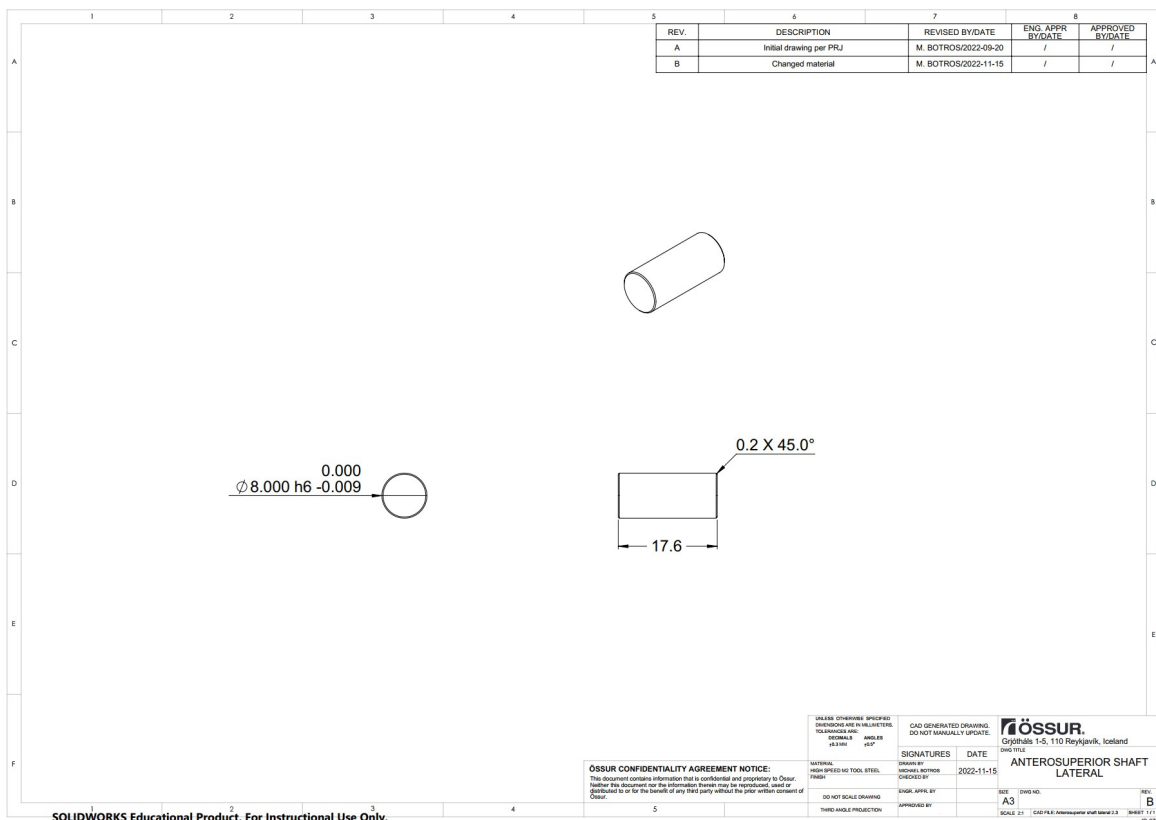


Figure I-18: Lateral anterosuperior shaft.

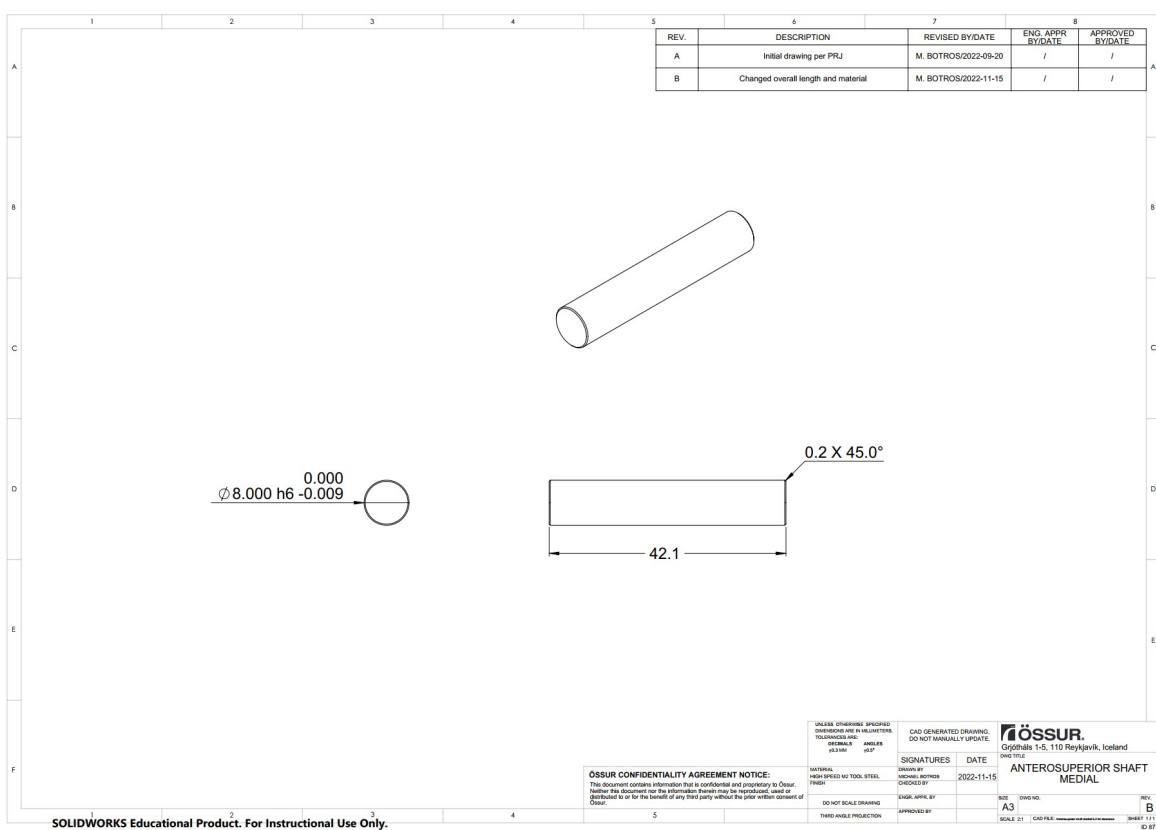


Figure I-19: Medial anterosuperior shaft.

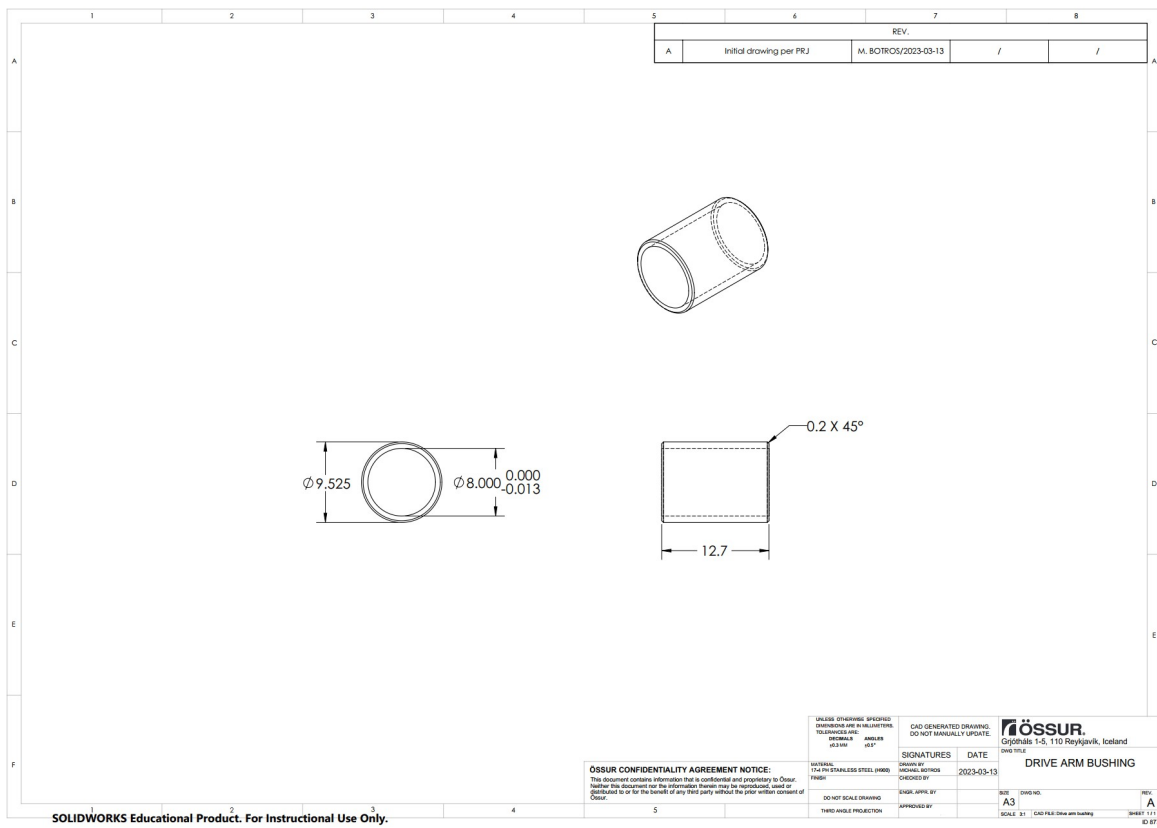


Figure I-20: Drive arm bushing.

Appendix J: Ethics Approval

18/09/2023

Université d'Ottawa

Bureau d'éthique et d'intégrité de la recherche

University of Ottawa

Office of Research Ethics and Integrity

CERTIFICAT D'APPROBATION ÉTHIQUE | CERTIFICATE OF ETHICS APPROVAL

Numéro du dossier / Ethics File Number

H-08-21-7062

Titre du projet / Project Title

DESIGN AND CLINICAL
EVALUATION OF AN
INTELLIGENT POWERED HIP
PROSTHETIC JOINT

Type de projet / Project Type

Recherche de professeur /

Professor's research project

Statut du projet / Project Status

Renouvelé / Renewed

Date d'approbation (jj/mm/aaaa) / Approval Date (dd/mm/yyyy)

18/10/2021

Date d'expiration (jj/mm/aaaa) / Expiry Date (dd/mm/yyyy)

17/10/2024

Équipe de recherche / Research Team

Chercheur / Researcher	Affiliation	Role
Hossein GHOLIZADEH	Département de génie mécanique / Department of Mechanical Engineering	Chercheur Principal / Principal Investigator
Natalie BADDOUR	Département de génie mécanique / Department of Mechanical Engineering	Co-superviseur / Co-supervisor
Michael BOTROS	Département de génie mécanique / Department of Mechanical Engineering	Étudiant-chercheur / Student-researcher
Farshad GOLSHAN	Département de génie mécanique / Department of Mechanical Engineering	Étudiant-chercheur / Student-researcher
Sarah MROZ	Département de génie mécanique / Department of Mechanical Engineering	Étudiant-chercheur / Student-researcher
Edward LEMAIRE	Département de médecine / Department of Medicine	Co-superviseur / Co-supervisor
Yousef BADER	Département de génie mécanique / Department of Mechanical Engineering	Étudiant-chercheur / Student-researcher
Kelly BRANNEN	Département de génie mécanique / Department of Mechanical Engineering	Étudiant-chercheur / Student-researcher

Conditions spéciales ou commentaires / Special conditions or comments

550, rue Cumberland, pièce 154 550 Cumberland Street, Room 154
Ottawa (Ontario) K1N 6N5 Canada Ottawa, Ontario K1N 6N5 Canada

613-562-5387 • 613-562-5338 • ethique@uOttawa.ca / ethics@uOttawa.ca
www.recherche.uottawa.ca/deontologie | www.recherche.uottawa.ca/ethics

Université d'Ottawa

Bureau d'éthique et d'intégrité de la recherche

University of Ottawa

Office of Research Ethics and Integrity

Le Comité d'éthique de la recherche (CÉR) de l'Université d'Ottawa, opérant conformément à l'*Énoncé de politique des Trois conseils* (2014) et toutes autres lois et tous règlements applicables, a examiné et approuvé la demande d'éthique du projet de recherche ci-nommé.

L'approbation est valide pour la durée indiquée plus haut et est sujette aux conditions énumérées dans la section intitulée "Conditions Spéciales ou Commentaires". Le formulaire « Renouvellement ou Fermeture de Projet » doit être complété quatre semaines avant la date d'échéance indiquée ci-haut afin de demander un renouvellement de cette approbation éthique ou afin de fermer le dossier.

Toutes modifications apportées au projet doivent être approuvées par le CÉR avant leur mise en place, sauf si le participant doit être retiré en raison d'un danger immédiat ou s'il s'agit d'un changement ayant trait à des éléments administratifs ou logistiques du projet. Les chercheurs doivent aviser le CÉR dans les plus brefs délais de tout changement pouvant augmenter le niveau de risque aux participants ou pouvant affecter considérablement le déroulement du projet, rapporter tout événement imprévu ou indésirable et soumettre toute nouvelle information pouvant nuire à la conduite du projet ou à la sécurité des participants.

The University of Ottawa Research Ethics Board, which operates in accordance with the *Tri-Council Policy Statement* (2014) and other applicable laws and regulations, has examined and approved the ethics application for the above-named research project.

Ethics approval is valid for the period indicated above and is subject to the conditions listed in the section entitled "Special Conditions or Comments". The "Renewal/Project Closure" form must be completed four weeks before the above-referenced expiry date to request a renewal of this ethics approval or closure of the file.

Any changes made to the project must be approved by the REB before being implemented, except when necessary to remove participants from immediate endangerment or when the modification(s) only pertain to administrative or logistical components of the project. Investigators must also promptly alert the REB of any changes that increase the risk to participant(s), any changes that considerably affect the conduct of the project, all unanticipated and harmful events that occur, and new information that may negatively affect the conduct of the project or the safety of the participant(s).

Coordonateur / COORDINATOR

Coordonnateur de l'éthique / Ethics Coordinator

Pour/For **Daniel LAGAREC** Président(e) du/ Chair of the **Comité d'éthique de la recherche en sciences de la santé et sciences / Health Sciences and Sciences Research Ethics Board**

550, rue Cumberland, pièce 154 550 Cumberland Street, Room 154
Ottawa (Ontario) K1N 6N5 Canada Ottawa, Ontario K1N 6N5 Canada

613-562-5387 • 613-562-5338 • ethique@uOttawa.ca / ethics@uOttawa.ca
www.recherche.uottawa.ca/deontologie | www.recherche.uottawa.ca/ethics